



CENTRUM ASTRONOMICZNE IM. MIKOŁAJA KOPERNIKA
& UNIVERSITÉ PARIS CITÉ

DOCTORAL SCHOOLS:

GeoPlanet & Astronomie et Astrophysique d'Ile-de-France (ED127)

LABORATORIES:

Centrum Astronomiczne im. Mikołaja Kopernika
& Laboratoire Univers et Théorie, Observatoire de Paris

DOCTORAL THESIS

**Dense matter properties and neutron star
modelling**

Author:

Lami SULEIMAN

THESIS FOR THE TITLES OF

Doktor nauk ścisłych i przyrodniczych w dyscyplinie
ASTRONOMII

Docteur de l'Université Paris Cité Spécialité
ASTRONOMIE ET ASTROPHYSIQUE

Publicly defended on March 31, 2023

at N. Copernicus Astronomical Center

in front of the jury composed of:

Reviewers

Dorota Rosińska, Dr hab. prof. UW (Poland)
Elias Khan, Professeur (IJCLAB, France)
Giuseppina Fiorella Burgio, Doctor (INFN, Italy)

Examiners

Tomasz Bulik, Prof. dr hab. (UW, Poland)
Sébastien Guillot, Astronome-Adjoint (IRAP,
France)
Violetta Sagun, Doctor (CFisUC, Portugal)

Supervisors

Prof. Julian Leszek ZDUNIK & Dr. Micaela OERTEL

Abstract

Lami SULEIMAN

Dense matter properties and neutron star modelling

Compact stars have a crucial role to play in the understanding of ultra dense and isospin asymmetric matter. Born in the extremely bright explosion of a massive star at the last stage of its life, neutron stars can present masses as high as twice the mass of the Sun, in a radius of around ten kilometers, thus gathering matter in their interior in extreme conditions of density and gravity. The nuclear physics probed by observing neutron stars is complementary in terms of density and isospin asymmetry to any terrestrial experiment. Multi-messenger astronomy is used to extract information on the interior of neutron stars, their structure and their composition. Connecting the observation of macroscopic parameters to the equation of state of neutron star matter requires a solid understanding of gravitation theories and modelling of the star's interior.

In this thesis, three aspects of dense matter modelling that are essential to understand neutron star properties and its macroscopic features are discussed.

The first point discussed is the construction of the equation of state of dense matter for the low and the high density parts of the neutron star interior. A common practice within the astronuclear physicists community consists in treating the core and the crust of the star with different nuclear models. However, this non-unified treatment of the equation of state results in errors on the macroscopic parameter modeling which are not negligible in the face of current and near future observational precision. In this thesis, the role of non-unified equations of state on the modeling of the mass, the radius, the moment of inertia, and the tidal deformability of a cold neutron star is assessed. Moreover, analytical representations of neutron star's equation of state based on the piecewise polytropic parametrization are provided for more than fifty modern and unified nuclear models.

The second subject presented in this thesis concerns the heat sources triggered deep in the crust of accreting neutron stars. The observed thermal relaxation of a few X-ray transients suggests that the standard approximation considering that the crust is entirely made of accreted material may not be valid for neutron stars that have accreted only small amounts of matter. In this manuscript, the equation of state of an accreting neutron star

which is partly made of a global equilibrium crust under compression, and partly of accreted material, is calculated. Heat sources in the compressed crust are determined and compared to the heat sources deposited in the fully accreted crust approximation. The impact of the kinetics of the non-equilibrium reactions leading to the crustal heating, which has been neglected in previously established calculations, is calculated for a few shells of the outer layers of accreting crusts. The reaction rate of electron captures leads to the increase of the heat release in the considered shells of the crust.

The final point discussed in this thesis concerns a neutrino emission process in the core of neutron stars, referred to as Modified Urca. Establishing the neutrino emissivity of Urca processes is important to understand the cooling of cold neutron stars, temperature dependent proto-neutron stars or binary merger remnants. Modified Urca combines the weak interaction and the strong interaction. In this thesis, the hadronic part of the Modified Urca process is derived in the framework of Thermal Quantum Field theory for finite temperature neutron star matter. A number of common approximations taken for the distribution of nucleons and the nucleon propagators are alleviated. The suppression of the Modified Urca process above the threshold of the weak interaction driven Direct Urca process is discussed for different regimes of temperature and density.

Własności gęstej materii i gwiazdy neutronowe

Gwiazdy zwarte odgrywają kluczową rolę dla zrozumienia własności ultragęstej materii. Powstałe w wyniku niezwykle silnej eksplozji masywnej gwiazdy na końcowym etapie swojego życia, gwiazdy neutronowe mogą mieć masę równą dwukrotności masy Słońca a promień rzędu 10 kilometrów stanowiąc obiekt o wyjątkowej gęstości i grawitacji. Fizyka jądrowa dostępna poprzez obserwacje gwiazd neutronowych jest uzupełnieniem ziemskich eksperymentów jądrowych pod względem gęstości i składu materii. Astronomia wieloaspektowa służy obecnie do zbierania informacji o wnętrzu gwiazd neutronowych, ich strukturze i składzie. Powiązanie obserwacji parametrów makroskopowych takich gwiazd z równaniem stanu ultragęstej materii wymaga obliczania struktury gwiazd neutronowych w ramach relatywistycznej teorii grawitacji.

W rozprawie dyskutowane są trzy aspekty badania gęstej materii istotne dla zrozumienia własności gwiazd neutronowych i ich makroskopowych cech. Pierwszym omawianym punktem jest konstrukcja równania stanu gęstej materii dla zakresu małej i dużej gęstości we wnętrzu gwiazdy neutronowej. Powszechne podejście do równania stanu gwiazdy neutronowej polega na traktowaniu jądra i skorupy gwiazdy za pomocą różnych modeli jądrowych. Taki traktowanie równania stanu skutkuje jednak błędami w wyznaczaniu parametrów makroskopowych, które nie są zanedbywalne biorąc pod uwagę precyzję obserwacji obecnie i w najbliższej przyszłości. W pracy oceniana jest rola tych efektów przy określaniu masy, promienia, momentu bezwładności i deformacji pływowej zimnej gwiazdy neutronowej. Ponadto, dla ponad pięćdziesięciu współczesnych, zunifikowanych modeli jądrowych podane są analityczne reprezentacje równań stanu gwiazdy neutronowej oparte na parametryzacji politropowej.

Drugi temat przedstawiony w tej rozprawie dotyczy źródeł ciepła zlokalizowanych głęboko w skorupie akreujących gwiazd neutronowych. Obserwowana ewolucja termiczna kilku źródeł rentgenowskich sugeruje, że standardowe przybliżenie uznające, że skorupa jest w całości zbudowana z zaakreowanej materii może nie być słuszne dla niektórych gwiazd neutronowych, które zaakreowały tylko niewielkie ilości materii. W rozprawie przedstawiono równanie stanu akreującej gwiazdy neutronowej, która jest częściowo zbudowana ze skatalizowanej skorupy poddanej kompresji, a częściowo z materiału zaakreowanego, porównując źródła ciepła w tych dwóch obszarach. Wpływ kinetyki tej reakcji, która była zanedbywana w poprzednich analizach, jest wyznaczany dla kilku powłok zewnętrznych skorup akrecyjnych. Pokazano, że tempo reakcji wychwytu elektronów ma wpływ na ciepło wydzielane w skorupie.

Ostatnie zagadnienie przedstawione w rozprawie dotyczy procesu emisji neutrin w jądrze gwiazd neutronowych, określanego jako Modified Urca. Ustalenie emisywności neutronowej w procesach Urca jest ważne dla zrozumienia chłodzenia gwiazd neutronowych, termicznej ewolucji proto-gwiazd neutronowych. W procesie Modified Urca istotne są zarówno oddziaływania słabe jak i silne. W rozprawie, hadronowa część procesu Modified Urca jest

wyprowadzona w ramach kwantowej teorii pola dla materii gwiazd neutronowych o skończonej temperaturze. Tłumienie procesu Modified Urca powyżej progu procesu Direct Urca jest dyskutowane dla różnych zakresów temperatury i gęstości.

Propriétés de la matière dense et modélisation d'étoiles à neutron

Les étoiles compactes jouent un rôle crucial dans la compréhension de la matière ultra dense et asymétrique en isospin. Nées de l'explosion extrêmement lumineuse d'une étoile massive au dernier stade de sa vie, les étoiles à neutrons peuvent avoir des masses aussi élevées que deux fois celle du Soleil, dans un rayon d'une dizaine de kilomètres, rassemblant ainsi la matière en leur sein dans des conditions extrêmes de densité et de gravité. La physique nucléaire sondée par l'observation des étoiles à neutrons est complémentaire en termes de densité et d'asymétrie en isospin aux expériences terrestres. Dans ce contexte, l'astronomie multi-messagers nous aide à extraire des informations sur l'intérieur des étoiles à neutrons, sur leur structure et sur leur composition. Relier les observations des paramètres macroscopiques à l'équation d'état de la matière des étoiles à neutrons nécessite une solide compréhension des théories de la gravitation et de la modélisation des paramètres macroscopiques de l'étoile.

Dans cette thèse, trois aspects de la modélisation de la matière dense qui sont essentiels pour comprendre les propriétés des étoiles à neutrons et leur caractéristiques macroscopiques sont discutés.

Le premier point abordé est la construction de l'équation d'état de la matière dense pour les parties à basse et à haute densité de l'intérieur de l'étoile à neutrons. Une pratique courante au sein de la communauté des astrophysiciens nucléaires consiste à traiter le cœur et la croûte de l'étoile avec des modèles nucléaires différents. Cependant, ce traitement non-unifié de l'équation d'état entraîne des erreurs sur la modélisation des paramètres macroscopiques qui ne sont pas négligeables au regard de la précision actuelle et future des observations. Dans cette thèse, le rôle des équations d'état non-unifiées sur la modélisation de la masse, du rayon, du moment d'inertie et de la déformabilité de marée d'une étoile à neutrons froide est évalué. De plus, des représentations analytiques de l'équation d'état de l'étoile à neutrons basées sur une paramétrisation polytropique par morceaux sont fournies pour plus de cinquante modèles nucléaires modernes et unifiés.

Le deuxième sujet présenté dans cette thèse concerne les sources de chaleur déclenchées dans les profondeurs de la croûte des étoiles à neutrons en accréation. La relaxation thermique observée de quelques astres/objets transitoires en rayons X suggère que l'approximation standard considérant que la croûte est entièrement constituée de matière accrétée peut ne pas être valide pour les étoiles à neutrons qui n'ont accrété que de petites quantités de matière. Dans ce manuscrit, l'équation d'état d'une étoile à neutrons en accréation qui est d'une part constituée d'une croûte en équilibre global sous compression, et d'autre part de matière accrétée, est calculée. Les sources de chaleur dans la croûte comprimée sont détaillées et comparées aux sources de chaleur déposées dans l'approximation de la croûte entièrement accrétée. Les captures électroniques sont des réactions qui enrichissent en neutrons la croûte des étoiles à neutrons en accréation ; ce processus est important pour modéliser la relaxation thermique de l'étoile puisque les captures électroniques déposent de la chaleur dans la croûte. L'impact de la cinétique de cette réaction, qui a été négligé dans les calculs

établis précédemment, est calculé pour quelques couches externes des croûtes en accréation. Le rôle que jouent les taux de réaction de captures électroniques sur la chaleur libérée dans la croûte est non négligeable pour les couches les plus surfaciques de la croûte.

Le dernier point abordé dans cette thèse concerne un processus d'émission de neutrinos dans le cœur des étoiles à neutrons, appelé Urca modifié. Etablir l'émissivité des neutrinos des processus Urca est important pour comprendre le refroidissement des étoiles à neutrons froides, des proto-étoiles à neutrons qui dépendent de la température, ou des restes de fusion de binaire d'étoiles à neutrons. L'Urca modifié combine interaction faible et interaction forte. Dans cette thèse, la partie hadronique du processus Urca modifié est dérivée dans le cadre de la théorie des champs quantiques thermiques pour la matière d'étoile à neutrons à température finie. Un certain nombre d'approximations couramment prises pour la distribution des nucléons et les propagateurs des nucléons sont retirées. La suppression du processus Urca modifié au-dessus du seuil du processus Urca direct est discutée pour différents régimes de température et de densité.

Acknowledgements

First, I would like to express my deepest gratitude to my two supervisors, Leszek and Micaela, who have been exceptional advisors during this PhD. Both of them, beyond being experts in their field, have been present and supporting for every aspect of this thesis. I am very aware of how lucky I was to have not one, but two supervisors who have made those three years and a half a pleasure. I would also like to thank them both for showing me a multitude of aspects of neutron star physics, and for introducing me to scientific collaborations.

I am also grateful to Morgane Fortin for taking the role of my unofficial mentor. She introduced me to neutron stars and how fascinating they are, but also made me meet my future supervisors. I thank her also for preparing me to the professional challenges that will await me. I am also very grateful to Pawel Haensel for his advise and expertise, which he shared with me throughout the studies.

Special thanks to the Neutron Star group at CAMK and the ROC team in LUTH for their warm welcome and professional atmosphere. Thanks should also go to collaborators Anthea Fantina and Nicolas Chamel for their expertise and input on accreting neutron stars. I also had the pleasure of being a member of the Virgo group of LUTH/Caen, and it is for me an example of a successful collaboration between very competent and also kind people.

Finally I want to thank all my family for their love and kindness. Thank you to my partner for his calming presence during those three years. Thank you to my sister for her support. And especially, thank you to my mother to whom I owe so much.

This work was supported by the N. Copernicus Astronomical Center, the National Science Center of Poland grant number 2018/29/B/ST9/02013 and number 2017/26/D/ST9/00591, the Observatoire de Paris, the Centre National de la Recherche Scientifique, the Laboratoire Univers et Théories, and the PHAROS collaboration.

Physical Constants

M_{\odot}	Solar mass = 1.989×10^{33} g
c	speed of light = 2.9979×10^{10} cm/s
G	gravitational constant = 6.6720×10^{-8} cm ³ /g/s ²
\hbar	reduced Planck constant = 6.582×10^{-16} eV/s
$\hbar c$	conversion constant = 197.33 MeV
n_0	baryon saturation density = 0.16 fm ⁻³
ρ_0	saturation mass density = 2.4×10^{14} g/cm ⁴
m_B	baryon mass-energy = 939 MeV
m_n	neutron mass-energy = 939.565 MeV
m_p	baryon mass-energy = 938.272 MeV
m_e	electron mass-energy = 0.511 MeV
k_B	Boltzmann constant = 1.3807×10^{-16} erg/K

List of Symbols

ρ	mass density	g/cm^3
P	pressure	dyn/cm^2
ϵ	energy density	MeV/fm^{-3}
n or n_B	baryonic density	fm^{-3}
Z	proton number	
N	neutron number	
A	nucleon number	
M	total mass	M_\odot
R	total radius	km
Λ	tidal deformability	
I	moment of inertia	g cm^3
C	compactness	
Γ	adiabatic index	
MSP	millisecond pulsar	
GW	gravitational wave	
EoS	equation of state	
\mathbf{v}	tri-dimensional vector v	
$\mathbf{a} \cdot \mathbf{b}$	scalar product of \mathbf{a} and \mathbf{b}	
$a \cdot b$	scalar product of a and b	
$a \wedge b$	vector product of a and b	
A^μ	tensor A with grec indices $\mu = 0, 1, 2, 3$	
A^i	tensor A with latin indices $i = 1, 2, 3$	
$\delta(x)$	Dirac delta function	
$\delta^{\mu\nu}$	Krönecker delta function	
δ	asymmetry parameter	

Contents

Abstract	iii
Acknowledgements	ix
Physical Constants	xi
List of Symbols	xiii
1 Outline of the manuscript	1
2 Introduction to neutron stars physics	3
2.1 Historical review	4
2.1.1 First theoretical approach	4
2.1.2 From a strange radio signal to the era of multi-messenger astronomy	4
2.2 The fate of main sequence stars	9
2.3 Structure of an "adult" neutron star	11
3 A laboratory for dense matter: the equation of state mystery	13
3.1 Theoretical framework of strong interaction modelling	15
3.1.1 Phenomenological models	15
3.1.2 Microscopic models	23
3.1.3 The unknown composition of the core	24
3.2 Microphysics constraints on the equation of state	28
3.2.1 Constraints on the outer crust	28
3.2.2 Incorporating constraints at moderate and high density	29
3.3 Astrophysical constraints on dense matter	34
3.3.1 Macroscopic parameter modelling and observations	34
3.3.2 Astrophysical constraints on the microphysics parameters	54
3.4 Consequence of non-unified models for dense matter on neutron star modelling	57
3.4.1 Unified <i>vs.</i> non-unified equations of state	57
3.4.2 Consequence on macroscopic parameter's modelling	63
3.4.3 Role of non-unified constructions in quasi-universal relations	70
3.5 Analytical representations of modern and unified equations of state	80
3.5.1 Piecewise polytropic fits	80
3.5.2 PPFRead <i>vs.</i> unified equations of state	81

3.5.3	Revising piecewise polytropic fits from modern and unified equations of state	84
4	Crust compression related astrophysical phenomena	93
4.1	Accreting neutron stars	95
4.1.1	From the donor to the neutron star crust	95
4.1.2	Deep crustal heating	97
4.2	Partially accreted crusts	102
4.2.1	Beyond the fully accreted crust approximation	102
4.2.2	Heat sources in a compressed catalyzed crust	105
4.2.3	Onset of the neutron drip	115
4.2.4	Applications for rotating neutron stars and magnetars	117
4.2.5	Properties of a compressed crust	118
4.3	Layers of electron captures in accreting neutron stars	126
4.3.1	Electron captures	126
4.3.2	The linear mixing rule approach to a mixture of nuclei	135
4.3.3	The continuity equation	138
4.3.4	Stationary solution	141
4.3.5	Solution to the full continuity equation	145
5	Modified Urca neutrino emission at finite temperature	151
5.1	Direct and Modified Urca processes	153
5.1.1	The Direct Urca process	153
5.1.2	The Direct Urca threshold	154
5.1.3	State of the art of Modified Urca derivations	155
5.2	Modified Urca neutrino opacity at finite temperature	157
5.3	Hadronic part of the Modified Urca process	169
5.3.1	Derivation of the spin and isospin terms	169
5.3.2	The hadronic polarization function treated in the Matsubara formalism	179
5.4	Numerical treatment of the momenta integrations with the Monte-Carlo method	182
5.5	Results of the Monte-Carlo integration for the hadronic part of Modified Urca	185
5.5.1	Numerical divergence above the Direct Urca threshold	185
5.5.2	The vector contribution	188
5.5.3	The role of the denominator of \mathcal{N} functions	190
5.5.4	Modified Urca suppression above the Direct Urca threshold	192
6	Conclusion and perspectives	201
A	Details for the spin part of the Modified Urca derivation	203
A.1	Self-energy contributions	203
A.2	Vertex V_2	205
A.3	Vertex V_3	206
B	Details on the Matsubara sums	209

B.1	Use of Residue theorem in sums on the imaginary axis	209
B.2	Properties of Bose-Einstein and Fermi distributions	210
C	Expression for the \mathcal{M} functions	211
C.1	Direct and exchange diagram	211
C.2	Second vertex diagram	212
C.3	Third vertex diagram	213
C.4	Center of mass change in variables	214
C.4.1	Details for the first self-energy correction	214
C.4.2	Expression for the second self-energy correction	215
C.4.3	Expression for the second vertex	216
C.4.4	Expression for the third vertex	217

1 Outline of the manuscript

The extreme conditions of matter inside neutron stars makes them fascinating objects to study in astronomy, in nuclear physics and in theories of gravitation. As the densest stars in the Universe, they are observed in all wavelengths of the luminosity spectrum, yet carry fundamental and intriguing mysteries. The innermost parts of neutron stars are subject to densities way beyond the limits of nuclear physics laboratories on Earth. Fortunately, the increase in accuracy of multi-messenger astronomy offers the possibility of exploring ultra dense matter in "neutron star laboratories" by comparing observations to nuclear models established by astronuclear physicists. In this manuscript, we explore the link between the microphysics of ultra dense matter and the modelling of neutron star's macroscopic features. The text is separated in four chapters.

In chapter 2, a brief historical overview of the theoretical and observational discovery of neutron stars is presented in section 2.1. Multi-messenger observations of neutron stars are also discussed in this section. The collapse supernova process leading to the birth of neutron stars is introduced in section 2.2. This chapter ends with the description of the neutron star structure in section 2.3.

Chapter 3 focuses on the microscopic description of neutron star's interior. First, the different approaches to the theoretical description of dense matter are presented in section 3.1. The nuclear physics constraints on the theories of neutron star matter are discussed in section 3.2. The modelling of neutron star's macroscopic parameters, and how measurements of the mass, the radius, the tidal deformability and the moment of inertia, can help constrain dense matter are discussed in section 3.3. We study a construction of neutron star's equations of state that leads to errors on macroscopic parameter's modelling in section 3.4, and propose an analytical representation of modern equations of state for cold matter equations of state. This chapter discusses studies described in two papers: the first one is entitled "Influence of the crust on the neutron star macrophysical quantities and universal relations" [Suleiman et al., 2021] and the second one is entitled "Polytropic fits of modern and unified equations of state" [Suleiman et al., 2022a].

In chapter 4, the compression of the neutron star's crust is discussed. The process of accretion is introduced in section 4.1. We also discuss a heating process deep in the crust of accreting neutron stars, and how this phenomenon is observed in the thermal relaxation of neutron stars. In section 4.2, we introduce partially accreted crusts and compute the catalogue of heat sources and properties of the crust for a neutron star that has accreted small amounts of matter; this was the subject of a paper entitled "Partially accreted crusts

of neutron stars" [Suleiman et al., 2022b]. In section 4.3, the common approximation to the kinetics of exothermic reactions in accreting neutron star's crusts is revised. The reaction rate of electron captures is derived, and the impact of layers of electron captures on the heat deposited in accreting neutron stars is calculated.

The neutrino emission process Modified Urca is discussed in chapter 5. After a brief introduction on the weak interaction driven Direct Urca process and its threshold in neutron star's core, the Modified Urca process is introduced in section 5.1. The framework of the derivation for the neutrino emissivity of the Modified Urca process at finite temperature is presented in section 5.2, and we also present the different Modified Urca reactions involving with electrons, positrons, neutrons and protons. Section 5.3 focuses on the derivation of the hadronic part of the process; details of this derivation are also given in Appendix A. The numerical method used to compute the hadronic polarization function of Modified Urca is presented in section 5.4. Results are presented and discussed in section 5.5.

2 Introduction to neutron stars physics

At the crossroads between the fields of nuclear physics, astronomy and theories of gravitation, neutron stars have become extraterrestrial laboratories used to test ultra dense matter, and the limits of Einstein's theory of general relativity. In consequence of the development of multi-messenger astronomy, neutron stars encompass a large variety of fields in physics, whose nomenclature are introduced in this chapter.

In section 2.1, we present a brief history of the neutron star field of study, starting with the emergence of neutron star theory and the first detection of neutron star's electromagnetic signatures, to today's multi-messenger astronomy, and the prospects for the next generation of observers.

In section 2.2, the birth of a neutron star in a core collapse supernova is briefly discussed.

In section 2.3, we present the general structure of a neutron star.

Contents

2.1	Historical review	4
2.1.1	First theoretical approach	4
2.1.2	From a strange radio signal to the era of multi-messenger astronomy	4
2.2	The fate of main sequence stars	9
2.3	Structure of an "adult" neutron star	11

2.1 Historical review

2.1.1 First theoretical approach

The story of neutron stars may have started with the publication of the paper entitled *Possible Existence of a Neutron* by Sir James Chadwick in February 1932 [Chadwick, 1932]. The discovery of a new elementary particle with no electric charge shifted the world of atomic physics to the era of nuclear physics. However, this same month of February, Lev Landau published a paper entitled *On the Theory of Stars* [Landau, 1932] in which he hypothesized the existence of a star that would "form one gigantic nucleus". The common knowledge is that the discovery of neutrons inspired the paper of Lev Landau but, upon closer inspection of the timeline of the paper, Landau's theory may have predated the discovery of neutrons, see Yakovlev et al. [2013] for details.

The first mention of "neutron stars" appeared in 1934 in a series of papers written by Walter Baade and Fritz Zwicky [Baade and Zwicky, 1934a,b,c], in which the authors who were attempting to explain observations of supernovae, suggested that neutron stars might be the result of the explosion of massive stars. They highlighted the role of ultra dense matter in the compactness of those stars: "Such a star may possess a very small radius and an extremely high density. As neutrons can be packed much more closely than ordinary nuclei and electrons [...] A **neutron star** would therefore represent the most stable configuration of matter as such."

A few years later, Richard Tolman as well as J. Robert Oppenheimer and George Volkoff, separately derived the equations of hydrostatic equilibrium for a spherically symmetric star [Tolman, 1939, Oppenheimer and Volkoff, 1939], and established the Tolman-Oppenheimer-Volkoff equations in the framework of Albert Einstein's theory of general relativity. Although Oppenheimer and Volkoff [1939] established a solution to those equations for a degenerate gas of relativistic neutrons, they did not take into account the effects of the repulsive nucleon interaction on the maximum mass of a neutron star, only suggested that it might increase it significantly. Twenty years later, Alastair Cameron [Cameron, 1959] solved the Tolman-Oppenheimer-Volkoff equations for a star made of a degenerate gas of relativistic neutrons with a repulsive neutron-neutron interaction, and obtained a maximum mass around twice the mass of the Sun, an approximate limit value still valid today.

In the early 1960s, a boom in the field of dense matter was triggered. Many theories on the presence in the core of "exotic" particles such as pions and kaons condensates, hyperons, deconfined quarks were suggested [Ambarsumyan and Saakyan, 1960]. From then on, the pursuit of the neutron star equation of state was launched for astronuclear physicists.

2.1.2 From a strange radio signal to the era of multi-messenger astronomy

In 1967, Dame Susan Jocelyn Bell Burnell, who was a graduate student at the time, was actively researching signatures of interplanetary scintillations in the radio wavelength. During this year, she observed a very regular signal whose periodicity suggested that it

originated from a compact star, and the paper *Observation of a Rapidly Pulsating Radio Source* [Hewish et al., 1968] was published a year later. Its first author, Antony Hewish who was Jocelyn Bell's supervisor was awarded the 1974 Nobel prize "for [...] pioneering research in radio astrophysics: [...] for his decisive role in the discovery of pulsars" [Nobel Prize Outreach AB, 2022]. At the end of the 1960s, neutron stars were decisively identified as pulsars when the Vela [Radhakrishnan and Manchester, 1969] and Crab [Boynton et al., 1969] sources were discovered. White dwarfs were excluded as candidates by Thomas Gold, who showed that only neutron stars could sustain the centrifugal force of such short rotation periods (of the order of tens of milliseconds) [Gold, 1968].

It is beyond the scope of this manuscript to present an exhaustive list of instruments observing neutron stars, but a few are mentioned in the following.

The catalog **SIMBAD** gathers around 3000 observations of pulsating neutron stars. Neutron stars spin and are magnetized, and the magnetic field is not necessarily aligned with the rotational axis. Depending on the line of sight of the observer, the rotating star's dipolar magnetic field produces electromagnetic radiation observed in the radio band, pulsating with a period directly related to the spin of the star. Pulsating neutron stars are called Pulsating Radio Sources, oftentimes abbreviated PSR to name observed sources, or simply pulsars. The physics of pulsar's emission relies on modelling the complex geometry of the emitting magnetosphere. The diagram of pulsar's periods and their time derivative, showed that pulsars can be categorized between millisecond pulsars and non-millisecond pulsars. This led to the understanding of the spin recycling from the accretion process in binaries [Radhakrishnan and Srinivasan, 1982]. Among the telescopes observing pulsars in radio are the observatories of Parkes (Australia), Green Bank (United States of America) and Nancay (France). The Arecibo observatory in Porto Rico has been operating for almost sixty years, although it fell in November 2020. The Five-hundred-meter Aperture Spherical radio Telescope [Nan et al., 2011] (China) was launched in 2017. The largest worldwide telescope Square Kilometer Array [Watts and et al., 2015] (Australia and South Africa) will be operational in a few years.

The pulses of neutron stars are precise clocks of our Universe. Pulsar timing is a technique used to extract the parameters of binary systems. The mass of the neutron star can be determined from a few of those parameters, and the over-determination of a binary system allows tests of gravitation laws. Data for the double pulsar PSR binary J0737–3039 has been collected for more than a decade and a half; the binary parameters were measured with an unprecedented precision, which showed that general relativity is accurate in the double pulsar binary, and allowed to test alternative theories of gravitation [Kramer and et al., 2021].

Neutron stars are also observed in X-rays. The spatial telescope X-ray Multi Mirror-Newton (XMM-Newton [Jansen and et al., 2001]) from the European Spatial Agency, and its American counterpart Chandra [Weisskopf et al., 2000], have been operating for more than 20 years providing X-ray data for isolated, accreting, and highly magnetized neutron

stars. The younger Nuclear Spectroscopic Telescope Array [Harrison and et al., 2013], and Neutron star Interior Composition Explorer (NICER [Gendreau et al., 2012]) observe respectively in hard, and soft X-ray. The NICER telescope is an instrument that can measure simultaneously the neutron star mass and its radius. This technology is based on the effects of general relativity on the exhibited luminosity from hot spots on the surface of a rotating neutron star. The next generation of X-ray telescopes is in preparation: the Enhanced X-ray Timing and Polarimetry [Watts and et al., 2019] mission is scheduled to be launched in 2027, and the highly anticipated Advanced Telescope for High ENergy Astrophysics (ATHENA [Hauf et al., 2011]) with a state of the art X-ray Integral Field Unit spectrometer will provide unprecedented spectral resolution for a wider effective area, with a fifteen time increase in sensitivity compared to XMM-Newton.

There has been a recent expansion of the gravitational wave area for neutron star physics. The theory of general relativity established by Albert Einstein, predicted that accelerating objects with a significant mass would perturb spacetime and emit detectable waves propagating at light speed [Einstein, 1916].

After more than a decade of rejected proposals, the Laser Interferometer Gravitational-Wave Observatory (LIGO) was finally approved: two facilities were built in the United States of America (in Hanford and Livingston) by the end of the 1990s. The first run of LIGO started in 2002, and the second one in 2010, but neither detect gravitational waves, which led to an improvement of the facilities that lasted for four years and to a significant increase in sensitivity of the detectors. From 2000 to 2003, the Virgo facility located in Italy (near Pisa) was constructed, and operated in 2007 and 2011, but reported no detection of gravitational waves either. The Virgo facility was also updated to the Advanced Virgo facility, which increased the sensitivity by a factor of ten. In September 2015, advanced LIGO detected the merger of two black holes, each of around thirty times the mass of the Sun, providing the first direct observational proof of gravitational waves [Abbott and et al., 2016].

The detection of gravitational waves is based on a large interferometer. Although the principle is simple, the technology used in gravitational wave detectors is the state of the art of noise reduction techniques. The facilities of the LIGO Scientific Collaboration, the Virgo Collaboration, and the Kamioka Gravitational Wave Detector (KAGRA) which joined the collaboration in 2019 (referred to as LVK collaboration [Abbott et al., 2020a]), provides a network of detectors able to triangulate the location of sources in the sky. The different facilities coordinate their operations with other gravitational wave detectors, but also with electromagnetic spectrum detectors.

In the catalogues of the LVK collaboration, compact objects of the binary whose mass is in the range of neutron star masses are considered to be detected neutron stars. The signature of tidal forces on neutron stars which appears in the late inspiral of the gravitational

wave signal, or the detection of a corresponding electromagnetic counterpart, can also confirm that the progenitor of the merger is a neutron star, and not just a very light black hole¹.

From the catalogues of O2 and O3 of the LVK collaboration, the following detections of compact binary mergers involving neutron stars have been reported:

- GW170817² [Abbott et al., 2017]: detected on the 17th of August 2017 by both facilities of LIGO and Virgo, as the merger of two neutron stars of roughly 1.3 and 1.5 solar mass in the galaxy NGC 4993 (about 140×10^6 light years from the Earth). The upper limit on the mass of the merger remnant was estimated to be 2.8 solar mass; whether it is a neutron star or a black hole is unclear, because this mass is located in the upper limit of neutron stars masses, but the gamma ray burst leads to a black hole signature. From this detection, the deformation of the two stars by their respective gravitational field could be extracted from the gravitational wave signal. In the few hours following the detection, electromagnetic counterparts of the transient denoted AT2017gfo were observed in various wavelengths and confirmed the transient nature of the merger remnant.
- GW190425 [Abbott and et al., 2020]: detected on the 25th of April 2019 only from the LIGO Livingston facility, as the merger of two neutron stars of respectively 2 and 1.4 solar mass, this merger resulted in a compact object of 3.2 solar mass (very likely a black hole). As the merger was detected by only one detector, no sky localization was possible, and no electromagnetic counterparts were detected.
- GW190814 [Abbott et al., 2020b]: detected on the 14th of August 2019 by LIGO Livingston and Virgo, as the merger of a 23 solar mass black hole, and a compact object of 2.6 solar mass whose nature is unclear. The location of the source was estimated to be at around 800×10^6 light years from the Earth, and despite tremendous effort, no electromagnetic counterpart was detected.
- GW200105_162426 [Abbott et al., 2021]: detected on the 5th of January 2020 by LIGO Livingston and Virgo, as the merger of a nine solar mass black hole and a 1.9 solar mass compact object (likely a neutron star), with no electromagnetic counterpart.
- GW200115_042309 [Abbott et al., 2021]: detected on the 15th of January 2020 by both facilities of LIGO and Virgo, as the merger of a 5.9 solar mass black hole and a 1.4 solar mass compact object (likely a neutron star), with no electromagnetic counterpart.

Prospects for gravitational wave detections are optimistic. The LVK collaboration shall continue to operate starting in Spring 2023, with the O4 run. Upgrade of the facilities includes the reduction of quantum noise (vacuum fluctuations) through squeezing, and of the

¹Let us note that the tidal deformability of black holes was recently discussed in the paper entitled "Spinning Black Holes fall in Love" [Le Tiec and Casals, 2021].

²The nomenclature for gravitational wave detection is GWYearMonthDay_HourMinutesSeconds. The notation of hours, minutes and seconds was introduced in anticipation of the increase in sensitivity of the detectors, which would lead to several detections per day. However, most sources are referred to with the notation GWYearMonthDay.

thermal noise through better mirror coatings. These improvements will increase the sensitivity of the Virgo detectors such that the Advanced Virgo facility which was able to detect binary neutron stars mergers down to a distance of 50 Mpc during O3, will be able to push it to 120 Mpc for O4. Further improvements for the O5 run of the Virgo detector should increase this number to 260 Mpc, and to 325 Mpc and 128 Mpc in the LIGO and KAGRA facilities, see [Abbott et al. \[2018\]](#).

Although the LVK collaboration was scheduled to operate five runs only, there are plans to push the facilities to their limit until the next generation of gravitational wave detectors are operational; for example, that is the plan for the Virgo_nExt project scheduled to start this decade, which will provide an upgrade with increased sensitivity.

The third generation of gravitational waves includes two projects of interest for neutron stars:

- Einstein telescope [[Maggiore and et al., 2020](#)]: a detector with arms of ten kilometers located in Europe, which includes cryogenic technology and is constructed underground to reduce seismic noise. The sensitivity of this instrument is expected to detect 10^5 binary neutron star mergers (and 10^6 binary black hole mergers) per year, with a significant improvement on the mass measurement, hence the deformability, in the inspiral signal of a neutron star binary merger. In addition, the detector will allow for the detection of continuous gravitational waves, for example the waves emitted by a rotating neutron star with a significantly high mountain. The underground and cryogenic characters of the Einstein telescope (which are also the most expensive) would benefit low frequency gravitational waves. The coalescence stage of a double neutron star binary merger emits in the kHz frequency, whereas the early stage of the inspiral emits at lower frequencies down to the Hz. Detecting low frequency gravitational waves is useful for multi-messenger astronomy because the merger signal is sent well in advance of the coalescence, such that the electromagnetic counterparts can be more easily searched for.
- Cosmic Explorer [[Evans and et al., 2021](#)]: two classic interferometers with forty kilometer and twenty kilometer long arms located in the United States of America.

2.2 The fate of main sequence stars

Neutron stars are born from the explosion of stars in the last stages of their life. There are several types of supernovae (for the first mention of the phenomenon, see [Baade and Zwicky \[1934a\]](#)), but we shall focus on the core-collapse supernovae in the following.

A main sequence star with a mass of at least eight times the mass of the Sun, undergoes a series of nuclear fusions, first burning Hydrogen, then Helium, Carbon, Oxygen, and continuing with heavier elements until it burns into Iron. At this stage in its life, the star is a giant which has exhausted its fuel: Iron presents the highest binding energy per nucleon of the periodic table, in other words it is an extremely stable nucleus, such that fusion beyond this element does not produce energy. The star presents an Iron core, and an onion like structure with the outer shells undergoing fusions, for details see [Bethe et al. \[1979\]](#). The end of the fusion chain is crucial in understanding core-collapse supernovae. As thermal fusion is no longer provided in the core made of Iron, the source of pressure counterbalancing the self-gravitation is purely that of degenerate electrons. At this stage in the life of the star, its mass can be approximated by the Chandrasekhar mass [[Chandrasekhar, 1931](#)]. Once the Iron core goes beyond the Chandrasekhar mass limit, the pressure from the electron gas is not sufficient to counterbalance self-gravitation, and the collapse of the star begins.

Supernovae are extreme events, in terms of energy and timescale; we refer to [Janka \[2012\]](#) for a review of the core-collapse supernova process. The iron core shrinks about thirty times its size in half a second, and it is transformed into a plasma of neutrons and protons. Nucleons closely compacted together interact in neutrino emission processes out of equilibrium, thus neutronizing matter, and emitting neutrinos. A critical density defines whether neutrinos can escape (taking energy away with them) or are trapped inside the core [[Janka et al., 2007](#)]. The outer layers of the core keep falling to the center with a speed around one tenth of the light velocity. The collapse of the Iron nuclei on the plasma core produces a shock wave. This wave propagates outwards until it stagnates because of lack of energy about 150 km away from the center. The explosion lasts for about two seconds, but the shock wave takes time to reach the surface of the star (a few hours), contrary to gravitational waves and the neutrinos emitted. As the shock wave reaches the surface, the first electromagnetic signal of the explosion is sent.

Supernovae are rare events, estimated to occur in our Galaxy around two times per century, [[Diehl and et al., 2006](#)]. The ejecta shines very brightly for a few months in the visible band of the electromagnetic spectrum. The supernova SN 1987A located in the Magellan constellation is the last observed supernova. To date, no supernova was observed in our Galaxy with telescopes. There are however written reports of these event, for example of the supernova SN 1054, whose nebula is well monitored, as well as the famous Crab pulsar remnant (for details on this extremely bright event, see [Li et al. \[2015\]](#)).

Supernovae are the host of heavy element nucleosynthesis driven by neutrino emission

[Arcones and Thielemann, 2013]; among the nucleosynthesis mechanisms, there is the rapid-neutron capture, also referred to as the r -process. This process is also present in merging neutron stars, and is the origin of a large number of elements in the periodic table [Woosley and Janka, 2005].

The remnant of the supernova implosion is the proto-neutron star, which contracts progressively to a radius of the order of ten kilometers in a few dozens of seconds. For details on the evolution of proto-neutron stars and the role of neutrinos, we refer to Prakash et al. [1997], Pascal et al. [2022].

2.3 Structure of an "adult" neutron star

In the following "adult" neutron stars refer to neutron stars which have cooled down from their proto-neutron star stage. The structure in layers of adult neutron stars is presented in Fig. 2.1, and we refer to section 1 of [Haensel et al. \[2007a\]](#) for further details.

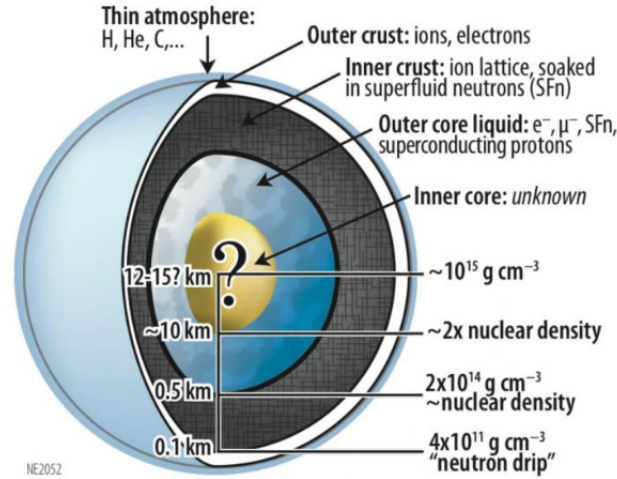


Figure 2.1: Layer structure of an adult neutron star, figure extracted from [Gen-dreau et al. \[2012\]](#).

The outer part of the star is the envelope, and is separated into the atmosphere (gas of light elements) and the ocean (Coulomb liquid of light elements). The envelope plays an important role in the luminosity spectrum exhibited by the star, although it is only a few centimeters thick.

Below the envelope, the crust extends from the bottom of the ocean at a mass density $\rho \sim 10^6 \text{ g/cm}^3$, to the crust-core transition; it is a few hundred meters thick. The crust is separated in two parts

- The outer crust: a lattice of ions permeated by a gas of electrons (mostly degenerate, except for a thin outer layer). The outer crust ends at the mass density $\rho \sim 10^{11} \text{ g/cm}^3$, defined by the neutron drip density.
- The inner crust: a lattice of neutron rich ions permeated by a gas of electrons and unbound neutrons. It is around one kilometer in thickness. Free neutrons are susceptible to superfluidity; the neutron superfluid in rotating neutrons stars can lead to glitches, which are irregularities in the rotation frequency of the star [[Fuentes et al., 2018](#)].

The transition between the lattice of ions and the homogeneous matter of the core occurs around the mass density $\rho \sim 10^{14} \text{ g/cm}^3$. In the deepest end of the inner crust, nuclei are deformed in what is referred to as the pasta phases [[Ravenhall et al., 1983](#), [Dinh Thi et al., 2022](#)].

The core is also separated into the outer core and the inner core; it concentrates most of the star's mass, and can reach densities as high as a few times $\rho \sim 10^{15} \text{ g/cm}^3$. The outer crust is made of a soup of neutrons, protons, electrons and muons. The inner core composition is an open question of neutron star's physics. Aside from the neutrons, protons, electrons and muons, one hypothesis assumes the appearance of hyperons. Another hypothesis consists in finding deconfined quarks instead of a hadronic structure.

In conclusion, there are a large number of different ways to detect neutron star's activity. Ultra dense matter can be explored from two perspectives: either as an astrophysicist trying to understand the behaviour of neutron stars, or as a nuclear physicist trying to explore dense matter. In the first case, the microscopic properties of dense matter are an input which is necessarily nuclear model dependent as conditions of density in the core are not understood for now. In the latter case, the macroscopic and observable behavior of neutron stars is used to probe the unknown physics of extremely dense matter. In both cases, multi-messenger astronomy is a tool that allows to probe neutron star interior in a way that is out of reach for Earth based laboratories.

3 A laboratory for dense matter: the equation of state mystery

Despite continuous efforts to push the limits of nuclear experiments, conditions of density and temperature in the deepest layers of neutron stars remain out of reach for laboratories. The microphysics of neutron star matter is a crucial element to determine the astrophysical features of neutron stars. The equations of relativistic hydrodynamics act as a bridge between ultra dense matter, and observable macroscopic parameters of neutron stars. In that sense, neutron stars are laboratories testing gravity theories and nuclear physics. Multi-messenger astronomy provides a chance to probe deep inside those extremely compact stars.

In this chapter, we discuss the role of the equation of state of neutron star's interior on macroscopic parameter modelling.

In section 3.1, the theoretical framework to model dense matter in neutron stars is presented.

Experimental and theoretical constraints on the equation of state from microphysics are discussed in section 3.2.

In section 3.3, the derivation of the main macroscopic parameters of neutron stars is presented, and we explore the different ways that multi-messenger astronomy can impose constraints on the equation of state of ultra dense matter.

In section 3.4, we discuss the importance of designing the high density part and the low density part of neutron stars with the same nuclear model, and the consequences on macroscopic parameter modelling if otherwise. Results presented in this section are the subject of the publication [Suleiman et al. \[2021\]](#).

Finally, in section 3.5, we present an analytical representation based on piecewise polytropes for modern and unified equations of state. Results presented in this section are the subject the publication [Suleiman et al. \[2022a\]](#).

Contents

3.1	Theoretical framework of strong interaction modelling	15
3.1.1	Phenomenological models	15
3.1.1.1	Relativistic mean field theory	15
3.1.1.2	Skyrme energy density functionals	20
3.1.1.3	Treating inhomogeneous matter	23
3.1.2	Microscopic models	23
3.1.3	The unknown composition of the core	24
3.2	Microphysics constraints on the equation of state	28
3.2.1	Constraints on the outer crust	28
3.2.2	Incorporating constraints at moderate and high density	29
3.3	Astrophysical constraints on dense matter	34
3.3.1	Macroscopic parameter modelling and observations	34
3.3.1.1	Mass and radius	34
3.3.1.2	Moment of inertia	44
3.3.1.3	Tidal deformability	50
3.3.2	Astrophysical constraints on the microphysics parameters	54
3.4	Consequence of non-unified models for dense matter on neutron star modelling	57
3.4.1	Unified <i>vs.</i> non-unified equations of state	57
3.4.2	Consequence on macroscopic parameter's modelling	63
3.4.3	Role of non-unified constructions in quasi-universal relations	70
3.4.3.1	Universal relation $C - \Lambda$	74
3.4.3.2	Universal relation $\Lambda - \bar{I}$	77
3.4.3.3	Universal relation $I - C$	77
3.5	Analytical representations of modern and unified equations of state	80
3.5.1	Piecewise polytropic fits	80
3.5.2	PPFRead <i>vs.</i> unified equations of state	81
3.5.3	Revising piecewise polytropic fits from modern and unified equations of state	84

3.1 Theoretical framework of strong interaction modelling

Astronuclear physicists rely on nuclear models to describe the equation of state (EoS) of dense matter. Throughout this thesis, no theory of quantum gravitation will be discussed, such that the model of nuclear interaction is established outside of the theory of gravitation, using the Minkowski metric

$$\eta_{\mu\nu} = \begin{pmatrix} 1 & 0 & 0 & 0 \\ 0 & -1 & 0 & 0 \\ 0 & 0 & -1 & 0 \\ 0 & 0 & 0 & -1 \end{pmatrix}, \quad (3.1)$$

in signature $(+, -, -, -)$ ¹. This is a correct approach when the curvature of space-time can be considered sufficiently small locally. Given their compactness, neutron stars should be an ideal candidate to probe the role of gravitation coupling to strong interaction, however, no such considerations will be taken in this manuscript.

In this section, we present several approaches to the strong interaction in dense matter. The discussion is focused on β -equilibrated and cold matter modelling, *i.e.* modelling of a neutron star, neither in its proto-neutron star stage, nor in or post merger. Such considerations result in one parameter equations of state: there is only one independent variable, which we choose to be the density. We shall also concentrate on catalyzed matter, or in other words, matter at ground state. Throughout this manuscript, a set of around sixty equations of state will be used; this set is non exhaustive. We refer to the database CompStar Online Supernovae Equations of State [CompOSE \[Typel and et al., 2022\]](#) for an extensive catalogue of cold and finite temperature equations of state of dense matter, and to [Oertel et al. \[2017\]](#) for a review on neutron star equations of state.

3.1.1 Phenomenological models

Nuclear interaction can be modelled as a parametrized effective interaction between hadrons, that is what we call a phenomenological approach. Parameters of the theory are then calibrated to the results of nuclear laboratory experiments. In the following, we introduce two phenomenological approaches to neutron star matter at β -equilibrium: relativistic mean field models and non-relativistic Skyrme theory.

3.1.1.1 Relativistic mean field theory

The relativistic mean field (RMF) description of nucleonic matter is a phenomenological approach in which particles are considered to be immersed in a self-consistent single particle potential established in quantum field theory. The strong interaction between nucleons is mediated by the following meson fields:

¹The metric signature usually depends on the field of study: the signature $(+, -, -, -)$ is used in nuclear physics, and $(-, +, +, +)$ is used in gravitation.

- Scalar-isoscalar² meson field, denoted σ , with a zero spin and zero isospin. The Lagrangian density of such fields is that of a typical scalar field with mass m_σ and self-interaction terms of j order

$$\mathcal{L}_\sigma = \frac{1}{2} \left(\partial^\mu \sigma \partial_\mu \sigma - m_\sigma^2 \sigma^2 \right) - \sum_{j=3}^{j_{\max}^\sigma} \frac{g_{\sigma_j}}{j!} \sigma^j, \quad (3.2)$$

with g_{σ_j} the coupling constants of the σ -field self-interaction of order j , and j_{\max}^σ the maximum order for the self-interaction of the field σ .

- Scalar-isovector meson field, denoted δ , with a spin zero and isospin one; its Lagrangian density resembles that of the meson field σ , but the meson field δ is a three-component vector

$$\mathcal{L}_\delta = \frac{1}{2} \left(\partial^\mu \delta \cdot \partial_\mu \delta - m_\delta^2 \delta^2 \right) - \sum_{j=3}^{j_{\max}^\delta} \frac{g_{\delta_j}}{j!} \delta^j, \quad (3.3)$$

with g_{δ_j} the coupling constants of the δ -field self-interaction of order j .

- Vector-isoscalar meson field, denoted ω , with spin one and isospin zero. The Lagrangian density is that of a typical vectorial field of mass m_ω

$$\mathcal{L}_\omega = -\frac{1}{2} \left(\frac{1}{2} \Omega^{\mu\nu} \Omega_{\mu\nu} - m_\omega^2 \omega_\mu \omega^\mu \right) + \sum_{j=3}^{j_{\max}^\omega} \frac{g_{\omega_j}}{j!} (\omega_\mu \omega^\mu)^j, \quad (3.4)$$

with g_{ω_j} the coupling constants of the ω -field self-interaction of order j , and $\Omega_{\mu\nu}$ the field strength tensor of meson ω given by

$$\Omega_{\mu\nu} = \partial_\mu \omega_\nu - \partial_\nu \omega_\mu. \quad (3.5)$$

- Vector-isovector meson field denoted ρ with spin and isospin one

$$\mathcal{L}_\rho = -\frac{1}{2} \left(\frac{1}{2} \mathbf{P}^{\mu\nu} \cdot \mathbf{P}_{\mu\nu} - m_\rho^2 \rho_\mu \cdot \rho^\mu \right) + \sum_{j=3}^{j_{\max}^\rho} \frac{g_{\rho_j}}{j!} (\rho_\mu \cdot \rho^\mu)^j, \quad (3.6)$$

with g_{ρ_j} the coupling constants of the ρ -field self-interaction of order j , and $\mathbf{P}_{\mu\nu}$ the field strength tensor of meson ρ given by

$$\mathbf{P}_{\mu\nu} = \partial_\mu \rho_\nu - \partial_\nu \rho_\mu - c_\rho (\rho_\mu \wedge \rho_\nu), \quad (3.7)$$

denoting c_ρ a constant.

In a parametrized theory such as relativistic mean field theory, more parameters allow for an increased precision, but too many parameters render the calibration to nuclear laboratory

²The nomenclature used for the tensorial order of mesons is (spin)-(isospin); for example, a scalar-isoscalar meson field corresponds to a meson field which is scalar in spin space, and scalar in isospin space.

experiments more difficult. For details on the value of the coupling constants for a large number of relativistic mean field models, see [Dutra et al. \[2014\]](#). It is also possible to establish a Lagrangian density with couplings dependent on the density n such that $g = g(n)$.

Both spin-scalar mesons σ and δ account for the attractive part of the strong interaction whereas spin-vector mesons ω and ρ account for the repulsive part; in the case of mesons σ and ω , the attractive and repulsive parts of strong interaction affect matter with null isospin, whereas mesons δ and ρ affect matter with non-zero isospin. It needs to be emphasized that these mesons are not "real" particles: they are only used as carriers of the strong interaction, and therefore only interact with nucleons and themselves, not with any other field that may be taken into account to describe dense matter.

Aside from the fields needed to mediate strong interaction, one must add the fields related to real particles, and their interaction with other fields. Assuming that neutron star matter is made of nucleons and leptons, we must include fields for:

- Bare³ nucleons

$$\mathcal{L}_N = \bar{\psi}_N (i\gamma_\mu \partial^\mu - m_N) \psi_N, \quad (3.8)$$

with ψ_N the field for the nucleon N (neutrons or protons), m_N the nucleon mass and γ the Dirac matrices.

- The interaction between nucleons and scalar meson fields

$$\mathcal{L}_{Ns} = \bar{\psi}_N (g_\sigma \sigma + g_\delta \delta \cdot \boldsymbol{\tau}) \psi_N, \quad (3.9)$$

with $\boldsymbol{\tau}$ the vector of isospin Pauli matrices.

- The interaction between nucleons and vector meson fields

$$\mathcal{L}_{Nv} = -\bar{\psi}_N (g_\omega \gamma_\mu \omega^\mu + \frac{g_\rho}{2} \gamma_\mu \boldsymbol{\rho}^\mu \cdot \boldsymbol{\tau}) \psi_N. \quad (3.10)$$

- The cross interactions of meson fields

$$\begin{aligned} \mathcal{L}_{\sigma\delta\omega\rho} = & \alpha_{\sigma\delta} \sigma \cdot \delta + \alpha'_{\sigma\delta} \sigma^2 \delta \cdot \delta + \alpha_{\sigma\omega} \sigma \omega_\mu \omega^\mu + \alpha'_{\sigma\omega} \sigma^2 \omega_\mu \omega^\mu + \alpha_{\sigma\rho} \sigma \boldsymbol{\rho}_\mu \cdot \boldsymbol{\rho}^\mu \\ & + \alpha'_{\sigma\rho} \sigma^2 \boldsymbol{\rho}_\mu \cdot \boldsymbol{\rho}^\mu + \alpha_{\delta\omega} \delta \cdot \delta \omega_\mu \omega^\mu + \alpha_{\delta\rho} \delta \cdot \delta \boldsymbol{\rho}_\mu \cdot \boldsymbol{\rho}^\mu + \alpha_{\omega\rho} \omega_\mu \omega^\mu \delta_\mu \cdot \delta^\mu, \end{aligned} \quad (3.11)$$

with α denoting coupling constants.

- The interaction between nucleons and the electromagnetic field A_μ

$$\mathcal{L}_{emN} = -\frac{e}{2} \bar{\psi}_N \gamma_\mu (1 + \tau_3) A^\mu \psi_N, \quad (3.12)$$

with e the elementary charge.

³The term bare refers to particles stripped of any interaction.

- Bare charged leptons

$$\mathcal{L}_l = \bar{\psi}_l (i\gamma_\mu \partial^\mu - m_l) \psi_l , \quad (3.13)$$

with ψ_l the lepton field of nature l and m_l the lepton mass;

- The interaction between leptons and the electromagnetic field

$$\mathcal{L}_{eml} = e \bar{\psi}_l \gamma_\mu A^\mu \psi_l ; \quad (3.14)$$

- Photons

$$\mathcal{L}_\gamma = -\frac{1}{4} F_{\mu\nu} F^{\mu\nu} , \quad (3.15)$$

with $F_{\mu\nu}$ the electromagnetic field strength tensor (also called the Faraday tensor).

Although baryons and leptons can interact through weak interaction via bosons W^+ , W^- and Z , the equation of state of β -equilibrated matter assumes chemical equilibrium between the particles, thus avoiding having to consider the channels of weak interaction in the derivation. The full Lagrangian density of neutron star matter designed in field theory is a sum of all above mentioned terms, such that

$$\mathcal{L} = \sum_{N=n,p} \mathcal{L}_N + \sum_{X=\sigma,\delta,\omega,\rho} \mathcal{L}_X + \mathcal{L}_{Bs} + \mathcal{L}_{Bv} + \mathcal{L}_{\sigma\delta\omega\rho} + \mathcal{L}_{emB} + \sum_l \mathcal{L}_l + \mathcal{L}_{eml} . \quad (3.16)$$

Once the Lagrangian density has been established, the mean field approximation is used. Instead of constructing the interaction between baryons by solving the N-body problem, all baryons are considered to be immersed in one mean field per meson type. The same approach is used for all terms of Eq. (3.16). The Euler-Lagrange equations -as many as there are fields in play- can be derived from this Lagrangian density, as well as the stress-energy tensor $T_{\mu\nu}$ defined as

$$T^{\mu\nu} = \sum_\phi \frac{\partial \mathcal{L}}{\partial(\partial_\mu \phi)} \partial^\nu \phi - \eta^{\mu\nu} \mathcal{L} , \quad (3.17)$$

with ϕ designating the field. The different components of the stress-energy tensor lead us to equation of state related quantities: the energy density is derived from the T^{00} component, and the pressure is derived from the diagonal space component.

Depending on the number of fields taken into account in the theory, or the value of the coupling constants, a large number of different models can be established. In order to categorize different nuclear models, we use the terminology of "equation of state family": different families in relativistic mean field theory correspond to which meson interaction are considered. In this manuscript, eight different relativistic mean field families for nucleonic models will be used, and the terms taken into account in the Lagrangian density are presented in Table 3.1. The difference between nuclear models within one family is often due to different values of the coupling constants.

Family	Mesons considered	Self-interaction	Cross-interaction	Model	References
BSR	$\sigma + \omega + \rho$	$\sigma + \omega$	$\sigma - \omega + \sigma - \rho + \omega - \rho$	BSR2 BSR6	Agrawal [2010]
DD	$\sigma + \omega + \rho$	none	none	DD2* \circ	Typel et al. [2010]
	$\sigma + \omega + \rho + \delta$			DDME2* DDh δ	Lalazissis et al. [2005] Gaitanos et al. [2004]
FSU2	$\sigma + \omega + \rho$	$\sigma + \omega$	$\omega - \rho$	FSU2 FSU2H* FSU2R	Chen and Piekarewicz [2014] Negreiros et al. [2018]
GM/H	$\sigma + \omega + \rho$	σ	none	GM1 H3 \diamond H4 \diamond	Glendenning and Moszkowski [1991] Lackey et al. [2006]
NL3	$\sigma + \omega + \rho$	σ	none $\omega - \rho$	NL3* NL3- $\omega\rho$ * \circ	Horowitz and Piekarewicz [2001] Lalazissis et al. [1997]
TM	$\sigma + \omega + \rho$	$\sigma + \omega$	none	TM1 TM2	Sugahara and Toki [1994]
			$\omega - \rho$	TM1- $\omega\rho$ TM2- $\omega\rho$	Providência and Rabhi [2013]

Table 3.1: Meson terms included in the Lagrangian density of seventeen relativistic mean field models for cold and β -equilibrated matter. The family of nuclear models DD contains no self or cross-interactions but the coupling constants are density dependent. Symbol \diamond designate nuclear models that include hyperons, symbol * designate models for which a hyperonic version has been calculated, and symbol \circ designates models for which a hybrid version has been calculated, see section 3.1.3 for details.

3.1.1.2 Skyrme energy density functionals

Another phenomenological approach to compute the equation of state of dense matter is based on the Skyrme force. It was first introduced by the English physicist Tony Skyrme in [Skyrme \[1956\]](#), to properly account for effective nucleon interaction in nuclei, a problem that was brought forth a few years before by Keith Brueckner in [Brueckner et al. \[1954\]](#). In the Skyrme energy density functional approach, an effective nuclear Hamiltonian is constructed from the expansion of the density matrix in the zero range interaction.

The Skyrme force is a non-relativistic approach to the nucleon interaction. From this force, one can derive a density functional which is used in the framework of the variational principle to obtain a Hamiltonian operator. In this theory, the baryons are solutions to an approximation of the Schrödinger equation, which can be that of the mean field method of Hartree-Fock for example. The Skyrme force is defined by a series of parameters, later on referred to as the Skyrme parameters. From the Skyrme parameters, one can define some microscopic quantities of interest, such as the energy per baryon or the symmetry energy, using analytical expressions; for details on those microscopic quantities, see section [3.2.2](#). The Skyrme parameters are adjusted to laboratory experiments such as nuclear data tables, or to properties of homogeneous neutron matter. Skyrme density functional theory can be separated in two classes: the standard Skyrme functionals, and the generalized Skyrme functionals. The latter were introduced to avoid neutron matter polarization that lead to ferromagnetic collapse of the star [[Chamel et al., 2009](#)]. To classify Skyrme models, we refer to the expression of the Skyrme force S ruling the interaction between nucleons presented in [Goriely et al. \[2010\]](#)

$$\begin{aligned}
S(\mathbf{r}_{ij}) = & t_0(1 + x_0P_s)\delta(\mathbf{r}_{ij}) + \frac{t_1(1 + x_1P_s)}{2\hbar^2} \left(\mathbf{p}_{ij}^2\delta(\mathbf{r}_{ij}) + \delta(\mathbf{r}_{ij})\mathbf{p}_{ij}^2 \right) \\
& + \frac{t_2(1 + x_2P_s)}{\hbar^2} \mathbf{p}_{ij} \cdot \delta(\mathbf{r}_{ij})\mathbf{p}_{ij} + \frac{t_3(1 + x_3P_s)}{6} \rho(\mathbf{r})^{\alpha_1} \delta(\mathbf{r}_{ij}) \\
& + \frac{t_4(1 + x_4P_s)}{2\hbar^2} \left(\mathbf{p}_{ij}^2\rho(\mathbf{r})^{\alpha_2}\delta(\mathbf{r}_{ij}) + \delta(\mathbf{r}_{ij})\rho(\mathbf{r})^{\alpha_2}\mathbf{p}_{ij}^2 \right) \\
& + \frac{t_5(1 + x_5P_s)}{\hbar^2} \mathbf{p}_{ij} \cdot \rho(\mathbf{r})^{\alpha_3} \mathbf{p}_{ij} + \frac{iW_0}{\hbar^2} (\boldsymbol{\sigma}_i + \boldsymbol{\sigma}_j) \cdot \mathbf{p}_{ij} \times \delta(\mathbf{r}_{ij})\mathbf{p}_{ij} . \quad (3.18)
\end{aligned}$$

The quantity \mathbf{r}_{ij} is defined as the difference between the spatial coordinates of nucleon i and j , and \mathbf{p}_{ij} designates the relative momentum (difference between the momentum operator of i and of j). The spin exchange operator between nucleons is denoted P_s , and $\rho(\mathbf{r}_{ij})$ is the local density, or in other words the density at the barycenter $\mathbf{r} = (\mathbf{r}_i + \mathbf{r}_j)/2$.

The terms of Eq. (3.18) can be understood as follows:

- Terms proportional to t_0 are the effect of the force at zero range (hence the Dirac δ -function).
- Terms proportional to t_1 and t_2 are effects for an effective range, and express the momentum dependence of the interaction - consequently finite temperature effects.

The parameters t_4 and t_5 represent the effective range in the generalized form of the Skyrme force, and introduce density dependence to the term.

- Terms proportional to t_3 account for a phenomenological three-body interaction expressed as a density-dependent two body interaction.
- Terms proportional to W_0 account for the two-body spin interaction with spin-orbit coupling.

To the Skyrme force can be added a pair force and Wigner force, as is the case for example in Brussels-Skyrme models. In this manuscript, 24 Skyrme based models for nucleonic matter at β -equilibrium are used, and the characteristics of their corresponding six equations of state families are presented in Table 3.2.

Family	Parameters	Model	Ref.
BSk	$t_2 = 0, t_2 x_2 \neq 0$	BSk-20/21 BSk-22/23/24/25	Goriely et al. [2010] Goriely et al. [2013]
SLy	$x_4 = x_5 = t_4 = t_5 = 0$	SLy-2/9 DH SLy230a	Chabanat [1995] Douchin and Haensel [2001] Chabanat et al. [1998]
KDE	$t_4 = t_5 = 0$	KDE0v1	Agrawal et al. [2005]
Rs	$x_1 = x_2 = t_5 = 0$		Friedrich and Reinhard [1986]
SK	$x_1 = x_2 = x_4 = x_5 = t_4 = t_5 = 0$	SK-a/b	Köhler [1976]
Sk	$x_4 = x_5 = t_4 = t_5 = 0$	Sk-255/272 SkMP SkOp SkI-1/2/3/4/5 SkI6	Agrawal et al. [2003] Bennour et al. [1989] Reinhard et al. [1999] Reinhard and Flocard [1995] Nazarewicz et al. [1996]

Table 3.2: Classification of Skyrme models from parameters of the Skyrme force presented in Eq. (3.18).

3.1.1.3 Treating inhomogeneous matter

The Lagrangian density presented in Eq. (3.16) presents baryons as degrees of freedom, and similarly for the expression of the Skyrme force. It is therefore straightforward to establish the equation of state for a homogeneous mixture of baryons and leptons, which is a state valid at high density in the core of neutron stars. However, the crust of neutron stars is made of a lattice, which requires an additional theoretical framework to describe nuclear structure.

The first calculation of the inner crust equation of state was established by Negele and Vautherin [1973]: the nuclear energy is calculated from the nucleon wave function in the Hartree-Fock formalism, and is minimized in a Wigner-Seitz cell; the Coulomb energy is derived from β -equilibrium for particles in play. Almost thirty years later, Douchin and Haensel [2001] emphasized the importance of calculating the crust with the same effective nucleon-nucleon interaction as the core, and established an equation of state denoted DH in the Compressible Liquid Drop Model [Douchin and Haensel, 2000]. Their approach includes terms of nuclear surface, Coulomb energy, as well nuclear shapes and nuclear structures, and of course nucleon bulk energy directly linked to the model of nucleon-nucleon interaction.

Later on, pairing correlations and shell effects were incorporated in the crust calculation. A formalism well suited to the relativistic mean field models is the Thomas-Fermi approximation [Avancini et al., 2009]: the density of particles in play are treated with a one-body Hamiltonian, before solving the Euler-Lagrange equations.

From the nuclear models mentioned above, the DH and Brussels-Skyrme models are established with the same nuclear model for the high and low density parts of the star in the references mentioned in Table 3.1 and Table. 3.2.

3.1.2 Microscopic models

Although it is computationally costly, microscopic models can be established by solving the N-body Schrödinger equation. Conceptually, microscopic models, which are also called *ab initio* models, are the most physically based models because they are constructed from scratch. In this framework, the only requirement to construct the equation of state is a solid understanding of the nucleon-nucleon interaction (calibrated to nuclear data). Different approaches exist, for example, the non-relativistic Brueckner-Hartree-Fock approach which is a technique to solve the many-body problem from the few-body interaction, or the relativistic Dirac-Brueckner-Hartree-Fock; for a description of microscopic models, see Taranto et al. [2013]. In practice, the N-body problem is reduced to a three-body problem, which is sometimes itself reduced to a density dependent two-body problem. The number of CPU hours required for such calculations has greatly restricted this type of models, but it is a field that is being actively developed. In this manuscript, we use one *ab initio* equation of state of dense matter at β -equilibrium, presented in Sharma et al. [2015], and referred to as BCPM.

Another promising microscopic approach which has been largely explored for neutron star matter in recent years is Chiral Effective Field Theory (χ EFT). With neutron stars, one can probe a temperature-density-isospin region of the Quantum Chromo-Dynamics (QCD) phase diagram which is otherwise unexplorable. Chiral effective field theory is a low energy effective field theory of QCD with hadrons as degree of freedoms, whose results can be applied to neutron star matter. It is constructed as an expansion in the four-momentum of the degrees of freedom that are baryons and pions, and not quarks and gluons as in QCD. Instead of constructing the full equation of state of dense matter through microscopic constructions, χ EFT can be used as a theoretical constraint, as it provides information on pure neutron matter to relatively high densities (up to around twice the saturation density), see [Drischler et al. \[2021\]](#). In this theory, the three-body force is not just an extension of the two-body force (established *e.g.* with a density dependence) but is constructed consistently. Thanks to high performing simulations, χ EFT is able to provide results for the three nucleon interaction, and operate up to the next-to-next-to-next-to leading order in the chiral expansion.

3.1.3 The unknown composition of the core

The supranuclear densities that can be reached in the most massive neutron stars leave the description of neutron star cores open to several composition hypotheses. The outer core is believed to contain a mixture of neutrons, protons, electrons and muons ($npe\mu$), but the inner core might be the host of particles such as hyperons or quarks.

Hyperons -baryons with with non-zero strangeness- in neutron stars were first introduced in the 1960s by [Ambartsumyan and Saakyan \[1960\]](#). They are expected to appear in the core through a series of reactions involving nucleons such as (but not exclusively)

$$p + e^- \rightarrow \Lambda + \nu_e, \quad (3.19)$$

$$p + e^- \rightarrow \Sigma^0 + \nu_e, \quad (3.20)$$

$$n + e^- \rightarrow \Sigma^- + \nu_e. \quad (3.21)$$

Hyperons Λ , Σ^0 , and Σ^- once created in Eqs. (3.19), (3.20), (3.21), can themselves be sources of double strange Ξ^- hyperons. Hyperons are heavier than nucleons, see Fig. 3.1.

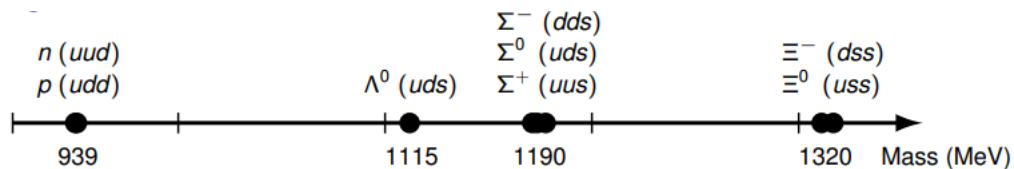


Figure 3.1: Masses of hyperons, as presented in the course of Dr. Morgane Fortin at the Pharos Training School of March 2019, "Equation of state and neutron star properties constrained by nuclear physics and observations".

Laboratory measurements of hyperons are performed in heavy-ion collision experiments at the Thomas Jefferson National Accelerator facility (Jlab, USA), the Mainz Microtron

accelerator (MAMI-C, Germany), and the Japan Proton Accelerator Research Complex (J-Parc, Japan); for details on experimental data of hypernuclei, see [Vidaña \[2021\]](#). However, only very short lived hypernuclei can be measured, making it difficult to give solid constraints on the parametrization of hyperon-nucleon or hyperon-hyperon interactions. For example, no scattering of hypernuclei has been measured, which is needed to accurately calculate properties of hyperons in dense matter.

The presence of hyperons softens *a priori* the core equation of state. The addition of a new species lowers the overall Fermi pressure because of the Pauli exclusion principle. A lower pressure at fixed density leads to a smaller radius of the neutron star such that the presence of hyperons results in smaller total radii. Softening the equation of state, however, leads to neutron stars with a lower maximum mass. This is a problem referred to as the "hyperon puzzle", which can be counteracted if one finds a way to stimulate hyperonic pressure [[Bednarek et al., 2012](#)]. One way to do so is to instigate repulsion from the nature of baryon interactions, see [Chatterjee and Vidaña \[2016\]](#), [Vidaña \[2013\]](#).

For hyperonic matter calculated in the relativistic mean field theory, terms for bare hyperons and for mesons mediating the hyperonic interactions are added to the Lagrangian density in Eq. (3.16). Coupling constants for the hyperon-hyperon and hyperon-nucleon interactions are presented *e.g.* in [Fortin et al. \[2017, 2020\]](#), [Providência et al. \[2019\]](#). Simplifications for the theory can be applied to the hyperonic sector, for example by not including cross terms between the hyperonic mesons fields [[Fortin et al., 2017](#)].

As the density increase, the nucleon structure may be disrupted by a phase transition from confined quarks (baryons) to deconfined quarks: part of the core might be made of quark matter [[Blaschke and Chamel, 2018](#)]. Models for dense matter which include deconfined quarks are referred to as hybrid models. The quark phase transition induces a density jump that ensures a softening of the equation of state. If this jump exceeds a critical value, the softening is such that the relation between the mass and the radius of the star presents a branch which is partly unstable with respect to radial oscillations. In this case, a single equation of state corresponds to the two stable branches of stellar models, and twin stars with the same mass but different radii can exist. To account for quark matter in the relativistic mean field approach, terms for scalar, vector, and pseudovector quark couplings are added to Eq. (3.16); we refer to [Pereira et al. \[2016\]](#) and [Ferreira et al. \[2020\]](#) for a discussion about the coupling constants in the quark matter Lagrangian density.

Amongst the models used to describe quark matter are the Nambu and Jona-Lasinio (NJL) model, the quark-meson model or the MIT bag model. Hybrid models considered in this manuscript are presented in [Pereira et al. \[2016\]](#), [Ferreira et al. \[2021\]](#) and were established within the SU(3) NJL model for quark matter, paired with a relativistic mean field description of hadronic matter. The confined phase follows the same Lagrangian density as nucleonic or hyperonic (strange quark) matter. The Lagrangian density of deconfined quarks established from the NJL model includes four-quark scalar and pseudoscalar interaction terms with coupling constant G_S , four-quark vector and pseudovector interaction

terms -both vector-isoscalar (VP) with coupling constant G_ω and vector-isovector (notation VIPI) with coupling constant G_ρ are considered-, and the six-quark t'Hooft term (ensures that the QCD $U(1)_A$ symmetry is broken). In the NJL models, the pressure and energy density are defined up to the pressure bag constant B . It is chosen to ensure either that the effective pressure falls to zero when the baryon chemical potential vanishes (notation B0) or to impose another type of constraint such as fixing the deconfinement baryonic density (notation B). Finally, the ratio between the vector and scalar coupling constants respectively $\xi = G_\omega/G_s$ and $\eta = G_\rho/G_s$, are parameters that characterize the models and define the intensity of the VP and VIPI channels (for more details, see [Pereira et al. \[2016\]](#) and [Ferreira et al. \[2020\]](#)). For the hybrid models used in this manuscript, we use the nomenclature $\text{EoS} - Bx - 100\xi - 100\eta$, where x characterizes the magnitude of the bag constant.

Hybrid stars have also been described with an *ab initio* approach to hadronic matter, such as the Brueckner-Hartree-Fock many-body theory with realistic two-body and three-body forces [Maieron et al. \[2004\]](#), [Chen et al. \[2011\]](#); for other *ab initio* models associated with quark matter, see the reviews [Oertel et al. \[2017\]](#), [Burgio et al. \[2021\]](#).

In [Table 3.1](#), models which are calculated with hyperons or deconfined quarks in the core are presented with the symbol \diamond or $*$, and \circ respectively. The softening of the equation of state related to hyperons or a quark phase transition can be illustrated by the value

of the adiabatic index as a function of the density in the star; this is presented in [Fig. 3.2](#) for the relativistic mean field model DD2; in this figure, we use the adiabatic index, defined as

$$\Gamma = \frac{n}{P} \frac{dP}{dn}, \quad (3.22)$$

with n the baryon density and P the pressure.

Overall, the extreme conditions of temperature and density in the innermost layers of neutron stars leave the modelling of neutron star's equation of state open to various core compositions and theoretical framework. There are two general approaches to the equation of state of dense matter, the phenomenological approach which include the relativistic mean field theory and the Skyrme density functionals, and the microscopic approach which

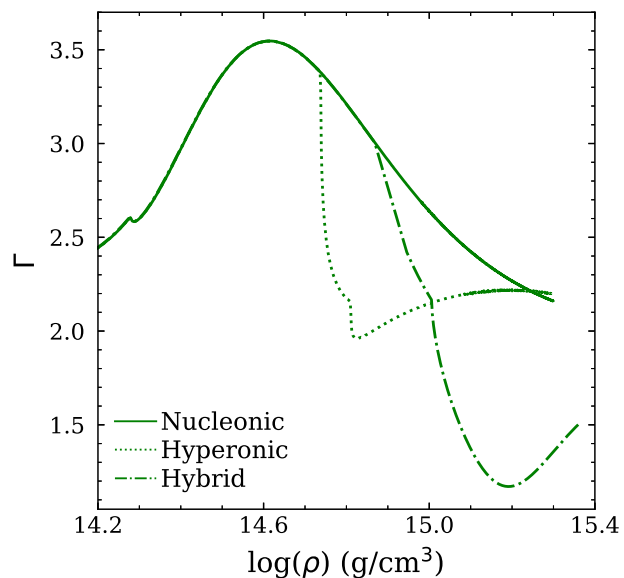


Figure 3.2: Adiabatic index Γ as a function of the mass density ρ for the nucleonic, hyperonic, and hybrid versions of the model DD2.

attempts to solve the N -body problem *ab initio*. The different models for the core composition include purely nucleonic matter, strange nuclei, as well as deconfined quarks.

3.2 Microphysics constraints on the equation of state

A large number of nuclear experiments are designed to constrain the equation of state of dense matter. Although, the densities and isospin asymmetries in the innermost parts of neutron stars are way beyond the reach of nuclear physics laboratories, it is possible to constrain some microscopic parameters.

3.2.1 Constraints on the outer crust

The crust of neutron stars is made of a lattice of nuclei, such that the equation of state of cold and catalyzed dense matter can be established by minimizing the Gibbs energy of nuclei at given pressure. Instead of using a theoretical model to determine the binding energy of nucleus, one can use the available measurement of atomic masses provided by nuclear experiments. In this manuscript, we use the Atomic Mass Evaluation (AME) tables presented in Wang et al. [2012, 2017, 2021a], which gather measurements for thousands of nuclei. Such tables are updated every few years, with additional nuclei measured, and an increase in the precision for previously measured nuclei.

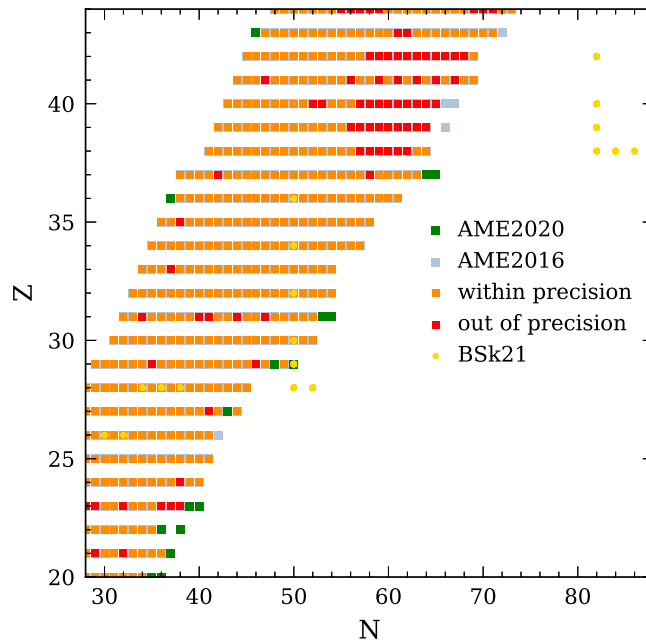


Figure 3.3: Nuclei of proton number Z and neutron number N measured in the AME2016 (in grey) and AME2020 tables. Nuclei which were not previously reported in AME2016 are presented in green; those whose value of the atomic mass have changed between AME2016 and AME2020, but for which the 2020 value stays within the precision presented in AME2016 are presented in orange; nuclei whose value of the atomic mass have changed between AME2016 and AME2020 and for which the 2020 value is outside the precision presented in AME2016 are presented in red. In yellow, we present nuclei in the catalyzed outer crust of BSk21.

Nuclei measured in the table AME2016 and AME2020 are presented in Fig. 3.3. Measured nuclei are relatively isospin symmetric, or in other words, not many neutron rich

nuclear measurements are provided. The composition of the outer crust for catalyzed matter (for an isolated neutron star), calculated with the Skyrme model BSk21 is also presented in this figure. The outer crust of BSk21 was calibrated to the table AME2016. Only ten nuclei out of eighteen were available in this table. The AME2020 table provided measurements for around fifteen new neutron rich nuclei, including ^{50}Cu and ^{56}Ca which appear in the crust of the above mentioned models. In overall, measured nuclei can be used to describe only the outer part of the outer crust, and not the entire crust.

In the computation of the outer crust, only the central value of the measurement in the AME tables is used, and not its error bars. Therefore, nuclei presented in orange in Fig. 3.3, *i.e.* nuclei whose value of the atomic mass has changed between the AME2016 and AME2020 tables but stay within the precision of AME2016, will affect slightly the equation of state. However, no nuclei reported in AME2020 that present a precision beyond that of the nuclei measured in the AME2016 table will affect the calibration in the outer crust of BSk21.

The nuclear chart of measured nuclei presented in Fig. 3.3 shows that laboratory measurements can only constrain part of the outer crust. Isospin asymmetric nuclei are more difficult to measure than symmetric ones, such that neutron rich nuclei in the outer crust are not all calibrated to laboratory measurements (yet). The neutron drip line has only been experimentally verified up to Neon [Ahn and et al., 2019]. Therefore, part of the outer crust and the entire inner crust are model dependent.

3.2.2 Incorporating constraints at moderate and high density

Matter in neutron stars is highly isospin asymmetric. Assuming purely nucleonic matter, the isospin asymmetry can be assessed by introducing

- The isoscalar density $n_s = n_n + n_p$, with n_n and n_p respectively the neutron and proton densities. It is a quantity which remains invariant under an exchange of neutrons and protons.
- The isovector density $n_v = n_n - n_p$. It changes sign under an exchange of neutrons and protons.

The isospin asymmetry parameter denoted δ is defined as the ratio between the isovector and the isoscalar density

$$\delta = \frac{n_v}{n_s}. \quad (3.23)$$

Pure neutron matter corresponds to $\delta = 1$ and symmetric matter corresponds to $\delta = 0$. The equation of state for catalyzed matter in a given nuclear model corresponds to calculations with δ suited for β -equilibrated matter. However, results can also be established for pure neutron matter and symmetric matter, in this same nuclear model.

The difference in energy between neutron matter and symmetric matter is related to the symmetry energy. The energy per baryon can be expanded around the isospin asymmetry

parameter according to the parabolic approximation.

$$\mathcal{E}(n, \delta) = \mathcal{E}(n, \delta = 0) + \delta^2 E_{\text{sym}}(n) + \mathcal{O}(\delta^4). \quad (3.24)$$

The symmetry energy E_{sym} is here defined as the second derivative in isospin direction for symmetric matter. Neglecting the terms of order $\mathcal{O}(\delta^4)$, the symmetry energy corresponds to the difference between the energy per baryon for pure neutron matter, and the energy per baryon for symmetric matter at a given density. In this case, the symmetry energy is the energy required for all protons of symmetric matter to be changed into neutrons.

The energy per baryon as a function of the baryon density for pure neutron matter and symmetric matter, calculated for the Skyrme model SLy4 is presented in Fig. 3.4.

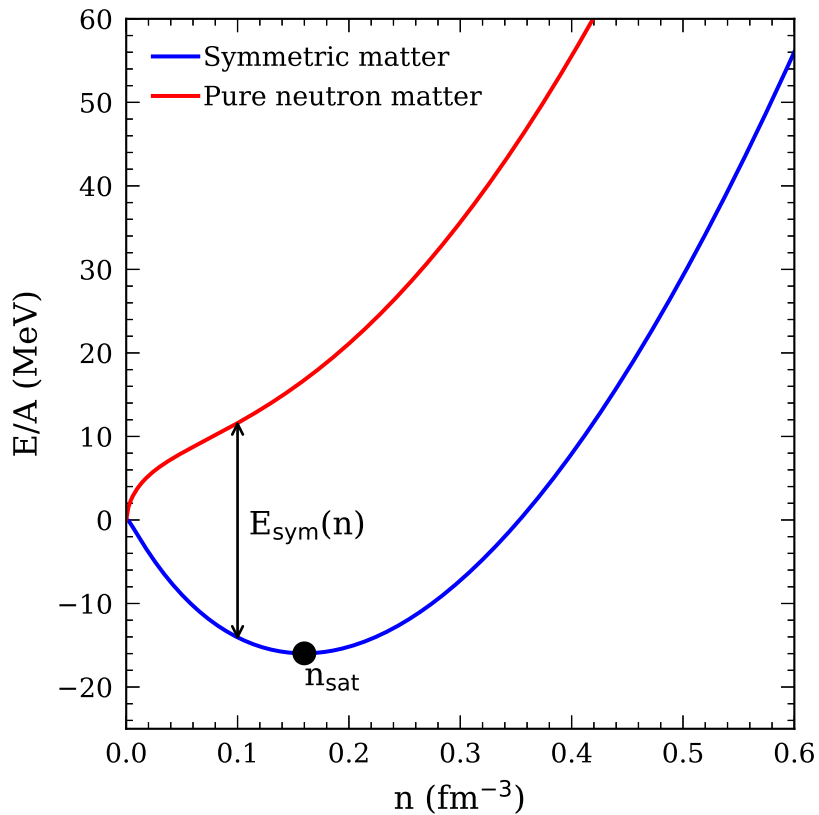


Figure 3.4: Energy per baryon E/A as a function of the baryon density n for symmetric and pure neutron matter for the Skyrme model SLy4.

The saturation density is defined as the density at which the energy per baryon for isospin symmetric matter is minimum and is denoted n_{sat} ; it can also be understood as the density below which symmetric matter is self-bound, and can no longer be treated as homogeneous. A typical value of the saturation density is often used as unit of measurement for the baryonic density; outside of this section, and unless otherwise stated, the saturation density $n_0 = 0.16 \text{ fm}^{-3}$ will be used. But in reality, the saturation density n_{sat} must be properly calculated for a given nuclear model.

The energy per baryon for symmetric matter (isoscalar energy), and the symmetry energy per baryon (isovector energy) can be developed around saturation density by introducing a dimensionless parameter expressing the deviation of the density from the saturation density

$$u(n) = \frac{n - n_{\text{sat}}}{3n_{\text{sat}}}. \quad (3.25)$$

The energy per baryon for symmetric matter can be expanded around this quantity as

$$\mathcal{E}(n, \delta = 0) = \mathcal{E}_{\text{sat}} + \mathcal{K}_{\text{sat}} \frac{u(n)^2}{2!} + \mathcal{Q}_{\text{sat}} \frac{u(n)^3}{3!} + \dots, \quad (3.26)$$

with:

- \mathcal{E}_{sat} the energy per baryon at saturation density for symmetric matter,
- \mathcal{K}_{sat} the isoscalar incompressibility modulus,
- \mathcal{Q}_{sat} the isoscalar skewness,
- and etc. for higher order parameters;

The symmetry energy per baryon gives

$$E_{\text{sym}}(n) = J + Lu(n) + K_{\text{sym}} \frac{u(n)^2}{2!} + Q_{\text{sym}} \frac{u(n)^3}{3!} + \dots,$$

with:

- J the symmetry energy at saturation density,
- L the slope of the symmetry energy at saturation density,
- K_{sym} the isovector incompressibility,
- Q_{sym} the isovector skewness,
- and etc. for higher order parameters.

The parameters introduced by this development around saturation density can be constrained by laboratory experiments, especially the isoscalar parameters, because symmetric matter is easier to probe. Ample details on the constraints on the symmetry energy are presented in [Tsang and et al. \[2012\]](#), [Oertel et al. \[2017\]](#), and we present in the following, a non-exhaustive list of experiments which probe the value of J , L and K .

The binding energy described by the Finite Range Droplet Model (FRDM) can be used to probe J and L , because it includes symmetry related terms whose values can be explored by using large tables of nuclear data. The formula for the FRDM binding energy presented in [Möller et al. \[2012\]](#) is combined with the nuclear data table in [Wang et al. \[2012\]](#) to extract: $L = 70 \pm 15$ MeV and $J = 32.5 \pm 0.5$ MeV. Coulomb effects are linked to the surface

symmetry term in the FRDM [Danielewicz, 2003]; experiments are performed also on isobaric nuclei [Danielewicz and Lee, 2014] in order to alleviate this entanglement. The same method has been used with Skyrme forces in Kortelainen et al. [2010].

The Heavy Ion Collisions (HIC) of nuclei such as gold has introduced constraints on symmetric matter beyond the saturation density. The collision of nuclei such as isotopes of tin allows one to probe the asymmetry between the number of protons and the number of neutrons [Tsang et al., 2009]; the slope L of the symmetry energy at saturation density was measured at a 95% confidence level to be in the interval $42 < L < 117$ MeV.

Neutron-rich nuclei are particularly interesting to investigate the symmetry energy when they present an asymmetric number of neutrons and protons. That is the case for some Sn isotopes or for ^{208}Pb that closes its nucleon shells, which simplifies the nuclear structure. An asymmetry in favor of neutrons implies that the nucleus will present a large difference in the radius distribution of neutrons and protons; this difference is referred to as the neutron skin. There are a few different ways of measuring the neutron skin thickness, one of which is to see how electroweak parity of ^{208}Pb is violated by polarized electrons in the experiments PREX-I and PREX-II [Horowitz et al., 2014, Adhikari et al., 2021] and of ^{48}Ca in the experiment CREX [Adhikari and et al., 2022]. To extract L from the measurement of the neutron skin, the correlation between the two quantities is exploited *via* a fit established within a theory of dense matter. In Chen et al. [2010], the Skyrme Hartree-Fock model is used on measurements of tin isotopes to constrain the relation between J and L . In Reed et al. [2021], the FSU2Gold relativistic mean field parametrization is used on PREX-II data to extract $J = 38.1 \pm 4.7$ MeV and $L = 106 \pm 37$ MeV; however, it is important to note that this result is in tension with other nuclear experiment constraints, as values of J and L are very large. An analysis of the compatibility between PREX-I, PREX-II and CREX experiments and other experiments determining J and L is discussed in Yüksel and Paar [2022]. In overall, the measurement of the neutron skin thickness in the CREX and PREX experiments are currently being questioned and should be cautiously reviewed before being used to constrain dense matter.

The collective motion of nuclei is a source of giant resonances: let there be an exterior isoscalar monopole operator, the strength function of excited states in response to that operator is directly linked to the nuclear incompressibility K for which experimental data are available, (see Tables I and II of Garg and Colò [2018]); again, the relation between experimental data and K is established within a theoretical framework (e.g. Skyrme or Gogny forces). Constraints on L and J can also be extracted, such as presented in Drischler et al. [2020], Trippa et al. [2008].

There are also some attempts at including results from cold atom experiments to constrain the low density part of the equation of state using the unitary Fermi gas approach. The idea is to consider that low-density neutron matter can be characterized by an infinite scattering length and can be considered as a unitary Fermi gas (see chapter 2 of Gandolfi et al. [2015] for details) in which the energy per nucleon is determined by a single and universal

parameter. There are, however, no considerations of lattice nor clusters with this approach, which are essential in the understanding of crust physics.

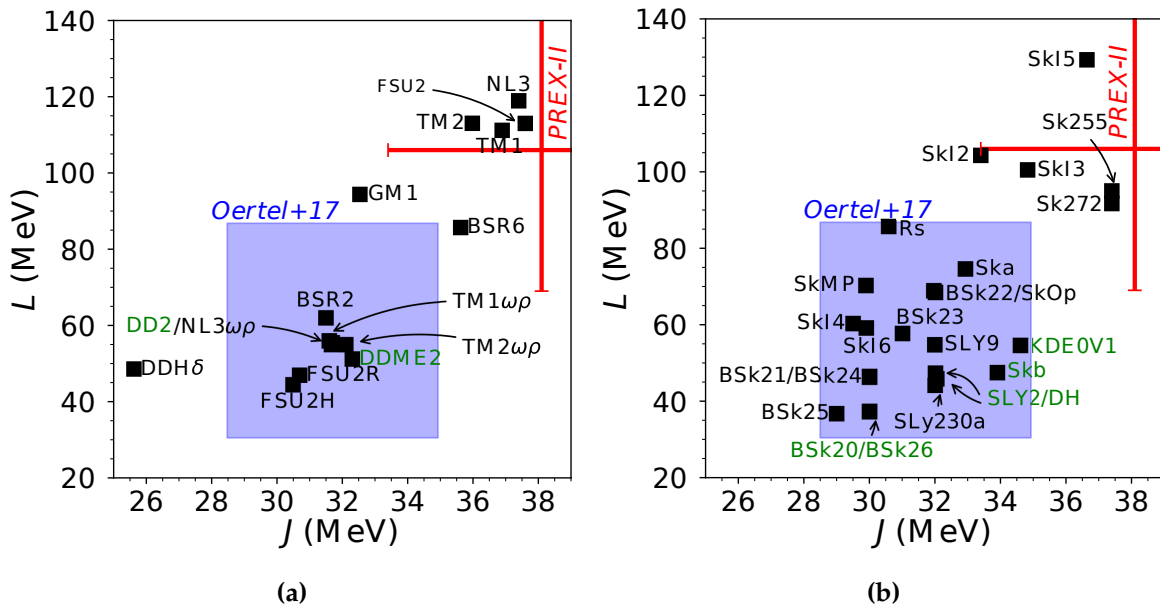


Figure 3.5: Symmetry energy and its slope at saturation density respectively denoted J and L for relativistic mean field and Skyrme models used in this manuscript. Experimental data constraints are presented: in blue is the compiled constraint presented in Ref. [Oertel et al. \[2017\]](#), and in red that of PREX-II. The names of the equations of state in green refer to nucleonic models that do not permit the Direct Urca process (see next section): these are DD2, DDME2, KDE0V1, Skb, SLY2, DH, BSk20 and BSk26.

The values of J and L for relativistic mean field models and Skyrme⁴ presented in section 3.1 are given in Fig. 3.5a and Fig. 3.5b respectively. The synthesis of laboratory constraints presented in [Oertel et al. \[2017\]](#), as well as the PREX-II experiment are shown in these figures. Five relativistic mean field models of our set of equations of state, and a few Skyrme based models from the Sk family are compatible with the PREX-II experiment.

Overall, part of the outer crust of neutron stars is well constrained by the measurement of atomic masses in laboratories. However, the inner crust and the core of neutron stars is not constrained and therefore, it is equation of state dependent. The microscopic parameters that are *e.g.* the symmetry energy and its slope can be constrained by laboratory measurements on isospin asymmetric matter, but some results are in tension and should be taken with caution.

⁴The parameters of Skyrme models presented in Eq. (3.18) can be directly linked to the microphysics parameters presented in this section, which makes it particularly convenient to understand the physics of the parametrization. For details, see [Chabanat et al. \[1997, 1998\]](#), [Danielewicz and Lee \[2009\]](#).

3.3 Astrophysical constraints on dense matter

Even if the equation of state of dense matter is constrained by laboratory measurements and theory, the highest density parts remain out of the reach of microphysics constraints. The conditions of density and temperature in the innermost parts of neutron stars are such that the core composition is left unknown. However, observations of neutron star's macroscopic parameters in multi-messenger astronomy can provide further constraints on dense matter.

3.3.1 Macroscopic parameter modelling and observations

The macroscopic features of neutron stars depend on their internal structure, or in other words, on the equation of state. The mass, the radius, the moment of inertia, and the tidal deformability of neutron stars can be derived within a theory of gravitation. By comparing macroscopic parameters modelled from a given equation of state, to observables of neutron stars, we can test the equation of state's ability to be consistent with observations.

The compactness of neutron stars denoted by $C = GM/(Rc^2) \sim 0.2$ implies that modelling their macroscopic parameters must be treated with a relativistic theory of gravitation. In the following, Albert Einstein's theory of general relativity is used.

3.3.1.1 Mass and radius

The variation of Einstein-Hilbert's action established from the least action principle leads to Einstein's equation [Einstein, 1915]

$$\mathcal{R}_{\mu\nu} - \left(\frac{\mathcal{R}}{2} - \Lambda_g\right)g_{\mu\nu} = \kappa_g T_{\mu\nu}, \quad (3.27)$$

$g_{\mu\nu}$ the metric (describes the geometry of space-time), $\mathcal{R}_{\mu\nu}$ and \mathcal{R} are the Ricci tensor and Ricci scalar respectively, and $T_{\mu\nu}$ is the stress-energy tensor which accounts for matter. The Ricci tensor is the contraction of a four-dimensional tensor, itself derived from derivatives of the metric; the Ricci scalar (or curvature radius) is the contraction of the Ricci tensor and the metric. The constant $\kappa_g = 8\pi G/c^4$ is the gravitational coupling, and the constant Λ_g accounts for the mean energy-density of vacuum on cosmological scales (we neglect it completely). Equation (3.27) is the tensorial form of a series of non-linear second order partial derivative equations, and describes how matter deforms space-time.

Let us assume that space-time is spherically symmetric, static and isotropic, such that the Schwarzschild metric is used

$$g_{\mu\nu} = \begin{pmatrix} -e^{2\phi} & 0 & 0 & 0 \\ 0 & \left(1 - \frac{2Gm}{rc^2}\right)^{-1} & 0 & 0 \\ 0 & 0 & r^2 & 0 \\ 0 & 0 & 0 & r^2 \sin^2(\theta) \end{pmatrix}, \quad (3.28)$$

with m the mass variable, r the radial variable, ϕ the gravitational field, and θ the azimuthal angle. The stress-energy tensor is that of an isolated neutron star filled by a perfect fluid, and is given by

$$T_{\mu\nu} = (\epsilon + P)u_\mu u_\nu - P g_{\mu\nu} , \quad (3.29)$$

with ϵ the energy density in rest frame, P the pressure, and u the velocity of the fluid. In addition to Einstein's equation, the conservation of energy in general relativity implies that the covariant derivative of the stress-energy tensor vanishes. The combination of those two equations render the Tolman-Oppenheimer-Volkoff [Tolman, 1939, Oppenheimer and Volkoff, 1939] set of differential equations

$$\frac{dm}{dr} = 4\pi r^2 \epsilon(r) , \quad (3.30)$$

$$\frac{d\phi}{dr} = \frac{Gm(r)}{r^2} \left(1 + \frac{4\pi r^3 P(r)}{m(r)c^2} \right) \left(1 - \frac{2Gm(r)}{rc^2} \right)^{-1} \quad (3.31)$$

$$\frac{dP}{dr} = - \left(\epsilon(r) + \frac{P(r)}{c^2} \right) \frac{d\phi}{dr} , \quad (3.32)$$

with r the radial variable, m the gravitational mass⁵ contained in a sphere of radius r , G the gravitational constant and c the light velocity. To solve those equations, one must specify the equation of state $P(\epsilon)$, as well as the boundary condition that is the central pressure denoted P_c . The total mass and radius of a neutron star for a given central pressure are denoted M denoted R respectively, and defined by $P(R) = 0$. We designate as a $M(R)$ sequence the relation between the total mass and the total radius.

There are theoretical constraints on the relation between the total mass and the total radius:

- The mass of a neutron star cannot increase indefinitely for a fixed radius in general relativity. The neutron star radius follows the strict limit of the Schwarzschild radius

$$R > \frac{2GM}{c^2} . \quad (3.33)$$

- The central pressure must be finite, such that in the limiting case of a uniform density

$$R \geq \frac{9GM}{4c^2} , \quad (3.34)$$

see Shapiro and Teukolsky [1986].

- The equation of state must be subluminal, such that the sound speed $v_{\text{sound}} < c$; for details concerning Lorentz invariance and causality we refer to Haensel et al. [2007b].

⁵It is important to distinguish the gravitational mass and the total baryon mass, which corresponds to the mass of baryons in the neutron star.

This leads to the lower bound radius

$$R \geq 2.9 \frac{GM}{c^2} . \quad (3.35)$$

- It is possible to solve Einstein's equation for a metric which includes the angular velocity of the star, in which case the relation $M(R_{\text{eq}})$, with R_{eq} designating the equatorial radius, is solved for a uniformly rotating neutron star. The rotational frequency of the star has a limit, referred to as the Keplerian frequency limit or mass shedding limit, over which the neutron star is disrupted by centrifugal forces.

There are also observational constraints on both the mass and the radius of a neutron star. The most crucial one, later referred to as the maximum mass criterion, is the maximum mass attainable for a given equation of state: it has to reach the largest mass observed to date. The measurement of neutron star masses are presented in Fig. 3.6 with the following classification:

- mass measured in a binary with two neutron stars (DNS),
- mass measured from millisecond pulsars (MSP) with a spin frequency $f \geq 50\text{Hz}$, in a binary with a companion star which is not a neutron star,
- mass measured from slowly rotating pulsars (SLOW) with a spin frequency $f \leq 50\text{Hz}$, in a binary with a companion star which is not a neutron star,
- mass measured in X-ray or optical (X/OPT) as opposed to radio in previous categories,
- mass measured from gravitational wave (GW) detections. Gravitational wave detections for which the neutron star nature of the binary component was confirmed by tidal deformability measurement or electromagnetic counterparts are presented in black; in grey, we present gravitational wave detections for which the neutron star nature of the component is only concluded from the mass.

Data is gathered from Freire [2021], Özel and Freire [2016], Table 1 in Alsing et al. [2018], Lattimer [2012] and Abbott et al. [2017], The LIGO Scientific Collaboration et al. [2021].

The most accurate determinations of pulsar masses are based on the measurement of the parameters in binary systems. By detecting the companion star, the gravitational interaction with the neutron star can be evaluated, and we can assess the Keplerian (Newtonian) parameters of the binary:

- orbital period,
- orbital eccentricity,
- projected semi major axis,
- longitude of the periastron,

- time of periastron passage,

and post-Keplerian (relativistic) parameters

- rate of the orbital decay due to gravitational radiation,
- relativistic advance of the periastron,
- time dilation and gravitational redshift,
- range and shape parameters of the Shapiro delay.

At least two post-Keplerian parameters, in addition to the classical parameters, are required to determine the masses of the stars in the binary⁶. For a complete derivation of post-Keplerian parameters, see [Misner et al., 1973]. In relativistic binaries involving neutron stars, one of the two components is observed as a pulsar (with the exception of J0737-3039 for which the two neutron stars were observed as pulsars until 2008). Whether it is possible or not to measure a specific post-Keplerian parameter depends on the shape, size and orientation of the binary orbit. For example, the rate of periastron advance is measurable for eccentric orbits, and Shapiro delay parameters for rather large companion mass with an edge-on orientation of the orbit.

Most of the millisecond pulsars in binaries have a white dwarf as a companion. The determination of the pulsar mass in those cases, is mainly based on Shapiro delay measurements, but there exists systems in which the spectroscopy of white dwarfs provides a measurement of the orbit's parameters needed to determine the mass of each star. For binary systems observed in X-ray, the analysis of the companion is crucial to estimate the neutron star mass; the systematic uncertainty in these cases is significantly larger than in the case of all double neutron star binary and many millisecond pulsar binaries. In general, the measurement of post-Keplerian parameters is the most reliable technique of neutron star mass determination; particularly, the Shapiro shape and delay are oftentimes used. It is also very common that the first estimation of the mass is revised a few years after the source was first observed. For example, in the binary source J0951+1807, the mass of the pulsar was first estimated to be $2.1 M_{\odot}$ (a record holder at the time), and later was revised to be $1.26 M_{\odot}$, and finally to $1.64 M_{\odot}$.

In this manuscript, the maximum mass criterion is set by the measurement of massive millisecond pulsar J1614–2230 [Arzoumanian et al. [2018]], with a mass of $1.908 \pm 0.016 M_{\odot}$. Sources with larger masses have been reported, such as the millisecond pulsar J0952–0607 [Romani et al., 2022], whose mass was estimated to be of $2.35 \pm 0.17 M_{\odot}$, and seems to be the fastest rotating pulsar in our galaxy (with a spin of 1.41 ms); however, this measurement is based on the analysis of the companion's spectroscopy. Also, the millisecond pulsar J0740+6620, was measured by [Cromartie et al. [2019]] using relativistic Shapiro delay for a

⁶If more than two post-Keplerian parameters are provided, the overdetermination of the binary allows one to test the theories of gravitation.

mass of $2.14^{+0.10}_{-0.09} M_{\odot}$; it was however recently revised to a $2.08 \pm 0.07 M_{\odot}$ [Fonseca and et al. \[2021\]](#).

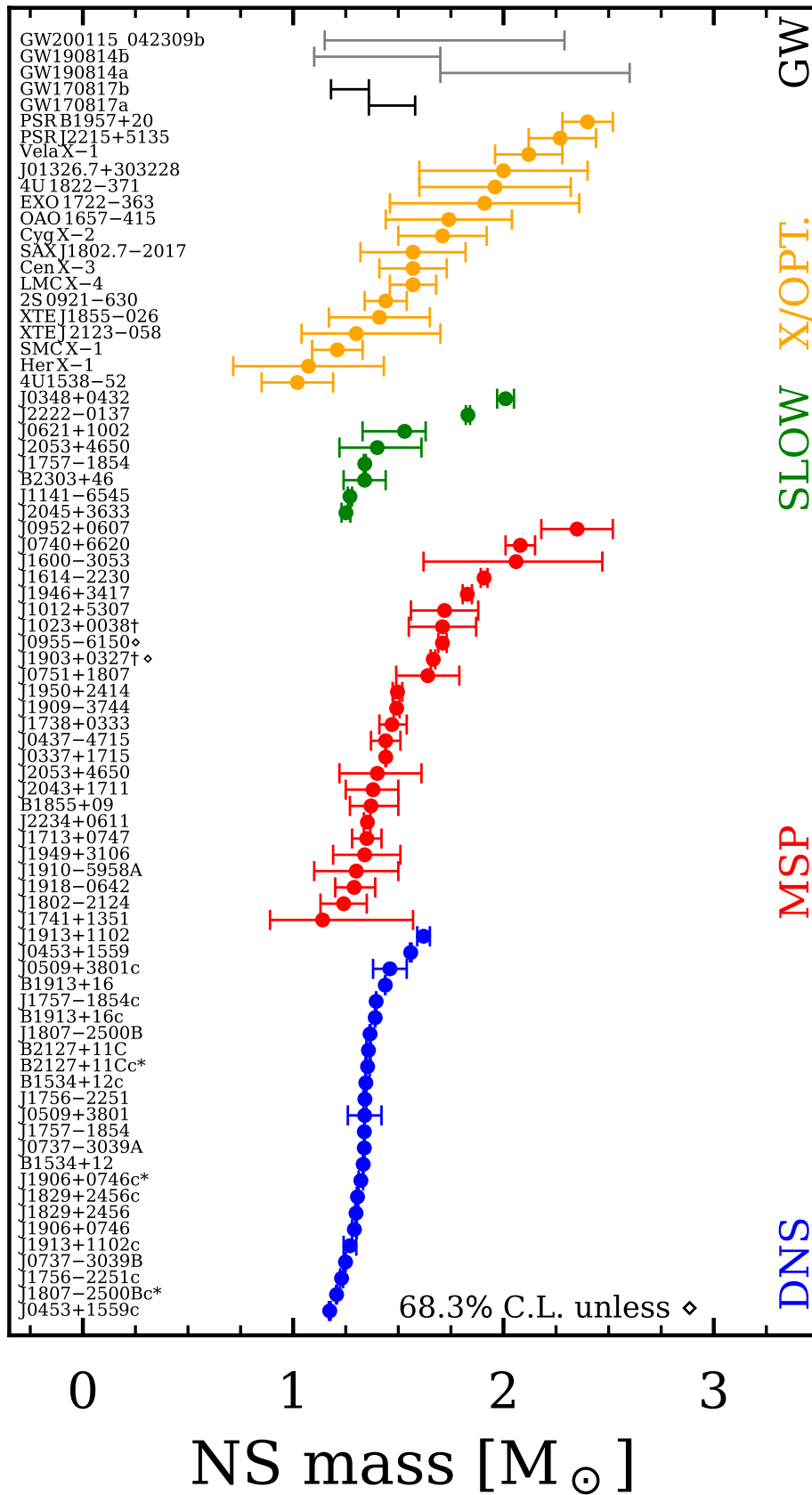


Figure 3.6: Mass measurements of seventy-five neutron stars presented for a 68.3% confidence level (1σ) except for sources presented with a \diamond symbol (99.7%) and gravitational wave detections.

The radius of a neutron star is directly connected to the equation of state's stiffness. For a significant range of pressures typical of neutron-star interior, the corresponding densities are smaller for a stiff equation of state than for a soft one. As a result, from the Tolman-Oppenheimer-Volkoff equations, the thickness of this region is larger for stiff equations of state, which can lead to a larger radius of the neutron star. A strong correlation exists between the pressure and the radius at densities $[1 - 2.5]n_0$ (saturation density $n_0 = 0.16 \text{ fm}^{-3}$), as shown by [Lattimer and Prakash \[2001\]](#). The radius and mass of two sources (PSR J0030+0451 and PSR J0740+6620), have been reported by the NICER telescope by two teams each. The measurement technique is based on an analysis of the surface emission of the pulsar, precisely of its hot spots. The source J0030+0451 was reported by [E. and et al. \[2019\]](#) to have a mass of $1.34_{-0.16}^{+0.15} M_\odot$ and radius of $12.71_{-1.19}^{+1.14} \text{ km}$ and reported by [Miller and et al. \[2019\]](#) to have a mass of $1.44_{-0.14}^{+0.15} M_\odot$ and a radius of $13.02_{-1.06}^{+1.24} \text{ km}$ within 1σ precision. The source J0740+6620 was reported by [Riley and et al. \[2021\]](#) to have a radius of $13.7_{-1.5}^{+2.6} \text{ km}$ and by [Miller et al. \[2021\]](#) to have a radius of $12.39_{-0.98}^{+1.3} \text{ km}$ within 1σ precision; prior knowledge from radio measurements of the mass and XMM-Newton telescope data were used. Because the uncertainty for the radius is quite large, measurements serve more as a proof of concept for an elegant radius determination, than a conclusive constraint on neutron star matter. The radius can also be determined from the thermal emission of the neutron star, but this method is strongly model dependent [[Potekhin, 2014](#)].

In [Abbott et al. \[2018\]](#), [Abbott and et al. \[2020\]](#), an indirect estimation of the radius was established from the detection of the tidal deformability extracted from the inspiral of the gravitational waves; the authors either used the so-called universal relations established in [Yagi and Yunes \[2017\]](#) to present a radius with 3.5 km error bars, or a collection of equations of state in a Bayesian analysis to give a likelihood for the radius. As a substitute for radius measurements, a series of papers attempt to impose limits on the radius. In [Steiner et al. \[2013\]](#), a prior distribution of equations of state is used to obtain a radius interval of $[10.4 - 12.9] \text{ km}$ for a $1.4 M_\odot$ neutron star, with a 95% confidence level. A similar approach is used by [Guillot et al. \[2013\]](#) in a Monte Carlo analysis with five low mass X-ray binary sources, to extract a minimum radius of $9.1_{-1.5}^{+1.3} \text{ km}$ within a 90% confidence level. In [Haensel et al. \[2009\]](#), a constraint on the radius is established, based on the assumption that neutron star's rotation follows a Keplerian frequency. However, neutron stars might not follow such frequencies when the rotation of the star is associated with gravitational wave emission or when triaxial deformability sets on.

It is important to note that the definition of the radius itself depends on the lowest density defined by the equation of state. The atmosphere of neutron stars is usually not presented in the equation of state; the lowest density provided by equation of state's tables ranges from 10^6 to 10^5 g/cm^3 for the mass density. There is therefore an ambiguity in the definition of the total radius: should the radius be defined at the surface of the outer crust, or at the surface of the atmosphere. However, the current precision on the determination of the radius implies that such consideration are not necessary yet, because the atmosphere is extremely thin ($\sim 1 \text{ m}$). In the following, we shall consider that the total radius is defined

as the radius at the surface of the outer crust.

The $M(R)$ sequence modelled from equations of state presented in section 3.1 are presented:

- in Fig. 3.7 for relativistic mean field models,
- in Fig. 3.8 for Skyrme models,
- in Fig. 3.9 for the *ab initio* model BCMP.

The maximum mass criterion from source J1614–2230, as well as the contours from NICER measurements of sources J0030+0451 and J0740+6620, are represented in those figures; only the Skyrme equation of state BSk19 and the relativistic mean field model H3 do not meet the maximum mass criterion.

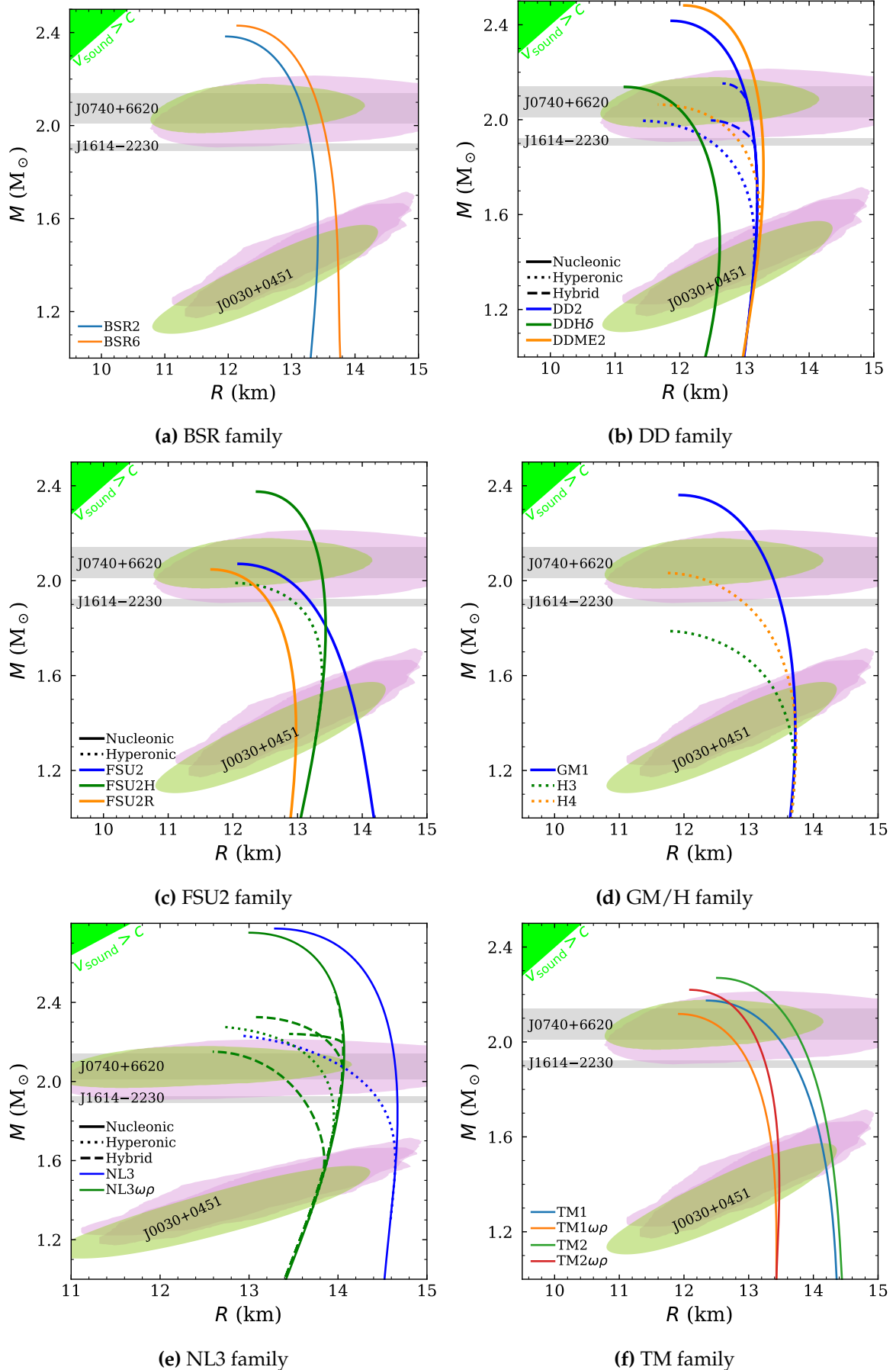


Figure 3.7: $M(R)$ sequence for relativistic mean field models presented in Table 3.1. The contour of the NICER measurements of J0740+6620 and J0030+2230 are represented in green and violet (see text for details). The maximum mass criterion from the source J1614–2230 is presented in grey. The sound speed velocity limit is presented in green.

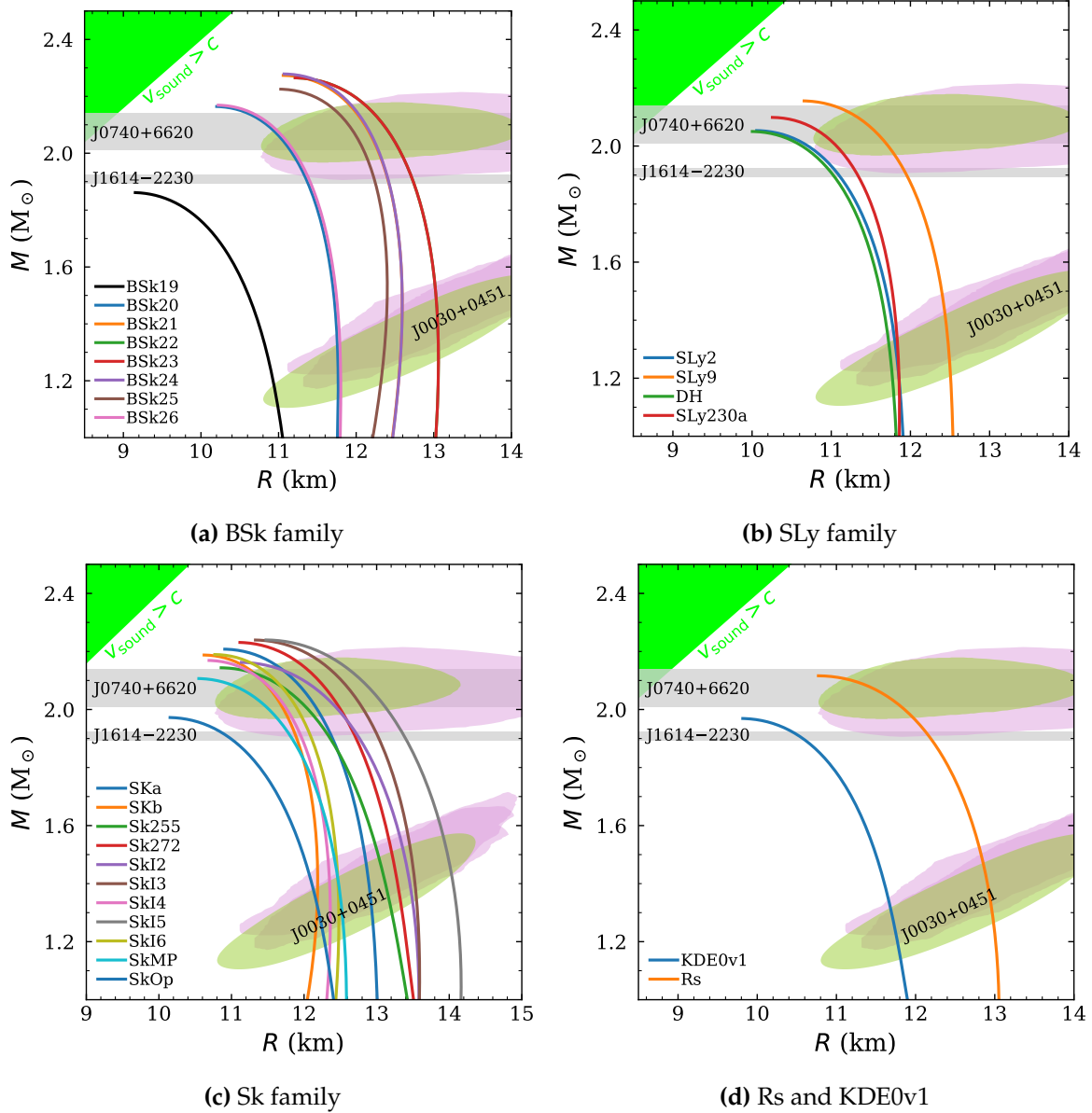


Figure 3.8: $M(R)$ sequence for Skryme models presented in Table 3.2. The contour of the NICER measurements of J0740+6620 and J0030–2230 are represented in green and violet (see text for details). The maximum mass criterion from the source J1614–2230 is presented in grey. The sound speed velocity limit is presented in green.

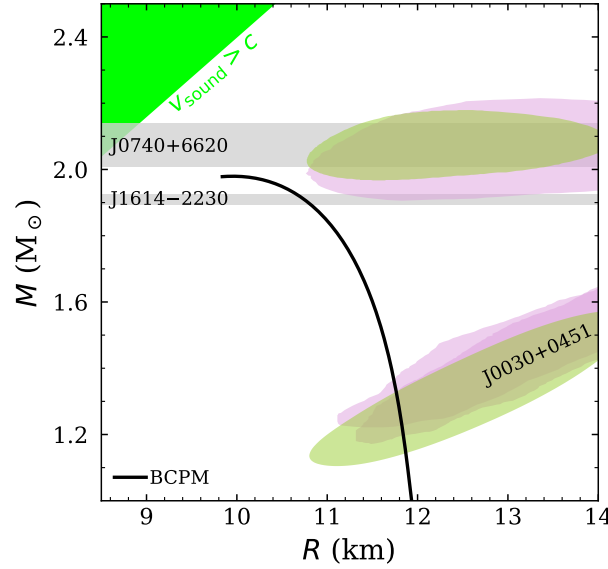


Figure 3.9: $M(R)$ sequence for the *ab initio* model BCPM. The contour of the NICER measurements of J0740+6620 and J0030+0451 are represented in green and violet (see text for details). The maximum mass criterion from the source J1614–2230 is presented in grey. The sound speed velocity limit is presented in green.

3.3.1.2 Moment of inertia

The moment of inertia, denoted I , measures the ability of an object to resist angular acceleration. The derivation of the moment of inertia can be approached in the slow rotation approximation, as presented in Hartle [1967]. The general idea of the slow rotation approximation is the following. Let us assume that the gravitational potential $\bar{\Phi}$ and the equation of state relation $\bar{\epsilon}(\bar{P})$, with ϵ the energy density, and P the pressure, are defined for the non-rotating self-gravitating body solution. To develop a solution for a rotating star from the solution of the non-rotating one, an expansion of leading term $(\bar{\Phi}, \bar{\epsilon}, \bar{P})$ in powers of the angular velocity Ω is performed. For a rotational axis along z , the polar angle is denoted θ , and the radial coordinate \bar{r} corresponds to the radius defined by isodensities, such that

$$\bar{\epsilon}(\bar{r}) = \epsilon(r, \theta). \quad (3.36)$$

The centrifugal force risen by rotation induces a displacement, denoted ζ , and a modification of the gravitational potential denoted χ . In the slow rotation approximation, it is reasonable to treat the radius and gravitational potential of the rotating star, as a development in angular velocity Ω with zeroth order \bar{r} and $\bar{\Phi}$. The quantities ζ and χ can be conveniently developed on the spherical harmonics basis

$$\zeta(\bar{r}, \theta) = \sum_l \zeta_l(\bar{r}) P_l(\theta), \quad (3.37)$$

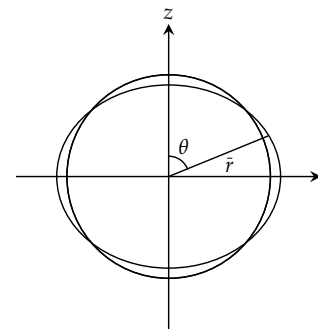


Figure 3.10: Illustration of the slow rotation configuration.

$$\chi(\bar{r}, \theta) = \sum_l \chi_l(\bar{r}) P_l(\theta), \quad (3.38)$$

with P_l the Legendre polynomials established at fixed $m = 0$ or in other words, for zonal harmonics. Because the system presented in Fig. 3.10 follows certain symmetries, some orders in the l^{th} development vanish:

- Symmetry with respect to the equatorial plane: $\forall \theta, \zeta(\bar{r}, \theta) = \zeta(\bar{r}, \pi - \theta)$. Because terms of the polynomial are proportional to $\sin^l(\theta)$, $\sin^{l-2}(\theta)$, the order l is necessarily even.
- Symmetry under the reversal of Ω direction: $\forall f, f(\Omega) \rightarrow f(-\Omega)$. The expansion must contain only even powers of the angular velocity

$$\mathbf{r} = [\bar{r} + \zeta(\bar{r}, \theta) + \mathcal{O}(\Omega^4)] \mathbf{e}_r, \quad (3.39)$$

$$\Phi = \bar{\Phi}(\bar{r}) + \chi(\bar{r}, \theta) + \mathcal{O}(\Omega^4). \quad (3.40)$$

Three equations are required to solve a rotating, self-gravitating object made of an ideal fluid:

- The field equations, which in the framework of Newtonian gravitation correspond to Poisson's equations, and in general relativity corresponds to Einstein's equation. Assuming rigid rotation, *i.e.* that the star rotates with an angular velocity which is constant in the star, the metric of space-time can be written as the sum of the Tolmann-Oppenheimer-Volkov metric $g_{\mu\nu}^{\text{TOV}}$, and an expansion in order of Ω of the slow rotation metric $h_{\mu\nu}$ such that

$$g_{\mu\nu} = g_{\mu\nu}^{\text{TOV}} + h_{\mu\nu}(\Omega) + \tilde{h}_{\mu\nu}(\Omega^2) + \dots \quad (3.41)$$

The metric h can be expressed in terms of Legendre polynomials, because the order l of the polynomial is linked to the chosen order of Ω through the symmetries presented above.

- The equilibrium equations that govern the fluid, and include the centrifugal potential. Within general relativity, this equation is derived from Einstein's equation [Hartle, 1967].
- The equation of state that relates the pressure and the density.

In the framework of general relativity, this leads to a set of differential equations to be solved simultaneously with the gravitational field $\Phi(r)$ equations

$$\frac{dI}{dr} = \frac{8\pi}{3} r^4 \left[\epsilon(r) + \frac{P(r)}{c^2} \right] e^{-\Phi(r)} \left(\sqrt{1 - \frac{2Gm(r)}{c^2 r}} \right)^{-1} \frac{\tilde{\omega}(r)}{\Omega}, \quad (3.42)$$

$$\frac{d\tilde{\omega}(r)}{dr} = \frac{6Ge^{\Phi(r)}}{c^2 r^4} \left(\sqrt{1 - \frac{2Gm(r)}{c^2 r}} \right)^{-1} j(r), \quad (3.43)$$

$$\frac{dj(r)}{dr} = \frac{8\pi}{3} r^4 \left[\epsilon(r) + \frac{P(r)}{c^2} \right] e^{-\Phi(r)} \left(\sqrt{1 - \frac{2Gm(r)}{c^2 r}} \right)^{-1} \tilde{\omega} \quad , \quad (3.44)$$

with $\tilde{\omega}(r)$ the spin frequency measured in a local inertial frame, $j(r)$ the contribution from the sphere of radius r to the stellar angular momentum such that $J = j(R)$, with R the total radius. The quantity Ω is the uniform angular frequency of the star measured at infinity

$$\Omega = \tilde{\omega}(R) + \frac{2GJ}{c^2 R^3} \quad . \quad (3.45)$$

The slow-rotation approximation is valid for stars with a rotating frequency well below the Keplerian frequency. To solve neutron stars with a consequent rotation frequency, the full treatment of a stationary axi-symmetric rotation for a self-gravitating body in general relativity is required; Einstein's equation for a metric whose conformal factors, and therefore the gravitational field, depend on the angular frequency must be solved. For instance, the numerical relativity software [LORENE Gourgoulhon et al. \[2016\]](#) can operate such calculations.

The moment of inertia calculated within the slow rotation approximation for the different equations of state used in this manuscript (see section 3.1) are presented in Fig. 3.12, Fig. 3.13 and Fig. 3.14. The moment of inertia is presented in those figures as a function of the central pressure, and not as a function of the total mass. In Fig. 3.11, we present the moment of inertia as a function of the total mass up to the maximum mass configuration for the family of equations of state DD. Around the maximum mass, it seems that the moment of inertia is decreasing drastically before reaching the maximum mass configuration. The moment of inertia treated in classical mechanics is approximately proportional to MR^2 . It can be seen from the $M(R)$ sequences presented in the previous section that around the maximum mass configuration, the mass stays almost constant, whereas the radius largely varies. This effect is absent for the dependence on the central density or pressure.

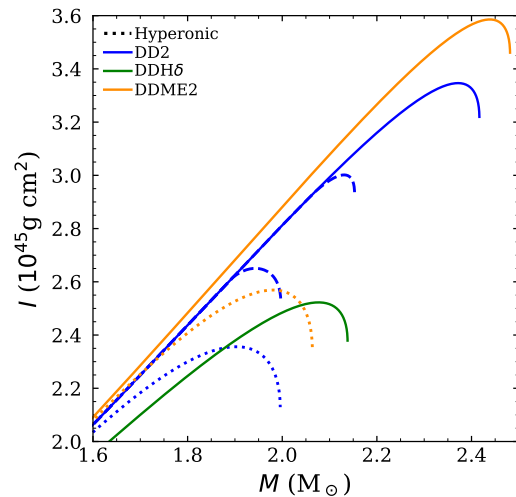
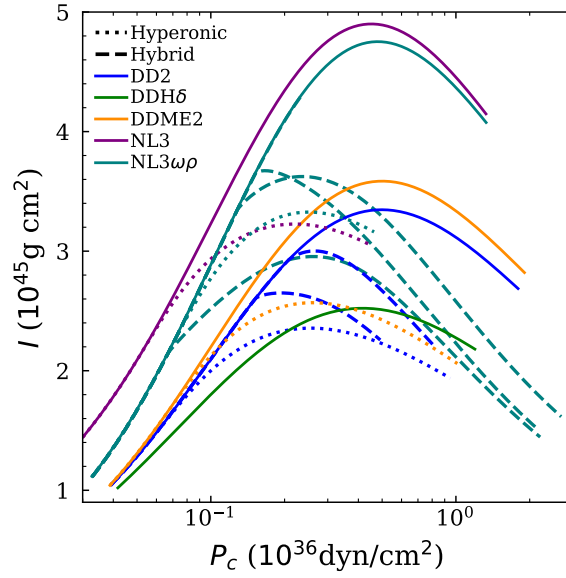
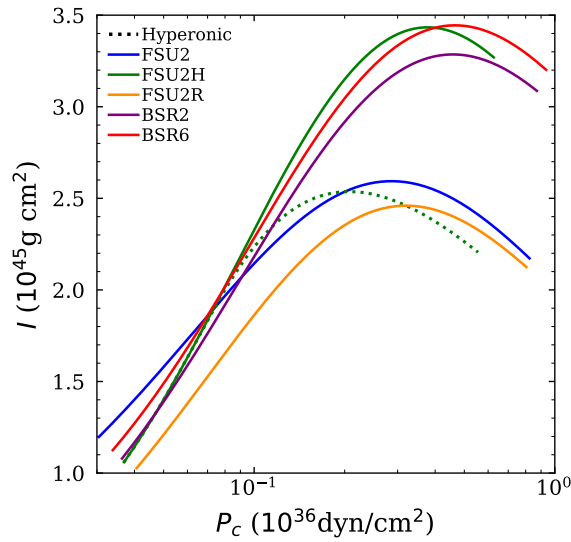


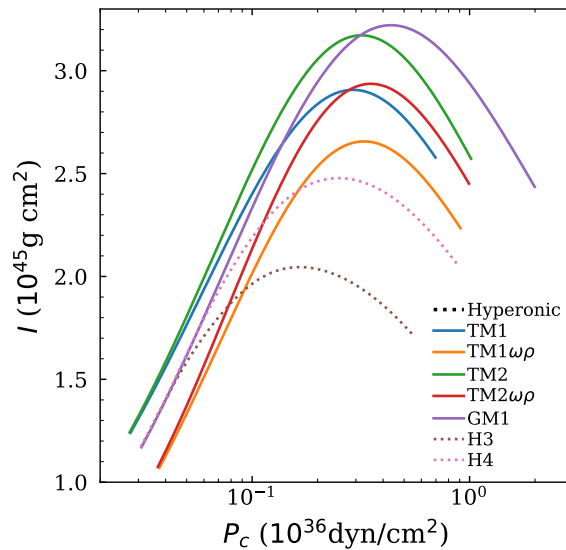
Figure 3.11: Moment of inertia calculated in the slow rotation approach for DD family relativistic mean field models.



(a) DD and NL families



(b) FSU2 and BSR families



(c) TM and GM/H families

Figure 3.12: Total moment of inertia I , as a function of the central pressure P_c , for stars in the range of $1.0 M_\odot$ to the maximum mass configuration, for the relativistic mean field models .

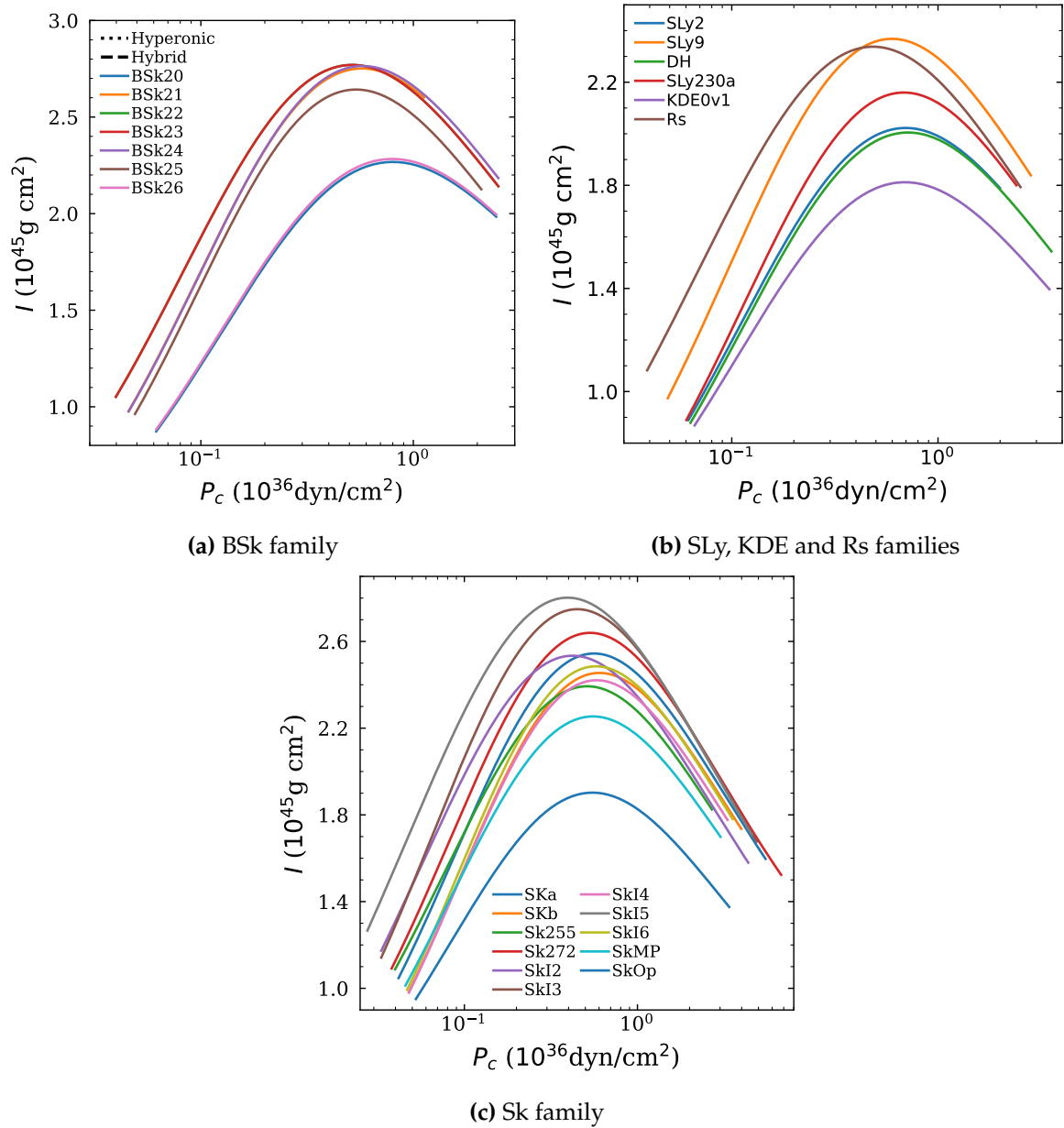


Figure 3.13: Total moment of inertia I , as a function of the central pressure P_c , for stars in the range of $1.0 M_\odot$ and the maximum mass configuration, for the Skyrme families.

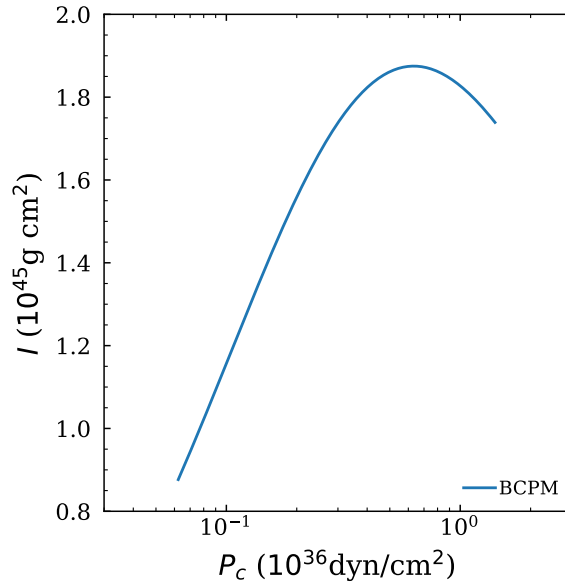


Figure 3.14: Total moment of inertia I , as a function of the central pressure P_c , for stars in the range of $1.0 M_\odot$ to the maximum mass configuration, for the *ab initio* BCPM model.

Rotation of the neutron star has consequences on the mass-radius relation of the star when considered beyond the slow-rotation approximation. The equatorial radius R_{eq} must be introduced for a rotating neutron star whose shape is not spherical. A large rotation frequency flattens the $M(R_{\text{eq}})$ sequence, because the equatorial radius is much larger. The gravitational mass of the star is also larger at fixed equatorial radius for rotating neutron stars than non rotating ones. The maximum mass for a given equation of state is therefore larger than the Tolmann-Oppenheimer-Volkoff maximum mass for high rotational frequencies [Haensel et al., 2016].

The measurement of I also holds great promises in the equation of state investigation, but has not been provided so far. Measuring the moment of inertia requires a monitoring of the relativistic features of the binary orbit (the more compact the better) over a long period of time, see Greif et al. [2020]. In a binary system, the gravitational spin-orbit coupling, which is a relativistic effect, causes the periastron to advance; the spin of a neutron star enters the second order of the advance of the periastron, and therefore might be extracted if observational precision allows, see Lattimer and Schutz [2005]. The best chance of measuring this parameter lies in highly compact binaries with high spinning neutron stars such as the binary pulsar PSR J0737–3039 McLaughlin et al. [2004], Kramer and et al. [2021]. The two pulsars of the system were observed, until pulsar B disappeared as a radio signal in 2008 due to precession. Fortunately, FAST and SKA radio-telescopes should hopefully increase the number of observations of pulsars by orders of magnitude, thus including thousands of millisecond pulsars, among which will be double pulsar binaries.

There are ways to provide an indirect measurement of the moment of inertia *via* the so-called universal relations: from the measurement of the compactness, one could extract

I with the help of those relations. [Silva et al. \[2021\]](#) used NICER measurement of PSR J0030+0451 compactness combined with a Markov chain Monte-Carlo analysis to provide a radius distribution of the $1.3381M_{\odot}$ neutron star of the double binary PSR J0737–3039, and extract I .

3.3.1.3 Tidal deformability

The tidal deformability can be defined as the susceptibility of the neutron star to be deformed by an external gravitation field. The equations determining this quantity are derived from the quadrupole moment of the star.

Let us consider an external tidal field denoted \mathcal{E} ; said field induces a response of the neutron star which is quantified by the multipole moment denoted \mathcal{Q} . Both \mathcal{E}_l and \mathcal{Q}_l can be developed on the basis of spherical harmonics \mathcal{Y}_l^m with mode l and expansion order m . Depending on the parity of the quantities, two tidal polarizabilities can be distinguished: the gravito-electric (or mass) multipole moment, and the magneto-electric (or spin) multipole moment.

In the following, we shall focus on the quadrupolar tidal deformability defined by the gravito-electric multipole moment of mode $l = 2$; for a complete study of both mass and spin multipole moments for any l , see [Damour and Nagar \[2009\]](#). The tidal deformability denoted $\lambda_2(r)$, is related to the tidal Love function denoted $k_2(r)$ according to

$$\lambda_2(r) = \frac{2}{3}k_2(r) \left[\frac{rc^2}{Gm(r)} \right]^5, \quad (3.46)$$

The derivation of the tidal Love function k_2 for a stationary and barotropic external gravitational field perturbation on the metric of an isolated neutron star is presented in [Hinderer \[2008\]](#), and is written in terms of the compactness as

$$\begin{aligned} k_2(r) = & \frac{8C(r)^5}{5} (1 - 2C(r))^2 [2 + 2C(r)(y(r) - 1) - y] \left\{ 2C(r) [6 - 3y(r) + 3C(r)(5y(r) - 8)] \right. \\ & + 4C(r)^3 [13 - 11y(r) + C(r)(3y(r) - 2) + 2C(r)^2(1 + y(r))] \\ & \left. + 3(1 - 2C(r))^2 [2 - y(r) + 2C(r)(y(r) - 1)] \ln(1 - 2C(r)) \right\}^{-1}. \end{aligned} \quad (3.47)$$

The function $y(r)$ is the solution to the set of equations presented in [Hinderer \[2008\]](#) that must be solved simultaneously with the Tolmann-Oppenheimer-Volkoff equations

$$r \frac{dy}{dr} + y(r)^2 + F(r)y(r) + Q(r) = 0, \quad (3.48)$$

$$F(r) = \left(1 - \frac{2Gm(r)}{rc^2} \right)^{-1} \left(1 - \frac{4\pi Gr^2}{c^4} [\epsilon(r) - P(r)] \right), \quad (3.49)$$

$$Q(r) = \frac{4\pi Gr^2}{c^4} \left(1 - \frac{2Gm(r)}{rc^2} \right)^{-1} \left[5\epsilon + 9P(r) + \frac{\epsilon(r) + P(r)}{v_{\text{sound}}(r)^2} c^2 - \frac{6c^4}{4\pi r^2 G} \right]$$

$$-4G \left(1 - \frac{2Gm(r)}{rc^2}\right)^{-2} \left[\frac{m(r)}{rc^2} + \frac{4\pi r^2}{c^4} P(r) \right]^2, \quad (3.50)$$

with the sound speed $v_{\text{sound}}^2 = c^2 dP/d\epsilon$, and the boundary condition $y(0) = 2$, for details on the boundary conditions see [Hinderer \[2008\]](#). In [Fig. 3.15](#), [Fig. 3.16](#) and [Fig. 3.16](#), we present the observable dimensionless tidal deformability denoted Λ and defined as $\Lambda = \lambda(R)$, as a function of the central pressure for the different models used in this manuscript.

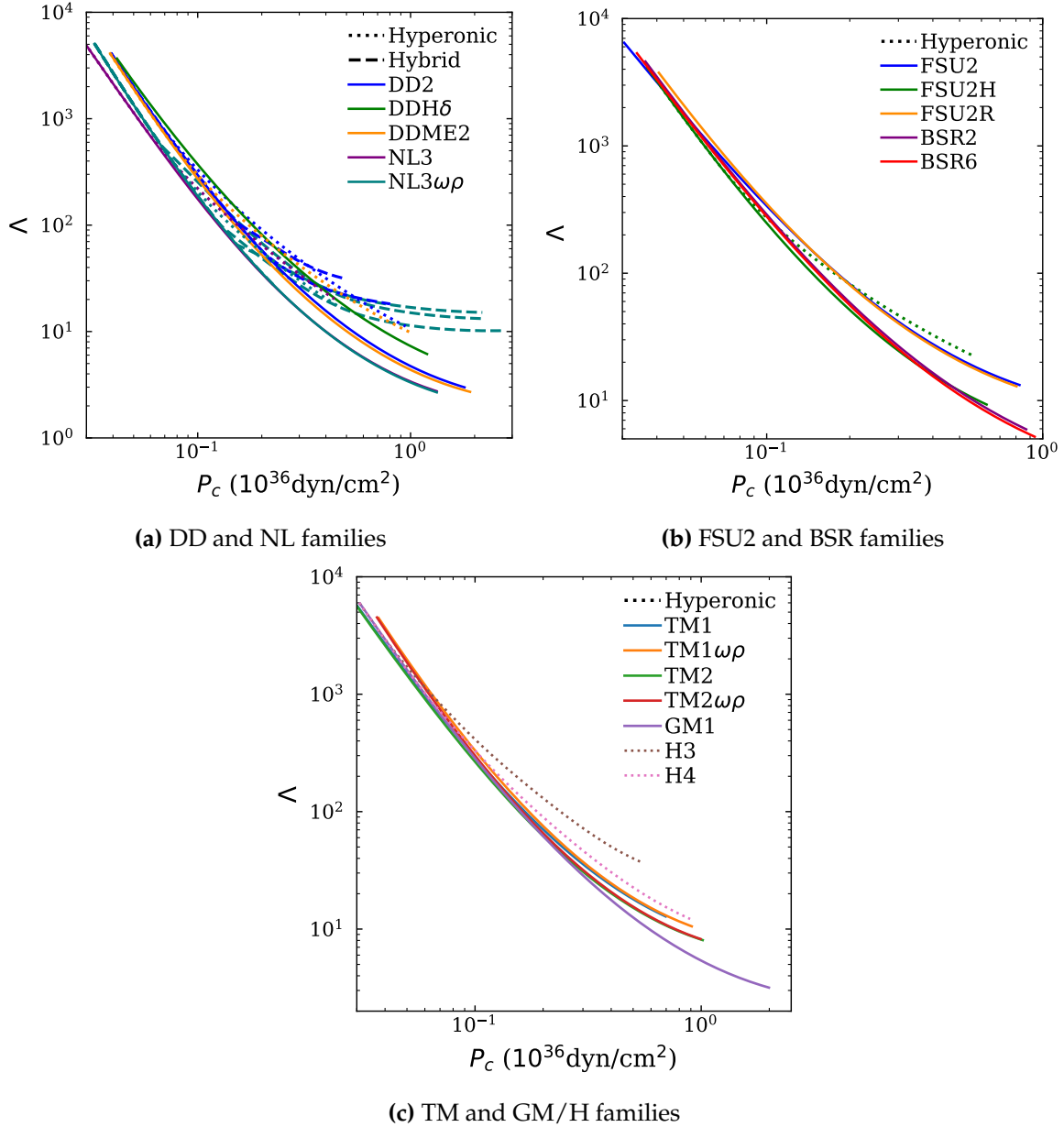


Figure 3.15: Tidal deformability Λ , as a function of the central pressure P_c , for stars in the range of $1.0 M_{\odot}$ to the maximum mass configuration, for relativistic mean field models.

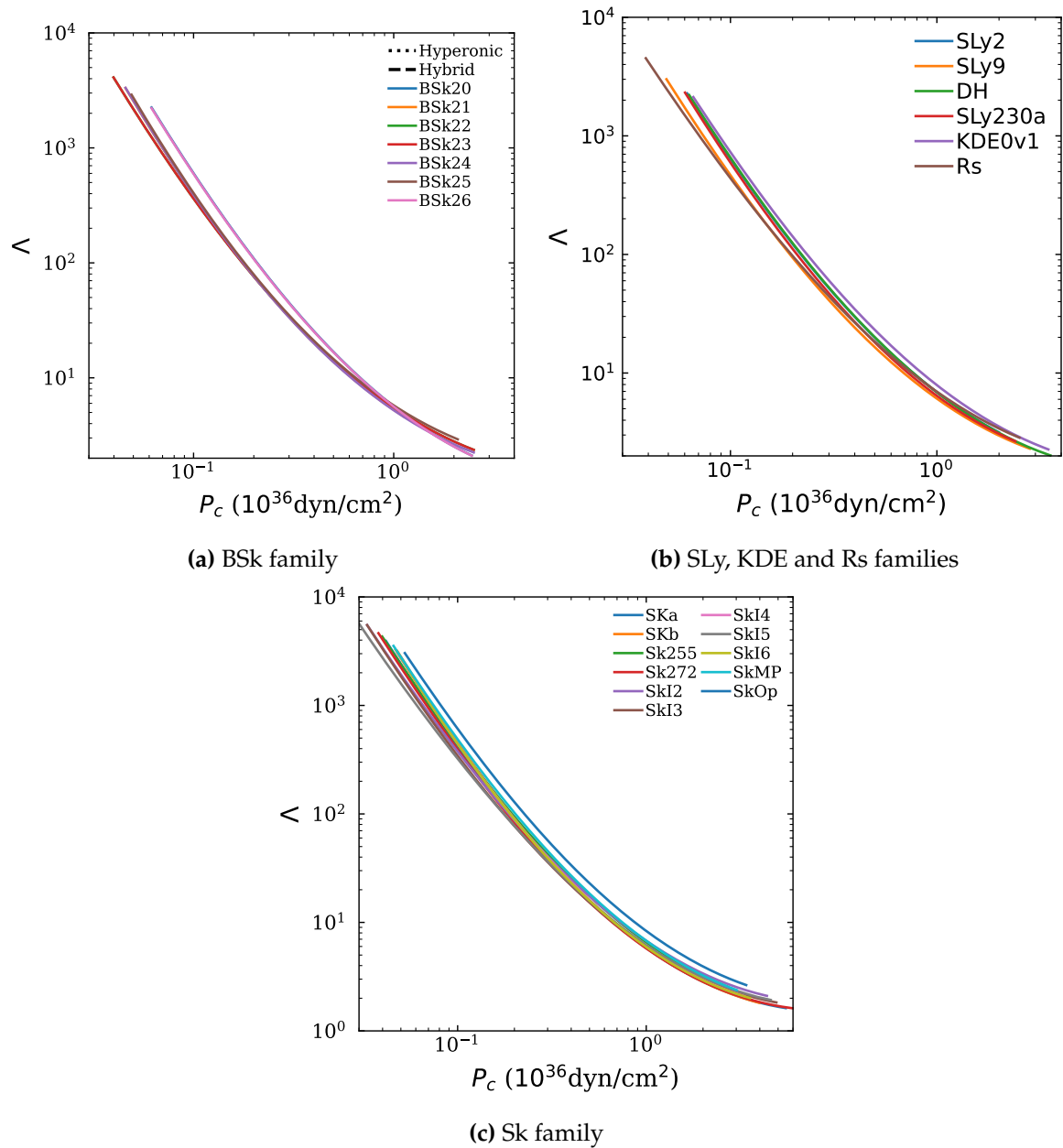


Figure 3.16: Tidal deformability Λ , as a function of the central pressure P_c , for stars in the range of $1.0 M_\odot$ to the maximum mass configuration, for Skyrme models.

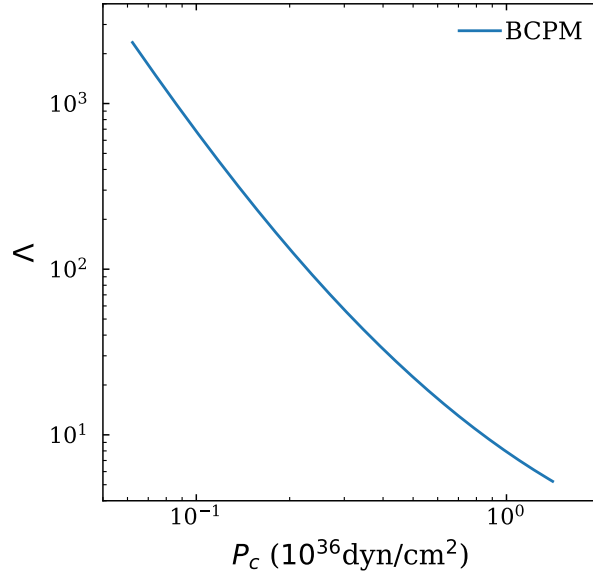


Figure 3.17: Tidal deformability Λ , as a function of the central pressure P_c , for stars in the range of $1.0 M_\odot$ to the maximum mass configuration, for the *ab initio* BCPM model.

Observational prospects for the tidal deformability rely on gravitational wave measurements. Indeed, the tidal deformability can be extracted from the inspiral of a neutron star binary system. The detection of the merger GW170817 [Abbott et al., 2017], which was the first double neutron star (NS-NS) binary merger to be detected with gravitational waves, provided a constraint on the relation between the tidal deformabilities of the two stars. The dominant tidal parameter which enters the inspiral GW waveform is the effective tidal deformability of the binary

$$\tilde{\Lambda} \equiv \frac{16 (M_1 + 12M_2)M_1^4\Lambda_1 + (M_2 + 12M_1)M_2^4\Lambda_2}{13 (M_1 + M_2)^5}. \quad (3.51)$$

To model this relation from the equation of state, the tidal deformability of the two stars is obtained while varying the mass of the heaviest neutron star M_1 in the range proposed in Abbott et al. [2017], *i.e.* $[1.365 - 1.60] M_\odot$; the mass of the lightest M_2 neutron star is determined by fixing the chirp mass

$$\mathcal{M} = \left(\frac{(M_1 M_2)^3}{M_1 + M_2} \right)^{1/5}, \quad (3.52)$$

at its measured value: $1.188 M_\odot$. In Fig.3.18, we present the 90% and 50% credibility lines presented in Abbott et al. [2017], as well as the relation between the tidal deformabilities of the two stars modelled with nucleonic relativistic mean field models NL3, DD2 and H3, and Skyrme models BSk21 and SLy4. In this figure, NL3, which is a very stiff model, does not comply with tidal deformability measurements within the 90% precision line.

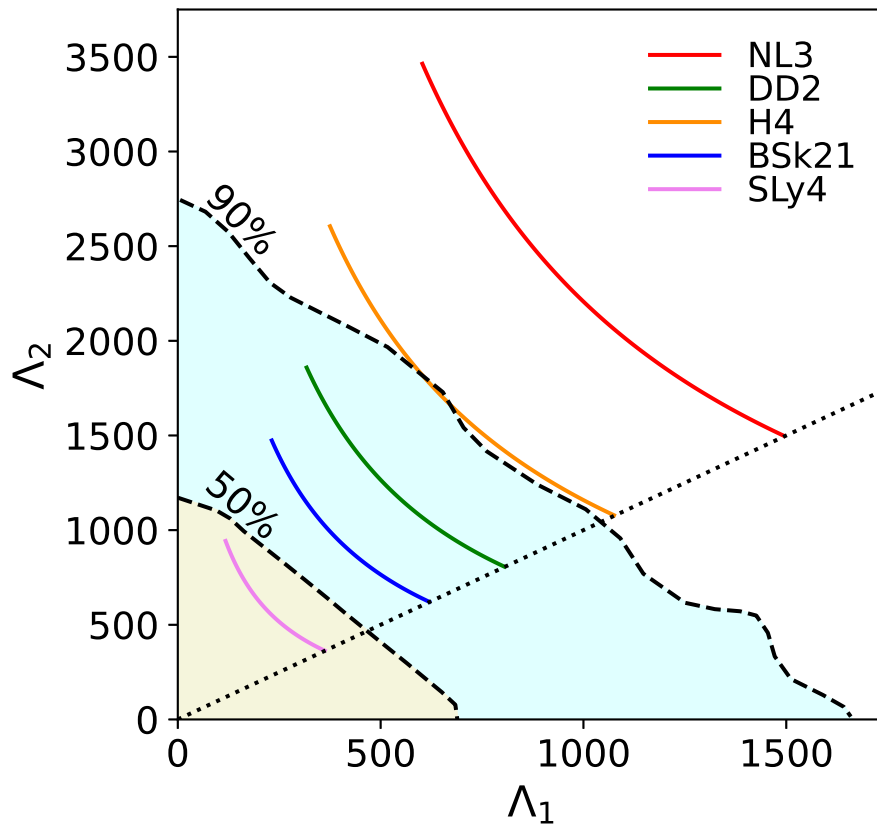


Figure 3.18: Relation between the tidal deformabilities of the heaviest star Λ_1 and the lightest star Λ_2 of the binary neutron star merger GW170817 for models NL3, DD2, H4, BSk21 and SLy4. We also represent the 90% and 50% credibility lines provided by [Abbott et al. \[2017\]](#).

3.3.2 Astrophysical constraints on the microphysics parameters

In addition to nuclear physics experimental constraints, it is possible to impose astrophysical constraints on the symmetry energy at saturation density J and its slope L .

Observations of neutron star cooling in the X-ray band has revealed the role of neutrino emission rapidly cooling processes in the core of accreting neutron stars (in a binary receiving matter from its companion) [[Fortin et al., 2018](#)]. The Direct Urca process [[Lattimer et al., 1991](#)] is permitted if the proton fraction is high enough, and is therefore triggered at a given value of the density n_{DUrca} . This threshold is constrained by the density dependence of the symmetry energy, such that a large L favors a large proton fraction, and a process allowed for lower n_{DUrca} - or equivalently for lower neutron star mass. The presence of hyperons in the core implies that there is no need for an elevated L to ensure that the DUrca process occurs [[Fortin et al., 2021](#)]. In [Fig. 3.5a](#) and [Fig. 3.5b](#) which present the values of L and J for the models presented in [section 3.1](#), the models which do not permit the process of DUrca ($n_{\text{DUrca}} > n_{\text{max}}$) are presented in green: DD2, DDME2, BSk20, BSk26, KDE0v1, SLy2, DH and Skb.

Techniques to infer knowledge relevant for microscopic parameters, based on Bayesian inference statistical analysis were recently designed; we refer to Ref. [Golomb and Talbot \[2022\]](#) for a recent study of this technique, and to Ref. [Vitale et al. \[2020\]](#) and references therein for a review. Instead of confronting equations of state one by one to macroscopic observables, it is possible to use a more systematic approach. Bayesian inference is a statistical technique using data to make an educated guess through the Bayes Theorem

$$\mathcal{P}(X|Y) = \frac{\mathcal{P}(Y|X) \times \mathcal{P}(X)}{\mathcal{P}(Y)}, \quad (3.53)$$

with:

- $\mathcal{P}(X)$ the probability distribution of the equation of state, called the prior: it corresponds to what we believe the equation of state is before any measurement is made.
- $\mathcal{P}(Y|X)$ the probability given an equation of state of getting a certain measurement is called the likelihood associated to the measurement.
- $\mathcal{P}(Y)$ the probability of making the measurement is called the marginal likelihood,
- $\mathcal{P}(X|Y)$ what is believed about the equation of state given the measurement is the posterior.

In overall, we start with a belief in what the equation of state should be (as vague as nuclear physics constraints of dense matter), then make the measurement and have a new belief in what the equation of state is. In practice, a random statistical method such as Monte-Carlo-Markov-Chain, or Gaussian process, is used to infer information on dense matter by implementing observational filters on agnostic equation of state priors. GW170817 detection was used in [Raithel and Özel \[2019\]](#), [Güven et al. \[2020\]](#) to constrain L : in [Raithel and Özel \[2019\]](#) the effective tidal deformability of the binary is strongly correlated to that quantity and GW170817 indicates a preference for a low L . [Malik et al. \[2018\]](#) discovered strong correlations between the tidal deformability and linear combination of pairs of nuclear parameters of different orders. [Miller et al. \[2021\]](#), [Riley and et al. \[2021\]](#) related to NICER observation of J0740+6620, used a Bayesian analysis based on likelihood of measurement to infer high density equation of state properties. Perfect knowledge of the equation of state below half the saturation density ($n_0/2 = 0.08 \text{ fm}^{-3}$) is assumed; above $n_0/2$, a parametrized equation of state and Gaussian-process-based models are used. A similar technique is used by Ref. [Essick et al. \[2021\]](#) with Chiral Effective Theory (CET) constraints.

Bayesian inference can be used with mass measurements, gravitational wave detection, radius measurements of NICER etc. see *e.g.* [Somasundaram et al. \[2021\]](#), [Al-Mamun et al. \[2021\]](#), [Malik and Providência \[2022\]](#). It is also possible to include nuclear physics constraints, such as the heavy ion collision data, or chiral effective field theory calculations, see *e.g.* [Ghosh et al. \[2022\]](#).

Overall, the observation of neutron star's macroscopic parameters can help constrain the microphysics of their interior beyond what is achievable in nuclear physics laboratory.

The maximum mass criterion is the most precise constraint available to us as of today. The NICER telescope provides simultaneous measurements of the mass and the radius of a few millisecond pulsars, with a precision which is yet not constraining for ultra dense matter properties, but is promising. The booming era of gravitational waves has lead to the detection of the double neutron star binary merger GW170817, and provided the first measurement of the neutron star tidal deformability.

3.4 Consequence of non-unified models for dense matter on neutron star modelling

Equations of state for neutron star matter are based on advanced calculations. Particularly, treating inhomogeneous matter in the crust is more complicated than treating the homogeneous matter in the core. It is a common practice within the astronuclear physics community to design equations of state separately for the core and the crust. In this section, we present the consequences of such constructions on the modelling of macroscopic parameters, as is detailed in [Suleiman et al. \[2021\]](#) and [Suleiman et al. \[2022a\]](#).

3.4.1 Unified vs. non-unified equations of state

Non-unified equations of state are defined as equations of state which have been calculated using different nuclear models for the core and for the crust. A widespread practice is to compute a core equation of state, and match to it a well-known, well-established crust. Examples for the use of non-unified equations of state are found in more simulations than can be listed: analytical representations used for gravitational wave data, finite temperature simulations, modelisation of neutron star's parameters in modified gravity, magneto-hydrodynamics, quasi-universal relations, etc.

This non-unified approach to constructing equations of state of dense matter is founded on two assumptions:

- The assumption that the crust is well-constrained by laboratory measurements, in which case the equation of state and composition of the crust should be the same for any nuclear model calibrated to laboratory measurements. However, only part of the outer crust is constrained by measurements of nuclear masses, as is presented in [Fig. 3.3](#).
- The assumption that the macroscopic parameters of neutron stars do not depend on the crust equation of state. Although it is true that some macroscopic parameters are more impacted by the core equation of state (as is the case for the mass and the moment of inertia), the radius is particularly influenced by the crust equation of state. Moreover, using non-unified equations of states with no care for the core-crust matching introduces errors that go beyond the model dependence of the crust, as we discuss in the following.

From unified computations, the core-crust transition density, denoted n_t , can be calculated as the density point for which uniform matter becomes unstable with respect to spatial variations in the particle densities. In [Tsang et al. \[2019\]](#), [Pais and Providência \[2016\]](#), the linear dependence of n_t on the slope of the symmetry energy at saturation density is discussed. To estimate n_t outside of complete unified equation of state models, several techniques were proposed, but the uncertainty in its value is large. For example, it was found that n_t ranges between $[0.3 - 0.6]n_0$, for the broad collection of equations of state considered in [Oyamatsu and Iida \[2007\]](#), [Ducoin et al. \[2011\]](#), [Pais and Providência \[2016\]](#). It is very common that n_t is

not calculated at all, hence a widely used approach when constructing a non-unified equation of state is to glue core and crust at some density around saturation density n_0 . However, we will show in the following that the microscopic parameters for different models of dense matter can be very different at such densities.

In principle, when gluing equations of state, one should match all thermodynamical quantities: the pressure P , the energy density ϵ , and the baryon density n . In other words, a pair of functions: $P(n)$ and $\epsilon(n)$ should be constructed so that thermodynamical consistency is fulfilled, ensuring that the chemical potential μ as a function of the pressure is continuous. However, the constructed equations of state in the literature do not always uphold this continuity. A matching technique is employed in [Margueron et al. \[2018\]](#): a cubic spline is used on the logarithm of the pressure and mass-energy density over the range of baryonic densities between $0.1n_0$ and n_0 . For this technique, later on referred to as the spline technique, the continuity in pressure is ensured, but not the continuity in chemical potential.

We can now identify four different flaws in non-unified constructions:

- the inner crust model dependence,
- the uncertainty on the estimated value of the core-crust transition density,
- the difference in the microscopic properties of the core and crust models,
- and the thermodynamic inconsistencies of the matching.

In order to assess the role of non-unified constructions of equations of state on neutron star modelling, we use the set of unified equations of state presented in section 3.1; note that figures presented in section 3.3.1 are established from unified constructions. For this set of unified equations of state, the inner crust is calculated consistently with the core, *i.e.* using the same nuclear parametrization. The resulting equation of state would be better qualified as quasi-unified, because the outer crust is not calculated consistently with the inner crust and the core. However, it was shown in [Fortin et al. \[2016\]](#) that the radius is hardly affected if a non-consistent outer crust is used, in the sense that the uncertainty that is introduced for masses above $1.0 M_\odot$ (which is the mass range of all neutron stars currently observed) is much less than the precision of any current or near-future measurements.

The set of unified equations of state based on relativistic mean field calculations are taken from [Fortin et al. \[2016, 2020\]](#), [Providência et al. \[2019\]](#); the relativistic mean field models which include hyperons are constructed consistently with the available experimental measurements of hypernuclei properties detailed in [Fortin et al. \[2017, 2020\]](#). The inner crust equation of state is calculated within the Thomas-Fermi approximation consistently with the equation of state for the core [[Grill et al., 2014](#), [Providência et al., 2019](#)]. The equation of state of the outer crust has not been obtained consistently, but was taken from [Rüster et al. \[2006\]](#). Several other outer crust equations of state are available, for example [Baym et al. \[1971\]](#), [Haensel and Pichon \[1994\]](#), [Pearson et al. \[2018\]](#), but they all are strongly constrained by nuclear physics data and therefore quite similar.

The set of unified equations of state based on Skyrme models is taken from Fortin et al. [2016], except for DH and Brussels-Skyrme models which are already constructed in a unified way. The construction of the crust does not include shell effects nor curvature terms, which results in a mass shift with respect to experimentally measured masses [Gulminelli and Raduta, 2015]. Therefore, the equation of state for the external part of the outer crust differs from that which employs experimental data; however, the differences are small enough to impact the relation between the mass and the radius by less than 1%.

For the *ab initio* equation of state, the outer crust is based on the formalism of Baym et al. [1971]; a density functional designed from Brueckner-Hartree-Fock computations is used in the deformed Hartree-Fock-Bogoliubov formalism for nuclei which are not included in the data table of Wang et al. [2012]. For the inner crust, the energy density functional derived from Brueckner-Hartree-Fock calculations is used in the Thomas-Fermi approximation.

Although we have chosen to focus on models presented in Fortin et al. [2016], several nuclear physics groups have put tremendous efforts in designing unified models, to name but a few Douchin and Haensel [2001], Gulminelli and Raduta [2015], Sharma et al. [2015], Pearson et al. [2018], Viñas et al. [2021], Parmar et al. [2022].

To assess the role of non-unified constructions of equation of state on macroscopic parameter modelling, we focus on three models for dense matter with a purely nucleonic core (uniform neutron, proton, electron and muon mixture) obtained from unified relativistic mean field calculations, classified from stiff to soft: NL3, BSR6, and DD2. To construct non-unified equations of state, we use the additional equations of state DH and BSk21 (with an accreted and nonaccreted crust) which are both based on Skyrme parametrizations.

We compare the following equation of state constructions:

- unified equations of state DD2, BSR6 and NL3;
- core of DD2, BSR6 and NL3, to which the crust of DH is matched at several densities;
- core of DD2, BSR6 and NL3, to which the catalyzed crust of BSk21 is matched at several densities;
- core of DD2, BSR6 and NL3, to which the accreted crust of BSk21 [Fantina et al., 2013] is matched at several densities.

The following matching densities are investigated

$$n_m = \begin{cases} 0.08 \text{ fm}^{-3}, \\ 0.1 \text{ fm}^{-3}, \\ 0.16 \text{ fm}^{-3}, \\ n_t \text{ extracted from unified calculations.} \end{cases} \quad (3.54)$$

Table 3.3: Nuclear properties of the models for dense matter used in this section. Are presented, the saturation density n_{sat} , the energy per nucleon at saturation density (\mathcal{E}_{sat}), the compression modulus at saturation density (K_{sat}), the symmetry energy at saturation density (J), and the slope of the symmetry energy at saturation density (L). The density at the interface between the core and the crust extracted from unified calculations, is denoted n_{t} . The last two columns present the value of the symmetry energy and its slope, at the density 0.1 fm^{-3} and are denoted respectively $J_{0.1}$ and $L_{0.1}$.

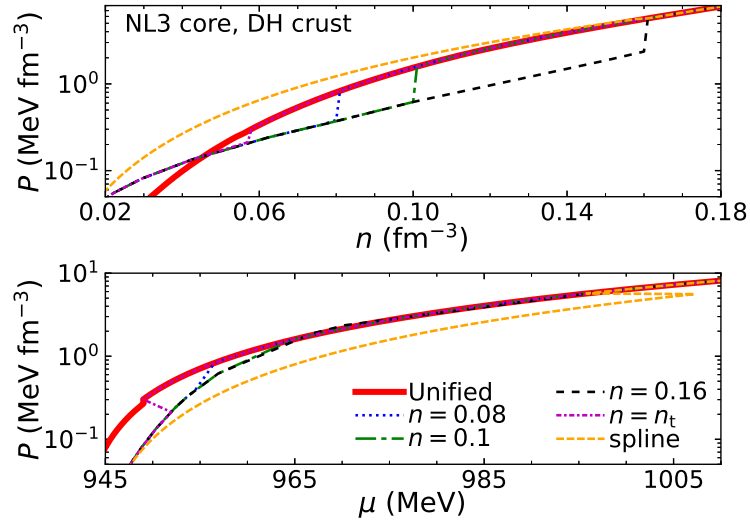
Model	n_{sat} (fm^{-3})	\mathcal{E}_{sat} (MeV)	K_{sat} (MeV)	J (MeV)	L (MeV)	n_{t} (fm^{-3})	$J_{0.1}$ (MeV)	$L_{0.1}$ (MeV)
Core								
NL3	0.149	-16.2	271.6	37.4	118.9	0.057	25.0	73.7
BSR6	0.149	-16.1	235.8	35.6	85.7	0.061	25.8	62.9
DD2	0.149	-16.0	242.6	31.7	55.0	0.067	24.9	70.1
Crust								
DH	0.159	-16.0	230.0	32.0	46.0	0.076	25.2	41.6
Bsk21	0.159	-16.1	245.8	30.0	46.6	0.081	23.7	36.8

Table 3.3 presents nuclear properties for all models at play at their respective saturation density and at 0.1 fm^{-3} . The core equations of state of NL3, BSR6 and DD2 have very different microscopic properties at saturation density from those of the crust equations of state. The differences are greater between NL3 core and DH crust, than between DD2 core and DH crust. The reason lies in the softness of DH: as DD2 has also a relatively soft core, the microscopic parameters are more similar to that of DH, than the stiff core of NL3. Matching the core and the crust, at values of the density at which models are microscopically incoherent, will induce inconsistencies in the equation of state. Note that the differences are not as pronounced at 0.1 fm^{-3} .

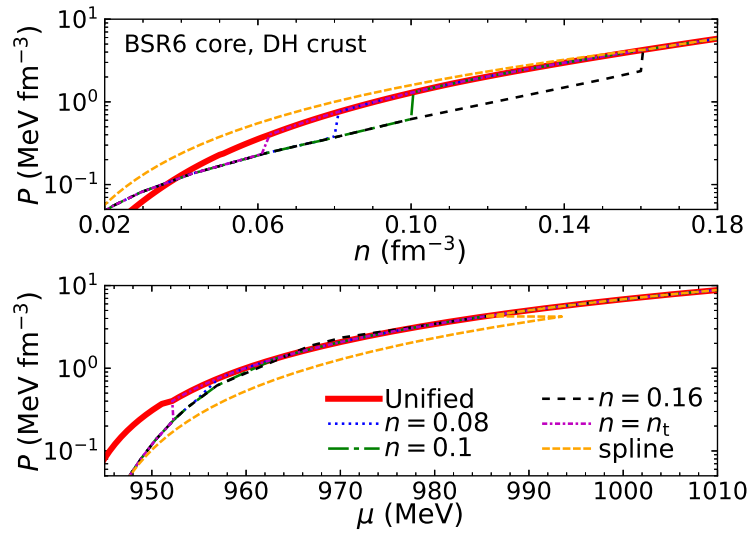
Figure 3.19 shows the pressure as a function of the baryon number density n , and as a function of the chemical potential μ for the different equations of state constructions that we consider. A jump in the pressure as a function of the baryon number density can be observed at the transition between the core and the crust for all matched constructions except the one employing a spline matching technique. All matched equations of state exhibit a jump in the chemical potential which attest to the thermodynamic inconsistency of the matching. In the case of the spline matching technique, the jump stems from the fact that even though the pressure is continuous, the energy density is not at the upper bound of the interpolated crust equation of state. Thermodynamic inconsistencies are introduced by non-unified constructions as jumps in the relation between the pressure and the chemical potential.

In the case of the matching at n_0 , the stiffer the core equation of state, the larger the pressure jump. The microscopic quantities of NL3 are further from that of DH than BSR6 and DD2; in others words at this value of the density, DH is soft, and therefore is better matched with a soft core model. Matching at the core-crust transition density ensues jumps as well, showing that to reduce the inconsistencies is not just about finding the core-crust transition, but also about matching the microscopic quantities as this value. Not only do

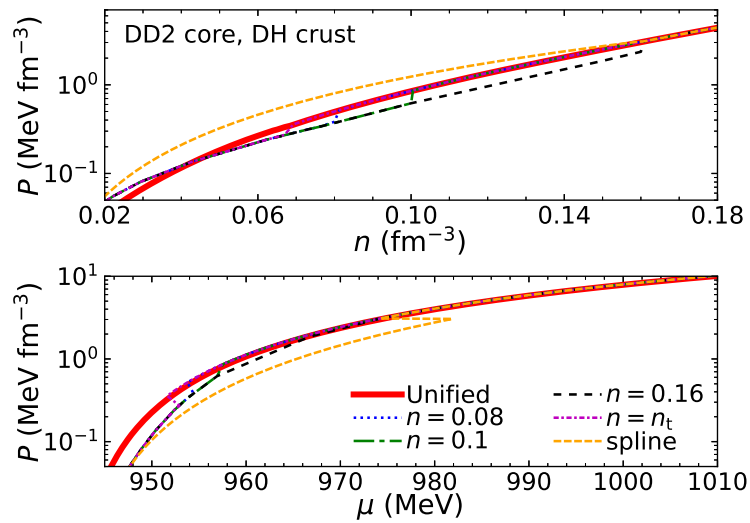
models for dense matter have different core-crust transition densities, but this region is not calibrated by laboratory measurement so that the equations of state at this transition point are different.



(a) NL3 core



(b) BSR6 core



(c) DD2 core

Figure 3.19: Relation between the pressure P and the baryonic density n , as well as the pressure and the chemical potential μ . Results are presented for the unified equations of state NL3, BSR6 and DD2, and for non-unified constructions designed for matching density n_m presented in Eq. (3.54) and with the spline technique.

3.4.2 Consequence on macroscopic parameter's modelling

The relativistic hydrostatics equations are nonlinear, and the neutron star interior is opaque to observations. Therefore, one cannot separate the contribution of different parts of the equation of state in the modeling of the total macroscopic parameters in a simple way. To evaluate the consequences of non-unified equations of state on the modeling of macroscopic parameters, the equations of hydrostatics are solved according to section 3.3 for the different constructions presented in the previous section.

Results are presented in Fig. 3.20: the total radius, the moment of inertia in the slow rotation approximation, and the dimensionless tidal deformability are presented as a function of the total mass of the star on the left hand side of the figure. To quantify the effect of the matching compared to unified equations of state, we calculate for a given total mass and variable $X = R, \Lambda, I$, the relative difference between the variable for a given matching X_m and the unified equation of state X_u

$$\frac{\Delta X}{X} = \frac{X_m - X_u}{X_u}. \quad (3.55)$$

This quantity is plotted in the right panels of Fig. 3.20.

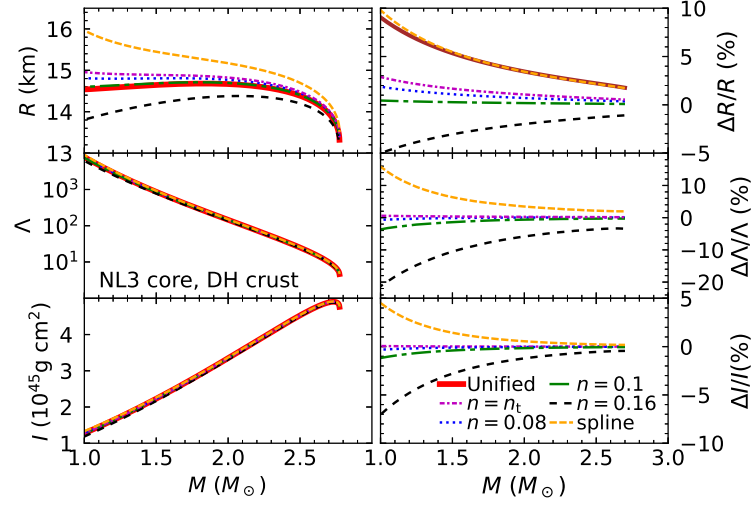
The error induced by non-unified constructions can be as large as $\sim 10\%$ for the radius, $\sim 20\%$ for the tidal deformability and $\sim 5\%$ for the moment of inertia, in the case of the stiff core model NL3. For the softer equation of state DD2, errors are much smaller, respectively $\sim 6\%$, $\sim 5\%$ and $\sim 1\%$. Therefore, core-crust matching of two equations of state with very different microscopic parameters, such as the symmetry energy J_m and its slope L_m , increases the error in the modeling of macroscopic parameters.

The errors are largest for small total masses of the neutron star: for large neutron star masses, the core plays relatively a more important part in the star than for small total masses, therefore the crust inconsistencies have less impact for large total masses.

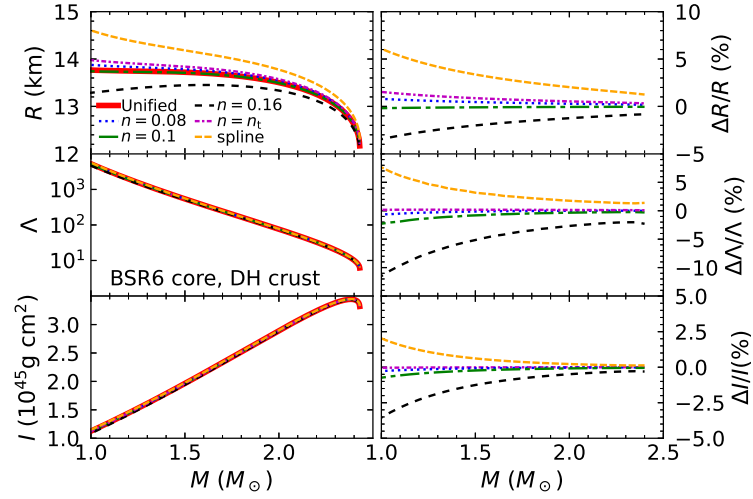
The matching between the core and the crust introduces a large relative difference with respect to the unified equation of state in the radius determination. In the case of the spline technique of matching presented in Fig. 3.20a, it is even as large as 10%, or 1.5 km for a $M \simeq 1 M_\odot$ neutron star. The error introduced by thermodynamical inconsistencies on the modeling of the radius can be anticipated using the relation between the jump in chemical potential and the radius presented in Zdunik et al. [2017]

$$\frac{\Delta R}{R} = -0.72\% \frac{\Delta\mu}{1 \text{ MeV}} \frac{R}{10 \text{ km}} \frac{M_\odot}{M} \left(1 - \frac{2GM}{Rc^2} \right); \quad (3.56)$$

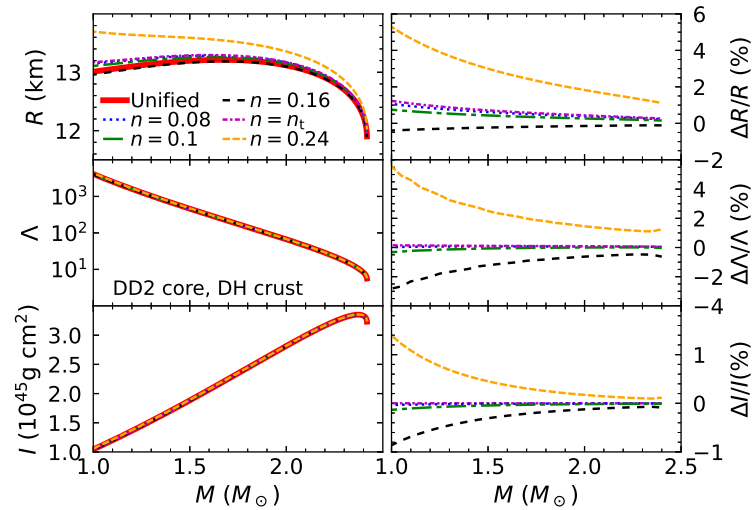
this estimation is very accurate, as is presented in Fig. 3.20a for the spline construction. The sign of the relative difference is related to the sign of the jump in the chemical potential: a drop in the chemical potential results in a larger radius, hence a positive $\Delta R/R$, and vice versa. The inaccuracy in the radius due to the discontinuity in the chemical potential can



(a) NL3 core



(b) BSR6 core



(c) DD2 core

Figure 3.20: M , R , I and Λ for the different matched constructions and the unified equations of state (left panels) and the relative differences with respect to the unified equation of state for the NL3, BSR6 and DD2 cores presented in Eq. (3.55) (right panels). For the NL3 model, the brown line on top of the one for the spline shows the results obtained using the approximate approach to the crust in Eq. (3.56) (see text for details).

also be anticipated using a similar formula for the compactness

$$\Delta C = \frac{\Delta\mu}{\mu_0}(1 - 2C), \quad (3.57)$$

with μ_0 the chemical potential at the surface of the star (at which $P = 0$).

The dimensionless tidal deformability seems always the most affected macroscopic quantity by the non-unified constructions while actually, the impact of microscopic inconsistencies are similar for all quantities. This is due to the fact that Λ spans over two orders of magnitude in the interesting range of masses. As a consequence, if the tidal deformability were to be measured with a precision of around 15%, the corresponding mass could be extracted with a precision of around 2%.

The uncertainties are the smallest when the core and crust are connected at densities $n_0/2 = 0.08 \text{ fm}^{-3}$ or 0.1 fm^{-3} , which is the value of the core-crust transition density found for a number of models [Oyamatsu and Iida \[2007\]](#), [Ducoin et al. \[2011\]](#), [Pais and Providência \[2016\]](#). In fact, laboratory experiments allow us to constrain relatively well the dense matter equation of state up to roughly $n_0/2$ [[Dutra et al., 2012](#)]. Because most equations of state are adjusted to reproduce the experimental data, they consequently have properties like the symmetry energy that are similar up to $\sim n_0/2$, as can be seen in Figure 2 of [Ducoin et al. \[2011\]](#). From Table 3.3, we can see that models have remarkably close values of the symmetry energy at a density 0.1 fm^{-3} , around 25 MeV. The spread of the slope of the symmetry energy over the different models studied is also smaller at 0.1 fm^{-3} than at the saturation density. In other words all equations of state used have similar softness around 0.1 fm^{-3} , which is why the jump in the chemical potential when gluing them is small in the range of densities $0.08 - 0.1 \text{ fm}^{-3}$. This results in relative differences for the macrophysical properties that are small, as can be seen from Fig. 3.20b and Fig. 3.20c. Overall, when constructing an equation of state for neutron stars in case a unified equation of state is not available, gluing the core to the crust at $n_B = 0.08 - 0.1 \text{ fm}^{-3}$ minimizes the relative differences with respect to the unified equation of state, and thus the artificial uncertainties in the radius, tidal deformability and moment of inertia modelling.

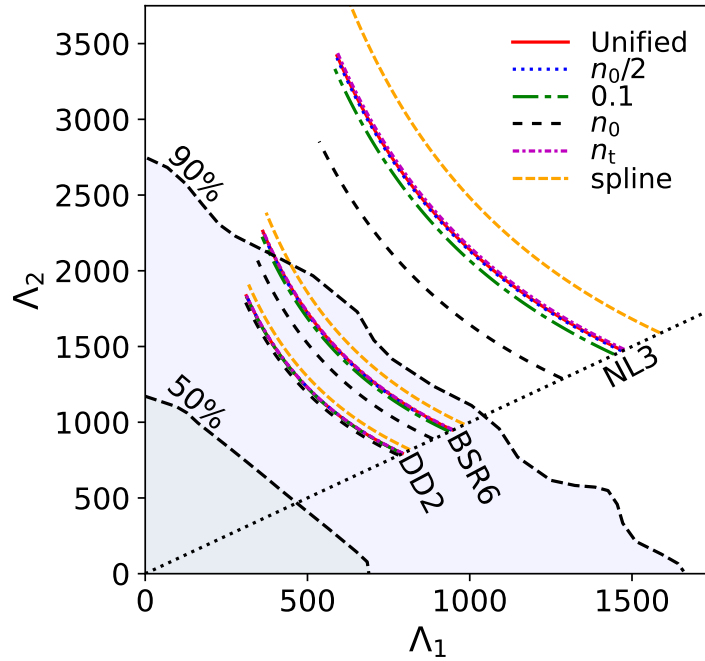


Figure 3.21: Relation between the tidal deformabilities of neutron stars in GW170817 event, with the 90% and 50% credibility lines presented in [Abbott et al. \[2017\]](#). Different constructions for NL3, BSR6 and DD2 are presented.

To better emphasize the role of non-unified equations of state in the investigation of dense matter from observations of neutron star's macroscopic parameters, let us use the example of the gravitational wave detection GW170817. In Fig. 3.21, we present the 50% and 90% credibility lines on the relation between the dimensionless tidal deformabilities of the two neutron stars (Λ_1 for the more massive and Λ_2 for the less massive) of the merger GW170817 presented in [Abbott et al. \[2017\]](#). The differences between the unified curve of NL3 in this figure, and the matching at the saturation density of NL3 and DH is as large as the difference between the two unified equations of state of DD2 and BSR6. Therefore, using non-unified equations of state matched at values of the density for which microscopic parameters are very different, can easily mislead into accepting or excluding an equation of state using observations.

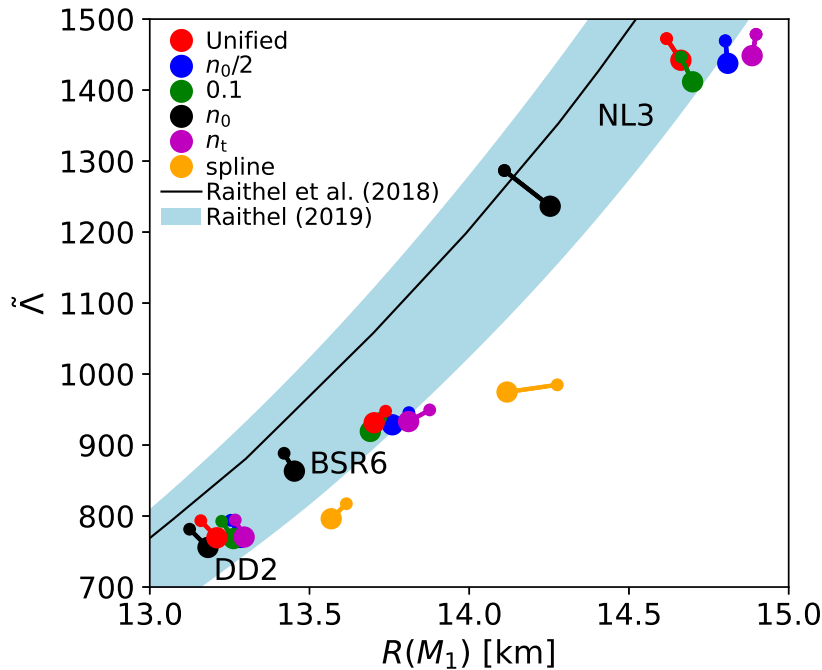


Figure 3.22: Relation between the effective tidal deformability of the binary $\tilde{\Lambda}$ and the radius of the lightest star of GW170817. Different constructions for NL3, BSR6 and DD2 are presented. See text for details.

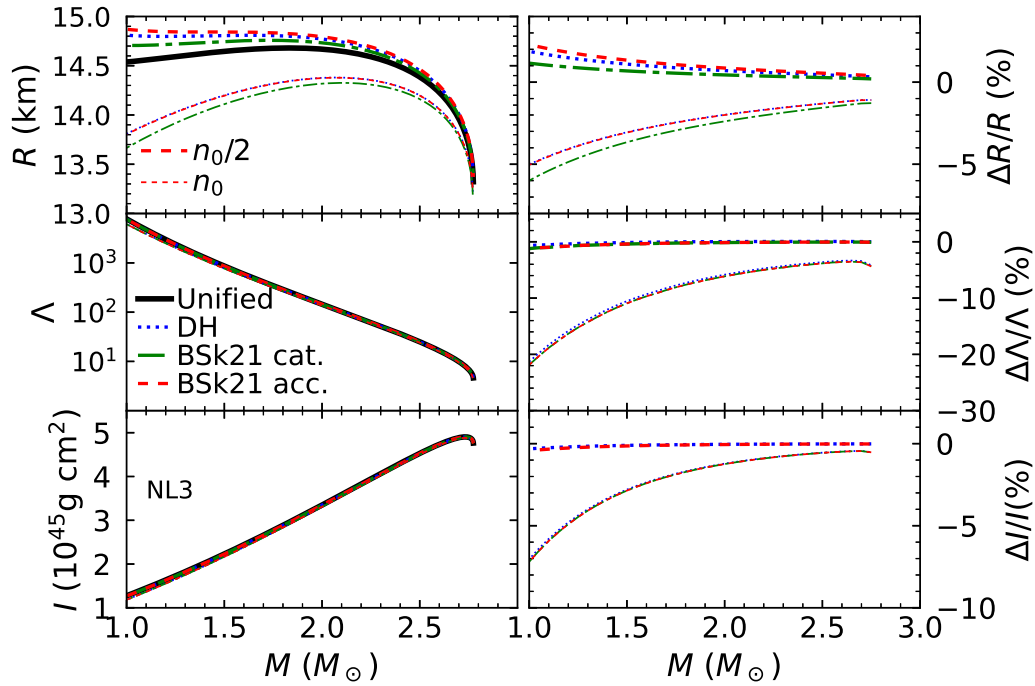
In Raithel et al. [2018], Raithel and Özel [2019], the authors present a relation between the effective tidal deformability of GW170817 defined in Eq. (3.51) and the radius of the more massive star $R(M_1)$. This relation is interesting because the effective tidal deformability is supposed to hardly depend on the mass of the component stars for a fixed chirp mass in binary neutron star mergers. This would allow one to use the effective tidal deformability to extract the radius of a neutron star in a merger. For each equation of state and each matching presented above, we present in Fig. 3.22 the relation between $\tilde{\Lambda}$ and $R(M_1)$ for $M_1 = 1.36 M_\odot$ (indicated by the smallest dot in the figure) and $M_1 = 1.6 M_\odot$ (indicated by the larger dot in the figure) for a chirp mass of $1.188 M_\odot$. The relation obtained by Raithel et al. [2018] as a fit from a sample of six equations of state in the form of polytropic fits based on non-unified constructions is represented with a black line. Similarly, we presented in blue the contour established from the approximate relation presented in Raithel and Özel [2019]. The influence of the core-crust matching is non-negligible for our three equations of state, and increases strongly with the stiffness of the equation of state. Hence the use of consistent microscopic parameters is required to assess the dependence of $\tilde{\Lambda}$ on the $R(M_1)$. The fits between $\tilde{\Lambda}$ and $R(M_1)$ obtained in Raithel et al. [2018], Raithel and Özel [2019] appear to strongly depend on the equation of state matching, and to be only marginally consistent with the results obtained when a unified equation of state is employed.

We finish this section with an analysis using the crusts of accreting neutron stars, to better understand the extent of the impact of non-unified equations of state on our understanding of dense matter. The crust of accreting neutron stars are fundamentally different

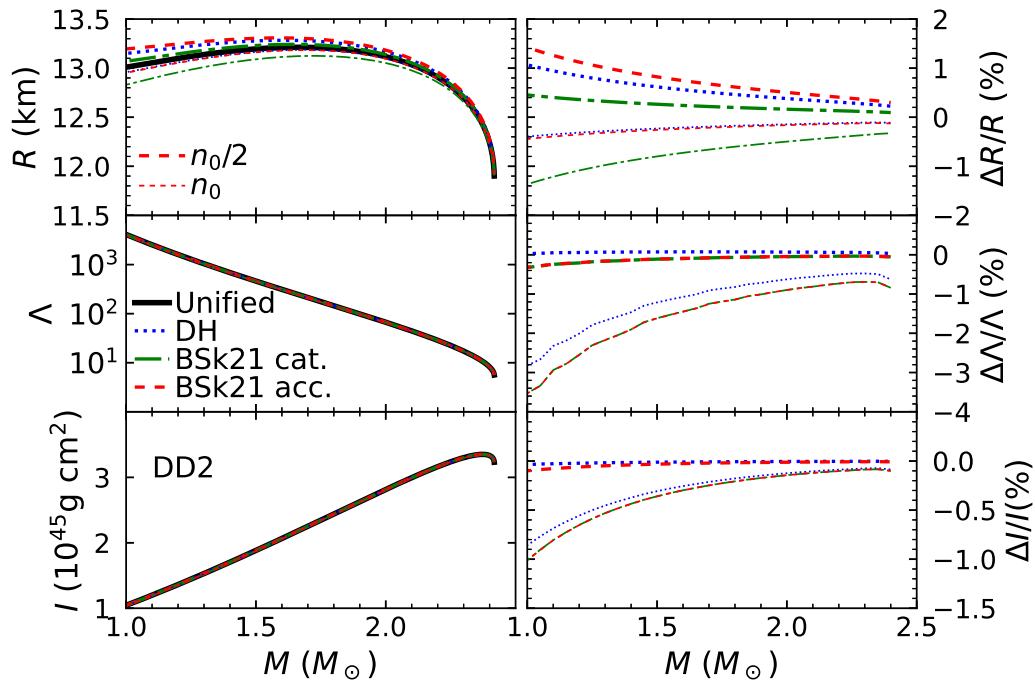
from those of an isolated neutron star, for details see chapter 5; to design an accreted crust equation of state, the computation is completely different, a local equilibrium is used contrary to a global one for catalyzed matter, and the compositions are also different. In the following, we assess if the error introduced by matching crusts of different nature is larger than the one introduced by the non-unified constructions themselves.

We design the following constructions:

- NL3 and DD2 cores, glued to the DH crust,
- NL3 and DD2 cores, glued to the catalyzed crust equation of state of BSk21,
- NL3 and DD2 cores, glued to the accreted crust equation of state of BSk21.



(a) Macroscopic parameters for NL3 core EoS glued to crusts of different nature.



(b) Macroscopic parameters for DD2 core EoS glued to crusts of different nature.

Figure 3.23: M , R , I and Λ for the matchings (left) and the relative differences with respect to the unified EoS (right). Thin lines correspond to a matching between the core and the crust of catalyzed or accreted matter at n_0 , and the thicker ones at $n_0/2$.

Results are not presented for BSR6, as they should lie in between the results of NL3 and DD2. Moreover, as we have shown that the least error is introduced by this matching,

we use only the matching density $n_m = 0.08 \text{ fm}^{-3}$, and $n_m = n_0$ as a reference. It can be seen in Fig. 3.23, that the main contribution to the uncertainty originates from the choice of the matching density, and very little from the nature of the crust equation of state. For the stiffest core equation of state (NL3) matched at $n_0/2$, the difference is at most of around 2.5% for the radius, $\sim 1\%$ in the deformability and 0.5% in the moment of inertia while it can reach 5%, 20%, and 7% for a matching at n_0 . The two models DH and BSk21 are based on the Skyrme force and are quite similar in their values of the microscopic parameters (see Table 3.3). Consequently they give very similar results for matchings of a catalyzed crust. The case of the matchings to an accreted crust is different because the density jumps inherent to accreted matter equations of state directly relate to an increase of the radius (see Eq. (3.56)). This is why matching a catalyzed core to an accreted crust gives larger relative differences compared with the unified equation of state. In the end, the choice of the core-crust transition density influences the results in larger differences with respect to the unified equation of state, than the use of a catalyzed or an accreted crust, which have fundamental difference in properties, composition and nature.

One disappointing comment can be made about the potential observational distinction between a catalyzed and accreted crust: the differences for a matching that introduces the least error in the unified sense, are so small that we are still a long way from distinguishing the crust nature with radius measurements.

We conclude that using non-unified equations of state results in artificial errors on macroscopic parameters which are non negligible in the face of next generation telescopes. If one wants to explore high density matter with neutron star observations, the artificial errors introduced by non-unified models can mislead into the acceptance or exclusion of the investigated nuclear model. Particularly, if the core-crust matching is performed with no care for thermodynamic consistency, it can lead to nonphysical jumps in the chemical potential. Gluing core and crust at values of the density 0.08 or 0.1 fm^{-3} leads to the smallest errors, but a more accurate study of the crust and the core microscopic properties at the matching density is required to establish non-unified equation of state constructions resulting in the least error possible. Overall, a large number of equations of state have been calculated in the last few years, and should be systematically used in simulations of neutron stars.

3.4.3 Role of non-unified constructions in quasi-universal relations

Even though observations have a crucial part to play in the investigation of dense matter, it is possible to extract some macroscopic parameters from so-called universal relations, also referred to as quasi-universal relations. Those relations are established between macroscopic parameters of neutron stars which weakly depend on the equation of state. Quasi-universal relations can be extremely powerful to predict one macroscopic parameter from the measurement of an another one: for example, a truly universal relation between the moment of inertia, and the compactness would provide insight into the moment of inertia of neutron stars, parameter that has yet to be measured.

The story of quasi-universal relations starts with [Yagi and Yunes \[2013\]](#), in which the authors establish the famous I-Love-Q (moment of inertia, tidal deformability and quadrupole moment) relations. In this paper, two finite temperature equations of state LS220 [[Lattimer et al., 1991](#)] and Shen [[Shen et al., 2011](#)], as well as APR Akmal et al. [1998], SLy, and a few polytropes, are used. Macroscopic parameters are modelled from those equations of state for a non-rotating neutron star, and the relations between some parameters is fitted using a logarithmic scale polynomial expression. Many other relations for different configurations (rotation and temperature) of neutron stars, and parameters (oscillations, frequencies, high order Love numbers etc.), were derived or discussed, for example in [Maselli et al. \[2013\]](#), [Steiner et al. \[2016\]](#), [Breu and Rezzolla \[2016\]](#), [Yagi and Yunes \[2017\]](#), [Zhao and Lattimer \[2018\]](#), [Wei et al. \[2019\]](#), [Raduta et al. \[2020\]](#), [Khadkikar et al. \[2021\]](#).

The physical meaning of this quasi-universality has been attributed to two main reasons. The first is the moderately low density dependence of some of those relations, as is discussed in [Yagi et al. \[2014\]](#) and reference therein: the authors investigate the relation between the quadrupole moment and the moment of inertia, and found that the universality of this relation was mostly attributed to the outer core part of the equations of state. However, it is important to note that the set of equations of state used for this analysis was based on non-unified equations of state with a DH crust for all equations of state of the set, and a technique of matching core and crust which does not respect the core-crust transition value (see next section for details about piecewise polytropic fits). The second main idea behind this universality is a sort of extension of the no-hair theorem. This theorem states that in general relativity all properties of a black hole depend solely on its mass, angular momentum and electric charge⁷. This argument is discussed in length in [Yagi et al. \[2014\]](#), [Sham et al. \[2015\]](#): the authors explore the analytical meaning of an extrapolated no-hair theorem in general relativity. They suggest that this quasi-universality arises from a symmetry acquired when equations of state parameters are tuned out; that is the case when one follows the path of increasing compactness, from main sequence stars, to relativistic stars, to black holes for which universality perfectly holds as per the no-hair theorem.

Quasi-universal relations have been established by fitting the modelled macroscopic parameters calculated from existing equations of state which are non-unified. In the following, the universality of the relations is not put into question, but we assess the role of a set of non-unified equations of state on the precision of fits proposed by [Maselli et al. \[2013\]](#), [Breu and Rezzolla \[2016\]](#), [Yagi and Yunes \[2017\]](#), [Zhao and Lattimer \[2018\]](#), [Godzieba et al. \[2021\]](#). We use the same approach as in the previous section, however, we focus on the matchings at densities n_0 , $n_0/2 = 0.08 \text{ fm}^{-3}$ and 0.1 fm^{-3} (except for the study of [Godzieba et al. \[2021\]](#)), as the former is used as a reference, and the other two result in the smallest uncertainties of all the matchings discussed previously. Again, we use the NL3, BSR6 and DD2 relativistic mean field models.

⁷This theorem does not necessarily hold in modified gravity, in which black holes can be hairy.

The quasi-universal relation for the different fits we want to explore are based on different sets of equations of state. In this section, we use the following:

- The fits presented in [Maselli et al. \[2013\]](#) (later on referred to as Maselli et al.), which are based on three purely nucleonic equations of state taken from non-unified piecewise polytropic fits presented in [Read et al. \[2009\]](#) (for details, see section 3.5) and consistent with the maximum mass criterion.
- The fits presented in [Yagi and Yunes \[2017\]](#) (later on referred to as Yagi & Yunes), which are based on a the set of thirty non-unified equations of state presented in [Read et al. \[2009\]](#), some of which are inconsistent with the maximum mass criterion.
- The fits presented in [Breu and Rezzolla \[2016\]](#) (later on referred to as Breu & Rezzolla), which are based on 28 equations of state all consistent with the maximum mass criterion, most of which are non-unified.
- The fits presented in [Zhao and Lattimer \[2018\]](#) (later on referred to as Zhao & Lattimer), which are consistent with the maximum mass criterion and are based on non-unified piecewise polytropic fits for which the crust is fixed, and the parameters of the core are varied to obtain a large set of equations of state.
- The fits presented in [Godzieba et al. \[2021\]](#) (later on referred to as Godzieba et al.), which are consistent with the maximum mass criterion, and are based on non-unified piecewise polytropic fits for which the crust is fixed, and the parameters of the core are varied to obtain a large set of equations of state. The matching density ranges from $0.15 n_0$ to $1.2 n_0$.

We investigate four quasi-universal relations

$$C_{\text{fit}} = \sum_{k=0}^{N=2,6} a_k (\ln \Lambda)^k, \quad (3.58)$$

$$\ln \bar{I}_{\text{fit}} = \sum_{k=0}^4 b_k \ln(\Lambda)^k \text{ with } \bar{I} = I \frac{c^4}{G^2 M^3}, \quad (3.59)$$

$$\bar{I}_{\text{fit}} = \sum_{k=1}^4 c_k C^{-k}, \quad (3.60)$$

$$\tilde{I}_{\text{fit}} = \sum_{k=0}^4 d_k C^{k/2} \text{ with } \tilde{I} = IC^2, \quad (3.61)$$

with a_k , b_k , c_k and d_k the parameters of the fits. Values for the parameters of the fit, as well as the reported relative errors between the modelling of macroscopic parameters from the set of equation of state and the fit, are presented in Table 3.4.

Table 3.4: Fits parameters of quasi-universal relations presented in this manuscript.

Relation	Fit	Parameters of the fit	Reported fit error
$C - \Lambda$	Maselli et al	$a_0 = 0.371$ $a_1 = 0.0391$ $a_2 = 0.001056$	$\leq 2\%$
	Yagi & Yunes	$a_0 = 0.360$ $a_1 = -0.0355$ $a_2 = 0.000705$	$\leq 6.5\%$
	Godzieba et al.	$a_0 = 0.3388$ $a_1 = -2.3 \times 10^{-2}$ $a_2 = -4.651 \times 10^{-4}$ $a_3 = -2.636 \times 10^{-4}$ $a_4 = 5.424 \times 10^{-5}$ $a_5 = -3.188 \times 10^{-6}$ $a_6 = 6.181 \times 10^{-8}$	Improvement on Yagi & Yunes
$\bar{I} - \Lambda$	Maselli et al	$b_0 = 1.95$ $b_1 = -0.373$ $b_2 = 0.155$ $b_3 = -0.0175$ $b_4 = 0.000775$	$\leq 5\%$
	Yagi & Yunes	$b_0 = 1.496$ $b_1 = 0.05951$ $b_2 = 0.02238$ $b_3 = -6.953 \times 10^{-4}$ $b_4 = 8.345 \times 10^{-6}$	$\leq 1\%$
$\bar{I} - C$	Yagi & Yunes	$c_1 = 1.317$ $c_2 = -0.05043$ $c_3 = 0.04806$ $c_4 = -0.002692$	$\leq 9\%$
	Breu & Rezzolla	$c_1 = 0.8134$ $c_2 = 0.2101$ $c_3 = 0.003175$ $c_4 = -0.0002717$	$\leq 3\%$
$\tilde{I} - C$	Zhao & Lattimer	$d_0 = 0.01$ $d_1 = 1.2$ $d_2 = -0.1839$ $d_3 = -3.735$ $d_4 = 5.278$	
	Breu & Rezzolla	$\tilde{d}_0 = 0.244$ $d_1 = d_3 = 0$ $d_2 = 0.638$ $d_4 = 3.202$	$\leq 6\%$

3.4.3.1 Universal relation $C - \Lambda$

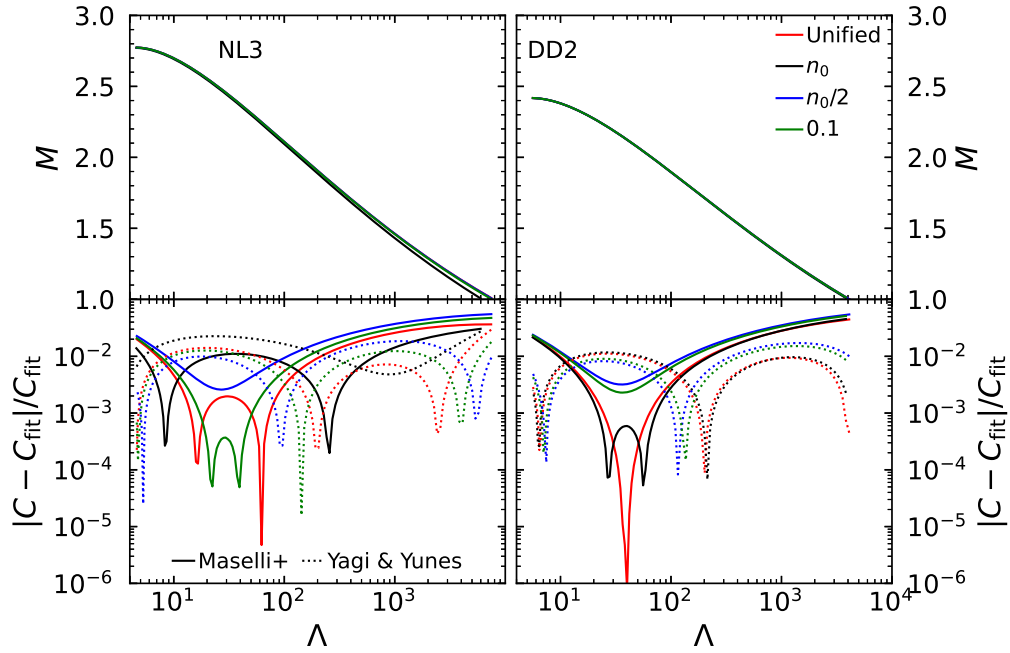


Figure 3.24: Relations between Λ and M in the top panel, and relative error between the Maselli et al. (solid lines) and the Yagi and Yunes (dotted lines) $C - \Lambda$ fits with respect to exact calculations.

Let us start by analyzing the fits presented by Yagi & Yunes and Maselli et al. for the relation

$$C_{\text{fit}} = \sum_{k=0}^2 a_k (\ln \Lambda)^k. \quad (3.62)$$

We compute the relation $C(\Lambda)$ from the fits, and compare them to unified NL3 (stiffest core model), BSR6, and DD2 (softest core model), as well as non-unified construction of NL3, BSR6 and DD2 with a DH crust, for masses ranging from $1.0 M_{\odot}$ to the maximum mass configuration; results for NL3 and DD2 are presented in Fig. 3.24. To confront results to reported errors of the fits, we present the maximum relative error between the fit and the NL3, BSR6, and DD2 constructions in Table 3.5.

Table 3.5: Maximum relative difference in % between the values obtained using the relation $C - \Lambda$ established from fits of Yagi & Yunes, Maselli et al., and Gozieba et al., as well as equation of state constructions for NL3, BSR6 and DD2. We consider unified equations of state (column "uni.") and three matched constructions to the crust of DH at different densities: n_0 , $n_0/2$ and 0.1 fm^{-3} . Numbers in parentheses correspond to the neutron star mass at which the relative difference is the largest. Numbers in bold correspond to the highest relative error of the fit.

$C - \Lambda$	uni.	n_0	$n_0/2$	0.1 fm^{-3}
EoS	Maselli et al.			
NL3	3.65 (1.02)	3.05 (1.01)	5.53 (1.01)	4.74 (1.00)
BSR6	5.57 (1.00)	4.35 (1.00)	6.38 (1.01)	5.77 (1.01)
DD2	4.45 (1.00)	4.54 (1.01)	5.46 (1.00)	5.14 (1.01)
	Yagi & Yunes			
NL3	2.94 (1.01)	2.74 (1.01)	1.85 (1.44)	1.78 (1.00)
BSR6	2.12 (1.33)	0.92 (1.35)	2.71 (1.30)	2.20 (1.31)
DD2	1.11 (2.22)	1.17 (2.21)	1.72 (1.23)	1.52 (1.23)
EoS	uni.	$0.15n_0$	$1.2n_0$	0.1 fm^{-3}
	Godzieba et al.			
NL3	2.37 (1.54)	7.14 (1.01)	2.90 (2.77)	2.88 (1.40)
BSR6	3.77 (1.21)	6.85 (1.00)	2.28 (1.01)	3.98 (1.01)
DD2	2.78 (1.00)	4.84 (1.01)	2.70 (1.01)	3.53 (1.01)

Overall the Yagi & Yunes fit gives a smaller relative error ($\sim 3\%$ at most) than the Maselli et al. fit (up to $\sim 6\%$). The maximum difference is larger for the Maselli et al. fit than for the Yagi & Yunes one for stars with masses $\leq 2 M_\odot$ while the situation is opposite for larger masses. Table 3.5 shows that the use of non-unified constructions matched at $n_0 = 0.08 \text{ fm}^{-3}$ or 0.1 fm^{-3} gives rise to an uncertainty which is smaller than the reported precision of the Yagi and Yunes fit, but larger by up to a factor ~ 3 for the Maselli et al. fit. Actually, for the latter fit, the relative difference in the compactness when using a unified equation of state is about two times larger than the reported precision. Hence, using three equations of state covering a large range of stiffness, we conclude that results obtained with the Yagi & Yunes fit are not affected by the treatment of the low-density part of the equation of state and the matching, while the Maselli et al. fit is.

We now go on to study the fit of Godzieba et al., given by

$$C_{\text{fit}} = \sum_{k=0}^6 a_k (\ln \Lambda)^k, \quad (3.63)$$

thus extending the polynomial to the sixth order, compared to the second order in the previous fits. In Godzieba et al. [2021], authors proposed a revision of quasi-universal relations for multipole Love numbers based on the fit of piecewise polytropic equations of state. Below approximately the saturation density, the equation of state is that of DH approximated

by one polytrope, whereas, in the core, three polytropes are used. Around two million equations of state are created by changing the parameters of the core: they follow basic rules of causality, maximum mass constraint around $2 M_{\odot}$, and GW170817 measurement of the tidal deformability. This construction is not unified; however, authors use a method that adapts the matching density between $[0.15-1.2] n_0$ at the junction of DH and their polytropic cores. Universal relations are established for dimensionless tidal deformability Λ of order two, three and four with the compactness, but we focus on the relation $C - \Lambda_2$ which relates the compactness and the tidal deformability as measurable by gravitational wave detectors now.

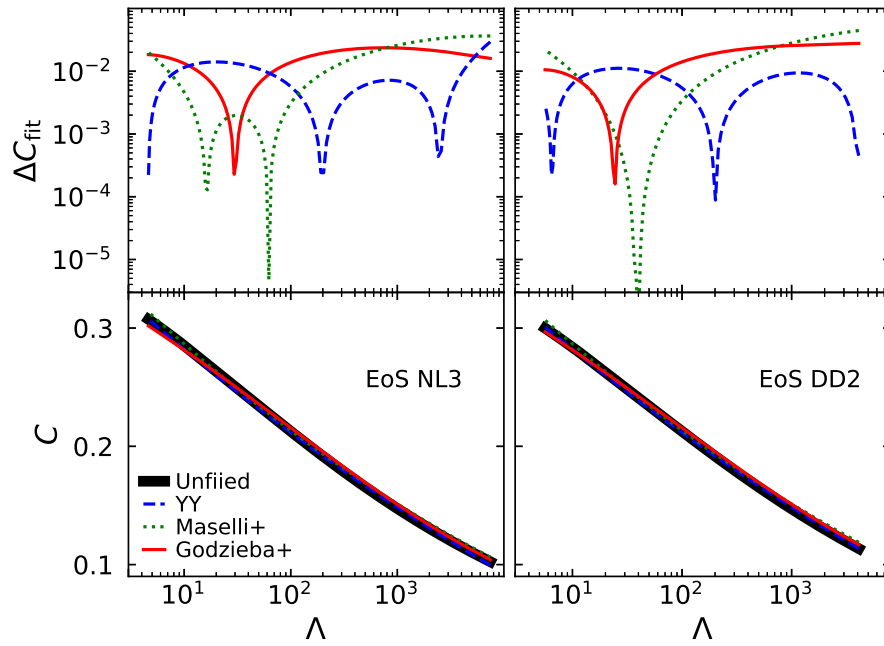


Figure 3.25: Relations between Λ and M in the top panel, and relative error between the Maselli et al. (solid lines) and the Yagi and Yunes (dotted lines) $C - \Lambda$ fits with respect to exact calculations.

We test this fit with respect to unified equations of state and non-unified constructions of NL3 and DD2, and present results in Fig. 3.25. In Table 3.5, we present the maximum relative difference between the fit and NL3, BSR6 and DD2 for the unified constructions, as well as matching at densities $0.15 n_0$, $1.2 n_0$ (boundary values of the matching technique), and 0.1 fm^{-3} .

It is evident from Fig. 3.25 that the universality of the relations stands with respect to the unified equations of state. In Godzieba et al. [2021], the authors emphasize that their fit is an improvement on the Yagi & Yunes one based on their collection of two million non-unified polytropic equations of state; however, when compared with tables of unified equations of state, the maximum relative difference is generally larger for Godzieba et al. (3.77%) than for Yagi & Yunes (2.94 %).

In overview, Yagi & Yunes fit performs the best out of the three fits. This fit falls within its reported precision when compared with unified, as well as non-unified constructions, for soft and stiff equations of state.

3.4.3.2 Universal relation $\Lambda - \bar{I}$

Fits from Maselli et al. and Yagi & Yunes are provided for the relation between the moment of inertia and the dimensionless tidal deformability presented in Eq. (3.59). Similarly to the previous section, results are presented in Table 3.6.

Table 3.6: Maximum relative difference in % between the values obtained using the relation $\Lambda - \bar{I}$ established from fits of Yagi & Yunes and Maselli et al., and constructions for NL3, BSR6 and DD2. Numbers in bold correspond to the highest relative error of the fit.

$\Lambda - \bar{I}$	uni.	n_0	$n_0/2$	0.1 fm^{-3}
EoS	Maselli et al.			
NL3	7.18 (1.01)	5.13 (1.01)	7.30 (1.01)	7.23 (1.00)
BSR6	4.49 (2.26)	4.56 (2.26)	4.47 (2.26)	4.49 (2.26)
DD2	4.55 (2.24)	4.55 (2.23)	4.53 (2.24)	4.53 (2.24)
	Yagi and Yunes			
NL3	0.28 (2.67)	0.38 (2.61)	0.26 (2.66)	0.27 (2.67)
BSR6	0.17 (2.32)	0.24 (2.29)	0.16 (2.33)	0.17 (2.32)
DD2	0.23 (2.30)	0.23 (2.30)	0.21 (2.30)	0.22 (2.30)

The relative differences between the fits and the exact calculations are similar for the three matched equations of state, and the unified one. The Yagi & Yunes fit gives rise to a maximum relative difference of at most 0.4%, well within the reported precision of the fit. However, for the Maselli et al. fit, the relative difference reaches up to 7% for the stiffest EoS and up to 4.5% for the softer ones. The unified equations of state and the three matched ones give similar values of the difference between the fits and the exact calculations. Overall, the Yagi & Yunes fit performs much better than the Maselli et al. fit.

3.4.3.3 Universal relation $I - C$

Fits from Breu & Rezzolla and Yagi & Yunes are provided for the relation between the moment of inertia and the compactness presented in Eq. (3.60). Other fits from Breu & Rezzolla and Zhao & Lattimer related to Eq. (3.61) have been established. Results are presented in Table 3.7.

Table 3.7: Maximum relative difference in % between the values obtained using the relation $\bar{I} - C$ established from fits of Brey & Rezzolla and Yagi & Yunes, and constructions for NL3, BSR6 and DD2. Numbers in bold correspond to the highest relative error of the fit.

	EoS	uni.	n_0	$n_0/2$	0.1 fm^{-3}
$\bar{I} - C$	Brey & Rezzolla				
	NL3	3.98 (2.77)	5.06 (2.77)	3.52 (2.77)	3.83 (2.77)
	BSR6	1.66 (1.00)	2.35 (2.40)	3.14 (1.01)	2.04 (1.01)
	DD2	2.81 (2.40)	2.89 (2.40)	2.46 (2.41)	2.56 (2.41)
	Yagi & Yunes				
	NL3	3.04 (2.51)	3.03 (2.11)	3.38(2.51)	3.14 (2.51)
	BSR6	3.15 (1.17)	1.00 (1.14)	4.35(1.14)	3.40 (1.14)
	DD2	2.06 (2.32)	2.00 (2.32)	2.92(1.06)	2.55 (1.06)
	$\tilde{I} - C$	Brey & Rezzolla			
NL3		4.44 (2.60)	5.90 (2.37)	5.33 (1.01)	4.23 (2.63)
BSR6		4.60 (1.00)	3.66 (2.14)	6.00 (1.01)	4.85 (1.01)
DD2		4.01 (2.14)	4.11 (2.12)	4.04 (1.00)	3.64 (2.19)
Zhao & Lattimer					
NL3		2.90 (2.51)	3.16 (2.40)	4.64 (1.01)	3.23 (1.00)
BSR6		4.58 (1.00)	2.36 (1.00)	6.01(1.01)	4.93 (1.01)
DD2		2.69 (1.00)	2.82 (1.01)	4.44(1.00)	3.91 (1.01)

Interestingly, the four fits, whether for \tilde{I} or \bar{I} , have a similar precision of 5% – 6% as shown in Table 3.7, with very little dependence on the core-crust transition density. The two fits obtained by Brey & Rezzolla appear to be more accurate (*i.e.*, give a smaller relative error) than the two other ones for low-mass stars $M \leq 1.2 - 1.3 M_{\odot}$.

All in all similar uncertainties are obtained whether one employs the unified constructions, or one matched with the crust at $n_0/2$, n_0 or 0.1 fm^{-3} . The precision of the Yagi & Yunes fits between Λ and C , and Λ and I is not affected by the treatment of the core-crust transition. The precision of the fits of Maselli et al., however, appears to be overestimated, in particular the precision of the $\Lambda - C$ fit, and turns out to be strongly affected by the matching. The reported improvement of Godzieba et al. does not hold when compared to unified equations of state. Finally, all fits between C and I are not affected by the core-crust matching for a precision of $\sim 6\%$.

Quasi-universal relations can be quite useful to extract one macroscopic parameter from the measurement of another. However, differences in the fit parametrization appear when the set of equations of state it is based on is not the same. It is also important that the construction of the equation of state be unified, otherwise, a systematic bias is introduced in the fit, and therefore in simulations that use such fits. With current gravitational wave observatories, the systematic errors on the estimation of parameters using quasi-universal

relations are smaller than the statistical uncertainties. Nevertheless, for future and more precise detectors, more accurate relations will be needed [Baiotti, 2019].

Overall, non-unified constructions of equations of state, for which the core and the crust are not calculated using the same nuclear model, result in artificial errors on macroscopic parameter modelling. Those constructions can mislead into accepting or rejecting a nuclear model on the basis of modelling errors on the mass, the radius, the tidal deformability or the moment of inertia. In the prospects of the next generation of detectors, using unified equations of state to model neutron star's observable will be critical for an accurate exploration of ultra dense matter properties.

3.5 Analytical representations of modern and unified equations of state

The standard output format for computations of cold matter equations of state is a three column table with the baryonic density n , the energy density ϵ , and the pressure P . However, an analytical representation of tabulated equations of state is convenient, particularly for simulations. To establish analytical representations of equations of state, one chooses a parametrized expression, and then adjusts parameters to the tabulated equation of state. Having one expression with easily comparable parameters is also a practical way to compare microscopic and macroscopic features of neutron stars.

In this section, the non-unified piecewise polytropic fits presented in [Read et al. \[2009\]](#) are analyzed, and their accuracy when compared to unified equations of state is studied. We revise this parametrization using the models for dense matter presented in this manuscript; this section discusses results presented in [Suleiman et al. \[2022a\]](#).

3.5.1 Piecewise polytropic fits

The relation between the pressure P and the mass density ρ^8 , can be described by a polytrope by using two parameters, the polytropic constant κ and the adiabatic index Γ , such that

$$P = \kappa \rho^\Gamma . \quad (3.64)$$

Such a crude approximation of the equation of state is well suited for the outer crust of neutron stars, for which the equation of state is dominated by the pressure of ultra-relativistic electrons, with $\Gamma = 4/3$. However, in order to represent analytically all density ranges of the neutron star interior, it is necessary to use several polytropes. The equation of state is divided in N parts, each of which is represented by a polytrope with fixed κ , Γ , and transition density ρ_t : that is what is referred to as piecewise polytropes. A practical fit contains a restricted number of polytropes in order for the parametrisation to be convenient. Piecewise polytropic fits presented in [Read et al. \[2009\]](#) (later on referred to as PPFRead⁹) are based on $N = 7$ polytropes with four in the crust and three in the core.

The number of parameters required to express an equation of state with N polytropes is not $3 \times N - 1$ with N Γ s, N κ s and $N - 1$ transition densities $\rho_{t[i \rightarrow i+1]}$ that defines parts of the equation of state by which the polytrope i is fitted (with $i \in [1, N]$). Indeed, the pressure continuity which renders

$$\kappa_i \rho_t^{\Gamma_i} = \kappa_{i+1} \rho_t^{\Gamma_{i+1}} , \quad (3.65)$$

reduces the number of parameters to $2 \times N$ with N adiabatic indices, $N - 1$ transition densities, and only one polytropic constant: at $\rho_{t[i \rightarrow i+1]}$, κ_{i+1} is calculated from Γ_i , κ_i , and Γ_{i+1} .

⁸The mass density is directly connected to the baryonic density n via the baryon mass $m_B = 939 \text{ MeV}/c^2$ ($\rho = n m_B$). Note that the notation ρ can be found in the literature designating the energy density.

⁹PPFRead are the most widely used analytical representations in neutron star simulations.

To reconstruct the energy density ϵ from the polytrope expression, the first law of thermodynamics in the zero temperature limit is used

$$d\left(\frac{\epsilon}{\rho}\right) = -Pd\left(\frac{1}{\rho}\right). \quad (3.66)$$

Integrating Eq. (3.66) with the help of Eq. (3.64) gives an expression for the energy density that depends on the adiabatic index, and polytropic constant

$$\epsilon(\rho) = (1 + a_i)\rho + \frac{\kappa_i}{\Gamma_i - 1}\rho^{\Gamma_i}, \quad (3.67)$$

with a_i a constant determined at the transition between polytropes and given by the expression

$$a_i = a_{i-1} + \frac{\kappa_{i-1}\rho_t^{\Gamma_{i-1}}}{\Gamma_{i-1}\rho_t} - \frac{\kappa_i\rho_t^{\Gamma_i}}{(\Gamma_i - 1)\rho_t}. \quad (3.68)$$

The value of a_0 is a physical requirement: given the non-relativistic nature of the components close to the surface, the mass density and energy density follow the requirement that $\epsilon = \epsilon_0 = \rho c^2$ at $P = 0$.

There exists other analytical representations, for example the spectral representation presented in Lindblom [2018]. It is important to note that piecewise polytropic fits have a conceptual flaw: the fact that the equation of state is cut in pieces implies the non-derivability of certain quantities: for example, simulations requiring the sound speed to be continuously defined cannot use piecewise polytropic fits without having to treat jumps by hand. Spectral representations are established as a polynomial of high order, fitting the whole density range of the equation of state, and therefore do not have such issues.

3.5.2 PPFRead vs. unified equations of state

We have shown earlier in this chapter, that non-unified constructions can lead to non-negligible errors in the modeling of macroscopic parameters. The analytical representation of PPFRead is based on the following construction

- the high density part of the equation of state is fitted by three polytropes,
- the low density part of the equation of state is fitted by four polytropes based on the DH equation of state;
- the point at which the high density and the low-density polytropes are matched is adapted to ensure a minimal fit error on the whole non-unified construction;
- the last polytrope of DH is prolonged or shortened to ensure that it crosses the first polytrope of the high-density part.

In order to assess the role of non-unified constructions on the accuracy of PPFRead, we focus on three equations of state of the set presented in this manuscript, which are in

common with the set of equations of state presented in Read et al. [2009]: nucleonic DH, and hyperonic H3 and H4. We investigate the following constructions:

- the unified equation of state H3 and H4,
- the unified equation of state DH,
- PPFRead for H3, H4 and DH.

We present the relation between pressure and mass density in Fig. 3.26; results are only presented for H3, because the difference between H3 and H4 lies in the hyperonic meson couplings, which are relevant only at higher densities than the region of interest.

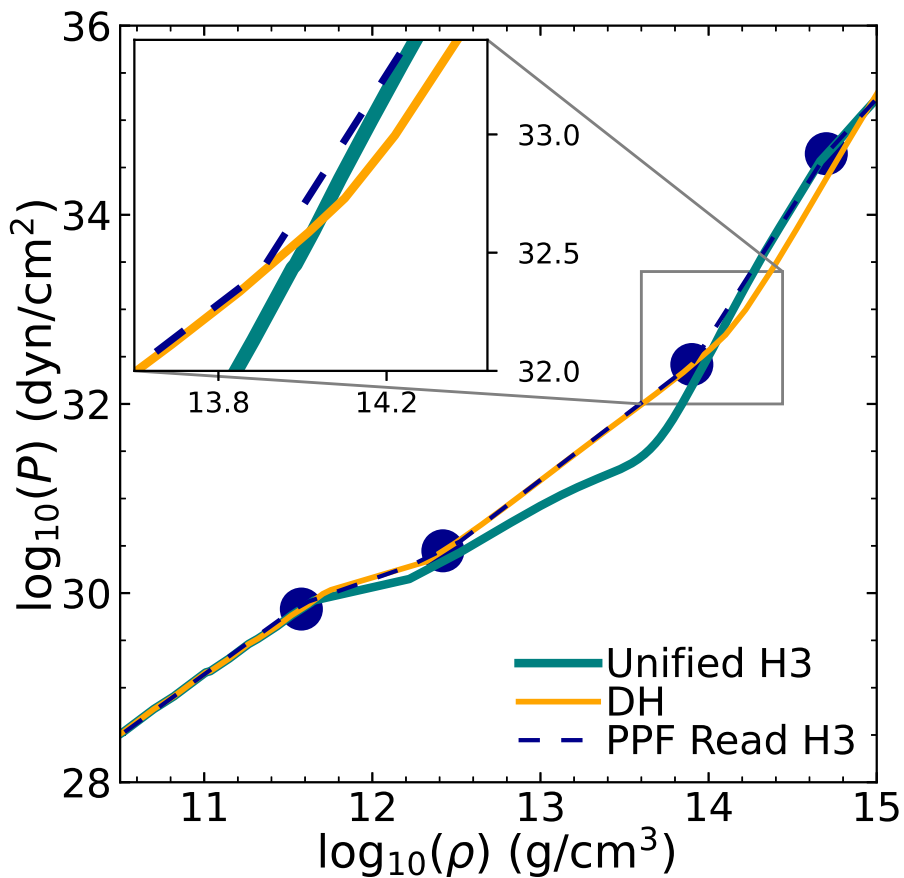


Figure 3.26: Relation between the pressure P and the mass density ρ for unified equation of state H3 compared with PPFRead of H3. Transition between polytropes of PPFRead are presented with blue points. A zoom is made at the transition between the DH polytropes and the H3 core polytropes.

In Fig. 3.26, the lowest-density parts, *i.e.* for $\rho < 10^{11.6}$ g/cm³, overlap for all constructions. This corresponds mostly to the outer crust which is calibrated to experimental data, therefore, it is similar for all models used. Over $10^{11.6}$ g/cm³, DH and unified H3 are different. The zoom in the figure highlights the matching area: for H3, the matching density is $\rho_m^{\text{H3}} = 7.9477 \times 10^{13}$ g/cm³; for H4, $\rho_m^{\text{H4}} = 8.8774 \times 10^{13}$ g/cm³. In between the last point of convergence for all constructions, and the matching of DH and H3 PPFRead, the curves are

different which attests to the limit of laboratory measurement calibrations of the low density part of the equation of state. Although precautions are taken to avoid jumps in the pressure, the differences between the sole DH crust and the core equations of state in PPFRead are not negligible.

From the above mentioned constructions, the total mass, the total radius, the tidal deformability and the moment of inertia are calculated and presented in Fig. 3.27.

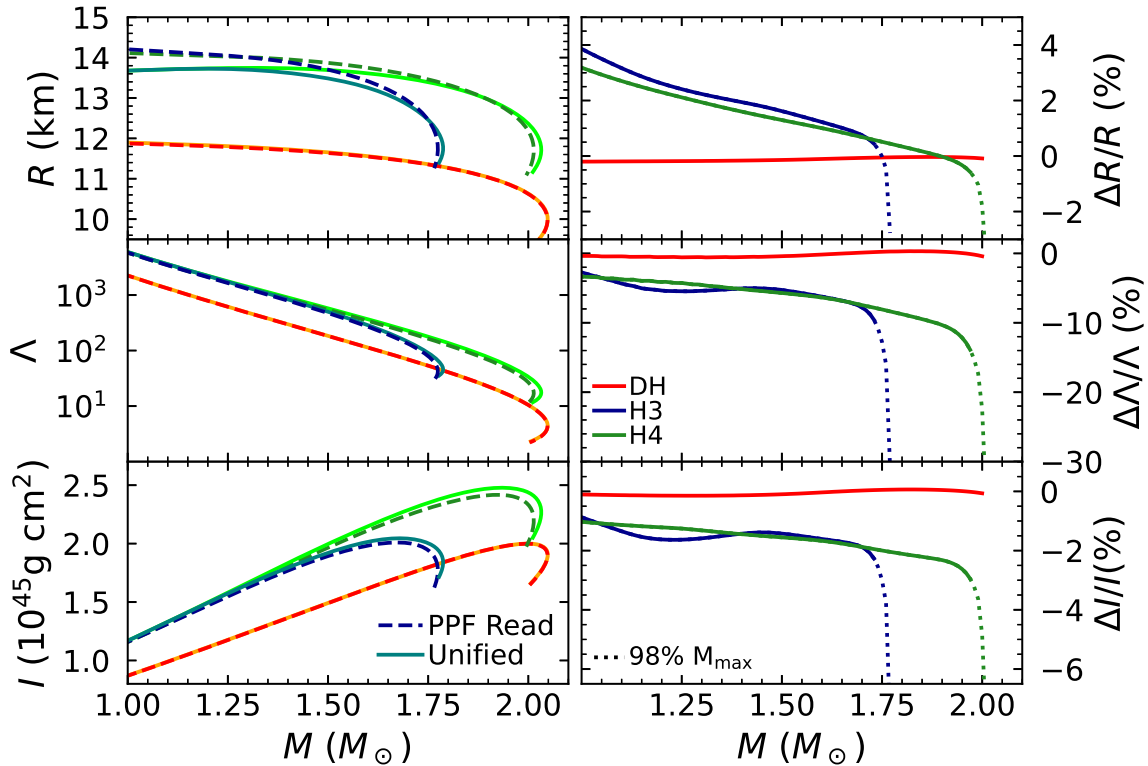


Figure 3.27: Radius R , tidal deformability Λ , and moment of inertia I as a function of the mass M for unified tables H3, H4, and DH, as well as PPFRead. In the right panel, the relative difference between unified tables and PPFRead for each macroscopic parameter in the three cases of equation of state is presented as a function of the total mass. For equations of state H3 and H4, the relative uncertainty is shown up to 98% of the maximum mass in plain lines, and the last two percent in dotted lines, see text for details.

DH PPFRead is constructed from DH equation of state at low density, and DH equation of state at high density, it is therefore unified: the red line in the right panel of Fig. 3.27 shows that it coincides with the tabulated unified equation of state of DH. From this, we can conclude that the fit method itself is powerful. For PPFRead H3 and H4, the low density polytropes of DH are matched to the high density polytropes of H3 and H4 at ρ_m^{H3} and ρ_m^{H4} respectively. Therefore, the whole fit is not unified and differs from our unified tables, as is shown for green and blue lines in Fig. 3.27. This indicates that using non-unified tabulated equations of state for piecewise polytropic fits induces an artificial error on the macroscopic parameters. In this figure, the relative error is presented as a function of the total

mass. The large increase of the relative error close to the maximum mass is a consequence of choosing the mass as an independent variable (see discussion on the central pressure in section 3.3.1.2). Close to the maximum mass point, the error increases significantly even for a small difference between the values of the maximum mass for the original and fitted equation of state. This effect is absent for the dependence of the error as a function of central density or pressure. For that reason, the relative error are presented in dotted lines from 98% of the total mass .

From Fig. 3.27, the uncertainty related to the tidal deformability leads to two interesting points. On the one hand, despite the largest relative error being that of the tidal deformability, in the left panels of Fig. 3.27 the accuracy looks very similar for all three quantities. This is due to the fact that Λ is plotted on a logarithmic scale, because it spans over two orders of magnitude in the interesting range of masses. As a consequence, the relative change of Λ by 15% corresponds to 2% in mass and such error bars would be of a similar size in Fig. 3.27 (left panel). On the other hand, one can notice that the sign of the relative difference in radius and that in tidal deformability are not the same. However, Λ is calculated according to the relation $\Lambda = \frac{2}{3}k_2C^{-5}$ [De et al., 2018, Malik et al., 2018], with k_2 being the tidal Love number. The dimensionless deformability is proportional to k_2R^5 , therefore an increase in radius should correspond to an increase in the tidal deformability. The sign difference in the relative uncertainty of the two quantities in Fig. 3.27 can be explained by the large error of PPFRead with respect to the unified equation of state on the Love number function k_2 . It is particularly large for low mass stars, such that it dominates the R^5 factor. For higher mass stars, the uncertainty on k_2 is smaller and the scale of R^5 dominates. This large k_2 error can be understood as the strong effect of the crust matching on this quantity. Indeed, the fit from H3 unified tables in which the crust is treated correctly with the core -as is presented in details in the next section- gives a relative error on k_2 which is at most 3% (for a $1.5 M_\odot$) whereas PPFRead give a relative error on k_2 of at most 50% (for a $1.0 M_\odot$).

We can conclude that, although the piecewise polytrope fitting method with seven polytropes is accurate, the use of non-unified equations of state introduces errors which are not negligible.

3.5.3 Revising piecewise polytropic fits from modern and unified equations of state

In Read et al. [2009], 34 non-unified equations of state are fitted, and twenty of them do not follow the maximum mass criterion. In the following, we present parameters for the unified nuclear models presented in section 3.1.

Our fitting method differs from that of PPFRead. An adaptive nonlinear least squares method is used to calculate the $N_{\text{poly}} - 1$ transition densities ρ_t , with the number of polytropes $N_{\text{poly}} = 7$. They are adapted such that the fit error is minimized for the entire unified equation of state (core and crust). For each unified table, we create a distribution for the

number of density points ρ different from the original tabulated equation of state. Our distribution of points allows us to give more importance to the accuracy of the fit in some parts of the star than others. We use a total of 1500 points, allocating 1/5 of the points in the crust and 4/5 of the points in the core, because it resulted in better fits of the full table. In each region, we distribute these points uniformly on a logarithmic scale. The fragment of the unified tables with the largest densities is not used because the density goes beyond the central density at maximum mass. We eliminate this highest density part by calculating the maximum mass of the star from the unified table, and only interpolate the equation of state up to n_{\max} , thus increasing the fit accuracy for astrophysical quantities.

The core-crust transition density has a particular influence on the success of our fit method. This area is particularly sensitive to changes in the polytropic parameters and in turn, the points could be miss-allocated. Therefore, we chose to test values of the core-crust transition densities from $n = 0.06$ to $n = 0.14 \text{ fm}^{-3}$ for each fit.

The relation $P(\rho)$ is interpolated by using a first-order spline method to establish the pressure points from our distribution of density points. Each polytrope is fitted using a nonlinear least squares method from Eq. (3.64); Γ and κ are determined for each polytrope. Then, transition densities are recalculated from the polytropic parameters just fitted and the whole process with these new transition densities starts over until the set of ρ_i stagnates. Finally, the energy density ϵ is calculated from Eq. (3.67).

Some alternatives to this fit method have been explored. First, we have tested the number of piecewise polytropes of the approach: we have found that the accuracy for nucleonic matter did not increase significantly beyond seven piecewise polytropes. However, the softening induced by hyperons or transitions to quark matter would require an additional polytrope in the core for the error to match that of nucleonic matter. But in an effort to provide a method for all models, we have chosen to keep three polytropes in the core, noting that the error on hyperonic and hybrid models is not so large that the fit cannot be considered accurate with respect to observational precision. The number of points for the interpolation were also tested for values between 200 and 10 000 points: we observed a plateau of accuracy for ~ 1500 points. We have also tested an inverse fit method, starting the fit from high density to low density which renders a similar accuracy on the equation of state fit.

The method described above is implemented to calculate the fit parameters which are presented in Table 3.8 and Table 3.9.

Table 3.8: Parameters of unified fits by seven polytropes of 15 nucleonic, seven hyperonic and five hybrid relativistic mean field equations of state. The logarithm of the transition densities ρ_{ti} between the polytropes is given in g/cm^3 . For each polytrope i , the adiabatic index Γ_i is presented. Only the first constant κ_0 is presented because all others can be calculated from pressure continuity.

EoS	$\log_{10}(\kappa_0)$	Γ_0	$\log_{10}(\rho_{t1})$	Γ_1	$\log_{10}(\rho_{t2})$	Γ_2	$\log_{10}(\rho_{t3})$	Γ_3	$\log_{10}(\rho_{t4})$	Γ_4	$\log_{10}(\rho_{t5})$	Γ_5	$\log_{10}(\rho_{t6})$	Γ_6
Nucleonic RMF EoS														
BSR2	12.4812	1.6379	6.9304	1.3113	11.3669	0.8349	12.7363	1.3136	14.0413	3.2464	14.8162	2.8221	14.9832	2.3788
BSR6	12.4804	1.6381	6.9312	1.3109	11.4161	0.7053	12.8819	1.2421	13.5005	2.5053	14.4823	3.1753	14.9091	2.4855
DD2	12.4878	1.6369	6.9309	1.3114	11.3929	0.6260	12.3993	1.2833	13.7322	2.3253	14.3792	3.4041	14.8719	2.6026
DDH δ	12.4849	1.6372	6.9466	1.3092	11.4523	0.5441	12.1843	1.1022	14.1019	4.1828	14.5019	3.1328	14.8150	2.4599
DDME2	12.4955	1.6353	6.9470	1.3106	11.4015	0.6160	12.3748	1.2921	13.6025	2.0223	14.3561	3.5998	14.8460	2.6395
FSU2	12.5074	1.6330	6.9793	1.3076	11.4658	0.6605	12.7237	0.8687	13.5102	2.9854	14.1278	2.6376	14.9194	1.9831
FSU2H	12.4979	1.6349	6.9546	1.3097	11.4067	0.7657	12.4968	1.3578	14.2427	3.9780	14.6581	3.1615	14.8787	2.1387
FSU2R	12.4986	1.6347	6.9527	1.3103	11.3870	0.7898	12.4679	1.3331	14.2033	3.7040	14.6178	2.8757	14.8944	2.0137
GM1	12.4928	1.6356	6.9626	1.3082	11.4783	0.5103	12.2341	0.9431	13.6981	3.2095	14.3853	2.8973	14.9312	2.5144
NL3	12.4945	1.6355	6.9470	1.3103	11.4119	0.6234	12.3397	0.9161	13.5283	2.8788	14.5470	3.4771	14.8390	2.5896
NL3 $\omega\rho$	12.4740	1.6396	6.8920	1.3155	11.2354	0.7958	12.8470	1.6250	14.2557	3.9080	14.7642	3.1231	14.9024	2.5096
TM1	12.4922	1.6360	6.9387	1.3113	11.3769	0.5885	12.2818	1.0673	13.6098	2.8867	14.2938	2.6964	14.8874	2.0656
TM1 $\omega\rho$	12.4834	1.6377	6.9197	1.3125	11.3283	0.8353	13.0023	1.7447	14.2658	3.2911	14.7090	2.6657	14.9376	2.0072
TM2	12.4986	1.6347	6.9558	1.3096	11.4258	0.7248	12.7689	1.0601	13.5766	2.8071	14.8360	2.4069	14.9871	1.9881
TM2 $\omega\rho$	12.4809	1.6382	6.9119	1.3133	11.3180	0.8364	13.0174	1.7590	14.2803	3.3754	14.7323	2.7264	14.9386	2.0438
Hyperonic RMF EoS														
DD2	12.4849	1.6373	6.9355	1.3108	11.4036	0.6167	12.3954	1.2856	13.7387	2.3656	14.4082	3.4499	14.7460	2.1317
DDME2	12.4797	1.6383	6.9258	1.3112	11.3963	0.6274	12.4257	1.3473	13.7718	2.1575	14.3628	3.6315	14.7501	2.1179
FSU2H	12.4855	1.6371	6.9377	1.3105	11.3993	0.7711	12.4958	1.3600	14.2574	4.1927	14.5282	3.6776	14.7324	1.9163
H3	12.7365	1.5950	7.1558	1.3021	11.5194	0.4741	12.2298	0.9455	13.7026	3.2473	14.3214	2.9180	14.6654	1.9421
H4	12.7332	1.5958	7.1362	1.3035	11.5018	0.4987	12.2443	0.9454	13.7026	3.2456	14.3267	2.9158	14.7047	2.1990
NL3	12.4804	1.6382	6.9277	1.3111	11.4092	0.6241	12.3368	0.9139	13.5225	2.8704	14.5487	3.4335	14.6612	2.1934
NL3 $\omega\rho$	12.4666	1.6409	6.8926	1.3141	11.3219	0.7170	12.5349	1.3253	13.5939	2.0372	14.3365	3.8767	14.7107	2.1491
Hybrid EoS														
DD2-B15-40-20	12.8916	1.5682	7.3053	1.3013	11.4524	0.5827	12.3650	1.2772	13.7478	2.3416	14.3675	3.3902	14.8872	1.2831
NL3 $\omega\rho$ -B20-50-0	12.6482	1.6090	7.0411	1.3126	11.1942	0.8373	13.0106	1.7766	14.2898	3.7905	14.6848	2.1843	15.0271	1.4575
NL3 $\omega\rho$ -B28-75-0	12.6539	1.6079	7.0516	1.3122	11.1957	0.8375	13.0148	1.7533	14.2720	3.8022	14.7582	1.8590	15.0730	1.4889
NL3 $\omega\rho$ -B0-50-0	12.6539	1.6079	7.0516	1.3122	11.1957	0.8375	13.0158	1.7541	14.2723	3.8042	14.8040	0.0344	14.9109	2.1239
NL3 $\omega\rho$ -B0-50-50	12.6539	1.6079	7.0557	1.3113	11.2603	0.7904	12.8250	1.5964	14.1493	3.0321	14.4147	3.9648	14.7511	3.1637

Table 3.9: Parameters of unified fits by seven polytropes of 24 nucleonic Skyrme and one *ab initio* equations of state. The logarithm of the transition densities ρ_{ti} between the polytropes is given in g/cm^3 . For each polytrope i , the adiabatic index Γ_i is presented. Only the first constant κ_0 is presented because all others can be calculated from pressure continuity.

EoS	$\log_{10}(\kappa_0)$	Γ_0	$\log_{10}(\rho_{t1})$	Γ_1	$\log_{10}(\rho_{t2})$	Γ_2	$\log_{10}(\rho_{t3})$	Γ_3	$\log_{10}(\rho_{t4})$	Γ_4	$\log_{10}(\rho_{t5})$	Γ_5	$\log_{10}(\rho_{t6})$	Γ_6
(Nucleonic) Skyrme EoS														
BSk20	12.4732	1.6396	6.9219	1.3117	11.3469	0.7499	12.4636	1.3408	14.1522	2.8323	14.4311	3.2096	14.8995	3.0780
BSk21	12.4958	1.6357	6.9433	1.3107	11.3651	0.7452	12.3329	1.2571	14.1610	3.4841	14.6921	3.1032	14.9021	2.8012
BSk22	12.5847	1.6208	7.0094	1.3087	11.3556	0.7443	12.5103	1.3024	14.0180	3.1330	14.6885	2.9089	14.8925	2.7427
BSk23	12.5847	1.6208	7.0094	1.3087	11.3556	0.7443	12.5103	1.3024	14.0180	3.1330	14.6885	2.9089	14.8925	2.7427
BSk24	12.5798	1.6215	7.0054	1.3093	11.3762	0.7402	12.3322	1.2579	14.1588	3.4628	14.7075	3.0922	14.9230	2.7773
BSk25	12.5907	1.6197	7.0119	1.3090	11.3885	0.7444	12.2107	1.2034	14.2131	3.7548	14.6893	3.1507	14.9108	2.6403
BSk26	12.4353	1.6458	6.9024	1.3126	11.3405	0.7526	12.4679	1.3404	14.1348	2.7472	14.4199	3.2064	14.9161	3.0628
DH	12.7007	1.6021	7.0898	1.3030	11.5622	0.6165	12.4163	1.3397	14.0053	2.1052	14.2804	3.0053	14.9602	2.8605
KDE0v1	14.7161	1.3184	10.1496	1.2477	11.5395	0.6476	12.4235	1.3753	14.0090	2.4045	14.4262	2.8665	15.0278	2.7822
Rs	14.7794	1.3089	10.2552	1.2161	11.7133	0.5642	13.0311	0.3835	13.3745	1.4335	13.5407	3.1815	14.2645	2.6712
Sk255	14.7118	1.3176	10.1273	1.2456	11.5501	0.5897	12.5538	1.2295	13.5409	2.4784	14.4910	2.7236	15.1723	2.6880
Sk272	14.7050	1.3188	10.1052	1.2497	11.5150	0.6131	12.4888	1.2939	13.6393	2.4588	14.4272	2.8096	15.1060	2.7603
Ska	14.7299	1.3149	10.1492	1.2381	11.5816	0.5908	12.4222	1.1598	13.5067	2.0177	14.0436	2.8420	15.0849	2.7774
Skb	14.7293	1.3142	10.1099	1.2372	11.5344	0.7113	13.2162	0.3365	13.7754	4.0702	14.2652	3.0945	14.7695	2.8537
SkI2	14.7376	1.3144	10.1308	1.2373	11.5685	0.6265	13.4248	1.7804	13.6041	3.2146	14.3183	2.6160	15.0811	2.6441
SkI3	14.7239	1.3164	10.1258	1.2435	11.5830	0.5858	12.3665	1.1000	13.7485	2.9839	14.4126	2.8078	14.6677	2.6923
SkI4	14.7263	1.3167	10.1323	1.2426	11.5727	0.5761	12.3014	1.1311	13.9299	3.1012	14.6916	2.9305	14.9658	2.7467
SkI5	14.7427	1.3139	10.2018	1.2345	11.6527	0.4384	12.0220	0.6561	13.5518	3.3975	14.2875	2.5666	14.9267	2.6828
SkI6	14.7290	1.3163	10.1451	1.2418	11.5705	0.5986	12.3258	1.1753	13.9557	3.0843	14.7293	2.9186	14.9817	2.7458
SkMP	14.7605	1.3113	10.1929	1.2251	11.6484	0.5811	12.6209	1.0106	13.6166	2.7978	14.4767	2.7814	14.9768	2.7302
SkOp	14.7348	1.3160	10.1478	1.2410	11.5968	0.5485	12.4485	1.0966	13.3943	1.8574	13.9326	2.6883	15.1036	2.6213
SLy230a	14.7200	1.3174	10.1478	1.2437	11.5337	0.6262	12.2329	1.2824	14.1720	3.1458	14.8556	2.9664	15.0878	2.7300
SLy2	14.7218	1.3170	10.1456	1.2429	11.5318	0.6369	12.3351	1.3217	14.0238	2.4088	14.3263	2.9840	14.9738	2.8379
SLy9	14.7253	1.3165	10.1345	1.2418	11.5328	0.6416	12.3443	1.3051	13.9715	2.5671	14.2802	2.9772	14.9302	2.7763
<i>ab initio</i> EoS														
BCPM	12.4703	1.6383	6.9467	1.3136	11.3401	0.7181	12.4647	1.3333	14.0080	2.7194	14.0053	2.9133	14.9915	2.6914

To assess the improvement of our method with respect to PPFRead, we present the relative error on H3 and H4 for our fitting method, and that of PPFRead in Fig. 3.28. The impact of using unified fits on the relative difference for the radius is particularly important for low mass stars, because the crust is relatively more significant for such objects. Overall, the relative difference for our fit is significantly smaller than for PPFRead for all macroscopic parameters considered. The relative inaccuracy of our fits for stellar configurations with the same central pressure is smaller in particular in the region close to maximum mass and for R , Λ and I are 0.1%, 1.8%, 1% respectively, compared with 1%, 8.7%, and 2% for a fixed mass $M = 2 M_\odot$ for equation of state H4.

Our fitting method is intended to provide accurate modeling of macroscopic parameters of neutron stars. Therefore, quantities M , R , I , and Λ are calculated from our fitted equations of state, and compared with that of unified tables. Results for macroscopic parameters of prime interest are presented in Table 3.10 and Table 3.11: we present the maximum mass M_{\max} , density at the maximum mass n_{\max} , the radius at $1.0 M_\odot$ and $1.4 M_\odot$ respectively denoted $R_{1.0}$ and $R_{1.4}$, as well as the radius at maximum mass R_{\max} , the moment of inertia at $1.338 M_\odot$ denoted $I_{1.338}$ and at the maximum mass I_{\max} , and the tidal deformability at $1.4 M_\odot$ denoted $\Lambda_{1.4}$ and at maximum mass Λ_{\max} . We provide the relative errors Δ on these quantities except those defined at the maximum mass. For the latter, we include instead the relative error δ defined as the relative difference between the quantities calculated at the maximum mass for the unified table, and at the maximum mass for our fit. Indeed, because the maximum mass of the unified equation of state and our fit are not exactly equal, Δ at the maximum mass and δ are different. The largest errors are presented in red in the tables.

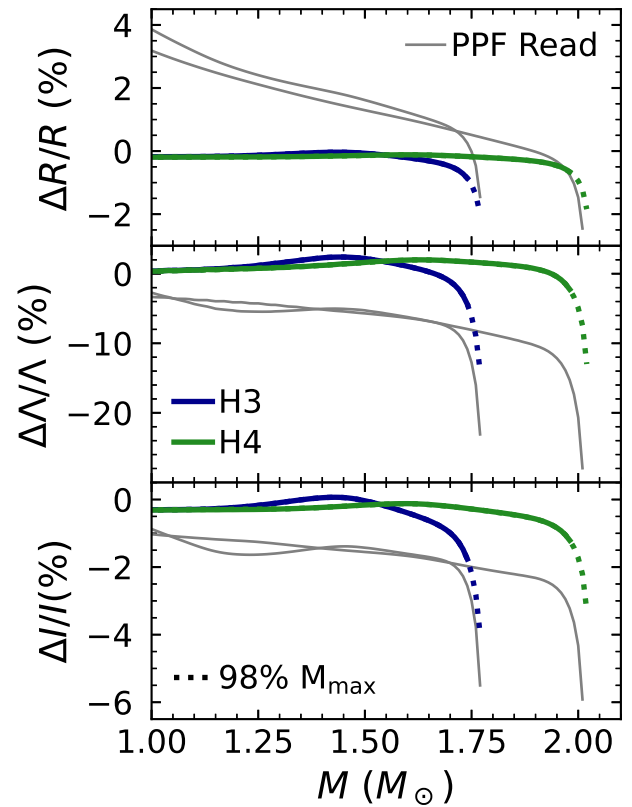


Figure 3.28: Relative difference as a function of the mass M in percent between unified tables and our fits for the radius $\Delta R/R$, the tidal deformability $\Delta\Lambda/\Lambda$ and the moment of inertia $\Delta I/I$ for equation of state H3 and H4. The relative difference between PPF Read and unified equations of state H3 and H4 is presented in gray. For our fits, the relative difference is presented up to 98% of the maximum mass in plain lines, and the last two percent in dotted lines, see text for details.

Table 3.10: Key macroscopic quantities calculated from the unified table of 15 nucleonic, seven hyperonic and five hybrid relativistic mean field models, and the relative errors Δ and δ in percent related to unified piecewise polytropic fit. The maximum mass (in solar mass) M_{\max} , the density (in fm^{-3}) at maximum mass n_{\max} , the radius (in km) for a $1 M_{\odot}$ NS $R_{1.0}$, the radius for a $1.4 M_{\odot}$ neutron star $R_{1.4}$, the radius at maximum mass $R_{M_{\max}}$, the moment of inertia (in $10^{45} \text{g}\cdot\text{cm}^2$) for a $1.338 M_{\odot}$ neutron star $I_{1.338}$ as measured in the double pulsar PSR J0737–3039, the moment of inertia at maximum mass $I_{M_{\max}}$, the tidal deformability for a $1.4 M_{\odot}$ neutron star $\Lambda_{1.4}$, and the tidal deformability at maximum mass $\Lambda_{M_{\max}}$ are presented. In **red**, we indicate the equations of state that give the largest relative fit error in each category. The maximum mass of equation of state H3 is indicated in **blue**, to emphasize that is not consistent with J1614 – 2230 mass measurement; results are shown only because this model is used for a comparison.

	M_{\max}	Δ	n_{\max}	δ	$R_{1.0}$	Δ	$R_{1.4}$	Δ	$R_{M_{\max}}$	δ	$I_{1.338}$	Δ	$I_{M_{\max}}$	δ	$\Lambda_{1.4}$	Δ	$\Lambda_{M_{\max}}$	δ
Nucleonic RMF equation of state																		
BSR2	2.383	-0.14	0.852	-0.25	13.30	-0.16	13.40	-0.19	11.96	-0.11	1.634	-0.28	3.149	-0.36	761.70	-1.00	6.72	0.45
BSR6	2.430	-0.21	0.827	0.00	13.77	0.12	13.73	0.06	12.13	-0.24	1.677	0.02	3.306	-0.77	836.16	0.01	6.28	-0.99
DD2	2.417	-0.20	0.851	0.63	12.99	0.22	13.16	-0.01	11.87	-0.47	1.593	-0.30	3.216	-1.14	697.89	-1.13	5.74	-3.81
DDH δ	2.138	-0.30	1.000	-0.00	12.40	-0.04	12.61	-0.04	11.14	-0.52	1.533	-0.37	2.376	-1.42	589.00	0.41	9.23	-2.72
DDME2	2.481	-0.24	0.817	-0.23	12.98	0.16	13.20	-0.07	12.06	-0.32	1.604	-0.41	3.456	-0.95	719.61	-1.56	5.39	-1.77
FSU2	2.071	-0.22	0.904	-0.00	14.18	-0.17	13.93	-0.16	12.08	-0.35	1.716	-0.10	2.441	-0.90	886.54	-0.56	20.11	-1.30
FSU2H	2.375	-0.25	0.802	-0.27	13.05	0.11	13.32	0.13	12.37	-0.23	1.638	0.17	3.306	-0.88	752.85	3.44	9.93	0.59
FSU2R	2.047	-0.30	0.943	-0.28	12.89	0.32	12.98	0.02	11.66	-0.30	1.552	-0.25	2.333	-1.16	608.63	1.61	18.35	0.03
GM1	2.361	-0.14	0.864	0.00	13.64	-0.08	13.72	-0.12	11.92	-0.20	1.729	-0.27	3.063	-0.52	922.33	-1.02	6.82	-0.82
NL3	2.773	-0.16	0.669	0.00	14.52	-0.32	14.61	-0.18	13.29	-0.23	1.898	-0.16	4.744	-0.57	1297.27	-0.48	4.71	-0.80
NL3 $\omega\rho$	2.753	-0.08	0.688	0.00	13.42	-0.31	13.75	-0.26	13.00	-0.15	1.732	-0.13	4.612	-0.27	953.91	-0.62	4.47	-0.30
TM1	2.175	-0.17	0.856	0.00	14.36	0.17	14.24	-0.00	12.34	-0.26	1.798	-0.21	2.739	-0.80	1051.06	-0.73	16.70	-1.52
TM1 $\omega\rho$	2.118	-0.36	0.908	-0.28	13.43	-0.37	13.41	-0.22	11.91	-0.34	1.607	-0.21	2.522	-1.08	712.90	-0.82	16.20	-0.01
TM2	2.270	-0.14	0.823	-0.00	14.44	-0.19	14.34	-0.12	12.50	-0.14	1.813	-0.22	3.010	-0.44	1087.63	-0.67	13.45	0.05
TM2 $\omega\rho$	2.220	-0.34	0.869	0.00	13.43	-0.37	13.47	-0.24	12.08	-0.37	1.626	-0.32	2.803	-1.09	748.94	-0.98	12.99	-0.46
Hyperonic RMF equation of state																		
DD2	1.996	0.02	1.007	-1.48	12.99	0.37	13.15	0.15	11.38	0.72	1.592	-0.11	2.125	1.18	694.86	-0.50	17.14	6.50
DDME2	2.064	0.06	0.947	-1.20	12.98	-0.11	13.20	-0.15	11.65	0.45	1.604	-0.19	2.342	1.00	719.19	-0.66	16.70	4.76
FSU2H	1.991	-0.03	0.901	-0.99	13.05	0.02	13.32	-0.01	11.99	0.33	1.638	-0.14	2.310	0.60	752.79	2.57	27.96	5.22
H3	1.787	-0.54	0.993	-0.28	13.66	-0.04	13.61	0.04	11.75	-0.76	1.707	-0.03	1.839	-2.39	852.60	0.07	47.43	-3.58
H4	2.032	-0.38	0.964	-0.00	13.66	-0.06	13.72	-0.08	11.71	-0.53	1.730	-0.27	2.268	-1.57	920.95	-0.94	18.32	-2.48
NL3	2.232	0.02	0.737	0.00	14.52	-0.15	14.61	-0.10	12.90	0.34	1.898	-0.13	3.058	0.72	1297.07	-0.45	20.05	3.65
NL3 $\omega\rho$	2.277	-0.08	0.751	0.00	13.42	0.50	13.75	0.23	12.69	0.23	1.732	-0.05	3.158	0.17	953.84	-0.34	16.87	2.30
Hybrid EoS																		
DD2-B15-40-20	2.153	0.04	0.771	-0.40	12.99	0.05	13.16	-0.14	12.65	0.02	1.593	-0.32	2.933	0.17	698.15	-1.35	28.25	0.13
NL3 $\omega\rho$ B20-50-0	2.151	-0.29	0.812	-0.37	13.40	0.59	13.73	0.16	12.58	0.04	1.730	-0.32	2.836	-0.61	950.32	-1.54	24.32	1.39
NL3 $\omega\rho$ -B28-75-0	2.326	-0.23	0.729	-0.36	13.40	0.41	13.73	0.16	13.07	-0.02	1.730	0.09	3.450	-0.45	950.32	0.02	19.36	1.40
NL3 $\omega\rho$ -B0-50-0	2.241	-0.45	0.666	-0.23	13.40	0.41	13.73	0.17	13.44	-0.15	1.730	0.11	3.428	-1.10	950.28	0.09	34.19	1.32
NL3 $\omega\rho$ -B0-50-50	2.455	-0.17	0.443	0.00	13.40	-0.03	13.73	-0.07	13.96	-0.06	1.730	-0.10	4.297	-0.35	950.29	-0.45	25.97	0.79

Table 3.11: Key macroscopic quantities calculated from the unified table of 24 Skyrme and one *ab initio* models, and the relative errors Δ and δ in percent related to unified piecewise polytropic fit. The maximum mass (in solar mass) M_{\max} , the density (in fm^{-3}) at maximum mass n_{\max} , the radius (in km) for a $1 M_{\odot}$ NS $R_{1.0}$, the radius for a $1.4 M_{\odot}$ neutron star $R_{1.4}$, the radius at maximum mass $R_{M_{\max}}$, the moment of inertia (in $10^{45} \text{g}\cdot\text{cm}^2$) for a $1.338 M_{\odot}$ neutron star $I_{1.338}$ as measured in the double pulsar PSR J0737–3039, the moment of inertia at maximum mass $I_{M_{\max}}$, the tidal deformability for a $1.4 M_{\odot}$ neutron star $\Lambda_{1.4}$, and the tidal deformability at maximum mass $\Lambda_{M_{\max}}$ are presented. In **red**, we indicate the equations of state that give the largest relative fit error in each category.

	M_{\max}	Δ	n_{\max}	δ	$R_{1.0}$	Δ	$R_{1.4}$	Δ	$R_{M_{\max}}$	δ	$I_{1.338}$	Δ	$I_{M_{\max}}$	δ	$\Lambda_{1.4}$	Δ	$\Lambda_{M_{\max}}$	δ
(Nucleonic) Skyrme EoS																		
BSk20	2.164	0.04	1.126	0.52	11.76	0.00	11.74	-0.00	10.17	-0.25	1.308	-0.06	2.176	-0.26	328.30	-0.19	3.53	-3.18
BSk21	2.274	0.06	0.975	0.77	12.47	0.04	12.59	-0.02	11.04	-0.31	1.484	-0.06	2.622	-0.34	533.99	-0.34	4.90	-3.93
BSk22	2.265	-0.12	0.969	0.24	13.03	-0.08	13.05	-0.08	11.19	-0.19	1.564	-0.13	2.622	-0.47	642.77	-0.52	5.39	-0.92
BSk23	2.265	-0.12	0.969	0.24	13.03	-0.08	13.05	-0.08	11.19	-0.19	1.564	-0.13	2.622	-0.47	642.77	-0.52	5.39	-0.92
BSk24	2.279	-0.15	0.978	0.24	12.47	-0.06	12.59	-0.07	11.05	-0.23	1.483	-0.11	2.637	-0.61	532.32	-0.53	4.84	-1.21
BSk25	2.225	-0.17	0.998	0.46	12.22	0.02	12.39	-0.07	10.99	-0.34	1.454	-0.16	2.516	-0.84	495.04	-0.74	5.86	-2.33
BSk26	2.169	-0.09	1.124	0.36	11.79	-0.05	11.78	-0.06	10.20	-0.25	1.314	-0.17	2.191	-0.51	333.57	-0.59	3.53	-2.01
DH	2.049	-0.04	1.207	0.00	11.90	-0.06	11.73	-0.03	9.99	-0.12	1.287	-0.08	1.904	-0.25	304.98	-0.20	4.64	-1.01
KDE0v1	1.969	-0.13	1.279	0.18	11.90	-0.07	11.61	-0.13	9.79	-0.18	1.255	-0.25	1.714	-0.47	274.01	-1.01	5.21	-0.72
Rs	2.116	-0.12	1.074	0.15	13.05	-0.09	12.91	-0.09	10.75	-0.15	1.547	-0.15	2.186	-0.42	605.14	-0.51	6.46	-0.47
Sk255	2.144	-0.15	1.057	0.19	13.42	0.11	13.12	0.08	10.84	-0.11	1.542	-0.01	2.248	-0.48	593.99	1.11	5.93	0.29
Sk272	2.231	-0.15	0.997	0.21	13.51	0.22	13.29	0.15	11.08	-0.11	1.577	0.07	2.495	-0.50	657.16	0.26	5.24	-0.28
Ska	2.208	-0.09	1.025	0.18	13.01	-0.21	12.89	-0.13	10.88	-0.17	1.522	0.05	2.409	-0.34	569.18	1.65	5.05	0.02
Skb	2.188	-0.13	1.060	0.69	12.05	-0.03	12.19	0.07	10.60	-0.49	1.449	0.17	2.333	-0.95	481.85	0.67	4.86	-4.29
SkI2	2.162	-0.07	1.015	0.01	13.58	-0.08	13.46	-0.15	11.11	-0.06	1.662	-0.31	2.354	-0.19	786.60	-1.07	6.95	0.20
SkI3	2.239	-0.10	0.967	0.08	13.59	0.00	13.53	-0.02	11.30	-0.08	1.666	-0.12	2.574	-0.30	801.58	-0.44	6.14	-0.04
SkI4	2.169	-0.13	1.061	0.24	12.31	-0.00	12.35	-0.07	10.66	-0.21	1.447	-0.16	2.297	-0.55	463.67	2.77	5.22	0.19
SkI5	2.240	-0.08	0.953	-0.05	14.16	-0.04	14.05	-0.10	11.46	-0.01	1.793	-0.25	2.598	-0.15	1029.71	-0.83	6.62	0.74
SkI6	2.189	-0.12	1.044	0.14	12.44	-0.06	12.47	-0.07	10.75	-0.17	1.464	-0.13	2.359	-0.47	501.68	-0.57	5.22	-0.70
SkMP	2.107	-0.11	1.107	0.15	12.58	0.02	12.48	-0.05	10.52	-0.13	1.459	-0.20	2.123	-0.40	489.63	-0.72	5.69	-0.49
SkOp	1.972	-0.13	1.224	0.19	12.41	-0.13	12.11	-0.17	10.12	-0.20	1.360	-0.18	1.781	-0.47	371.34	-0.83	6.76	-0.53
SLy230a	2.099	-0.08	1.145	0.08	11.86	-0.21	11.81	-0.13	10.24	-0.16	1.319	-0.09	2.063	-0.33	338.00	-0.35	4.92	-0.63
SLy2	2.053	-0.11	1.197	0.26	11.91	-0.13	11.76	-0.14	10.04	-0.25	1.301	-0.23	1.924	-0.52	318.13	-0.82	4.77	-1.62
SLy9	2.156	-0.12	1.074	0.38	12.54	-0.11	12.45	-0.15	10.63	-0.30	1.431	-0.29	2.249	-0.63	446.12	2.13	5.13	-0.85
(Nucleonic) <i>ab initio</i> equation of state																		
BCPM	1.980	-0.09	1.241	-0.24	11.93	0.00	11.71	-0.08	9.96	-0.08	1.283	-0.21	1.773	-0.29	299.68	-0.76	5.97	-0.08

With respect to nucleonic relativistic mean field models, errors associated with the fit on M_{\max} , n_{\max} , and quantities related to the radius are systematically below 1%. For astrophysical quantities related to the moment of inertia, it stays below 1.5%, and for the tidal deformability below 4%. For hyperonic relativistic mean field models equations of state consistent with the maximum mass criterion (all but H3), the errors associated to the fit on M_{\max} , n_{\max} , and quantities related to the radius stay below 1.5%. Quantities related to the moment of inertia stay below 2.5%, and for the tidal deformability below 7%. For hybrid relativistic mean field models, the errors associated with the fit stays below 2% for all quantities.

For Skyrme models, the error associated with the fit for M_{\max} , n_{\max} , quantities related to the radius and the moment of inertia are below 1%. Once again, the tidal deformability does not fair as well, with an error up to 5%.

The maximum mass is the most accurately reproduced quantity, with an error below 0.5%. The tidal deformability is systematically the quantity with largest errors associated with the fit. Generally, nucleonic models are more accurately reproduced by our fits than hyperonic or hybrid ones. This is understandable because the number of polytropes chosen in the core is fixed to three, and the presence of hyperons or a phase transition to deconfined quarks in the core produces respectively an additional softening and drop of the adiabatic index as a function of the baryonic density, see Fig. 3.2.

Overall, we have provided a revision of an analytical representation of β -equilibrated and cold neutron star matter's equation of state based on piecewise polytropes, for dozens of modern and well constrained nuclear models. Our fits perform well beyond the expected precision on the detection of the mass, the radius and the tidal deformability.

4 Crust compression related astrophysical phenomena

Neutron stars are subject to astrophysical phenomena leading to the compression of their crust: accretion processes in binary systems, spinning down of a rapidly rotating star, or the decay of the magnetic field in magnetars. The exothermic reactions triggered in the crust by compression have an impact on the exhibited luminosity of the star. Therefore, X-ray observations can help us explore the crust composition and properties. In this chapter, we explore the compression of the neutron star crust beyond commonly used approximations.

This chapter treats mainly of accreting neutron stars, a brief introduction to the accretion process in neutron star binaries is given in section 4.1. The exothermic reactions triggered by the compression of the crust are presented, and calculated for a simple nuclear model of a compressible liquid drop.

The fully accreted crust approach, which is the common approximation chosen to model the accreting neutron star crust, is abandoned in section 4.2. The equation of state and composition of an originally catalyzed outer crust under compression is derived using a simple nuclear model. Heat sources of a partially accreted crust are reconstructed and applications for compressed crusts in magnetars and rotating neutron stars are briefly discussed. Results in this section are the subject of the publication [Suleiman et al. \[2022b\]](#).

In section 4.3, the commonly used approach to the kinetics of electron captures in accreting neutron stars is revised. The impact of the reaction rate on the heat release in the shallowest shells of the crust is derived, and the role of layers of electron captures in the heat release of accreting neutron stars is discussed.

Contents

4.1	Accreting neutron stars	95
4.1.1	From the donor to the neutron star crust	95
4.1.2	Deep crustal heating	97
4.2	Partially accreted crusts	102
4.2.1	Beyond the fully accreted crust approximation	102
4.2.2	Heat sources in a compressed catalyzed crust	105
4.2.3	Onset of the neutron drip	115
4.2.4	Applications for rotating neutron stars and magnetars	117
4.2.5	Properties of a compressed crust	118
4.2.5.1	Composition and transport properties	118
4.2.5.2	Neutron drip anomaly	120
4.2.5.3	Density inversion related instability	124
4.3	Layers of electron captures in accreting neutron stars	126
4.3.1	Electron captures	126
4.3.1.1	Derivation of the reaction rate	127
4.3.1.2	Application for the first few shells of an accreting crust	131
4.3.1.3	For the process: ${}^{56}_{26}\text{Fe} \rightarrow {}^{56}_{25}\text{Mn} \rightarrow {}^{56}_{24}\text{Cr}$	132
4.3.1.4	For the process: ${}^{56}_{24}\text{Cr} \rightarrow {}^{56}_{23}\text{V} \rightarrow {}^{56}_{22}\text{Ti}$	133
4.3.1.5	For the process: ${}^{56}_{22}\text{Ti} \rightarrow {}^{56}_{21}\text{Sc} \rightarrow {}^{56}_{20}\text{Ca}$	134
4.3.2	The linear mixing rule approach to a mixture of nuclei	135
4.3.3	The continuity equation	138
4.3.3.1	Formulation of the continuity equation	138
4.3.3.2	Astrophysically motivated accretion rate	139
4.3.3.3	Heat release	140
4.3.4	Stationary solution	141
4.3.5	Solution to the full continuity equation	145

4.1 Accreting neutron stars

Binary systems involving a neutron star can host the process of accretion: matter from the companion star, whether it is a low mass star or a high mass star, is transferred to the neutron star surface. In this section, the accretion process operating on neutron stars is briefly introduced, from the origin of this process in the binary, to the crash of accreted matter on the surface of the neutron star's crust. The heat sources triggered in the crust by the accretion process are presented.

4.1.1 From the donor to the neutron star crust

Neutron stars, whether isolated or in a binary, emit in the electromagnetic band of X-ray. The process of transferring matter from the companion star to the neutron star in accreting binary systems also emits in X-ray. In a Low Mass X-ray Binary (LMXB), the companion is either a main sequence star or a white dwarf with a mass typically under one solar mass; it evolves into a donor once its Roche lobe has been filled, and transfers matter to a disk orbiting the neutron star. A loss of angular momentum in the accretion disk triggers the falling of material onto the neutron star envelope. In the case of a High Mass X-ray Binary system (HMXB), the companion is a massive star (*e.g.* a red giant) which transfers matter through stellar winds or a decretion disk. A stable accretion process in a double neutron star binary is excluded because the Roche lobe of a neutron star is filled only at merger stages of the binary system's evolution.

The accretion process is a highly luminous phenomenon in the X-ray band, with values of the exhibited luminosity up to 10^{39} erg/s for low mass X-ray binaries. This process is intermittent, with short and luminous stages that can last from days to weeks, interspersed by quiescence stages -absence of accretion- that can last from months to decades. A few sources, such as KS 1731–260 [Rutledge et al., 2002], are referred to as quasi-persistent transients; they have been observed accreting for rather long periods, from years to decades [Cackett et al., 2006]. Sources emit in the soft X-ray band, with the photon energy below 10 keV, and are referred to as Soft X-ray Transients (SXT). Their emission is observed in both active accretion and quiescent stages, thus allowing for a study of the thermal evolution of neutron stars [Wijnands et al., 2017].

The exhibited luminosity of accreting neutron stars depend on the accretion rate. In a simple way, the accretion rate is defined as the mass of matter accreted per unit time. A more rigorous definition can be used: it is the baryon mass of a diluted gas of baryons infalling onto the neutron star, per unit time, as measured by a distant observer. The second definition puts into light the relativistic nature of neutron stars: the gravitational mass and baryon mass of accreted matter can be considered equal in the accretion disk; however, it is no longer the case when matter crashes onto the neutron star, is pushed deeper in the crust, and is subjected to an increasing pressure. In the following, the accretion rate is defined by the baryon mass of accreted matter. It is important to distinguish the mean accretion rate, denoted $\langle \dot{M} \rangle$ which includes the time of quiescence, and the accretion rate during active

accretion phases, which we denote \dot{M} . The order of magnitude for the accretion rate ranges from 10^{-10} to 10^{-8} solar mass per year, see e.g [Degenaar et al., 2015, Wijnands et al., 2017].

When matter falls from the accretion disk orbiting the neutron star, angular momentum is transferred such that accreting neutron stars are spun-up. The gravitational wave emission from a rotating neutron star decreases the neutron star spin as the star ages, however, accretion recycles the spin, such that oldest pulsars are spinning fast [Tauris et al., 2013, Suvorov and Melatos, 2020]¹. Moreover, the accretion process on the timescale of the binary life time increases the mass of the neutron star; this is neglected in this chapter, which is reasonable given the timescale of the accretion process in X-ray transients.

X-ray bursts are bright flashes in low-mass X-ray binaries, with a rising time of around one second, a typical duration of one minute, and they are recurrent every few hours. The matter transferred from the disk is a plasma rich in Hydrogen and/or Helium originating from the companion star. It falls onto the neutron star, forming an envelope of light elements. Bursts are powered by the burning of Helium in the thermally unstable fusion of α -particles, which is ignited at the bottom of the freshly accreted plasma. The freshly accreted plasma is compressed under the weight of newly accreted matter, and accumulates in a layer of growing mass, typically during a few hours. Thermonuclear burning, quenched by the exhaustion of Helium and the decrease in temperature from the peak value exceeding 10^9 K, produces ashes of isotopes with nucleon number $A = [50 - 110]$. The current understanding of the mechanism of X-ray bursts and their theoretical models is described in Bildsten [1998], Parikh et al. [2013], Meisel et al. [2018]. The evolution of the accreted layer depends on the metallicity of freshly accreted material and the active accretion rate \dot{M} [Bildsten, 1998]:

- For $2 < \dot{M}_{-10} < 10$, with \dot{M}_{-10} the accretion rate in $10^{-10} M_{\odot}$ per year, Hydrogen burns into Helium in a stable way. When no Hydrogen is left in the accreted bottom layer, the pure Helium layer starts to grow. Helium burning, which is initiated after crossing the ignition line in the density-temperature plane, is associated with thermal instability, resulting in thermonuclear runaway. The accreted envelope is then heated, and reaches in a second a peak temperature of around 10^9 K.
- For $10 < \dot{M}_{-10} < 260$, Helium is ignited before Hydrogen burning has been completed, such that the thermonuclear runaway of Helium takes place in the Hydrogen-Helium mixture.

In both accretion regimes, nucleosynthesis is driven mainly by the rapid proton captures and positron decays, but other nuclear processes with α -particles and protons are also involved. Generally, nuclear ash abundances peak around $A \sim 60$ and/or $A \sim 100$, depending on the accretion rate and metallicity of the accreted material [Parikh et al., 2013]. As the accretion

¹The NICER telescope has observed fast rotating pulsars, whose spin is likely to have been recycled by accretion. The radius of an isolated neutron star and an accreting crust differs by approximately a hundred meters, therefore the increase in accuracy of the telescope will require accreting crust modelling.

process continues, ashes accumulate and are pushed to higher pressures by freshly accreted material.

In the following, we shall focus on what happens to the crust of neutron stars after the ashes have been deposited on the outer crust surface.

4.1.2 Deep crustal heating

The temperature exhibited by neutron stars in quiescence is higher than expected for isolated neutron stars. This suggests that accretion has induced heating processes deep enough below the surface to be still visible in quiescence, because the heat diffuses to the surface. As accreted matter accumulates on the surface of the crust, a series of exothermic reactions are triggered by the compression of matter.

The common approximation to establish the equation of state and composition of accreting neutron stars is that of a fully accreted crust: the original crust, *i.e.*, the crust before the star is subjected to accretion, is not considered because it is assumed to have been completely replaced by accreted material. The crust of a typical neutron star amounts to a total mass $M_{\text{crust}} \sim 10^{-2} M_{\odot}$ [Chamel and Haensel, 2008]. The time of accretion required to replace the original crust, denoted t_{oc} , is

$$t_{\text{oc}} = \frac{M_{\text{crust}}}{\langle \dot{M} \rangle} \sim \frac{10^8}{\langle \dot{M} \rangle_{-10}} \text{ yr}, \quad (4.1)$$

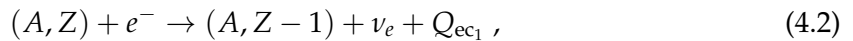
where $\langle \dot{M} \rangle_{-10}$ is the time-averaged accretion rate in 10^{-10} solar mass per year. After t_{oc} has passed in an accreting binary, the crust of the neutron star is made entirely of accreted material, and it is different in composition from the crust of an isolated neutron star. Because low mass X-ray binaries involving neutron stars can exist for as long as 10^9 years, a fully accreted crust is a reasonable approach. It is important to note that the effect on the core -into which the original crust is pushed-, and the effect on the total mass of the neutron star, shall be neglected in this chapter. Indeed, accretion of matter can increase the neutron star's mass, but it does so with a timescale sufficiently large that the Tolmann-Oppenheimer-Volkoff equations need not be solved for each time of the accretion process.

Designing the equation of state of an accreted crust is fundamentally different from the derivation for a catalyzed crust. The catalyzed matter assumption is stringent: it requires that the composition of the crust is at global minimum, or in other words that all reactions that could have happened did occur, and that the crust is made of nuclei with globally minimized Gibbs energy at given pressure. This approach is appropriate for adult neutron stars which have not accreted matter, in the assumption that their proto-neutron star stage imposed temperatures high enough, with slow enough cooling, that all nuclei have reshuffled, and that the ground state has been reached. The equation of state for accreted crusts is calculated under completely different assumptions. Ashes that accumulate on the crust surface, with a nucleon number $A = [50, 110]$ [Haensel et al., 2007b], are pushed towards the core and subject to compression related reactions, changing their proton and neutron number.

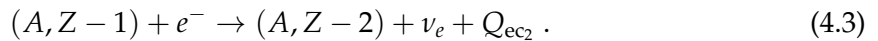
Therefore, the local equilibrium with respect to reactions on the ashes element is looked for, and not the global equilibrium. In practice, calculating the equation of state of a catalyzed crust takes longer than computing an accreted crust: in the former case, the stability of all possible nuclei must be tested at a given pressure, whereas in the latter case, the ash nuclei are tested with respect to compression related reactions.

The most common approach to model nuclei in the accreted crust is the Wigner-Seitz cell approximation in the framework of the single-nucleus model [Haensel and Zdunik, 2008, Fantina et al., 2018, Potekhin and Chabrier, 2021]: Wigner-Seitz cells consist of a spherical and positively charged nucleus permeated by a quasi-uniform gas of relativistic electrons. In the inner crust, nuclei are additionally immersed in a gas of free neutrons. There is an inherent flaw to the single-nucleus approach: if one considers that a single cell can explain the whole physics of the crust, then no considerations of interactions between cells can be taken into account. The neutron diffusion is therefore excluded from the theory, and dripped neutrons can only stay in their cell. Recently, the non-diffusive approach was put into question by Shchepochin et al. [2022], the authors arguing that neutron diffusion affects the exothermic reactions in the accreted crust. In the following, we however use the single-nucleus model, but discuss neutron diffusion. A_{cell} refers to the number of nucleons per cell, A to the number of nucleons in the nucleus, N is the number of neutrons inside the nucleus, and N_{out} is the number of neutrons outside the nucleus. The neutron star envelope is neglected in the sense that the equation of state and the composition are established above the mass density $\rho \sim 10^6 \text{ g/cm}^3$; its importance in the cooling of soft X-ray transients is not forgotten, but the infalling accreted material has undergone enough transformations that the final nucleus of the burning (the ash) is ^{56}Fe .

The first and most common compression related reactions on the nucleus (A, Z) are electron captures



with the electron denoted e^- , the electronic neutrino denoted ν_e , and the energy release denoted Q_{ec_1} . Odd number nuclei are energetically disfavored, therefore it is common that electron captures are operated in pairs, *i.e.* if (A, Z) is an even-even nucleus, reaction Eq. (4.2) is immediately followed by



Further details on electron captures are presented in section 4.3.

The second type of compression-related exothermic reactions are pycnonuclear fusions. Electron captures triggered by compression decrease the number of protons in the nucleus. As density continues to increase, the Coulomb repulsion localizing nuclei on the crust lattice is challenged by the kinetic energy of the zero-point quantum vibrations of nuclei around the crystal lattice sites. The Coulomb barrier can be penetrated, such that the non-thermal

fusion of two nuclei is possible

$$(A, Z) + (A, Z) \rightarrow (2A, 2Z) + Q_{\text{pyc}} , \quad (4.4)$$

with Q_{pyc} the energy release. The rate of pycnonuclear fusions is subject to very large uncertainty [Yakovlev et al., 2006]. As a result, the nucleus for which pycnonuclear fusion occurs, and the pressure (and density) at which this energy source is located, are poorly defined. However, some global quantities such as the total energy release do not depend significantly on this rate [Haensel and Zdunik, 2008].

Above the neutron drip line, both reaction chains can be accompanied by neutron emission such that

$$(A, Z) + e^- \rightarrow (A - N_{\text{out};\text{ec}_1}, Z - 1) + \nu_e + N_{\text{out};\text{ec}_1} + Q_{\text{ec}_1} , \quad (4.5)$$

$$(A, Z - 1) + e^- \rightarrow (A - N_{\text{out};\text{ec}_2}, Z - 2) + \nu_e + N_{\text{out};\text{ec}_2} + Q_{\text{ec}_2} , \quad (4.6)$$

$$(A, Z) + (A, Z) \rightarrow (2A - N_{\text{out}}, 2Z) + Q_{\text{pyc}} + N_{\text{out};\text{pyc}} , \quad (4.7)$$

with N_{out} the number of emitted neutrons.

As a simple example, we compute the accreted crust from ^{56}Fe ashes in the semi phenomenological approach presented in Mackie and Baym [1977], later on referred to as Mackie & Baym. In this paper, authors provide a parametrized formula for the Gibbs energy in the compressible liquid drop model; note that shell effects are not taken into account. The nucleus is approximated by a spherical drop, at the center of a non-interacting spherical Wigner-Seitz cell. If atomic masses are available, we substitute the Mackie & Baym formula of the Gibbs energy by measurements provided in the AME2016 table [Wang et al., 2017]. In practice, at a given pressure, we evaluate the Gibbs energy of the following proton and nucleon number combinations

- (A_{cell}, A, Z) ,
- $(A_{\text{cell}}, A, Z - 1)$,
- $(A_{\text{cell}}, A - N_{\text{out}}, Z - 1)$,
- $(2A_{\text{cell}}, 2A, 2Z)$,
- $(2A_{\text{cell}}, 2A - N_{\text{out}}, 2Z)$.

The combination of A_{cell} , A and Z with the minimum Gibbs energy is selected. Evaluation of G_{cell} includes free neutrons outside the nucleus, which determines the neutron drip point at pressure P_{nd} , *i.e.*, the limit of between the outer crust and the inner crust. The composition of the ^{56}Fe ashes accreted crust calculated in the Mackie & Baym model, as well as the functional density Brussels-Skyrme 21 (BSk21) model discussed in Fantina et al. [2022], are presented in Fig. 4.1. The two models are different when they are not calibrated by the AME2016 table. The BSk21 model takes into account shell effects which stabilize the proton

number in the inner crust, as well as neutron skin effects. Pycnonuclear fusions are triggered when the proton number $Z < 8$ as is discussed in [Haensel and Zdunik \[2008\]](#), [Fantina et al. \[2018\]](#), which is in the inner crust for both models.

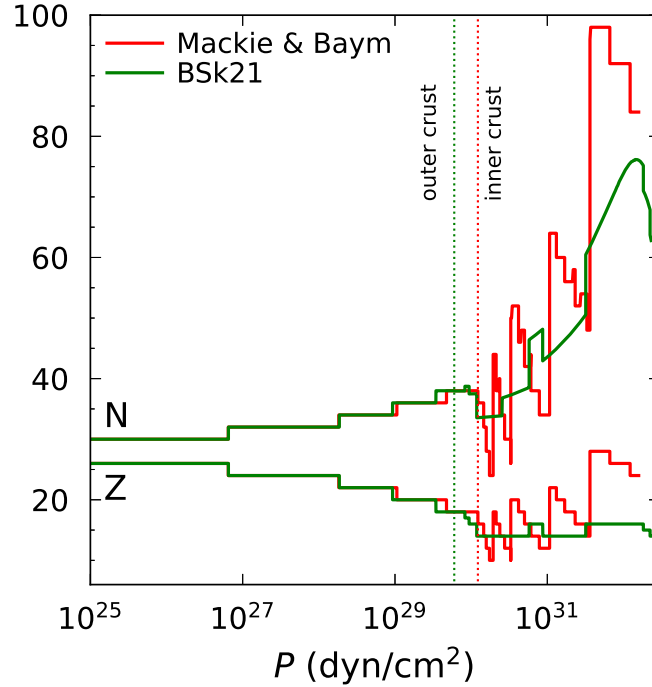


Figure 4.1: The proton number Z and neutron number N as a function of the pressure P in the ^{56}Fe ashes accreted crust calculated in the Mackie & Baym and BSk21 models. The neutron drip pressure P_{nd} is presented in vertical dotted lines.

The exothermic nature of the above mentioned reactions leads to the deposit of heat sources in the crust during active accretion. This phenomenon is referred to as deep crustal heating [[Brown et al., 1998](#)]. In that sense, a compressed crust is a reservoir of heat at local equilibrium. In [Fig. 4.2](#), we present the heat sources of the ^{56}Fe accreted crust calculated in the Mackie & Baym and BSk21 models. Depending on the model, the number of sources and the location of the heat sources can vary, but the total amount of heat deposited in the crust is roughly the same. One can note that heat sources in the Mackie & Baym model are smaller but more numerous than for the BSk21 model: the shell effects taken into account in BSk21 stabilizes nuclei in the crust for a large range of pressure, such that there are fewer reactions and they release more heat.

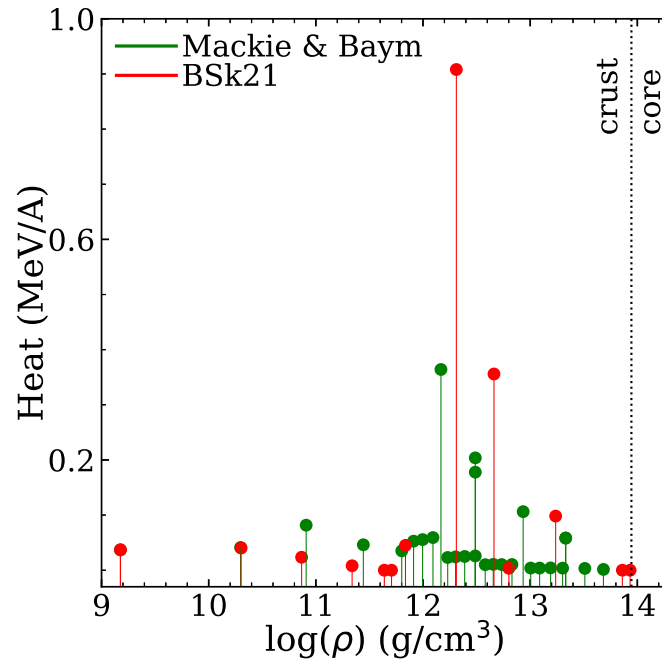


Figure 4.2: Heat sources per nucleon as a function of the mass density ρ in the ^{56}Fe ashes accreted crust calculated with the models of Mackie & Baym and BSk21.

Finally, let us mention a timescale important for accreted crusts. For a star in hydrostatic equilibrium, the pressure and gravity counterbalance one another. If an imbalance between the two occurs in a given region of the crust, the crust structure adjusts on a timescale called the dynamical timescale: it is the time required to cancel this imbalance, and reach a new hydrostatic equilibrium, *i.e.*, the time needed for a sound wave to cross the crust. This timescale is about 0.1 ms, thus completely negligible on our context.

4.2 Partially accreted crusts

Although the fully accreted crust approximation has proven partly successful for some soft quiescent X-ray transients, the X-ray emission of other sources indicate an accretion regime for which this approximation is not valid. In this section, we present the theoretical framework related to partially accreted crust, and then derive the equation of state and composition of the different parts of the crust. The catalogue of heat sources in the partially accreted crust is reconstructed, and interesting properties that appear in this crust are discussed.

4.2.1 Beyond the fully accreted crust approximation

In the fully accreted crust approximation, the crust is solely made of accreted material, while the original crust is considered to have been completely pushed into the core by pressure from the accreted material. Exothermic reactions are continuously triggered for as long as accretion is active, and the heat sources are located at fixed pressures. However, some sources suggest that this approximation cannot be applied [Brown and Cumming, 2009]. One of those sources is IGR J17480–2446 [Bonanno and Urpin, 2015], which has been observed before accretion, then during a two-month outburst in 2010, and two months after the accretion had stopped. It presents a low-frequency spin of 11 Hz [Degenaar, 2015], which suggests that the star’s rotation has not been recycled by accretion. If this source has only accreted a small amount of matter [Degenaar et al., 2015], the original crust has not been fully replaced, and the star would present a partially accreted crust. In this case, a hybrid crust made of the original crust as it is pushed toward the core, and of the accreted material pushing it, needs to be studied. The thermal evolution of 1RXS J180408–342058 has been observed during its 4.5-month outburst in 2015 prior to quiescence [Baglio et al., 2016, Marino et al., 2019]. In Parikh et al. [2017], it is suggested that the luminosity of this source can be explained by a hybrid crust.

The role of a hybrid crust in the thermal properties of accreting neutron stars was recently studied without a detailed description of the crust in Potekhin and Chabrier [2021]. In the following, we present the full derivation of the partially accreted crust in a simple nuclear model. The study is however restricted to the evolution of the original outer crust, considered catalyzed in its original state, under a uniform radial increase in pressure in spherical symmetry. From Eq. (4.1) and the Tolman-Oppenheimer-Volkoff equations in the crust ($P/\rho c^2 \ll 1$ and $PR^3/Mc^2 \ll 1$), we can deduce the compression, denoted ΔP , required to fulfill the fully accreted crust approximation: $\Delta P = \Delta P_{\text{fac}} = 10^{32}$ dyn/cm²; our calculations are established up to this value.

There are three different components of the partially accreted crust that must be evaluated within the same nuclear model:

- the catalyzed outer crust, which is the sole constituent of the partially accreted crust at $\Delta P = 0$,

- the accreted material which dominates the partially accreted crust at $\Delta P > \Delta P_{\text{fac}}$,
- the originally catalyzed compressed outer crust which should be followed under an increasing compression $0 < \Delta P < \Delta P_{\text{fac}}$.

First, we compute the catalyzed outer crust in the Mackie & Baym model. The Gibbs energy per cell is evaluated for a large set of nuclei at each pressure P , and the combination (A_{cell}, A, Z) presenting the minimum Gibbs energy is the ground state cell at this pressure. Contrary to the accreted crust, the catalyzed crust is at global equilibrium. The proton and neutron number as a function of the pressure in the star for the Mackie & Baym catalyzed outer crust are presented in Fig. 4.3. This outer crust is made of 24 shells², with a neutron drip line $P_{\text{nd}} \simeq 1.1 \times 10^{30}$ dyn/cm², and a last outer crust shell of ¹³²Zr. As a comparison, the catalyzed outer crust calculated in the BSk21 model consists of 18 shells, and a neutron drip line $P_{\text{nd}} \simeq 7.8 \times 10^{29}$ dyn/cm². The models of Mackie & Baym and BSk21 are similar up to $P \simeq 6 \times 10^{28}$ dyn/cm², with ⁸⁰Zn the last common nucleus; up to this pressure, compositions are calibrated to experimentally determined masses of nuclei from the AME2016 table. For the next shell, the Gibbs energy of the odd proton number element ⁷⁹Cu calculated in BSk21 is lower than the calibrated ⁸²Zn that was selected in Mackie & Baym; from then on to deeper shells, the compositions differ. One thin shell of ⁵⁸Fe appears for Mackie & Baym and BSk21 models: as discussed in Sect. 7.4.1 of Blaschke and Chamel [2018], this shell does not exist when a particular consideration for electron charge polarization is taken.

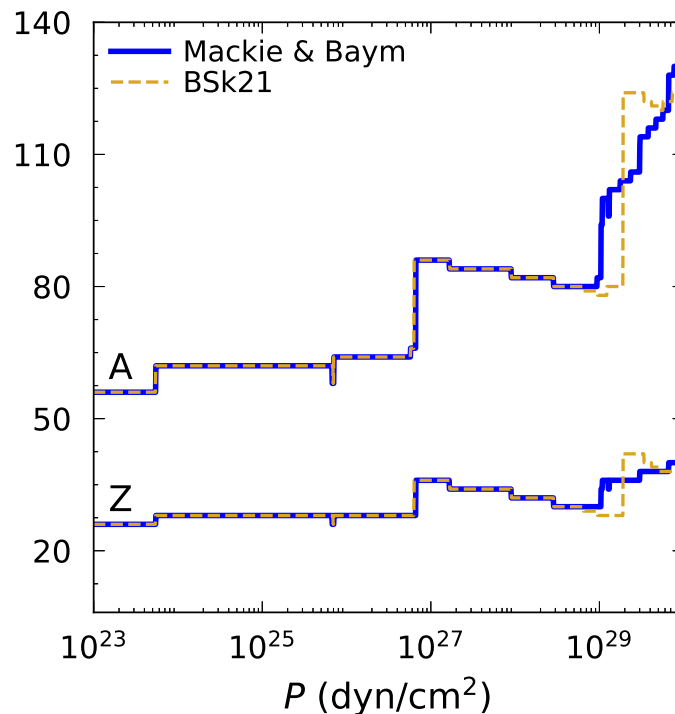


Figure 4.3: Catalyzed outer crust composition, with the nucleon number A and proton number Z , as a function of the pressure P in the crust, calculated in the Mackie & Baym and BSk21 nuclear models.

²We refer to shells as layers of the crust in which a nucleus is stable.

The mass and thickness of each shell of the catalyzed outer crust are presented for the Mackie & Baym and BSk21 models in Fig. 4.4. The thickness and the gravitational mass of the shells for a given stellar configuration (R, M) can be approximated with high accuracy from formulas established in Zdunik et al. [2016]

$$\Delta R = 73 \text{ m} \Delta\mu_{\text{MeV}} \frac{R_6^2}{M/M_\odot} \left(1 - 0.295 \frac{M/M_\odot}{R_6}\right), \quad (4.8)$$

$$\frac{\Delta M}{M_\odot} = 4.7 \times 10^{-5} \Delta P_{30} \frac{R_6^4}{M/M_\odot} \left(1 - 0.295 \frac{M/M_\odot}{R_6}\right), \quad (4.9)$$

where R_6 is the neutron star radius divided by 10^6 cm, $\Delta\mu_{\text{MeV}}$ and ΔP_{30} correspond to the thickness of the shell in baryon chemical potential and pressure respectively; those quantities are given in MeV and 10^{30} dyn/cm². In Fig. 4.4, the structure of the crust is established for a $1.4 M_\odot$ neutron star; the total radius of the star is calculated by constructing the equation of state with the Mackie & Baym crust associated to the SLy4 core on the one hand, and using the unified equation of state equation of state of BSk21 on the other hand. A $1.4 M_\odot$ neutron star calculated with the Mackie & Baym/SLy4 equations of state and the BSk21 equation of state corresponds to a total radius of the star of 11.7 km and 12.6 km respectively. The outer crust of the SLy4/Mackie & Baym model is thinner than that of the BSk21 model, 429 m and 494 m respectively.

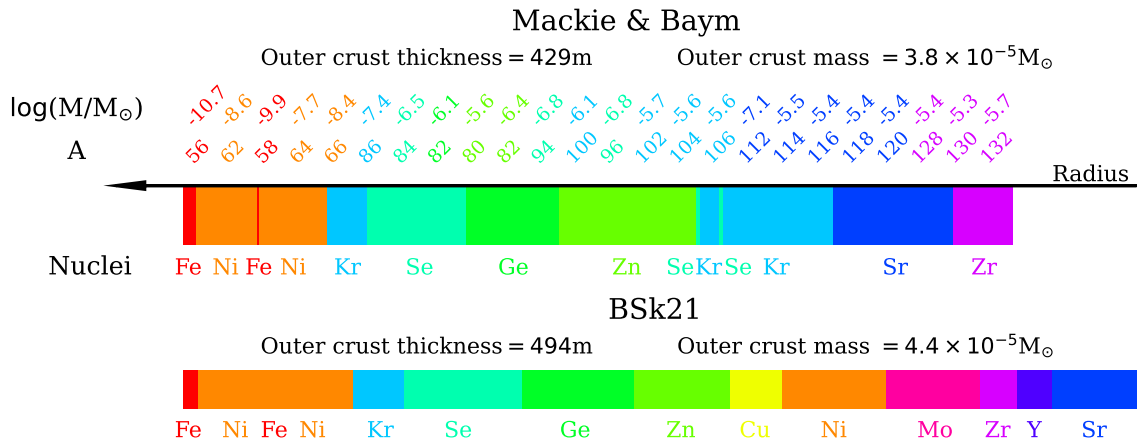


Figure 4.4: Structure of the Mackie & Baym catalyzed outer crust compared to that calculated in the BSk21 model, for a $1.4 M_\odot$ neutron star. Colors divide areas with different proton numbers. For Mackie & Baym, the nucleon number A is presented to give a complete definition of the shell (A_{cell}, A, Z), for which the decimal logarithm of the gravitational mass in solar mass is presented.

For the accreted material part of the partially accreted crust, we choose the Mackie & Baym ^{56}Fe ashes accreted crust presented in section 4.1.2. The accreted material part of the crust will progressively invade the partially accreted crust as the compression increases. It is made of 36 shells, including 5 in the outer crust, for a total thickness of 722 m and a mass of $3 \times 10^{-3} M_\odot$.

4.2.2 Heat sources in a compressed catalyzed crust

To describe the original outer crust under compression, each shell of the catalyzed outer crust must be evaluated under an increase of pressure ΔP : in that sense, we need to design 24 accreted material equations of state which ash nuclei correspond to the catalyzed shell nuclei. We denote $P_{\text{bot}}^{\text{cat}}$ and $P_{\text{top}}^{\text{cat}}$ the bottom (highest) and top (lowest) pressure boundaries of the catalyzed outer crust shells. For each shell of the catalyzed outer crust, the composition and equation of state must be evaluated from the pressure $P_{\text{bot}}^{\text{cat}}$ to $P_{\text{bot}}^{\text{cat}} + \Delta P_{\text{fac}}$. After a given compression ΔP , the above-mentioned shells have evolved to pressure boundaries $P_{\text{bot}}^{\text{cat}} + \Delta P$ and $P_{\text{top}}^{\text{cat}} + \Delta P$. In the following, each shell of the originally catalyzed outer crust will be subject to reactions such that it might host several nuclei, but in order to avoid confusion, shells shall refer to the delimitation of shells in the catalyzed outer crust.

The compression of each shell of the catalyzed outer crust leads to exothermic reactions and heat deposition, as is the case for the accreted material part of the crust. To compute the location and amount of heat release in the partially accreted crust, the simple model of Mackie & Baym is used once again. A piece of matter located at a pressure P_{ori} in the original crust is pushed to a pressure threshold P_{th} at which a specific reaction takes place within a timescale denoted τ_{acc}

$$\tau_{\text{acc}} = 4.8 \times 10^5 \frac{\alpha_*}{\langle \dot{M} \rangle_{-10}} (P_{\text{th},30} - P_{\text{ori},30}) \text{ yr} , \quad (4.10)$$

where P_{30} is the pressure in 10^{30} dyn/cm². The factor α_* depends on the neutron star mass and radius and is given by the formula

$$\alpha_* = \frac{R_6^4}{M/M_\odot} \sqrt{1 - 0.295 \frac{M/M_\odot}{R_6}} , \quad (4.11)$$

such that for a $1.4 M_\odot$ neutron star

$$\frac{4\pi R^4}{GMm_0} \sqrt{1 - \frac{2GM}{Rc^2}} = 9.06 \times 10^{16} \alpha_* \frac{\text{cm}^3}{\text{MeV}} . \quad (4.12)$$

In Table 4.1, we present the reactions and associated heat release in the 24 shells of the originally catalyzed compressed outer crust up to the first neutron emission, as a function of the compression ΔP and relative compression $\delta P/P$.

Table 4.1: Reactions triggered in the originally catalyzed compressed outer crust calculated in the Mackie & Baym model up to the first neutron emission. Nuclei based on experimentally determined masses from AME2016 are presented in bold. The neutron-drip points calculated in the continuous approach are presented in blue, for details see section 4.2.3. In order of columns, we give the pressure P , the mass density ρ_{ini} right before the reaction, $\lambda = \Delta\rho/\rho$ the relative change in density due to the reaction, the reaction concerned, the energy per nucleon Q of the reaction, the compression ΔP , and relative compression $\delta P/P$ at which the reaction is triggered. The table is separated into 24 parts, one for each shell of the catalyzed crust: the first line (before the dashed lines) includes the top pressure and density of the original shell (first and second column) as well as the nuclei of the catalyzed shell.

P (dyn/cm ²)	ρ_{ini} (g/cm ³)	λ	Reaction	Q (keV)	ΔP (dyn/cm ²)	$\delta P/P$ (in %)
1.442×10^{22}	7.753×10^5	-	⁵⁶Fe			Shell 1
6.468×10^{26}	1.374×10^9	8.2	⁵⁶Fe + 2e ⁻ → ⁵⁶Cr + 2ν _e	37.0	6.463×10^{26}	1.2×10^5
1.829×10^{28}	1.811×10^{10}	8.9	⁵⁶Cr + 2e ⁻ → ⁵⁶Ti + 2ν _e	41.2	1.829×10^{28}	3.4×10^6
1.059×10^{29}	7.365×10^{10}	9.8	⁵⁶Ti + 2e ⁻ → ⁵⁶Ca + 2ν _e	81.7	1.059×10^{29}	2.0×10^7
4.747×10^{29}	2.496×10^{11}	10.9	⁵⁶Ca + 2e ⁻ → ⁵⁶Ar + 2ν _e	46.1	4.747×10^{29}	8.8×10^7
1.064×10^{30}	5.078×10^{11}	4.3	⁵⁶Ar + 2e ⁻ → ⁵²S + 4n + 2ν _e	41.9	1.064×10^{30}	2.0×10^8
1.226×10^{30}	5.649×10^{11}	12.1	⁵⁶Ar + 2e ⁻ → ⁵²S + 4n + 2ν _e	35.1	1.226×10^{30}	2.3×10^8
5.441×10^{23}	8.489×10^6	-	⁶²Ni			Shell 2
2.468×10^{27}	3.846×10^9	7.5	⁶²Ni + 2e ⁻ → ⁶²Fe + 2ν _e	44.9	2.401×10^{27}	3.6×10^3
2.987×10^{28}	2.679×10^{10}	8.2	⁶²Fe + 2e ⁻ → ⁶²Cr + 2ν _e	44.2	2.981×10^{28}	4.4×10^4
4.283×10^{28}	3.796×10^{10}	4.3	⁶²Cr + 1e ⁻ → ⁶²V + 1ν _e	0.0	4.276×10^{28}	6.4×10^4
6.314×10^{28}	5.297×10^{10}	4.5	⁶²V + 1e ⁻ → ⁶²Ti + 1ν _e	0.0	6.308×10^{28}	9.4×10^4
4.735×10^{29}	2.511×10^{11}	9.8	⁶²Ti + 2e ⁻ → ⁶²Ca + 2ν _e	41.3	4.734×10^{29}	7.1×10^5
1.014×10^{30}	4.889×10^{11}	3.8	⁶²Ca + 2e ⁻ → ⁵⁸Ar + 4n + 2ν _e	32.2	1.014×10^{30}	1.5×10^6
1.170×10^{30}	5.444×10^{11}	10.9	⁶²Ca + 2e ⁻ → ⁶⁰Ar + 2n + 2ν _e	29.5	1.170×10^{30}	1.7×10^6
6.723×10^{25}	2.654×10^8	-	⁵⁸Fe			Shell 3
4.641×10^{27}	6.207×10^9	8.2	⁵⁸Fe + 2e ⁻ → ⁵⁸Cr + 2ν _e	43.1	4.571×10^{27}	6.5×10^3
4.552×10^{28}	3.718×10^{10}	8.9	⁵⁸Cr + 2e ⁻ → ⁵⁸Ti + 2ν _e	110.6	4.545×10^{28}	6.5×10^4
2.003×10^{29}	1.231×10^{11}	9.8	⁵⁸Ti + 2e ⁻ → ⁵⁸Ca + 2ν _e	45.0	2.003×10^{29}	2.8×10^5
6.598×10^{29}	3.311×10^{11}	7.1	⁵⁸Ca + 2e ⁻ → ⁵⁶Ar + 2n + 2ν _e	35.4	6.597×10^{29}	9.4×10^5
6.892×10^{29}	3.421×10^{11}	10.9	⁵⁸Ca + 2e ⁻ → ⁵⁸Ar + 2ν _e	44.3	6.891×10^{29}	9.8×10^5
1.507×10^{30}	6.830×10^{11}	26.4	⁵⁸Ar + 4e ⁻ → ⁴⁶Si + 12n + 4ν _e	108.6	1.507×10^{30}	2.1×10^6
7.053×10^{25}	2.821×10^8	-	⁶⁴Ni			Shell 4
8.042×10^{27}	9.615×10^9	7.5	⁶⁴Ni + 2e ⁻ → ⁶⁴Fe + 2ν _e	39.0	7.471×10^{27}	1.3×10^3
5.228×10^{28}	4.208×10^{10}	8.2	⁶⁴Fe + 2e ⁻ → ⁶⁴Cr + 2ν _e	38.9	5.171×10^{28}	9.1×10^3
7.795×10^{28}	6.143×10^{10}	4.3	⁶⁴Cr + 1e ⁻ → ⁶⁴V + 1ν _e	0.0	7.738×10^{28}	1.4×10^4
1.143×10^{29}	8.538×10^{10}	4.5	⁶⁴V + 1e ⁻ → ⁶⁴Ti + 1ν _e	0.0	1.138×10^{29}	2.0×10^4
6.487×10^{29}	3.284×10^{11}	6.4	⁶⁴Ti + 2e ⁻ → ⁶²Ca + 2n + 2ν _e	20.8	6.481×10^{29}	1.1×10^5
6.674×10^{29}	3.355×10^{11}	9.8	⁶⁴Ti + 2e ⁻ → ⁶⁴Ca + 2ν _e	39.8	6.669×10^{29}	1.2×10^5
1.418×10^{30}	6.493×10^{11}	10.7	⁶⁴Ca + 2e ⁻ → ⁶⁰Ar + 4n + 2ν _e	42.4	1.418×10^{30}	2.5×10^5
5.725×10^{26}	1.375×10^9	-	⁶⁶Ni			Shell 5
2.261×10^{28}	2.152×10^{10}	7.5	⁶⁶Ni + 2e ⁻ → ⁶⁶Fe + 2ν _e	49.6	2.195×10^{28}	3.3×10^3
7.860×10^{28}	5.893×10^{10}	8.2	⁶⁶Fe + 2e ⁻ → ⁶⁶Cr + 2ν _e	79.1	7.794×10^{28}	1.2×10^4
3.254×10^{29}	1.852×10^{11}	8.9	⁶⁶Cr + 2e ⁻ → ⁶⁶Ti + 2ν _e	38.6	3.247×10^{29}	4.9×10^4
7.992×10^{29}	3.962×10^{11}	6.5	⁶⁶Ti + 2e ⁻ → ⁶⁴Ca + 2n + 2ν _e	16.6	7.986×10^{29}	1.2×10^5

9.018×10^{29}	4.338×10^{11}	9.8	${}^{66}\text{Ti} + 2e^- \rightarrow {}^{66}\text{Ca} + 2\nu_e$	38.4	9.011×10^{29}	1.4×10^5
1.556×10^{30}	7.179×10^{11}	23.2	${}^{66}\text{Ca} + 4e^- \rightarrow {}^{54}\text{S} + 12\text{n} + 4\nu_e$	102.4	1.556×10^{30}	2.4×10^5
6.610×10^{26}	1.561×10^9	-	${}^{86}\text{Kr}$		Shell 6	
P (dyn/cm ²)	ρ_{ini} (g/cm ³)	λ	Reaction	Q (keV)	ΔP (dyn/cm ²)	$\delta P/P$ (in %)
9.884×10^{27}	1.180×10^{10}	5.7	${}^{86}\text{Kr} + 2e^- \rightarrow {}^{86}\text{Se} + 2\nu_e$	29.2	8.236×10^{27}	499
4.723×10^{28}	4.031×10^{10}	6.1	${}^{86}\text{Se} + 2e^- \rightarrow {}^{86}\text{Ge} + 2\nu_e$	23.2	4.558×10^{28}	2.8×10^3
1.333×10^{29}	9.319×10^{10}	6.5	${}^{86}\text{Ge} + 2e^- \rightarrow {}^{86}\text{Zn} + 2\nu_e$	18.8	1.317×10^{29}	8.0×10^3
4.385×10^{29}	2.427×10^{11}	7.0	${}^{86}\text{Zn} + 2e^- \rightarrow {}^{86}\text{Ni} + 2\nu_e$	28.3	4.369×10^{29}	2.7×10^4
8.422×10^{29}	4.239×10^{11}	5.0	${}^{86}\text{Ni} + 2e^- \rightarrow {}^{84}\text{Fe} + 2\text{n} + 2\nu_e$	14.7	8.406×10^{29}	5.1×10^4
9.668×10^{29}	4.702×10^{11}	7.5	${}^{86}\text{Ni} + 2e^- \rightarrow {}^{86}\text{Fe} + 2\nu_e$	28.3	9.652×10^{29}	5.9×10^4
1.478×10^{30}	6.956×10^{11}	27.1	${}^{86}\text{Fe} + 6e^- \rightarrow {}^{66}\text{Ca} + 20\text{n} + 6\nu_e$	104.7	1.476×10^{30}	9.0×10^4
1.653×10^{27}	3.195×10^9	-	${}^{84}\text{Se}$		Shell 7	
P (dyn/cm ²)	ρ_{ini} (g/cm ³)	λ	Reaction	Q (keV)	ΔP (dyn/cm ²)	$\delta P/P$ (in %)
2.827×10^{28}	2.679×10^{10}	6.1	${}^{84}\text{Se} + 2e^- \rightarrow {}^{84}\text{Ge} + 2\nu_e$	28.6	1.934×10^{28}	216
1.189×10^{29}	8.353×10^{10}	6.5	${}^{84}\text{Ge} + 2e^- \rightarrow {}^{84}\text{Zn} + 2\nu_e$	33.1	1.100×10^{29}	1.2×10^3
3.255×10^{29}	1.895×10^{11}	7.0	${}^{84}\text{Zn} + 2e^- \rightarrow {}^{84}\text{Ni} + 2\nu_e$	29.2	3.166×10^{29}	3.5×10^3
7.167×10^{29}	3.668×10^{11}	5.0	${}^{84}\text{Ni} + 2e^- \rightarrow {}^{82}\text{Fe} + 2\text{n} + 2\nu_e$	18.9	7.078×10^{29}	7.9×10^3
7.690×10^{29}	3.867×10^{11}	7.5	${}^{84}\text{Ni} + 2e^- \rightarrow {}^{84}\text{Fe} + 2\nu_e$	29.1	7.601×10^{29}	8.5×10^3
1.398×10^{30}	6.514×10^{11}	17.0	${}^{84}\text{Fe} + 4e^- \rightarrow {}^{72}\text{Ti} + 12\text{n} + 4\nu_e$	64.8	1.389×10^{30}	1.6×10^4
8.954×10^{27}	1.172×10^{10}	-	${}^{82}\text{Ge}$		Shell 8	
P (dyn/cm ²)	ρ_{ini} (g/cm ³)	λ	Reaction	Q (keV)	ΔP (dyn/cm ²)	$\delta P/P$ (in %)
6.325×10^{28}	5.077×10^{10}	6.5	${}^{82}\text{Ge} + 2e^- \rightarrow {}^{82}\text{Zn} + 2\nu_e$	23.0	3.488×10^{28}	122
2.991×10^{29}	1.736×10^{11}	7.0	${}^{82}\text{Zn} + 2e^- \rightarrow {}^{82}\text{Ni} + 2\nu_e$	44.3	2.708×10^{29}	954
5.970×10^{29}	3.121×10^{11}	7.5	${}^{82}\text{Ni} + 2e^- \rightarrow {}^{82}\text{Fe} + 2\nu_e$	29.9	5.686×10^{29}	2.0×10^3
1.032×10^{30}	5.065×10^{11}	2.9	${}^{82}\text{Fe} + 2e^- \rightarrow {}^{78}\text{Cr} + 4\text{n} + 2\nu_e$	25.4	1.004×10^{30}	3.5×10^3
1.201×10^{30}	5.676×10^{11}	8.0	${}^{82}\text{Fe} + 2e^- \rightarrow {}^{78}\text{Cr} + 4\text{n} + 2\nu_e$	22.1	1.173×10^{30}	4.1×10^3
2.846×10^{28}	2.897×10^{10}	-	${}^{80}\text{Zn}$		Shell 9	
P (dyn/cm ²)	ρ_{ini} (g/cm ³)	λ	Reaction	Q (keV)	ΔP (dyn/cm ²)	$\delta P/P$ (in %)
2.529×10^{29}	1.493×10^{11}	7.0	${}^{80}\text{Zn} + 2e^- \rightarrow {}^{80}\text{Ni} + 2\nu_e$	56.3	1.597×10^{29}	171
4.503×10^{29}	2.464×10^{11}	7.5	${}^{80}\text{Ni} + 2e^- \rightarrow {}^{80}\text{Fe} + 2\nu_e$	30.8	3.571×10^{29}	383
8.818×10^{29}	4.389×10^{11}	5.5	${}^{80}\text{Fe} + 2e^- \rightarrow {}^{78}\text{Cr} + 2\text{n} + 2\nu_e$	16.1	7.886×10^{29}	846
1.022×10^{30}	4.902×10^{11}	8.2	${}^{80}\text{Fe} + 2e^- \rightarrow {}^{80}\text{Cr} + 2\nu_e$	29.5	9.284×10^{29}	996
1.500×10^{30}	7.076×10^{11}	18.4	${}^{80}\text{Cr} + 4e^- \rightarrow {}^{66}\text{Ca} + 14\text{n} + 4\nu_e$	80.9	1.407×10^{30}	1.5×10^3
9.346×10^{28}	7.248×10^{10}	-	${}^{82}\text{Zn}$		Shell 10	
P (dyn/cm ²)	ρ_{ini} (g/cm ³)	λ	Reaction	Q (keV)	ΔP (dyn/cm ²)	$\delta P/P$ (in %)
2.991×10^{29}	1.736×10^{11}	7.0	${}^{82}\text{Zn} + 2e^- \rightarrow {}^{82}\text{Ni} + 2\nu_e$	44.3	1.954×10^{29}	188
5.970×10^{29}	3.121×10^{11}	7.5	${}^{82}\text{Ni} + 2e^- \rightarrow {}^{82}\text{Fe} + 2\nu_e$	29.9	4.932×10^{29}	475
1.032×10^{30}	5.065×10^{11}	2.9	${}^{82}\text{Fe} + 2e^- \rightarrow {}^{78}\text{Cr} + 4\text{n} + 2\nu_e$	25.4	9.287×10^{29}	894
1.201×10^{30}	5.676×10^{11}	8.0	${}^{82}\text{Fe} + 2e^- \rightarrow {}^{78}\text{Cr} + 4\text{n} + 2\nu_e$	22.1	1.098×10^{30}	1.1×10^3
1.041×10^{29}	7.973×10^{10}	-	${}^{94}\text{Se}$		Shell 11	
P (dyn/cm ²)	ρ_{ini} (g/cm ³)	λ	Reaction	Q (keV)	ΔP (dyn/cm ²)	$\delta P/P$ (in %)
2.337×10^{29}	1.463×10^{11}	6.1	${}^{94}\text{Se} + 2e^- \rightarrow {}^{94}\text{Ge} + 2\nu_e$	25.5	1.261×10^{29}	117
5.492×10^{29}	2.949×10^{11}	6.5	${}^{94}\text{Ge} + 2e^- \rightarrow {}^{94}\text{Zn} + 2\nu_e$	25.4	4.416×10^{29}	410
9.293×10^{29}	4.663×10^{11}	2.4	${}^{94}\text{Zn} + 2e^- \rightarrow {}^{90}\text{Ni} + 4\text{n} + 2\nu_e$	16.8	8.217×10^{29}	763
1.084×10^{30}	5.234×10^{11}	7.0	${}^{94}\text{Zn} + 2e^- \rightarrow {}^{94}\text{Ni} + 2\nu_e$	22.1	9.760×10^{29}	907
1.372×10^{30}	6.684×10^{11}	15.4	${}^{94}\text{Ni} + 4e^- \rightarrow {}^{80}\text{Cr} + 14\text{n} + 4\nu_e$	54.7	1.264×10^{30}	1.2×10^3
1.079×10^{29}	8.242×10^{10}	-	${}^{100}\text{Kr}$		Shell 12	
P (dyn/cm ²)	ρ_{ini} (g/cm ³)	λ	Reaction	Q (keV)	ΔP (dyn/cm ²)	$\delta P/P$ (in %)
2.316×10^{29}	1.462×10^{11}	5.7	${}^{100}\text{Kr} + 2e^- \rightarrow {}^{100}\text{Se} + 2\nu_e$	23.7	1.051×10^{29}	83
5.256×10^{29}	2.861×10^{11}	6.1	${}^{100}\text{Se} + 2e^- \rightarrow {}^{100}\text{Ge} + 2\nu_e$	23.6	3.992×10^{29}	315
8.827×10^{29}	4.481×10^{11}	2.3	${}^{100}\text{Ge} + 2e^- \rightarrow {}^{96}\text{Zn} + 4\text{n} + 2\nu_e$	13.6	7.562×10^{29}	597

1.030×10^{30}	5.034×10^{11}	6.5	$^{100}\text{Ge} + 2e^- \rightarrow ^{100}\text{Zn} + 2\nu_e$	22.7	9.039×10^{29}	714
1.382×10^{30}	6.683×10^{11}	14.3	$^{100}\text{Zn} + 4e^- \rightarrow ^{86}\text{Fe} + 14n + 4\nu_e$	57.7	1.255×10^{30}	992
1.269×10^{29}	9.446×10^{10}	-	^{96}Se		Shell 13	
P (dyn/cm ²)	ρ_{ini} (g/cm ³)	λ	Reaction	Q (keV)	ΔP (dyn/cm ²)	$\delta P/P$ (in %)
3.149×10^{29}	1.869×10^{11}	6.1	$^{96}\text{Se} + 2e^- \rightarrow ^{96}\text{Ge} + 2\nu_e$	24.8	1.845×10^{29}	141
6.630×10^{29}	3.470×10^{11}	4.3	$^{96}\text{Ge} + 2e^- \rightarrow ^{94}\text{Zn} + 2n + 2\nu_e$	19.5	5.327×10^{29}	408
6.921×10^{29}	3.584×10^{11}	6.5	$^{96}\text{Ge} + 2e^- \rightarrow ^{96}\text{Zn} + 2\nu_e$	24.8	5.618×10^{29}	431
1.246×10^{30}	5.935×10^{11}	6.9	$^{96}\text{Zn} + 2e^- \rightarrow ^{92}\text{Ni} + 4n + 2\nu_e$	22.0	1.115×10^{30}	855
1.307×10^{29}	9.709×10^{10}	-	^{102}Kr		Shell 14	
P (dyn/cm ²)	ρ_{ini} (g/cm ³)	λ	Reaction	Q (keV)	ΔP (dyn/cm ²)	$\delta P/P$ (in %)
3.076×10^{29}	1.846×10^{11}	5.7	$^{102}\text{Kr} + 2e^- \rightarrow ^{102}\text{Se} + 2\nu_e$	23.1	1.322×10^{29}	75
6.369×10^{29}	3.372×10^{11}	4.0	$^{102}\text{Se} + 2e^- \rightarrow ^{100}\text{Ge} + 2n + 2\nu_e$	19.6	4.616×10^{29}	263
6.566×10^{29}	3.449×10^{11}	6.1	$^{102}\text{Se} + 2e^- \rightarrow ^{102}\text{Ge} + 2\nu_e$	23.0	4.813×10^{29}	274
1.178×10^{30}	5.679×10^{11}	6.4	$^{102}\text{Ge} + 2e^- \rightarrow ^{98}\text{Zn} + 4n + 2\nu_e$	18.5	1.003×10^{30}	572
1.759×10^{29}	1.237×10^{11}	-	^{104}Kr		Shell 15	
P (dyn/cm ²)	ρ_{ini} (g/cm ³)	λ	Reaction	Q (keV)	ΔP (dyn/cm ²)	$\delta P/P$ (in %)
3.976×10^{29}	2.282×10^{11}	5.7	$^{104}\text{Kr} + 2e^- \rightarrow ^{104}\text{Se} + 2\nu_e$	22.5	1.646×10^{29}	70
7.340×10^{29}	3.824×10^{11}	4.1	$^{104}\text{Se} + 2e^- \rightarrow ^{102}\text{Ge} + 2n + 2\nu_e$	11.8	5.009×10^{29}	214
8.051×10^{29}	4.099×10^{11}	6.1	$^{104}\text{Se} + 2e^- \rightarrow ^{104}\text{Ge} + 2\nu_e$	22.5	5.720×10^{29}	245
1.338×10^{30}	6.369×10^{11}	21.3	$^{104}\text{Ge} + 6e^- \rightarrow ^{86}\text{Fe} + 18n + 6\nu_e$	75.9	1.105×10^{30}	473
2.337×10^{29}	1.561×10^{11}	-	^{106}Kr		Shell 16	
P (dyn/cm ²)	ρ_{ini} (g/cm ³)	λ	Reaction	Q (keV)	ΔP (dyn/cm ²)	$\delta P/P$ (in %)
5.025×10^{29}	2.774×10^{11}	5.7	$^{106}\text{Kr} + 2e^- \rightarrow ^{106}\text{Se} + 2\nu_e$	22.0	2.037×10^{29}	68
8.389×10^{29}	4.309×10^{11}	4.1	$^{106}\text{Se} + 2e^- \rightarrow ^{104}\text{Ge} + 2n + 2\nu_e$	11.2	5.401×10^{29}	180
9.713×10^{29}	4.811×10^{11}	6.1	$^{106}\text{Se} + 2e^- \rightarrow ^{106}\text{Ge} + 2\nu_e$	22.0	6.724×10^{29}	225
1.385×10^{30}	6.665×10^{11}	21.1	$^{106}\text{Ge} + 6e^- \rightarrow ^{86}\text{Fe} + 20n + 6\nu_e$	83.6	1.086×10^{30}	363
2.997×10^{29}	1.886×10^{11}	-	^{112}Sr		Shell 17	
P (dyn/cm ²)	ρ_{ini} (g/cm ³)	λ	Reaction	Q (keV)	ΔP (dyn/cm ²)	$\delta P/P$ (in %)
4.799×10^{29}	2.686×10^{11}	5.4	$^{112}\text{Sr} + 2e^- \rightarrow ^{112}\text{Kr} + 2\nu_e$	20.5	1.784×10^{29}	59
7.977×10^{29}	4.147×10^{11}	3.8	$^{112}\text{Kr} + 2e^- \rightarrow ^{110}\text{Se} + 2n + 2\nu_e$	10.4	4.962×10^{29}	164
9.103×10^{29}	4.579×10^{11}	5.7	$^{112}\text{Kr} + 2e^- \rightarrow ^{112}\text{Ge} + 2\nu_e$	20.6	6.087×10^{29}	201
1.344×10^{30}	6.490×10^{11}	19.6	$^{112}\text{Se} + 6e^- \rightarrow ^{92}\text{Ni} + 20n + 6\nu_e$	76.6	1.043×10^{30}	345
3.024×10^{29}	1.933×10^{11}	-	^{114}Sr		Shell 18	
P (dyn/cm ²)	ρ_{ini} (g/cm ³)	λ	Reaction	Q (keV)	ΔP (dyn/cm ²)	$\delta P/P$ (in %)
5.865×10^{29}	3.178×10^{11}	3.6	$^{114}\text{Sr} + 2e^- \rightarrow ^{112}\text{Kr} + 2n + 2\nu_e$	19.4	2.091×10^{29}	55
5.906×10^{29}	3.195×10^{11}	5.4	$^{114}\text{Sr} + 2e^- \rightarrow ^{114}\text{Kr} + 2\nu_e$	20.1	2.131×10^{29}	56
1.058×10^{30}	5.218×10^{11}	5.7	$^{114}\text{Kr} + 2e^- \rightarrow ^{114}\text{Se} + 2\nu_e$	18.0	6.806×10^{29}	180
1.270×10^{30}	6.330×10^{11}	12.3	$^{114}\text{Se} + 4e^- \rightarrow ^{98}\text{Zn} + 16n + 4\nu_e$	42.2	8.928×10^{29}	236
3.786×10^{29}	2.328×10^{11}	-	^{116}Sr		Shell 19	
P (dyn/cm ²)	ρ_{ini} (g/cm ³)	λ	Reaction	Q (keV)	ΔP (dyn/cm ²)	$\delta P/P$ (in %)
6.694×10^{29}	3.572×10^{11}	3.6	$^{116}\text{Sr} + 2e^- \rightarrow ^{114}\text{Kr} + 2n + 2\nu_e$	13.0	2.039×10^{29}	43
7.152×10^{29}	3.753×10^{11}	5.4	$^{116}\text{Sr} + 2e^- \rightarrow ^{116}\text{Kr} + 2\nu_e$	19.7	2.496×10^{29}	53
1.192×10^{30}	5.807×10^{11}	11.9	$^{116}\text{Kr} + 4e^- \rightarrow ^{106}\text{Ge} + 10n + 4\nu_e$	35.9	7.265×10^{29}	156
4.669×10^{29}	2.772×10^{11}	-	^{118}Sr		Shell 20	
P (dyn/cm ²)	ρ_{ini} (g/cm ³)	λ	Reaction	Q (keV)	ΔP (dyn/cm ²)	$\delta P/P$ (in %)
7.587×10^{29}	3.992×10^{11}	3.6	$^{118}\text{Sr} + 2e^- \rightarrow ^{116}\text{Kr} + 2n + 2\nu_e$	9.7	1.948×10^{29}	34
8.540×10^{29}	4.362×10^{11}	5.4	$^{118}\text{Sr} + 2e^- \rightarrow ^{118}\text{Kr} + 2\nu_e$	19.3	2.901×10^{29}	51
1.305×10^{30}	6.322×10^{11}	18.5	$^{118}\text{Kr} + 6e^- \rightarrow ^{100}\text{Zn} + 18n + 6\nu_e$	70.9	7.407×10^{29}	131
5.656×10^{29}	3.256×10^{11}	-	^{120}Sr		Shell 21	
P (dyn/cm ²)	ρ_{ini} (g/cm ³)	λ	Reaction	Q (keV)	ΔP (dyn/cm ²)	$\delta P/P$ (in %)
8.543×10^{29}	4.438×10^{11}	1.9	$^{120}\text{Sr} + 2e^- \rightarrow ^{116}\text{Kr} + 4n + 2\nu_e$	12.1	1.953×10^{29}	29

1.004×10^{30}	5.009×10^{11}	5.4	$^{120}\text{Sr} + 2e^- \rightarrow ^{120}\text{Kr} + 2\nu_e$	18.5	3.448×10^{29}	52
1.272×10^{30}	6.310×10^{11}	18.4	$^{120}\text{Kr} + 6e^- \rightarrow ^{100}\text{Zn} + 20n + 6\nu_e$	61.2	6.134×10^{29}	93
6.609×10^{29}	3.714×10^{11}	-	^{128}Zr	Shell 22		
P (dyn/cm ²)	ρ_{ini} (g/cm ³)	λ	Reaction	Q (keV)	ΔP (dyn/cm ²)	$\delta P/P$ (in %)
8.955×10^{29}	4.666×10^{11}	0.2	$^{128}\text{Zr} + 2e^- \rightarrow ^{122}\text{Sr} + 6n + 2\nu_e$	14.7	1.324×10^{29}	17
1.067×10^{30}	5.321×10^{11}	5.1	$^{128}\text{Zr} + 2e^- \rightarrow ^{128}\text{Sr} + 2\nu_e$	14.8	3.036×10^{29}	39
1.150×10^{30}	5.919×10^{11}	5.2	$^{128}\text{Sr} + 2e^- \rightarrow ^{118}\text{Kr} + 10n + 2\nu_e$	16.5	3.871×10^{29}	50
7.654×10^{29}	4.212×10^{11}	-	^{130}Zr	Shell 23		
P (dyn/cm ²)	ρ_{ini} (g/cm ³)	λ	Reaction	Q (keV)	ΔP (dyn/cm ²)	$\delta P/P$ (in %)
8.969×10^{29}	4.744×10^{11}	-1.4	$^{130}\text{Zr} + 2e^- \rightarrow ^{122}\text{Sr} + 8n + 2\nu_e$	14.6	9.688×10^{27}	1.092
1.188×10^{30}	5.860×10^{11}	16.4	$^{130}\text{Zr} + 6e^- \rightarrow ^{112}\text{Se} + 18n + 6\nu_e$	54.0	3.009×10^{29}	33
8.895×10^{29}	4.787×10^{11}	-	^{132}Zr	Shell 24		
P (dyn/cm ²)	ρ_{ini} (g/cm ³)	λ	Reaction	Q (keV)	ΔP (dyn/cm ²)	$\delta P/P$ (in %)
1.248×10^{30}	6.174×10^{11}	16.2	$^{132}\text{Zr} + 6e^- \rightarrow ^{112}\text{Se} + 20n + 6\nu_e$	64.4	3.047×10^{29}	32

The nuclei found in the originally catalyzed compressed outer crust are presented in Fig. 4.5, with those of the accreted material part of the crust, and those of the catalyzed outer crust. There are around 170 nuclei appearing in the originally catalyzed compressed outer crust; they overlap with the catalyzed nuclei at the compression $\Delta P = 0$, and also with the accreted material nuclei when the stage of compression reaches the fully accreted crust approximation.

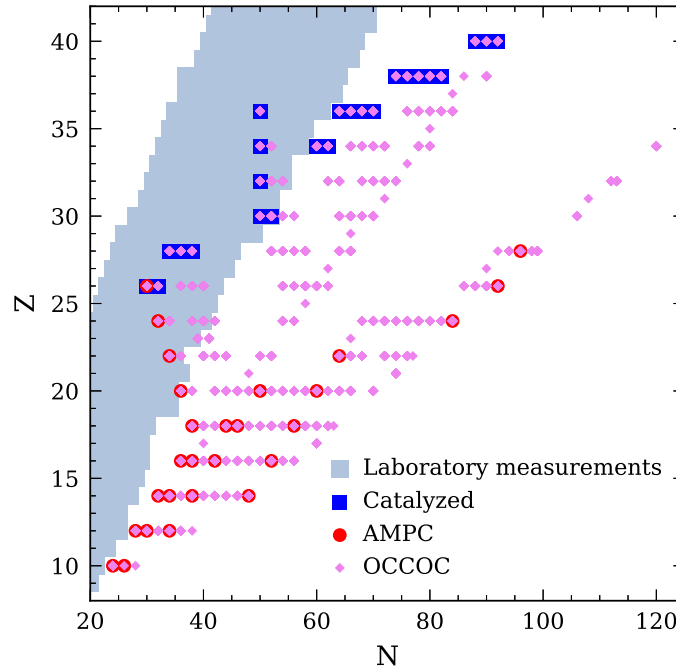


Figure 4.5: Abundance of nuclei in the partially accreted crust calculated in the Mackie & Baym model, compared to laboratory measurements from the AME2016 table. (N, Z) for the catalyzed outer crust are shown in blue, (N, Z) for the accreted material part of the crust (AMPC) are shown in red, and (N, Z) for the originally catalyzed compressed outer crust (OCCOC) are shown in violet.

The exothermic reactions leading to nuclei presented in Fig. 4.5 deposit heat in the originally catalyzed compressed outer crust. The first electron capture occurs for an increase in pressure $\Delta P \simeq 7.5 \times 10^{27}$ dyn/cm²; the largest energy release per nucleon due to electron capture is of about 110 keV per nucleon and occurs at $\Delta P \simeq 4.6 \times 10^{28}$ dyn/cm². Pycnonuclear fusions are far more rare than electron captures, with a maximum energy release of about 340 keV per nucleon for an increase in pressure $\Delta P \simeq 1.9 \times 10^{30}$ dyn/cm²; this is also the first pycnonuclear reaction and occurs in the first shell of the originally catalyzed compressed outer crust for the parent nuclei ($A_{\text{cell}} = 56, Z = 10, N = 24$).

The details of the exothermic reactions in the originally catalyzed compressed outer crust up to the neutron drip point are presented in Table 4.1. Let us give a description of what occurs for the shallowest shell of the catalyzed outer crust. Originally, that is when no compression is applied, this shell is made of ⁵⁶Fe and is 5.27×10^{23} dyn/cm² thick in pressure. Then, we apply compression until the neutron drip is reached: six pairs of electron captures occur in this shell until it reaches a pressure $P_{\text{nd}} = 1.226 \times 10^{30}$ dyn/cm² (in the single nucleus model approach), at which a total of ~ 241 keV per nucleon has been released. The compression applied to the original crust required to release this energy is $\Delta P = 1.226 \times 10^{36}$ dyn/cm². Let us note that no pycnonuclear fusions appear in Table 4.1, because all of them occur above the neutron drip point.

The maximum heat release per nucleon, denoted Q_{max} , in each of the 24 shells during the compression of the originally catalyzed outer crust is presented in Fig. 4.6. Generally, Q_{max} decreases when considering shells initially located deeper in the original crust. In the same figure, the total energy per nucleon released in a shell, denoted E/A_{cell} , follows the same trend. The energy per nucleon is only defined per one shell of the compressed outer crust and not for the whole compressed outer crust: the energy per nucleon of different shells cannot be summed directly. The decrease in energy release per nucleon as a function of the depth in the star can be explained from the catalyzed composition of the outer crust presented in Fig. 4.3. The nucleon number A is generally larger in deeper shells of the crust. Large nuclei are more stable than small ones; applying a compression to the shells of the catalyzed outer crust induces a state of local equilibrium that is closer to global equilibrium for shells with high nucleon number. In other words, catalyzed shells of the outer crust with large nucleon number are more stable with respect to compression related reactions than shells with small nucleon number. Shells deeper in the crust release less energy per nucleon than shells close to the surface. A few shells do not follow this trend of decrease with the depth in the crust, and this can be explained with the same reasoning: in Fig. 4.6, the third shell (very thin layer of ⁵⁸Fe) presents a higher maximum energy per nucleon than its shallower neighbor ⁶²Ni; there is also a slight increase in Q_{max} for shells 6 (⁸⁶Kr), 7 (⁸⁴Se), 8 (⁸²Se), and 9 (⁸⁰Ge). These shells follow the catalyzed nucleon number logic stated above.

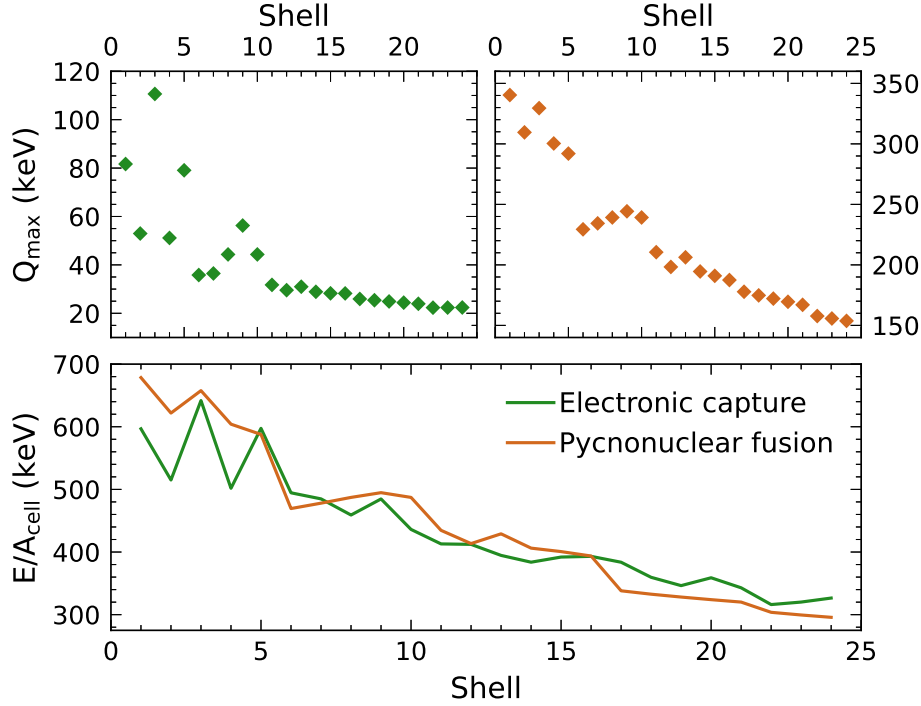


Figure 4.6: Maximum energy release per nucleon Q_{\max} in each shell of the originally catalyzed compressed outer crust for electron captures (upper left plot) and pycnonuclear fusions (upper right plot), as well as the sum of all electron captures and pycnonuclear fusion heat release E/A_{cell} as a function of the shell number (lower plot).

To compute the total energy released in the originally catalyzed compressed outer crust, we allocated the exothermic reactions to the number of baryons that go through these reactions in each shell. The number of baryons was calculated using the Tolman-Oppenheimer-Volkoff equations approximated in the crust (where it is reasonable to consider that $\epsilon = \rho c^2$), as well as the expression for the baryon number in a thin spherical shell, dN_b , of thickness dr

$$dN_b = \frac{4\pi r^2 n}{\sqrt{1 - \frac{2Gm}{rc^2}}} dr. \quad (4.13)$$

Therefore, an approximate number of baryons ΔN_i in an i -th shell of pressure range $P_{\text{bot}}^i - P_{\text{top}}^i$ is

$$\Delta N_i = \frac{4\pi R^4}{GMm_0} \sqrt{1 - \frac{2GM}{Rc^2}} (P_{\text{bot}}^i - P_{\text{top}}^i), \quad (4.14)$$

with m_0 the mean bound nucleon mass in ^{56}Fe . In contrast to the decreased energy per nucleon, the number of nucleons per shell generally increases as we go deeper in the crust: this can be explained by the gravitational mass of each shell presented in Fig. 4.4.

The formula for the total energy released in the compressed outer crust is given by

$$E = \sum_i \Delta N_i (\Sigma_j E_{ij}) = \frac{4\pi R^4}{GMm_0} \sqrt{1 - \frac{2GM}{Rc^2}} \sum_i \Delta P_i (\Sigma_j E_{ij}), \quad (4.15)$$

with E_{ij} the j -th energy source located in the i -th shell, and $\Delta P_i = P_{\text{bot}}^i - P_{\text{top}}^i$ the thickness in pressure of the i -th shell. For the accreted material part of the crust, Eq. (4.15) simplifies to

$$E = \frac{4\pi R^4}{GMm_0} \sqrt{1 - \frac{2GM}{Rc^2}} \sum_j P_j E_j. \quad (4.16)$$

In Fig. 4.7, we present the total energy E_{sh} released in each of the 24 shells of the originally catalyzed compressed outer crust. The trend of decrease in maximum energy per nucleon shown in Fig. 4.6 is overcompensated by the number of nucleons in the shells, thus ensuring that most of the energy is released in the deepest shells of the compressed outer crust. Shell 17 (^{112}Sr) has a particularly small pressure range, which explains why this shell in Fig. 4.7 presents a low total energy, as well as a low mass in Fig. 4.4. The total energy released by the originally catalyzed compressed outer crust, up to $\Delta P = 10^{32}$ dyn/cm², corresponds to the sum of sources displayed in Fig. 4.7 for a total of $E_{\text{tot}} = 4.25 \times 10^{47}$ erg.

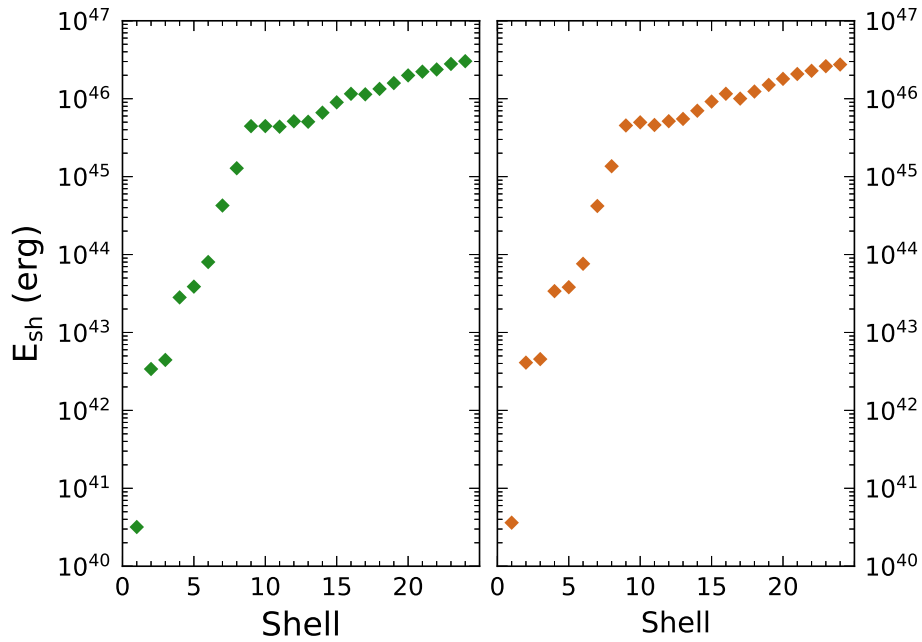


Figure 4.7: Total energy per shell E_{sh} released in each of the 24 shells of the originally catalyzed compressed outer crust for electron captures (left) and pycnonuclear fusions (right).

Our calculations for the heat release were established for an originally catalyzed outer crust. Now let us compare it to the heat release if the compressed crust was accreted, which would correspond to the fully accreted crust approximation. We compute the total energy needed to sink the 24 shells of the originally catalyzed outer crust over their neutron drip point from Eq. (4.15), and the five shells of an originally accreted outer crust over their neutron drip point from Eq. (4.16). Results are respectively 7.8×10^{45} erg and 7.4×10^{45} erg. These numbers indicate that the total energy available from the compression of the catalyzed

and accreted crust are similar. Therefore, it is not reasonable to neglect the heat sources of the originally catalyzed compressed outer crust when studying partially accreted crusts.

To compress the original outer crust (originally catalyzed or accreted) fully into the inner crust, *i.e.* that the top part of the shallowest shell has been pushed over its neutron drip point, an accretion of the amount of matter equal to the outer crust mass is needed. We denote ΔP_{oc} the compression for this scenario. Pushing the initially catalyzed outer crust to the point that the outer crust of the partially accreted crust is made of accreted matter, leads to a pressure at the bottom of the original crust of around 1.5×10^{30} dyn/cm². In addition to the 7.8×10^{45} erg released when each shell of the originally catalyzed outer crust are pushed to the neutron drip point (see paragraph above), this scenario also leads to chains of reactions above the neutron drip point: the additionally released energy is approximately 5×10^{45} erg. In total, the replacement of the outer crust by accreted matter releases 1.3×10^{46} erg in the originally catalyzed compressed outer crust. The total energy released by the accreted material part of the crust in this scenario is about 2.2×10^{46} erg.

Another crucial point needs to be raised with respect to heat sources in the partially accreted crust. In a fully accreted crust and in the accreted material part of the partially accreted crust, the energy release is continuous and the sources are located at fixed densities. For the originally catalyzed compressed outer crust, many energy sources exist, they appear as long as the shell takes to be sunk to pressures beyond the reaction threshold, then disappear. The heat sources are therefore temporary, and not located at fixed pressures in the crust. This is illustrated in Fig. 4.8 for the 24 shells of the originally catalyzed compressed outer crust at various values of the compression. Temporary as they are, the sources of the originally catalyzed compressed outer crust last for a certain compression range: the exothermic reaction associated to the heat source is first triggered in the deepest part (bottom) of the shell, and then invades the shell progressively until the entire shell i has been transformed from parent to daughter nuclei. In the left plot of Fig. 4.8, for $\Delta P = [0.5 - 1]10^{29}$ dyn/cm², heat sources occur in the shallowest shells, which are thin: there are periods of heat extinction. The shallowest shells have narrow pressure ranges. It takes less compression to fill them with daughter nuclei, and they allow for more lull than in the deepest shells. A timescale related to this phenomenon can be established: when a reaction pressure threshold is reached at the bottom of the original shell i , the additional compression required to ensure that the entire shell goes through this reaction is directly related to the thickness in pressure of the shell. This "shell filling" timescale is denoted τ_{sf} ,

$$\tau_{sf} = 4.8 \times 10^5 \frac{\alpha_*}{\langle \dot{M} \rangle_{-10}} (P_{bot,30}^i - P_{top,30}^i) \text{ yr} . \quad (4.17)$$

For deep shells, which present a wider pressure range ($P_{bot}^i - P_{top}^i$), one exothermic reaction sometimes has not yet filled the entire shell before another starts at the bottom end P_{bot}^i , which results in an overlap of reactions within one shell. In the upper right plot, there is no extinction because a reaction proceeds in at least one shell. For the highest values of the compression, there are fewer heat sources, as presented in the lower right plot of Fig. 4.8.

As the accreted material part of the crust invades the partially accreted crust, permanent sources settle and then dominate at the fully accreted crust approximation.

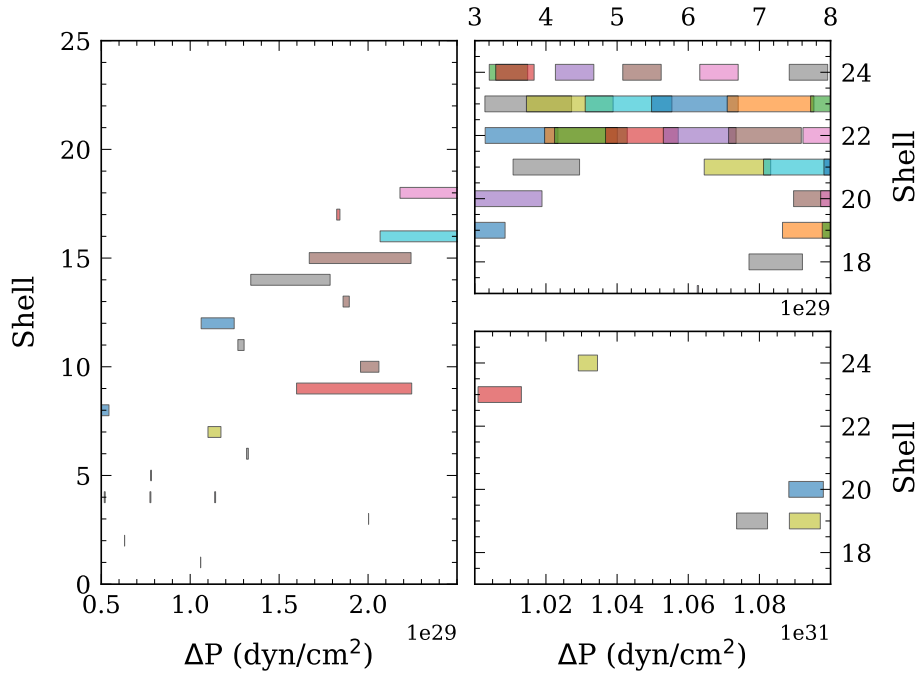


Figure 4.8: Heating activity expressed in terms of the compression ΔP required for heat sources to transform each shell of the originally catalyzed compressed outer crust from the parent to the daughter nuclei. The colors have no specific meaning other than to distinguish between overlapping reactions in a shell.

The problem of the interplay of neutrino losses and matter heating deserves an additional discussion. The electron capture chain is initiated by the process described in Eq.(4.2) after the chemical potential of electrons μ_e reaches the threshold $\mu_e = W_1$, with W the threshold of the reaction, and the subscript 1 designating the first electron capture. This process proceeds in a quasi-equilibrium way, *i.e.* with no heat release, because the electron capture that follows can be considered instantaneous. The nucleus $(A, Z - 1)$ has odd neutron number N and proton number Z , therefore has a significantly lower threshold for the second electron capture because of the pair term: $W_2 < W_1$. Moreover, an odd-odd nucleus $(A, Z - 1)$ has a dense spectrum of excited states with excitation energies (relative to the ground state) denoted E_{exc} , which follows $0 < E_{\text{exc}} < E_e - W_2$. An excited state denoted $(A, Z - 1)^*$ decays to the ground state denoted $(A, Z - 1)_{\text{gs}}$. The important effect connected with the transition to the excited state of $(A, Z - 1)$ nucleus is the increase in the threshold pressure of the reaction due to the excitation energy. This also leads to a larger energy release in the second electron capture [Chamel et al., 2021]. In Gupta et al. [2007], authors found that the net contribution of excited states balances the neutrino losses. Therefore, the neutrino losses can be neglected, and our approximation for the heating of matter $Q_2 \simeq \mu_e - W_2$ is valid.

4.2.3 Onset of the neutron drip

Above a certain density, nuclei are subject to neutron emission: this is the neutron drip phenomenon. In the framework of the single-nucleus model, the neutron drip point is given by the solution to the equation

$$G_{\text{cell}}(A_{\text{cell}}, A, Z) = G_{\text{cell}}(A_{\text{cell}}, A - N_{\text{out}}, Z - 1), \quad (4.18)$$

with N_{out} the number of neutrons outside the nucleus, and G_{cell} the Gibbs energy per cell. The timescale of strong interaction is much shorter than that of weak interaction. The former fulfills the energy requirement imposed by the weak process, therefore neutron emission is always triggered by an electron capture.

The single-nucleus model is equivalent to the assumption that N_{out} neutrons drip simultaneously in all Wigner-Seitz cells at given pressure P_{nd} . As a consequence, the number density of the neutron gas outside nuclei n_{out} is discontinuous at P_{nd} . For $P > P_{\text{nd}}$, n_{out} is larger by a factor N_{out} than the number density of nuclei $n_{\mathcal{N}} = 1/V_{\text{cell}}$, with V_{cell} the volume of the cell. To accurately determine the neutron drip point, one must go beyond the single-nucleus model, as is presented in [Chamel et al. \[2015\]](#), later on referred to as the continuous approach. It considers that one nuclei first drips neutrons, in which case the density of the neutron gas is assumed to be negligible at the neutron drip point, and the only energy considered for free neutrons is their rest energy. The chain of reactions corresponds to

$$(A_{\text{cell}}, A, Z) \rightarrow (A_{\text{cell}} - N_{\text{out}}, A - N_{\text{out}}, Z - 1) + N_{\text{out}}, \quad (4.19)$$

for which the number of nucleons in the Wigner-Seitz cell decreases by N_{out} . The onset of neutron drip occurs when the Gibbs energy of left and right nuclei in Eq. (4.19) follows

$$G_{\text{cell}}(A_{\text{cell}}, A, Z) = G_{\text{cell}}(A_{\text{cell}} - N_{\text{out}}, A - N_{\text{out}}, Z - 1) + m_n c^2 N_{\text{out}}. \quad (4.20)$$

In our model, we considered only ground-state to ground-state transitions driven by electron captures and associated with neutron emission. Electron captures leading to the excited state daughter nucleus, which de-excites by neutron emission, were considered in [Gupta et al. \[2008\]](#) and [Lau and et al. \[2018\]](#), but are not taken into account in this manuscript. Neutron emission driven by photon absorption on nuclei can be neglected too, because at temperature $T \simeq 10^8$ K and $\rho \simeq 10^{11}$ g/cm³ (typical of our study's conditions), plasmon suppression of photons dominates, for details see [Gupta et al. \[2008\]](#).

The neutron drip point depends on the density and on the parent nucleus (A_{cell}, Z, N) . Because the catalyzed outer crust is made of 24 shells, there are 24 different nuclei that undergo neutron drip, such that the neutron drip point P_{nd} is different for each shell of the originally catalyzed compressed outer crust. The compression at which neutrons start dripping out of nuclei, as well as the additional compression needed to produce free neutrons throughout the entire shell, is displayed in Fig. 4.9 for the 24 shells of the originally catalyzed compressed outer crust; this is also presented in Table 4.1. The exothermic reactions up to

the neutron drip point calculated in the single-nucleus model are shown in black, and those calculated with the continuous approach are shown in blue.

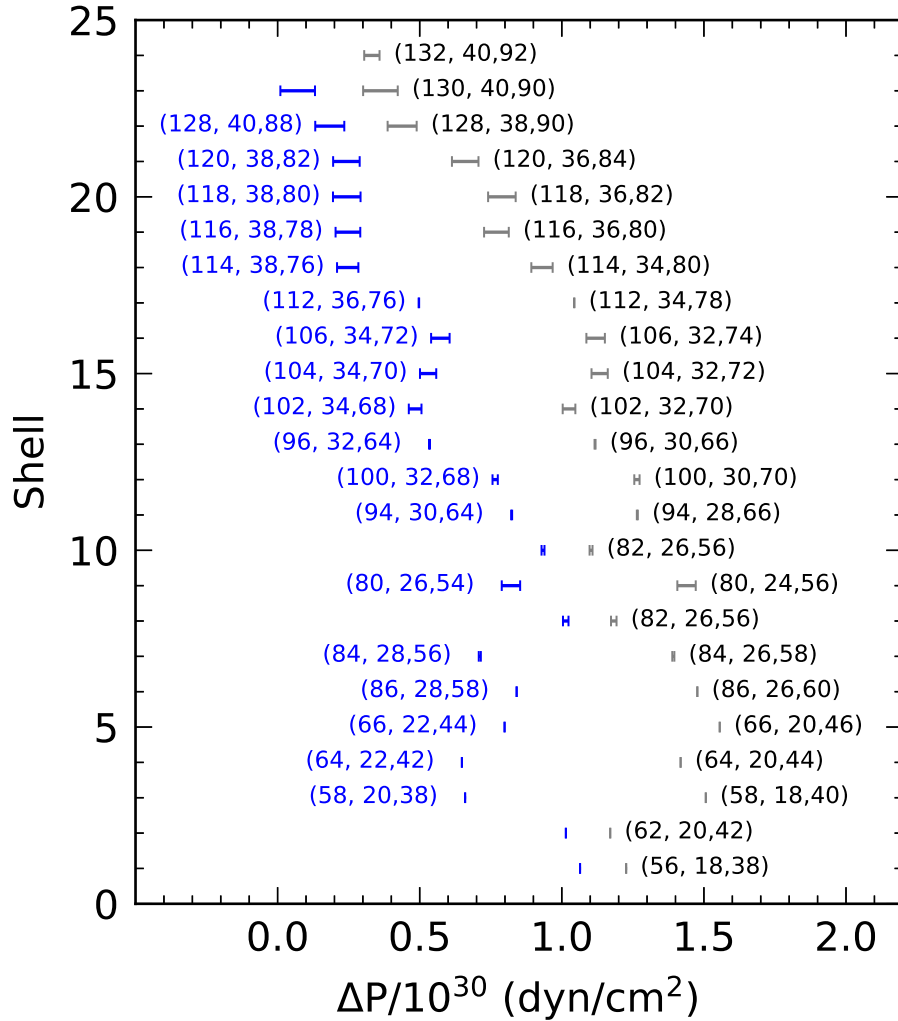


Figure 4.9: Compression ΔP required to reach the neutron drip point in the single-nucleus model (black) and the continuous approach (blue) for each shell of the originally catalyzed compressed outer crust. The error bars refer to the additional compression needed for the entire shell to undergo neutron emission from bottom (left end of the error bar) to top (right end of the error bar). The parent nuclei undergoing electron capture that precedes the neutron emission are indicated with the notation (A_{cell}, Z, N) . In the case of a continuous approach, it is presented only if the parent nucleus is different than that in the single-nucleus models.

Because the onset of neutron drip occurs for lower compression in the continuous approach than in the single-nucleus model, the number of reactions in the compressed outer crust is reduced: in the third shell, the neutron drip calculated in the continuous approach occurs for the nucleus which is the parent of the nucleus for which the neutron drip occurs in the single-nucleus model. In shell 18, it is the grandparent nucleus (see Table 4.1). For the same reason, the last shell of the outer crust for which the neutron drip is calculated in

the continuous approach is shell 23 (^{130}Zr) of the outer crust, calculated within the single-nucleus approach.

As an example, we considered the 19th shell of the originally catalyzed compressed outer crust, which corresponds to an original (catalyzed) shell composed of ^{116}Sr . In the single-nucleus model, the neutron drip onsets at the bottom of the shell, after a compression $\Delta P \simeq 7.3 \times 10^{29} \text{ dyn/cm}^2$; an additional compression $\Delta P \simeq 8.8 \times 10^{28} \text{ dyn/cm}^2$ is required for the entire shell to change from ^{116}Kr to ^{106}Ge . The process associated with this neutron drip consists of four electron captures triggering the neutron drip at a pressure approximately $1.2 \times 10^{30} \text{ dyn/cm}^2$. The energy release associated with this process is about 35 keV per nucleon (from $G_{\text{cell}}/A_{\text{cell}} = 940.471 \rightarrow 940.435 \text{ MeV}$). The number density of neutrons trapped in one Wigner-Seitz cell at the onset, denoted n_{out} , is an order of magnitude larger than the number density of nuclei n_N , and about only one order of magnitude smaller than the average baryon number density n . In the continuous approach, the neutron drip for the 19th shell is triggered earlier, for a compression $\Delta P \simeq 2 \times 10^{29} \text{ dyn/cm}^2$, with a double electron capture in the reaction ^{116}Sr . The energy release per nucleon associated with the reaction is about 13 keV. By construction, in this approach, the average number density of free neutrons is negligibly small.

4.2.4 Applications for rotating neutron stars and magnetars

We have described a phenomenon that is related to the compression of the crust in accreting binaries, but there are other astrophysical phenomena that are related to the crust compression.

One of the scenarios leading to an increase in pressure in the neutron star crust is the process of slowing-down of the stellar rotation. The theory behind neutron star spin down is related to wave emission. The loss of rotation can be due to the emission of the magnetic field of the star. Another source of rotation loss is the emission of continuous gravitational waves: a neutron star can present non spherical features if it has, for example, accretion induced mountains. The braking index is about three for magnetic field loss and five for gravitational wave emission loss, and it can be used to estimate the timescale of the spin down [Hamil et al., 2015, Haskell and Patruno, 2017]. If we consider that the loss of rotational frequency is related to gravitational wave emission, the maximum quadrupolar deformation presented in Ushomirsky et al. [2000], Johnson-McDaniel and Owen [2013] leads to a timescale of 10^6 years to decrease the rotational frequency by a factor of two.

The rotation of the star leads to axisymmetric deformation and an oblate shape of the star. As the gravitational force and the centrifugal force balance one another, the spin decrease leads to a deformation. The star is deformed from an oblate shape to a more spherical one, which is equivalent to a compression of the crust. This case has been studied by Iida and Sato [1997] and Gusakov et al. [2015], and both their result give a relative increase in pressure by some 25% for an initial frequency of 1 kHz. A similar conclusion can be drawn from the consideration of the (baryon) mass of the outer crust for a rotating strange quark

star, as is presented in [Zdunik et al., 2001]. The relative increase in pressure is approximately equal to the relative increase in baryon mass of a given shell, which is about 30% for an initial rotation at 1 kHz, and about 100% at most for a spin-down from an initial rotating configuration close to the Keplerian frequency. For such a relative increase in pressure, detailed calculations show the existence of exothermic reactions in the very deep ($A_{\text{cell}} \sim 100$) region of the outer crust. Assuming a 100% limit for the maximum relative increase in pressure due to spin-down, only a few of the deepest shells can reach the onset of neutron drip in our study, see Table 4.1.

The estimation of the rotation frequency of a newly born neutron star that is not spun up by accretion is a complicated task that depends on many assumptions. The analysis of observed pulsars gives initial rotation periods between ten and several hundreds of milliseconds [Faucher-Giguère and Kaspi, 2006]; these results can be supported by theoretical supernova modeling [Janka et al., 2022]. Even for the lower limit of this range, *i.e.* for periods around [10 – 20] ms, the relative increase in pressure after slowing down would be less than 1%. A small increase like this would not trigger any exothermic reaction in the catalyzed crust. This is not the case for a fully accreted crust when reactions occur continuously with the pressure increase [Gusakov et al., 2015].

Another scenario hosting the compression of the crust are decaying magnetic fields in magnetars. The gravitational force and the Lorentz force also counterbalance one another, such that a decrease in magnetic field leads to a crust compression. Recently, Chamel et al. [2021] proposed an analytical estimation, as well as numerical computation of heat sources and their location for magnetars with a decreasing magnetic field. The timescale for the evolution of the magnetic field in neutron star’s crust is of the order of 10^6 years. In this paper, the authors conclude that the magnetic field, of the order 10^{16} to 10^{17} G, has no impact on the maximum heat release of each reaction in the compressed crust. However, the magnetic field has an almost linear impact on the location of the heat sources. The magnetic field also has an impact on the relative compression required to trigger the reactions.

4.2.5 Properties of a compressed crust

The properties of the partially accreted crust differ from that of the fully accreted crust and that of the catalyzed crust. In the following, we present the thermal and transport properties of the originally catalyzed compressed outer crust, a peculiar neutron drip configuration in the context of diffusing neutrons, and a density related instability source of gravitational energy.

4.2.5.1 Composition and transport properties

Thermal and transport properties of the crust depend on the crust composition. For example, the melting temperature and shear modulus are both proportional to $Z^2/A_{\text{cell}}^{1/3}$ [Chamel and Haensel, 2008]; this quantity is presented as a function of the pressure for the catalyzed outer crust, the fully accreted crust and the originally catalyzed compressed

outer crust calculated in the Mackie & Baym model in Fig. 4.10. The melting temperature in the fully accreted crust is much lower than that of the originally catalyzed compressed outer crust: for a range of temperatures, the fully accreted crust is liquid while the originally catalyzed compressed outer crust is solid. The shear modulus is also larger for the originally catalyzed compressed outer crust than for the fully accreted crust: the former is more rigid than the latter.

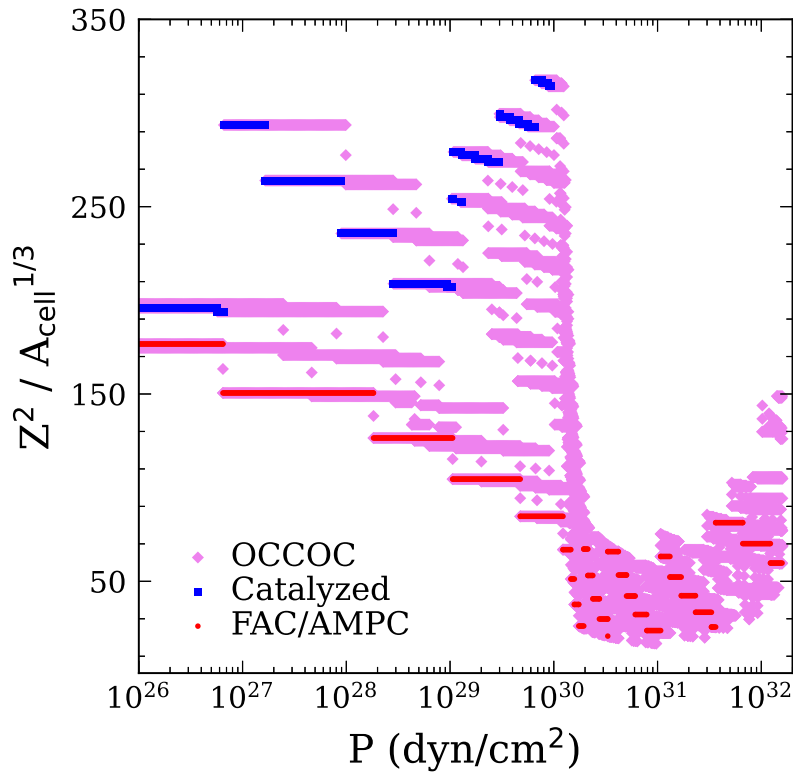


Figure 4.10: $Z^2 / A_{\text{cell}}^{1/3}$ as a function of the pressure P for the catalyzed outer crust (blue), for the fully accreted crust (red), and for the originally catalyzed compressed outer crust (purple).

The composition of the crust also affects the modeling of the thermal evolution of accreting neutron stars. On the one hand, the thermal conductivity of the crust is mostly contributed by the electrons; it is inversely proportional to the scattering frequency of electrons, which is proportional to Z^2 . The proton number of the originally catalyzed compressed outer crust being generally larger than that of the fully accreted crust at fixed density, thermal conductivity is lower, and the crust exhibits a lower heat transfer rate for the originally catalyzed outer crust than for the fully accreted crust. On the other hand, the heat capacity of the crust enters the relativistic heat balance equations. In the crust, the electron contribution scales as $\sim Z^{2/3} / A^{2/9}$, and the lattice as $A^{1/3}$ [Fortin et al., 2010].

The relation between the pressure P and the mass density ρ for the partially accreted crust is presented in Fig. 4.11: $P(\rho)$ is presented at the compression $\Delta P = 2.3 \times 10^{29}$ and 1.1×10^{30} dyn/cm². The equation of state for catalyzed matter is softer, as it corresponds

to a global minimum of energy at a given pressure. The stiffest equation of state is obtained in the fully accreted crust approximation. Nuclei have A smaller than in the case of the catalyzed and also originally catalyzed compressed matter. As a result, matter in the fully accreted crust is further away from global equilibrium (catalyzed matter), and of the originally catalyzed compressed matter.

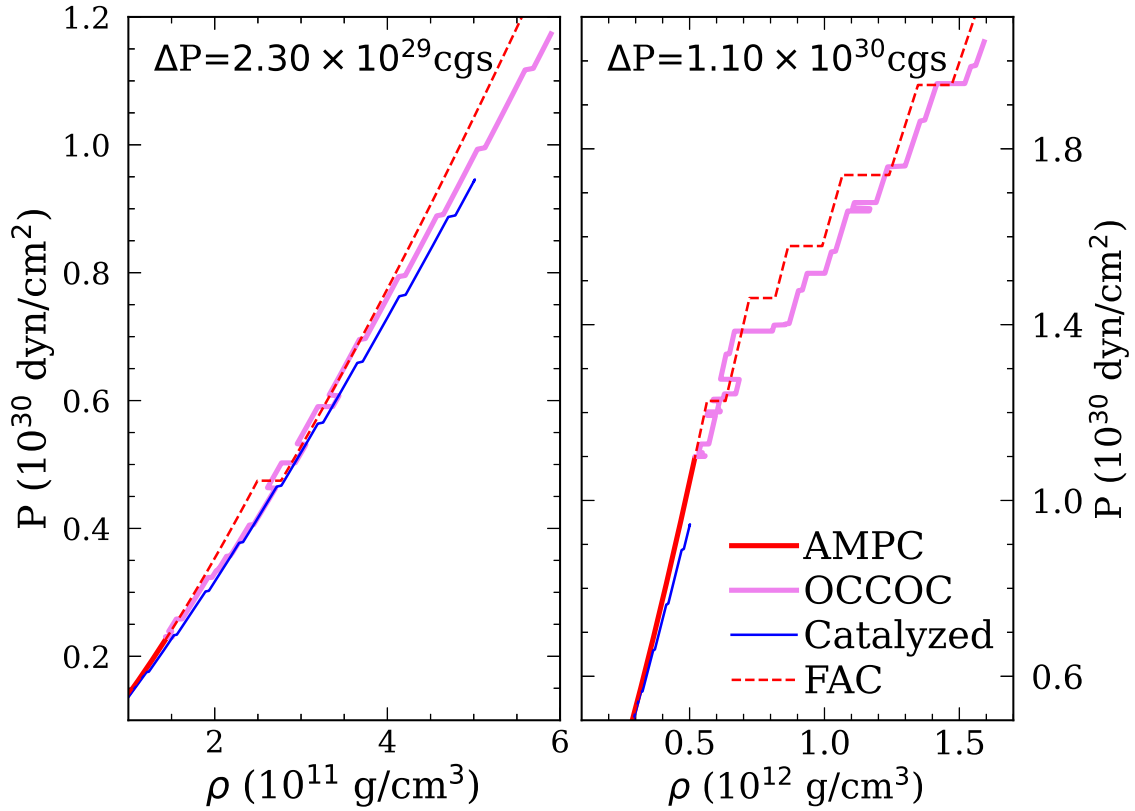


Figure 4.11: Equation of state $P(\rho)$ of the partially accreted crust for compression $\Delta P = 2.3 \times 10^{29}$ dyn/cm 2 and $\Delta P = 1.1 \times 10^{30}$ dyn/cm 2 . The originally catalyzed compressed outer crust is presented in violet, and the accreted material part of the crust is presented in red. The catalyzed outer crust is presented in blue, and the fully accreted crust is shown as dashed red lines.

4.2.5.2 Neutron drip anomaly

For the compressed crust, the neutron-drip point depends on the shell it occurs in. There is a configuration represented in Fig. 4.12 of alternating shells with and without dripped neutrons, which occurs for a range of compression $\Delta P = [8 \times 10^{29} - 1.5 \times 10^{30}]$ dyn/cm 2 : the shallower shell i presents a layer with free neutrons, and its deeper neighbor, shell $i + 1$ does not. In this case, shell i has started neutron drip at an earlier stage of compression than shell $i + 1$. We are left with a layer in shell $i + 1$ without free neutrons surrounded by two layers with free neutrons. This configuration emerges due to the compression of different shells, therefore it cannot appear in a fully accreted crust approximation, nor in the accreted material part of the partially accreted crust. It is referred to as the neutron drip anomaly.

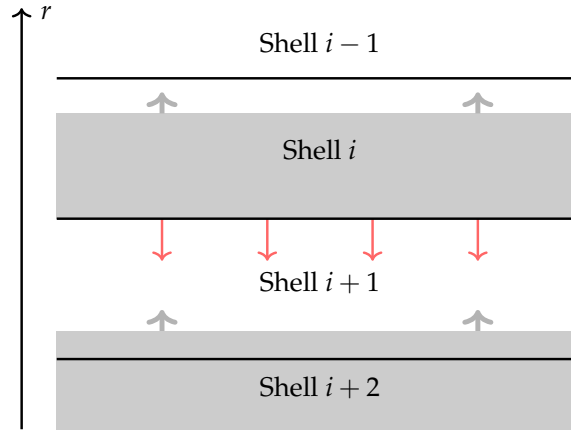


Figure 4.12: Schematic of the neutron-drip anomaly. Areas of the shells with free neutrons are represented in gray.

For example, in the single-nucleus model, after a compression $\Delta P \sim 10^{30}$ dyn/cm², (equivalently around $2.5 \times 10^{-5} M_{\odot}$ accreted on the surface of the original crust), neutron drip occurs at the bottom of the 14th shell when it has not yet in the deepest end of shell 15. This neutron-drip anomaly can be tracked in Fig. 4.9: from the deepest to the shallowest shell, the global trend of the neutron-drip onset is from left (lowest compression) to right (highest compression). When two neighbor shells do not follow this trend, the anomaly occurs. In the continuous approach, the anomaly does occur, but not necessarily for the same shells as in the single-nucleus model.

As the scheme of Fig. 4.12 suggests, the timescale described in Eq. (4.17) entails that if shell i (shallower) starts neutron drip (at its deepest end) before shell $i + 1$ (deeper) has ended emitting free neutrons, the layers of these shells will present an anomalous configuration. This is the case for shells 21 and 22 in the continuous approach: in Fig. 4.9, shell 22 starts dripping at relative compression $\delta P/P = 17\%$, while shell 21 starts at $\delta P/P = 29\%$, which is in accordance with the neutron-drip trend. However, the additional compression required for the reaction to go through the entire shell after starting at its bottom implies that shell 22 will finish filling up with free neutrons at $\delta P/P = 35\%$, that is, well after shell 21 starts dripping neutrons.

For certain values of the compression, this phenomenon is repeated several times: at $\Delta P \simeq 9 \times 10^{29}$ dyn/cm² (in the single-nucleus model), no shell of the originally catalyzed compressed outer crust has started to drip; at $\Delta P \simeq 1.56 \times 10^{30}$ dyn/cm², all shells have been pushed to the inner crust. For $\Delta P \simeq 1.23 \times 10^{30}$ dyn/cm², six layers are involved in the anomaly, thus alternating layers with and without free neutrons. In the single-nucleus model, after a compression $\Delta P \simeq 1.6 \times 10^{30}$ dyn/cm², all shells of the originally catalyzed compressed outer crust have undergone neutron drip and have been pushed to depth corresponding to the inner crust. In the continuous approach, the whole outer crust has been pushed to the inner crust after a compression $\Delta P \simeq 1.1 \times 10^{30}$ dyn/cm², .

Now let us put this neutron drip anomaly outside of the single-nucleus model in order

to assess how neutrons diffuse in the crust. Up to now, we considered a quasi-static scenario for an anomalous neutron drip. From now on, the kinetics of dripped neutrons is included. In the following, we focus on a layer of daughter nuclei from two successive electron captures, but the same reasoning can be applied to pycnonuclear fusion. The emitted neutrons scatter on nuclei via strong interaction; scattering on electrons can be neglected because it is due to magnetic moments coupling only. Under the gravitational field acceleration denoted g , neutrons drift downward (towards the center), with a flow velocity denoted V_n . The neutron number current is denoted $j_n = n_n V_n$, with n_n the neutron number density. The balance of the gravitational force $m_n g$ with a resistance force from the scattering of neutrons on nuclei results in the relation

$$V_n = b m_n g , \quad (4.21)$$

with b the mobility parameter of the neutron gas in the lattice of nuclei, as presented in [Pitaevskii and Lifshitz \[2012\]](#). The neutron-nucleon scattering is treated as elastic: nuclei are approximated by hard spheres of radius $r_A = 1.2 A^{1/3}$ fm, with 1.2 fm being the radius of one nucleon. The transport cross-section for neutron scattering is given by $\sigma_t = \pi r_A^2$. The mass of a nucleus with nucleon number $A \simeq 100$, is two orders of magnitude higher than the neutron mass m_n . Moreover, the number density of the neutron gas n_n is smaller than the number density of nuclei n_N . At a prevailing temperature of 10^8 Kelvin, the neutron gas is non degenerate, such that the treatment presented in [Pitaevskii and Lifshitz \[2012\]](#) can be applied: the diffusion of the Boltzmann gas of light particles in the gas of heavy particles approximated by hard elastic spheres. We use the Stokes-Einstein relation for diffusion to relate the diffusion coefficient D and the mobility parameter b as is presented in [Landau and Lifshitz \[1987\]](#), such that

$$D = k_B T b , \quad (4.22)$$

with k_B is the Boltzmann constant.

Neutrons drift downward under the action of the external gravitational force, such that the formula for drift velocity [[Pitaevskii and Lifshitz, 2012](#)] gives

$$V_n = \frac{g m_n v_T^n}{3 n_A \sigma_t k_B T} , \quad (4.23)$$

with v_T the mean microscopic (thermal) speed of neutrons given by

$$v_T^n = \sqrt{\frac{k_B T}{m_n}} = 9.1 \times 10^7 \sqrt{\frac{T}{10^8 \text{ K}}} \text{ cm/s} . \quad (4.24)$$

The mean free path of neutrons denoted λ_n , which is defined as the inverse of the product between the nuclei density and the cross section for neutron scattering is

$$\lambda_n = 1.705 \times 10^{-9} \frac{(A_{100})^{1/3}}{\rho_{11}} \text{ cm} , \quad (4.25)$$

with ρ_{11} the density in 10^{11} g/cm³, and A_{100} the nucleon number divided by 100. The drift velocity of neutrons gives

$$V_n = 478 \frac{(A_{100})^{1/3}}{\rho_{11}} \left(\frac{T}{10^8 \text{ K}} \right)^{-1/2} \frac{g}{g_*} \text{ m/yr} , \quad (4.26)$$

with $g_* = 1.3 \times 10^{14} M/M_\odot / R_6^2$ the Newtonian surface gravitational acceleration of the star in cm/s².

The neutron drift process was considered in the reference frame associated with a lattice of nuclei, which actually moves inwards due to compression. The radial velocity due to accretion, denoted V_c , is given by

$$V_c = \frac{\dot{M}}{4\pi R^2 \rho} = 1.5 \frac{\dot{M}_{-10}}{R_6^2 \rho_{11}} \text{ mm/yr} , \quad (4.27)$$

with ρ_{11} the density in 10^{11} g/cm³. V_c is negligibly small compared to V_n , therefore, neutrons leave the layer right after their emission and thermal equilibration, and drift downward through the outer crust to the inner crust.

Now, let us check *a posteriori* that the Boltzman condition is correct. The number density of the gas of the emitted neutrons is

$$n_n = k_n n \frac{V_c}{V_n} , \quad (4.28)$$

with k_n the number of neutrons emitted from the nucleus, such that the free neutron fraction denoted x_n is

$$x_n = \frac{n_n}{n} \simeq 10^{-7} k_n . \quad (4.29)$$

This corresponds to a diluted ideal neutron gas, described by Boltzmann statistics, because the condition for the kinetic energy ε_p of a neutron of momentum p , and the chemical potential (without rest energy) μ_n [Landau and Lifshitz, 1980] satisfies

$$e^{(\mu_n - \varepsilon_p)/k_B T} \ll 1 . \quad (4.30)$$

For an ideal gas of neutrons, the chemical potential is given by

$$\mu_n = k_B T \ln \left[n_n \left(\frac{2\pi\hbar^2}{m_n k_B T} \right)^{3/2} \right] , \quad (4.31)$$

therefore a sufficient condition for the validity of Boltzmann statistics is that the dimensionless parameter

$$n_n \left(\frac{2\pi\hbar^2}{m_n k_B T} \right)^{3/2} \ll 1 . \quad (4.32)$$

We find that at density $\sim 10^{11}$ g/cm³, this dimensionless parameter for neutron gas is indeed very small ($\sim 10^{-3}$). Because the neutron number is conserved, the thickness of the layer of neutron emission can be estimation at hydrostatic equilibrium. Let us introduce the dimensionless variable

$$y = \frac{\mu_e - W}{W}. \quad (4.33)$$

An element of matter is pushed to the threshold pressure of the electron capture P_{th} , at which the chemical potential of the electrons equals the threshold of the reaction W . If this piece of matter is compressed further, the dimensionless variable y increases but can be considered small ($y \ll 1$). Assuming that the pressure is given by that of a ultra-relativistic gas of degenerate particles (for which $P \simeq \mu^4$), above the pressure threshold the pressure can be approximated by

$$P \simeq P_{\text{th}}(1 + 4y). \quad (4.34)$$

From the relativistic equations for hydrostatic equilibrium, the dimensionless variable is also given by

$$y = \frac{g\rho z}{4P_{\text{th}}}, \quad (4.35)$$

with z the depth relative to the capture threshold location and $g \simeq 10^{14}$ cm/s². Electron captures with neutron emission involved in the neutron-drip anomaly occur typically at a mass density $\rho \simeq 10^{11}$ g/cm³, and at a pressure $P \simeq 10^{30}$ dyn/cm². From the drift and radial velocity estimated in Eq. (4.26) and Eq. (4.27), and from the threshold energy of the electron capture $W \simeq 20$ MeV, the dimensionless variable at the bottom of the neutron emission layer gives $y \simeq 10^{-5}$ and the thickness of the neutron emission layer is of around three centimeters.

On the one hand, the shells from which free neutrons escape have a lower nucleon number per cell: with the example of shells 14 and 15 at $\Delta P \simeq 10^{30}$ dyn/cm², after neutron drip the daughter nucleus ($A_{\text{cell}} = 102, A = 98, Z = 30$) with four free neutrons is present at pressure $P = 1.2 \times 10^{30}$ dyn/cm². This nucleus, after losing its four free neutrons that drifted downward, is stable at this pressure. On the other hand, the shells into which the free neutrons have drifted will present a higher neutron number density. Overall, the composition of the compressed crust must be reevaluated. However, treating the interaction of drifting neutrons with deeper shells in the crust requires considerations outside the single-nucleus approach, which is beyond the scope of this study.

4.2.5.3 Density inversion related instability

The final property of the compressed crust we shall mention is related to density inversion triggered by reactions in the crust. Each exothermic reaction triggered at the bottom of one shell of the originally catalyzed compressed outer crust is accompanied by a density jump. After this reaction, the density of the layer just below this shell may be lower. This density inversion can be subject to the Rayleigh-Taylor instability applied to a lattice, also

referred to as the elastic Rayleigh-Taylor instability. The study of this type of instability indicates that it develops when the density jump is larger than 10%, for details see [Blaes et al. \[1990\]](#). A 10% or more density jump appears in our study for an increase in pressure in the range $[8 \times 10^{29} - 3 \times 10^{30}]$ dyn/cm², or equivalently after $\sim 10^{-4} M_{\odot}$ has been accreted.

Because the instability must be corrected, the two shells involved in the unstable configuration with a density jump will swap to ensure that the shell with the highest density will be located deeper than the shell with the lowest density. The displacement of matter related to this swapping will release gravitational energy ΔE that one can estimate using the formula in [Blaes et al. \[1990\]](#)

$$\begin{aligned} \Delta E &= \frac{4\pi R^4}{GM} (P_{1,\text{bot}} - P_{1,\text{top}}) (P_{2,\text{bot}} - P_{2,\text{top}}) \left(\frac{1}{\rho_2} - \frac{1}{\rho_1} \right) \\ &\simeq 10^{44} \frac{R_6^4}{M/M_{\odot}} (P_{1,\text{bot}} - P_{1,\text{top}})_{28} (P_{2,\text{bot}} - P_{2,\text{top}})_{28} \left(\frac{1}{\rho_{2,11}} - \frac{1}{\rho_{1,11}} \right) \text{ erg}, \end{aligned} \quad (4.36)$$

with $(P_{i,\text{bot}} - P_{i,\text{top}})_{28}$ the pressure thickness in 10^{28} dyn/cm² of the layer i , and $\rho_{i,11}$ the mean density in 10^{11} g/cm³ of the layer i . The pressure range of the layers subject to elastic Rayleigh-Taylor instability is typically 10^{28} or 10^{29} dyn/cm². This corresponds to a layer mass of mass $\sim 10^{-6} M_{\odot}$, and to a timescale of the formation of these layers of approximately 10^4 yr for an accretion rate of 10^{-10} solar mass per year.

Overall, partially accreted crusts composed of the original crust under compression and of freshly accreted material must be considered for neutron stars that have accreted small amounts of matter. We have calculated the heat sources in an originally catalyzed outer crust under compression, and showed that the total heat release is of the same order than the heat released in a fully accreted outer crust. The properties of the compressed crust are different from that of a fully accreted crust, and will have an impact on the modelling of the thermal relaxation of some sources. The neutrons emitted from the nucleus in the compressed crust travel to deeper layers in the star, an effect that has not been taken into account in our calculations. Further results require including neutron diffusion in the crust when establishing the equation of state and composition of the partially accreted crust. The exothermic reactions triggered in the compressed outer crust lead to a density related instability; shells involved in this instability should swap and release gravitational energy, in a mechanism which dynamics are beyond the scope of this manuscript.

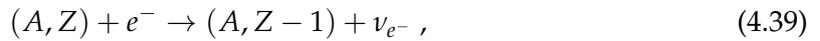
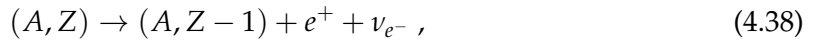
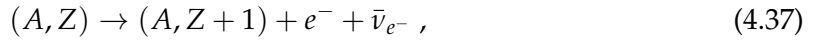
4.3 Layers of electron captures in accreting neutron stars

So far, we have treated the kinetics of exothermic reactions in a very simplistic approach: reaction are instantaneous, so to be clear, we have not treated the kinetics at all. However, the reaction rate affects the heat release in accreting crusts.

In this section, we concentrate on the role of electron capture rates in deep crustal heating. First, we present the derivation of the reaction rate of electron captures, and how nuclear data from β^- -decay can be used for a few reactions in the outer crust of accreted neutron stars. A simple approach for the equation of state of a mixture of nuclei is presented, and the equation followed by the mixture of parent and daughter nuclei of electron captures is established. Finally, the role of the reaction rate on heat release and cooling of the crust is explored.

4.3.1 Electron captures

The β -decay family of reactions includes the β^- -decay in Eq. (4.37), the β^+ -decay in Eq. (4.38), and electron capture in Eq. (4.39)



with Z the proton number, A the nucleon number, the notation e^- and e^+ designating electrons and positrons respectively, and ν_{e^-} and $\bar{\nu}_{e^-}$ designating electronic neutrinos and anti-neutrinos. Historically, this family of reactions brought forth the role of neutrino particles in radioactive channels. The puzzling continuous spectrum of β particles (e^+ , e^-) was discussed by Wolfgang Ernst Pauli in a series of letters to Lise Meitner and discussions at the Tübingen 1930 convention [Gustafson \[2010\]](#). This led to the discovery of neutrinos, which were first called neutrons, when those had not been discovered yet.

Let us consider a lattice of nuclei permeated by a sea of relativistic electrons. In the heavy nucleus approximation, the energy of the nucleus (A, Z) is given by its nuclear mass denoted $\mathcal{M}(A, Z)$ such that

$$\mathcal{M}(A, Z)c^2 = \mathcal{M}_{\text{at}}(A, Z)c^2 - Zm_e c^2 + B_{\text{el}}(Z) , \quad (4.40)$$

with $\mathcal{M}_{\text{at}}(A, Z)$ the atomic mass which can be extracted from tables of experimental data presented in [Wang et al. \[2021b\]](#), m_e the electron mass, and B_{el} the total binding energy of electrons approximated by the formula presented in [Lunney et al. \[2003\]](#)

$$B_{\text{el}}(Z) = 14.4381 \times Z^{2.39} + 1.55468 \times 10^{-6} \times Z^{5.35} \text{ eV} . \quad (4.41)$$

Neutrinos are considered massless, and we consider that they escape immediately after being emitted. In this framework, the electron capture is permitted when the energy of electrons -or chemical potential- reaches the threshold denoted W , given by

$$W \equiv \mathcal{M}_{\text{at}}(A, Z - 1)c^2 - \mathcal{M}_{\text{at}}(A, Z)c^2 + B_{\text{el}}(Z - 1) - B_{\text{el}}(Z) + m_e c^2 . \quad (4.42)$$

4.3.1.1 Derivation of the reaction rate

In the following, we present the derivation of the rate of electron captures. Because most experimental data of nucleus half-lives are presented for β^- -decay, we shall derive the reaction rate of both the β^- -decay and electron captures. To do so, the Fermi golden rule is used. Based on a perturbation theory derived by Paul Adrien Maurice Dirac [Dirac, 1927], the formula for the probability of transition from one initial state to one final state $\Gamma_{i \rightarrow f}$ was treated again by Enrico Fermi to give

$$\Gamma_{i \rightarrow f} = \frac{2\pi}{\hbar} |\mathcal{M}|^2 \rho(E_f) , \quad (4.43)$$

with $\rho(E_f)$ the density of states with final energy E_f , and \mathcal{M} the matrix element of the transition. Let us study the following electron capture and its corresponding β^- -decay

$$(A, Z) + e^- \rightarrow (A, Z - 1) + \nu_e , \quad (4.44)$$

$$(A, Z - 1) \rightarrow (A, Z) + e^- + \bar{\nu}_e . \quad (4.45)$$

The constituents k of the two processes are each defined by their momenta denoted p_k . The projection of the electron spin is denoted s_e , and the spin of the neutrino is denoted s_{ν_e} ; the spin of the nucleus is denoted M and its projection on the spin quantization axis is denoted J . The matrix elements of the electron capture, denoted \mathcal{M}_{ec} , and of the β^- -decay, denoted \mathcal{M}_{β} , are given by

$$\mathcal{M}_{\text{ec}} = \langle \vec{p}_{\nu_e}, s_{\nu} | \langle \vec{p}_f, M_f J_f | \hat{H}_w | \vec{p}_i, M_i J_i \rangle | \vec{p}_e, s_e \rangle , \quad (4.46)$$

$$\mathcal{M}_{\beta} = \langle \vec{p}_{\bar{\nu}_e}, s_{\bar{\nu}_e} | \langle \vec{p}_e, s_e | \langle \vec{p}_f, M_f J_f | \hat{H}_w | \vec{p}_i, M_i J_i \rangle , \quad (4.47)$$

with \hat{H}_w the Hamiltonian of the weak interaction mediating the interaction between initial and final states. The subscript notation i and f designate the initial nucleus and final nucleus respectively. For Eq. (4.46), the initial nucleus is (A, Z) and the final nucleus is $(A, Z - 1)$, whereas for Eq. (4.47), the initial nucleus is $(A, Z - 1)$ and the final nucleus is (A, Z) ; in the following, the proton number is used in the notation. The transition probability from one initial to one final state is not the quantity we are interested in, but rather its sum over all final states, averaged over all initial states. In other words, the quantity of interest is the reaction rate denoted \mathcal{R} .

$$\mathcal{R}_{\text{ec}} = \frac{2\pi}{\hbar} \left\langle \sum_{\vec{p}_{\nu_e}} \sum_{\vec{p}_{Z-1}} \sum_{J_{Z-1}} |\mathcal{M}_{\text{ec}}|^2 \delta(E_e - W - E_{\nu_e}) \right\rangle_{\vec{p}_e, s_e, \vec{p}_Z, J_Z} , \quad (4.48)$$

$$\mathcal{R}_\beta = \frac{2\pi}{\hbar} \left\langle \sum_{\vec{p}_{\bar{\nu}_e}} \sum_{\vec{p}_e} \sum_{s_e} \sum_{J_Z} |\mathcal{M}_\beta|^2 \delta(W - E_e - E_{\bar{\nu}_e}) \right\rangle_{\vec{p}_{Z-1}, J_{Z-1}}, \quad (4.49)$$

with E_e and $E_{\bar{\nu}_e}/E_{\nu_e}$ the energy of electrons and (anti-)neutrinos respectively. Note that there is no sum over the neutrino spin, because the direction of the spin of the (anti-)neutrino which is a massless particle is determined by the direction of its momentum [Goldhaber et al., 1958].

From now on, a number of approximations are used to drastically simplify the derivation:

1. The study follows the heavy nucleus approximation such that no transfer of momentum between the parent and daughter nuclei is taken into account. Therefore

$$\mathcal{R}_{ec} = \frac{2\pi}{\hbar} \left\langle \sum_{\vec{p}_{\bar{\nu}_e}} \sum_{J_{Z-1}} |\mathcal{M}_{ec}|^2 \delta(E_e - W - E_{\nu_e}) \right\rangle_{\vec{p}_e, s_e, J_Z}, \quad (4.50)$$

$$\mathcal{R}_\beta = \frac{2\pi}{\hbar} \left\langle \sum_{\vec{p}_{\bar{\nu}_e}} \sum_{\vec{p}_e} \sum_{s_e} \sum_{J_Z} |\mathcal{M}_\beta|^2 \delta(W - E_e - E_{\bar{\nu}_e}) \right\rangle_{J_{Z-1}}. \quad (4.51)$$

2. We shall only study reactions referred to as allowed, *i.e.* reactions which matrix element does not vanish in the limit of state final nucleus

$$\langle \Psi_f^{\text{nuc}} | \hat{H}_w | \Psi_i^{\text{nuc}} \rangle = 0, \quad (4.52)$$

with $\Psi_{i/f}^{\text{nuc}}$ the wave function of initial and final nuclei, and \hat{H}_w the weak interaction operator. The concept of allowed and forbidden decays and electron captures can be represented by a Taylor expansion of the electron and (anti-)neutrino wave functions, assuming that they are plane wave. Let us denote \vec{q} the sum or difference of the momentum of electrons \vec{p}_e and the momentum of neutrinos $\vec{p}_{\bar{\nu}_e}$. If we consider that the quantity $\vec{q} \cdot R/\hbar$ is small enough on the scale of nuclear energy, with R the radius of the nucleus, the wave function of electrons and neutrinos can be expanded as

$$e^{i\vec{q} \cdot \vec{r}/\hbar} \simeq 1 + \frac{i\vec{q} \cdot \vec{r}}{\hbar} + \frac{1}{2!} \left(\frac{i\vec{q} \cdot \vec{r}}{\hbar} \right)^2 + \dots; \quad (4.53)$$

for details, see chapter 17 of Povh et al. [2004]. The zero order term dominates the contribution to the matrix element, and we refer to the reaction reduced to the zeroth order term as allowed. However, if the inner product of the nuclei states at zero order vanishes, higher order terms in the Taylor expansion must be considered, and the reaction is referred to as forbidden.

In the following, we shall focus on allowed reactions, although forbidden reactions are briefly mentioned in the next paragraph. Because the first order of the Taylor expansion around zero of the exponential function (for the plane waves) is 1, the matrix

element does not depend on the momenta of electrons and neutrinos but is constant, so that

$$\mathcal{R}_{\text{ec}} = \frac{2\pi}{\hbar} \left\langle \sum_{J_{Z-1}} |\mathcal{M}_{\text{ec}}|^2 \sum_{\vec{p}_{\nu_e}} \delta(E_e - W - E_{\nu_e}) \right\rangle_{\vec{p}_e, s_e, J_Z}, \quad (4.54)$$

$$\mathcal{R}_{\beta} = \frac{2\pi}{\hbar} \left\langle \sum_{s_e} \sum_{J_Z} |\mathcal{M}_{\beta}|^2 \sum_{\vec{p}_{\bar{\nu}_e}} \sum_{\vec{p}_e} \delta(W - E_e - E_{\bar{\nu}_e}) \right\rangle_{J_{Z-1}}. \quad (4.55)$$

3. We suppose that the modulus of the matrix element does not depend on the spin of leptons, such that

$$\mathcal{R}_{\text{ec}} = \frac{2\pi}{\hbar} |\mathcal{M}_{\text{ec}}|^2 \left\langle \sum_{\vec{p}_{\nu_e}} \delta(E_e - W - E_{\nu_e}) \sum_{J_{Z-1}} \right\rangle_{\vec{p}_e, s_e, J_Z}, \quad (4.56)$$

$$\mathcal{R}_{\beta} = \frac{2\pi}{\hbar} |\mathcal{M}_{\beta}|^2 \left\langle \sum_{\vec{p}_{\bar{\nu}_e}} \sum_{\vec{p}_e} \delta(W - E_e - E_{\bar{\nu}_e}) \sum_{s_e} \sum_{J_Z} \right\rangle_{J_{Z-1}}. \quad (4.57)$$

Because electrons and (anti-)neutrinos have a continuous spectrum, the sums and averages over their momenta translates into three dimensional integrals³, such that

$$\mathcal{R}_{\text{ec}} = \frac{2\pi}{\hbar} |\mathcal{M}_{\text{ec}}|^2 \left\langle \int \frac{d^3 p_{\nu_e}}{(2\pi\hbar)^3} \int \frac{d^3 \vec{p}_e}{(2\pi\hbar)^3} \delta(E_e - W - E_{\nu_e}) \sum_{J_{Z-1}} \right\rangle_{s_e, J_Z}, \quad (4.58)$$

$$\mathcal{R}_{\beta} = \frac{2\pi}{\hbar} |\mathcal{M}_{\beta}|^2 \left\langle \int \frac{d^3 p_{\nu_e}}{(2\pi\hbar)^3} \int \frac{d^3 \vec{p}_e}{(2\pi\hbar)^3} \delta(W - E_e - E_{\bar{\nu}_e}) \sum_{J_Z} \right\rangle_{J_{Z-1}}. \quad (4.59)$$

We define the following integrals

$$I_{\text{ec}} = \frac{2\pi}{\hbar} \int \frac{d^3 p_e}{(2\pi\hbar)^3} \int \frac{d^3 p_{\nu_e}}{(2\pi\hbar)^3} \delta(E_e - W - E_{\nu_e}) = \frac{4m_e^5 c^4}{(2\pi)^3 \hbar^7} \left[\mathcal{F}(\bar{E}_F) - \mathcal{F}(\bar{W}) \right], \quad (4.60)$$

$$I_{\beta} = \frac{2\pi}{\hbar} \int \frac{d^3 p_e}{(2\pi\hbar)^3} \int \frac{d^3 p_{\bar{\nu}_e}}{(2\pi\hbar)^3} \delta(W - E_e - E_{\bar{\nu}_e}) = \frac{4m_e^5 c^4}{(2\pi)^3 \hbar^7} \underbrace{\left[\mathcal{F}(\bar{W}) - \mathcal{F}(1) \right]}_f, \quad (4.61)$$

with the barred quantities defined as $\bar{X} = X/(m_e c^2)$, E_F the Fermi energy of electrons, and

$$\mathcal{F}(x) = \frac{\sqrt{x^2 - 1}}{60} \left[20\bar{W}^2(x^2 - 1) + \bar{W}x(15 - 30x^2) + x^2(12x^2 - 4) - 8 \right] + \frac{\bar{W}}{4} \ln(\sqrt{x^2 - 1} + x). \quad (4.62)$$

³To operate the average over the momentum of electrons, one must sum all possible infinitesimally small states (in a discretization of the continuous spectrum) and divide by the total number of states available for the electron. This average appears for the electron capture, in which the electron is an initial and only predefined energy state.

The reaction rates of allowed electron captures and β^- -decay under the approximations described above render

$$\mathcal{R}_{\text{ec}} = \frac{2J_{Z-1} + 1}{2(2J_Z + 1)} |\mathcal{M}_{\text{ec}}|^2 \frac{4m_e^5 c^4}{(2\pi)^3 \hbar^7} [\mathcal{F}(\bar{E}_F) - \mathcal{F}(\bar{W})], \quad (4.63)$$

$$\mathcal{R}_{\beta} = \frac{2J_Z + 1}{2J_{Z-1} + 1} |\mathcal{M}_{\beta}|^2 \frac{4m_e^5 c^4}{(2\pi)^3 \hbar^7} f. \quad (4.64)$$

Electron captures and β -decays are subject to selection rules [Povh et al., 2004] with respect to the nuclear spin and parity denoted π . It defines whether the reaction is a Fermi process or a Gamow-Teller process

$$J_f = J_i = 0 \quad \text{and} \quad \pi_i = \pi_f \quad \rightarrow \quad \text{Fermi reaction} \quad (4.65)$$

$$J_f = -J_i = 1, -1 \quad \text{and} \quad \pi_i = \pi_f \quad \rightarrow \quad \text{Gamow-Teller reaction} \quad (4.66)$$

Experimental data is usually available for β^- -decays and not for electron captures. The quantity provided in nuclear data sheets is $ft_{1/2}$, with f the function given in Eq. (4.61) which is linked to the reaction rate according to

$$\mathcal{R}_{\beta} = \frac{\ln(2)}{t_{1/2}}. \quad (4.67)$$

To express the modulus of the matrix element of electron captures from that of the β^- -decays, one can use two fundamental symmetries:

- the charge conjugation transforms a particle onto its anti-particle; its related symmetry states that diagrams presented in Fig. 4.13, with an horizontal time axis, are equivalent

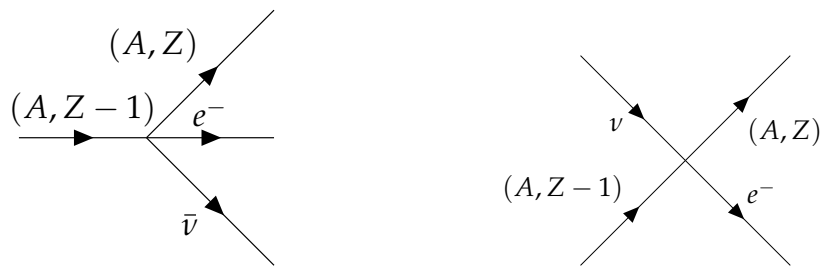


Figure 4.13: Equivalent diagrams for the weak interaction involving nuclei (A, Z) and $(A, Z - 1)$, through charge conjugation symmetry.

- the time reversal symmetry stating that diagrams presented in Fig. 4.14 are equivalent,

such that

$$|\mathcal{M}_{\text{ec}}| = |\mathcal{M}_{\beta}|. \quad (4.68)$$

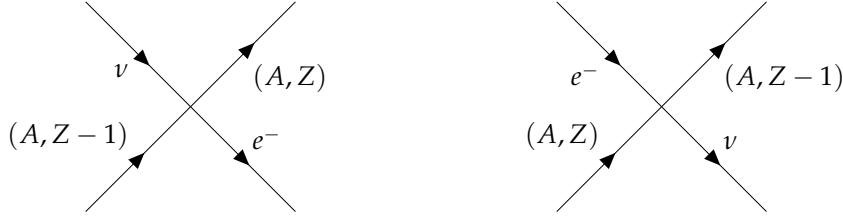


Figure 4.14: Equivalent diagrams for the weak interaction involving nuclei (A, Z) and $(A, Z - 1)$, through time reversal symmetry.

We can finally write the reaction rate of electron captures per one nucleus using the experimentally measured quantity $ft_{1/2}$ as

$$\mathcal{R}_{ec} = \frac{\ln(2)}{ft_{1/2}} \frac{2J_{Z-1}^{ec} + 1}{2(2J_Z^{ec} + 1)} \frac{2J_{Z-1}^{\beta} + 1}{2J_Z^{\beta} + 1} \left[\mathcal{F}(\bar{E}_F) - \mathcal{F}(\bar{W}) \right], \quad (4.69)$$

with J^{ec} and J^{β} the spin projections for nuclei of the electron capture and β^{-} -decay respectively. We can introduce the timescale of the electron capture defined as

$$\frac{1}{\tau_{ec}} = \frac{\ln(2)}{ft_{1/2}} \frac{2J_{Z-1}^{ec} + 1}{2(2J_Z^{ec} + 1)} \frac{2J_{Z-1}^{\beta} + 1}{2J_Z^{\beta} + 1}, \quad (4.70)$$

such that the reaction rate is written as

$$\mathcal{R}_{ec} = \frac{1}{\tau_{ec}} \left[\mathcal{F}(\bar{E}_F) - \mathcal{F}(\bar{W}) \right] \quad (4.71)$$

Before using this formula in the next section, let us make one final point about the plane wave function assumption for the β -particles to realize that one element has been overlooked. One should write the wave function of β -particles solving the Z -body Coulomb effect that protons have on the electron. Instead of solving this quite involved problem, we will consider that the momentum of the electron is affected by a charge factor which changes the β -spectrum. This factor is however included in the experimental data for the β^{-} -decay.

4.3.1.2 Application for the first few shells of an accreting crust

Assuming ^{56}Fe type of ashes for an accreting neutron star in the fully accreted crust approximation, the following chain of reactions occurs starting from the surface of the outer crust



with W the energy threshold of the reaction given in MeV, and the index $*$ designating an excited state. Because of the disfavor of odd proton number nuclei, the kinetics of the first, third and fifth reaction in this chain will dominate the study: the second electron capture occurs so fast after the first one that it can be considered instantaneous. In this section,

we present the reaction rate of the three electron captures that dominate the kinetics of the chain.

For each electron capture:

- the energy level diagrams are drawn for its corresponding β^- -decay, such that the quantity $ft_{1/2}$ extracted from nuclear data sheets on β^- -decays in the [ENSDF website \[National Nuclear Data Center, 2022\]](#) can be used;
- all channels of the β^- -decay are not presented, only the channel through which most of parent nuclei go through;
- the projection of the spin of the nucleus X and its parity J_X^π , as well as the energy level E_X in keV (denoted 0.0 for the ground state) are presented in the diagram.

The diagram takes the generic form

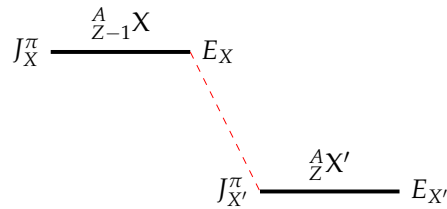


Figure 4.15: Generic energy level diagram of the β^- -decay.

4.3.1.3 For the process: ${}^{56}_{26}\text{Fe} \rightarrow {}^{56}_{25}\text{Mn} \rightarrow {}^{56}_{24}\text{Cr}$

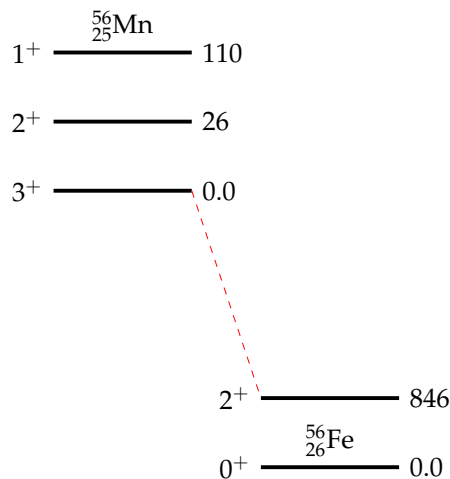


Figure 4.16: Energy level diagram for the Gamow-Teller transition ${}^{56}_{25}\text{Mn} \rightarrow {}^{56}_{26}\text{Fe}$.

This first process is the most peculiar of our reaction chain. The allowed transition is not energetically favorable, such that an allowed electron capture operated on ${}^{56}\text{Fe}$ produces an excited state ${}^{56}\text{Mn}^*$, with a 110 keV excitation energy. The most energetically favorable transition would be a doubly forbidden transition, for which the final nucleus is in its ground

state. However, the time required for the doubly forbidden reaction to occur is particularly long⁴. As we are studying an accreting crust for which the pressure is continuously increased during the active phase of accretion, the chemical potential of electrons increases as well. Assuming an active accretion rate of 10^{-8} solar mass per year, the time required for the chemical potential to reach the threshold of the next electron capture is of ~ 0.3 years. Given the time required for the doubly forbidden transition to occur, the chemical potential of electrons shall reach the threshold for the allowed transition in a much shorter timescale than it takes for the forbidden decay to operate. Therefore, we consider the reaction $^{56}\text{Fe} \rightarrow ^{56}\text{Mn}^*$; the daughter nucleus being in its excited state will decay through γ rays in a very short timescale (of the order of $\sim 10^{-10}\text{s}$).

The nuclear data sheets of this β^- -decay is provided for the allowed Gamow-Teller transition from the ground state nucleus $^{56}\text{Mn}^{3+}$ to the excited state $^{56}\text{Fe}^{2+}$, whereas we need data for the allowed Gamow-Teller electron capture from the ground state $^{56}\text{Fe}^{0+}$ to the excited state nucleus $^{56}\text{Mn}^{1+}$. As both transitions are allowed, and we approximate that the matrix element of the transition does not depend on the recoil momentum of nuclei, the timescale of both reactions is approximated to be the same such that

$$\frac{1}{\tau_{\text{ec}}} = \frac{\ln(2)}{ft_{1/2}} \frac{21}{10} = 1.154 \times 10^{-7} \text{ s}, \quad (4.72)$$

with

$$ft_{1/2} = 10^{7.101} \text{ s}. \quad (4.73)$$

The diagram of the second electron capture is

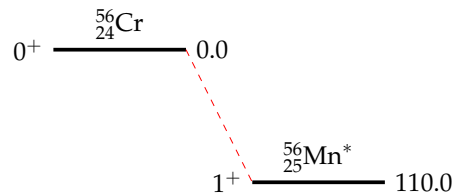


Figure 4.17: Energy level diagram for the Gamow-Teller transition $^{56}_{24}\text{Cr} \rightarrow ^{56}_{25}\text{Mn}$.

4.3.1.4 For the process: $^{56}_{24}\text{Cr} \rightarrow ^{56}_{23}\text{V} \rightarrow ^{56}_{22}\text{Ti}$

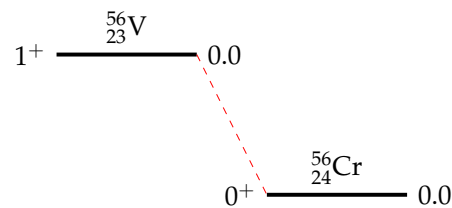


Figure 4.18: Energy level diagram for the Gamow-Teller transition $^{56}_{23}\text{V} \rightarrow ^{56}_{24}\text{Cr}$.

⁴A quick estimation of the half-time for a forbidden β^- -decay of order l can be done using the half-life for the allowed β^- -decay, and the Taylor expansion of electron and neutrino plane wave functions in the matrix element of the reaction [Povh et al., 2004].

The timescale of the reaction rate for this electron capture gives

$$\frac{1}{\tau_{\text{ec}}} = \frac{\ln(2) 9}{ft_{1/2} 2} = 7.482 \times 10^{-5} \text{ s}^{-1}, \quad (4.74)$$

with

$$ft_{1/2} = 10^{4.62} \text{ s}. \quad (4.75)$$

The diagram of the second electron capture is

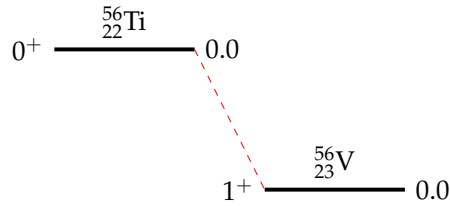


Figure 4.19: Energy level diagram for the Gamow-Teller transition ${}^{56}_{22}\text{Ti} \rightarrow {}^{56}_{23}\text{V}$.

4.3.1.5 For the process: ${}^{56}_{22}\text{Ti} \rightarrow {}^{56}_{21}\text{Sc} \rightarrow {}^{56}_{20}\text{Ca}$

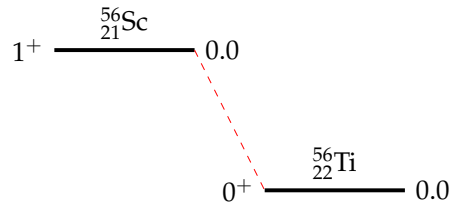


Figure 4.20: Energy level diagram for the Gamow-Teller transition ${}^{56}_{21}\text{Sc} \rightarrow {}^{56}_{22}\text{Ti}$.

The timescale of the reaction rate for this electron capture gives

$$\frac{1}{\tau_{\text{ec}}} = \frac{\ln(2) 9}{ft_{1/2} 2} = 1.107 \times 10^{-3} \text{ s}^{-1}, \quad (4.76)$$

with

$$T_{1/2} = 26 \text{ ms}, \quad (4.77)$$

defined as the half time for all channels of the reaction, whose value was taken from [Crawford et al. \[2010\]](#). Assuming that the one channel presented in Fig.4.20 dominates all other channels of the reaction, we approximate

$$ft_{1/2} = 10^{3.45} \text{ s}. \quad (4.78)$$

The diagram of the second electron capture is represented as

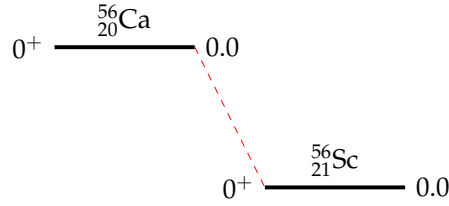


Figure 4.21: Energy level diagram for the Fermi transition ${}^{56}_{20}\text{Ca} \rightarrow {}^{56}_{21}\text{Sc}$.

4.3.2 The linear mixing rule approach to a mixture of nuclei

In order to assess the role of the kinetics of electron captures on deep crustal heating, we must first establish an equation of state model for a mixture of two nuclei. The mixture is made of even proton number parent nuclei of the first electron capture, and the daughter nuclei of the next electron capture, later on referred to as the grand-daughter nuclei. Because odd proton number nuclei are unstable, the electron capture from an odd proton number nucleus to an even proton number nucleus is considered instantaneous, such that the mixture does not contain the daughter nuclei of the first electron capture.

A simple approach is taken to establish the relation between the pressure and the density -equation of state- in the outer crust: a lattice allowing for the mixture of two nuclei is permeated by a gas of electrons. It is a reasonable approximation to consider that the contribution to the outer crust pressure is dominated by the pressure of degenerate electrons, denoted P_e . The total pressure in the crust is given by

$$P = P_e + P_{\text{lat}} , \quad (4.79)$$

with P_{lat} the pressure associated to the lattice correction. The pressure of a degenerate gas of relativistic electrons is derived in chapter 2 of [Shapiro and Teukolsky \[1986\]](#) such that

$$P_e = \frac{(m_e c^2)^4}{(\hbar c)^3} \phi \left(n_e^{1/3} \frac{(3\pi^2)^{1/3} \hbar}{m_e c} \right) . \quad (4.80)$$

The dimensionless function $\phi(x)$ is given by

$$\begin{aligned} \phi(x) &= \frac{x(1+x^2)^{1/2} \left(\frac{2x^2}{3} - 1 \right) + \ln \left(x + (1+x^2)^{1/2} \right)}{8\pi^2} \\ &= \frac{1}{12\pi^2} (x^4 - x^2) + \frac{\ln(2x)}{8\pi^2} - \frac{1}{16\pi^2} + \mathcal{O} \left(\frac{1}{x^4} \right) , \end{aligned} \quad (4.81)$$

with $\mathcal{O} \left(\frac{1}{x^4} \right)$ designating terms of order x^{-4} or lower. The quantity x is the relativity parameter and is defined as the ratio between the Fermi momentum of the particle over its mass energy.

The lattice correction pressure, or in other words the Coulomb correction to a rigid electron background, must be established for a mixture of parent and grand-daughter ions with proton number Z and $Z - 2$ respectively. According to the linear mixing rule discussed in

section 2.4.7 of [Haensel et al. \[2007a\]](#), the Coulomb correction energy density denoted \mathcal{E}_{lat} is given by

$$\mathcal{E}_{\text{lat}}(Z, n_e) \simeq \frac{1}{n_I} (n_{I,Z} \mathcal{E}_{\text{Coul}}(Z) + n_{I,Z-2} \mathcal{E}_{\text{Coul}}(Z-2)), \quad (4.82)$$

with n_I the density of ions, $n_{I,Z}$ the density of ions with proton number Z . The Coulomb correction energy density for the ion with proton number Z is given by

$$\mathcal{E}_{\text{Coul}}(Z) = -0.9 n_{I,Z}^{4/3} \left(\frac{4\pi}{3} \right)^{1/3} Z^2 e^2. \quad (4.83)$$

We introduce the quantity denoted X , which corresponds to the ratio between the number of parent nuclei, over the total number of nuclei. The relation between the electron density n_e , and the ion density for a rigid electron background is given by

$$n_e = n_I (X_0 Z_0 + X_2 Z_2); \quad (4.84)$$

Z_0 and Z_2 designate the proton number of the parent and grand-daughter nuclei. X_0 designates the ratio of the parent nucleus over the total number of nuclei, and X_2 designates the ratio of the grand-daughter nucleus over the total number of nuclei. In the zero temperature limit, the relation between the lattice correction pressure and the Coulomb correction for a mixture of nuclei with proton number Z and $Z-2$ gives

$$P_{\text{lat}} = \frac{\mathcal{E}_{\text{lat}}}{3} = -0.3 \left(\frac{4\pi}{3} \right)^{1/3} n_e^{4/3} e^2 \mathcal{F}(X), \quad (4.85)$$

with the linear mixing rule function

$$\mathcal{F}(X) = \frac{(Z-2)^{5/3} + X(Z^{5/3} - (Z-2)^{5/3})}{Z + 2(X-1)}. \quad (4.86)$$

The relation between the baryon density, denoted n , and the density of electrons is given by

$$n = \frac{n_e A}{XZ + (1-X)(Z-2)}, \quad (4.87)$$

such that the expression for the equation of state renders

$$P = \frac{(m_e c^2)^4}{(\hbar c)^3} \phi(\alpha(X) n^{1/3}) + \beta(X) n^{4/3}, \quad (4.88)$$

with

$$\alpha(X) = (3\pi^2)^{1/3} \frac{\hbar c}{m_e c^2 A^{1/3}} [XZ + (1-X)(Z-2)]^{1/3}, \quad (4.89)$$

$$\beta(X) = -0.3 \left(\frac{4\pi}{3} \right)^{1/3} e^2 \mathcal{F}(X) \frac{[XZ + (1-X)(Z-2)]^{4/3}}{A^{4/3}}. \quad (4.90)$$

The chemical potential of a degenerate gas of electrons in a lattice is

$$\mu_e(X) = \sqrt{n^{2/3}[\alpha(X)m_e c^2]^2 + (m_e c^2)^2} + 4\beta(X)n^{1/3}, \quad (4.91)$$

with $\mathcal{E}_{F,e}$ the energy density of electrons on their Fermi surface. The relation between the chemical potential and the baryon density, assuming that the electron captures are instantaneous ($X = 1$ for each shell), is presented in Fig. 4.22 for the first three shells of the accreted outer crust with ^{56}Fe ashes. In this figure, we also present the relative difference between the above mentioned approach (relativistic approach), and the ultra-relativistic approach. For the shallowest shell of the outer crust, the ultra-relativistic approximation leads to an error of $\sim 13\%$, for the lowest densities, which falls to 1% at the upper boundary density of the shell. We are interested in designing the equation of state for a mixed layer of nuclei after the threshold that leads to the next shell, therefore, at densities around $\sim 10^{-6} \text{ fm}^{-3}$. Using the ultra-relativistic approach is therefore reasonable.

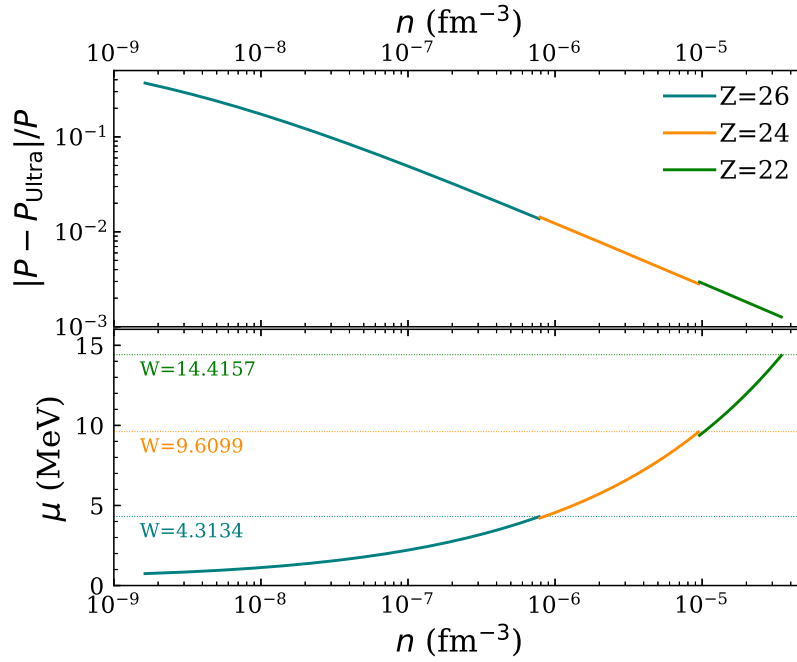


Figure 4.22: Relation between the chemical potential μ and the baryon density n in the first three shells of the accreted outer crust, in the bottom panel. Relative difference between the equation of state calculated in the relativistic approach, and the ultra-relativistic approach in the upper panel.

In the above mentioned mixture of nuclei approach, the properties of the six electron captures of the chain we study are presented in Table 4.2.

Z_0	P_{th} (MeV/fm ⁻³)	n_{th} (fm ⁻³)	W_1 (MeV)	W_2 (MeV)
26	3.776×10^{-7}	7.872×10^{-7}	4.313	2.135
24	9.547×10^{-6}	9.521×10^{-6}	9.610	7.269
22	4.824×10^{-5}	3.491×10^{-5}	14.416	12.514

Table 4.2: Properties of the electron capture pairs $(56, 26) \rightarrow (56, 24)$, $(56, 24) \rightarrow (56, 22)$ and $(56, 22) \rightarrow (56, 20)$ calculated in the framework of the linear mixing rule equation of state. The pressure threshold P_{th} of the reaction, the equivalent baryon density n_{th} and the reaction energy of the first and second electron capture, respectively W_1 and W_2 , are presented for three parent proton number Z_0 .

4.3.3 The continuity equation

In the previous section, we have introduced the quantity X : the ratio of the number of parent nuclei of an electron capture on nucleus (A, Z) , over the total number of nuclei (sum of parent and grand-daughter nuclei). In the accreting crust of a neutron star, X depends on the depth in the star, and on the time variable t through the accretion rate of the binary system. In the following, we present and solve the equation followed by X during the active and quiescence phases of accretion.

4.3.3.1 Formulation of the continuity equation

During accretion, for a spherically symmetric accretion rate, freshly accreted matter is flowing and sinking towards the core with a velocity

$$v(z) = \frac{\dot{M}}{4\pi R^2 m_B n(z)}, \quad (4.92)$$

with \dot{M} the accretion rate, R the total radius of the star, m_B the mass of a baryon, z the radial variable defined as $z = R - r$ (the variable r is oriented towards the surface), and n the baryon density. The product of the ratio X with the baryon density is governed by the continuity equation

$$\partial_t(nX) + \partial_z(vnX) = -nX\mathcal{R}, \quad (4.93)$$

with \mathcal{R} the reaction rate of the first electron capture defined as the number of reactions per unit time, and per nucleus. Using the Tolman-Oppenheimer-Volkoff equations approximated in the crust, cut to the Newtonian limit⁵, we operate a change from the radial variable z to the pressure

$$\frac{\partial P}{\partial r} = -\frac{GM}{R^2}\epsilon, \quad (4.94)$$

with M the total mass of the star, and ϵ the energy density which is considered equivalent to the mass density ρ such that $\epsilon \simeq \rho = m_0 n$ with m_0 the mass of a baryon. The continuity

⁵The Newtonian limit of the Tolman-Oppenheimer-Volkoff equations falls to the Poisson's equation.

equation is therefore given by

$$\frac{\partial}{\partial t} \ln(nX) + \frac{GM\dot{M}}{4\pi R^4} \frac{\partial \ln X}{\partial P} = -\mathcal{R}(X, P). \quad (4.95)$$

The reaction rate was explicitly derived in section 4.3.1.1, and depends on the pressure through the dependence of the function \mathcal{F} on the Fermi energy of electrons, see Eq. (4.69) in section 4.3.1.1. The accretion timescale is defined in the Newtonian limit, as the time required to push accreted matter to the pressure threshold P_{th} of the reaction

$$\tau_{\text{acc}}(t) = \frac{4\pi R^4}{GM\dot{M}(t)P_{\text{th}}}. \quad (4.96)$$

The continuity equation can be rewritten in a dimensionless form as

$$\tau_{\text{ec}} \frac{\partial}{\partial t} \ln(nX) + \frac{\tau_{\text{ec}}}{\tau_{\text{acc}}(t)} \frac{\partial \ln X}{\partial \tilde{P}} = -\left[\mathcal{F}(\bar{E}_F(P)) - \mathcal{F}(\bar{W})\right], \quad (4.97)$$

with $\tilde{P} = P/P_{\text{th}}$.

4.3.3.2 Astrophysically motivated accretion rate

We intend to study a realistic accretion rate motivated by X-ray observations of various sources in accreting low-mass X-ray binaries. Several sources have been observed alternating between active accretion stages lasting from weeks to years, and quiescence stages lasting from months to decades. The typical duration of active accretion can be informed by the observation of X-ray outbursts (lasting surge in luminosity) of quasi-persistent sources EXO 0748–676 (see Parikh et al. [2020] and reference therein), KS 1731–260 (see Merritt [2017] and reference therein), XTE J1701–462 Fridriksson et al. [2010] and IGR J17480–2446 (see Ootes et al. [2019] and reference therein) which lasted respectively 24 years, 12.5 years, 1.6 years and 10 weeks.

Because the field of X-ray astronomy in transient neutron star observations flourished only a few decades ago, we have not observed many stars repeating the alternation of active accretion and quiescence. However, the source MXB 1659–29 (see Parikh et al. [2019] and reference therein) presented two well monitored outbursts lasting respectively 2.5 and 1.7 years interspersed by a quiescence period of 14 years; this source was first observed in 1976 during an outburst estimated to last between 2 and 2.5 years. In this study, we use the active accretion time of four years, and consider that the duration of quiescence is one order of magnitude larger than the active accretion time, such that $t_q = 10t_a$.

The average accretion rate during active phases were estimated for the sources XTE J1701–462 Fridriksson et al. [2010] and IGR J17480–2446 Degenaar and Wijnands [2011] to be respectively $1.7 \times 10^{-8} M_{\odot}$ per year and $3 \times 10^{-9} M_{\odot}$ per year. The observation of X-ray bursts indicate a luminosity variability in the active phase from which the accretion rate as a function of time during active phases can be inferred, however we do not intend to discuss such variability, but rather to use a mean value of the accretion rate in the active phase. The

active accretion rate, denoted \dot{M}_a , is described by an exponential onset and offset such that

$$\dot{M}_a(t) = \dot{M}_{\max} \left(\frac{1}{1 + e^{\alpha(t-t_a+t_0)}} + \frac{1}{1 + e^{-\alpha(t-t_0)}} - 1 \right), \quad (4.98)$$

with \dot{M}_{\max} the accretion rate outside the onset and offset of active accretion, t_0 the time allocated to the onset and offset chosen to be 5% of the active time, and α a constant set such that after t_0 , the maximum accretion is reached. In this study, unless otherwise stipulated, the accretion rate is $\dot{M}_{\max} = 10^{-8} M_{\odot}$ per year, a reasonable value with respect to observed mean accretion rate during active accretion.

4.3.3.3 Heat release

The heat release per nucleus of each process of the pair of electron captures, respectively denoted q_1 and q_2 , assuming that the neutrinos escape the system immediately, is given by

$$q_1 = \mathcal{M}(A, Z)c^2 - \mathcal{M}(A, Z-1)c^2 + \mu_e, \quad (4.99)$$

$$q_2 = \mathcal{M}(A, Z-1)c^2 - \mathcal{M}(A, Z-2)c^2 + \mu_e, \quad (4.100)$$

with μ_e the chemical potential of electrons. The heat per nucleus released by the pair of electron captures is the sum of the heat release of the two electron captures

$$q(X, P) = 2\mu_e(X, P) - (W_1 + W_2), \quad (4.101)$$

with W_1 and W_2 the reaction thresholds of the first and second electron capture respectively. In the instantaneous approach, all the heat is released at exactly the pressure threshold such that $\mu_e(P_{\text{th}}) = W_1$, and

$$q_{\text{instan}} = W_1 - W_2. \quad (4.102)$$

Less than the heat release per nucleus, we are interested in the heat released in the whole layer of electron capture during a cycle of accretion. To that purpose, we define the heating rate per unit volume at given pressure and given time as follows

$$\dot{q}(P, t) = q(X, P)\mathcal{R}(P)\frac{n}{A}X(P, t), \quad (4.103)$$

with n/A the density of nuclei (required because the reaction rate is defined per nucleus). Because spherical symmetry is considered, the integral over the volume corresponds to the heating rate in the layer as a function of time

$$\dot{Q}(t) = \frac{4\pi R^4 P_{\text{th}}}{GMm_B} \int_1^{P(X=0)/P_{\text{th}}} \frac{\dot{q}(\bar{P}, t)}{n} d\bar{P}. \quad (4.104)$$

Finally, the total heat released during one cycle of accretion, denoted Q , is given by

$$Q = \int_0^{t_a+t_q} \dot{Q}(t) dt. \quad (4.105)$$

To compare our results to the instantaneous approach, it is convenient to define this quantity per baryon, by dividing Q by the number of accreted baryons during the cycle of accretion

$$N_b = \int_0^{t_a} \frac{\dot{M}_a(t)}{m_B} dt. \quad (4.106)$$

In the following, neutrino losses are neglected in our study of matter heating in the crust.

4.3.4 Stationary solution

As a first step, let us solve a simplified version of Eq. (4.97), in which the solution does not depend on the time variable: $X(P, t) \rightarrow X(P)$. Therefore, we solve the stationary form of the continuity equation in the active phase of accretion

$$\frac{\tau_{\text{ec}}}{\tau_{\text{acc}}} \frac{\partial \ln X}{\partial \bar{P}} = - \left[\mathcal{F}(\bar{E}_F(P)) - \mathcal{F}(\bar{W}) \right], \quad (4.107)$$

with the accretion timescale defined by the accretion rate at peak activity $10^{-8} M_\odot$ per year. One boundary condition is required to solve this equation: $X(P = P_{\text{th}}) = 1$, which is equivalent to stating that right before the threshold pressure is reached, all nuclei are parent nuclei. Results are presented in Fig. 4.23, Fig. 4.24 and Fig. 4.25:

- For the shallowest shell, with parent nuclei proton number $Z_0 = 26$:

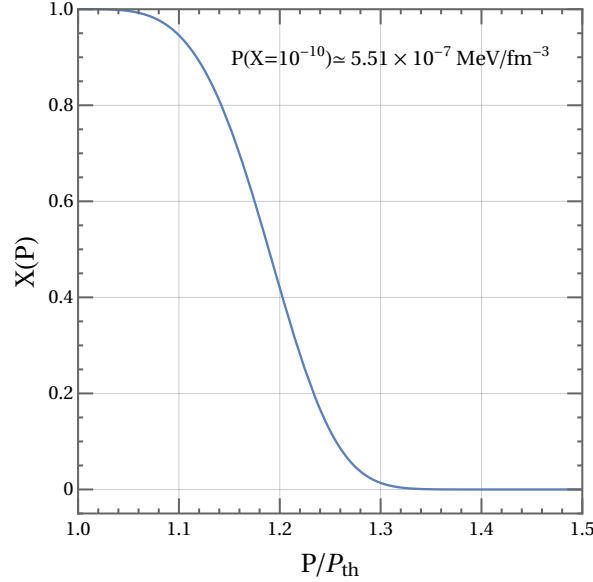


Figure 4.23: Solution to the stationary form of the continuity equation for parent proton number $Z_0 = 26$.

The range of pressure required for the parent nuclei fraction X to fall to zero is referred to as the layer of electron capture. It is defined by the pressure at which the ratio X numerically vanishes (10^{-10}), such that the range of pressure for the layer is $[3.78 \times 10^{-7} - 5.51 \times 10^{-7}] \text{ Mev}/\text{fm}^{-3}$.

- For the reaction with parent proton number $Z_0 = 24$:

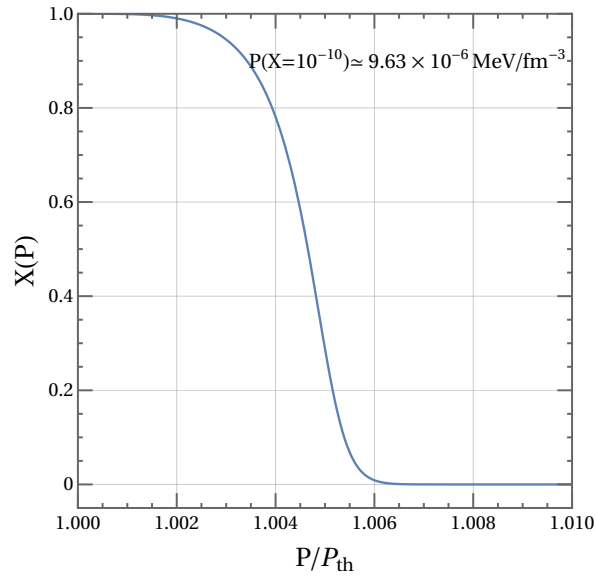


Figure 4.24: Solution to the stationary form of the continuity equation for parent proton number $Z_0 = 24$.

The range of pressure for the layer is: $[9.55 \times 10^{-6} - 9.63 \times 10^{-6}] \text{ MeV/fm}^{-3}$.

- For the reaction with parent proton number $Z_0 = 22$:

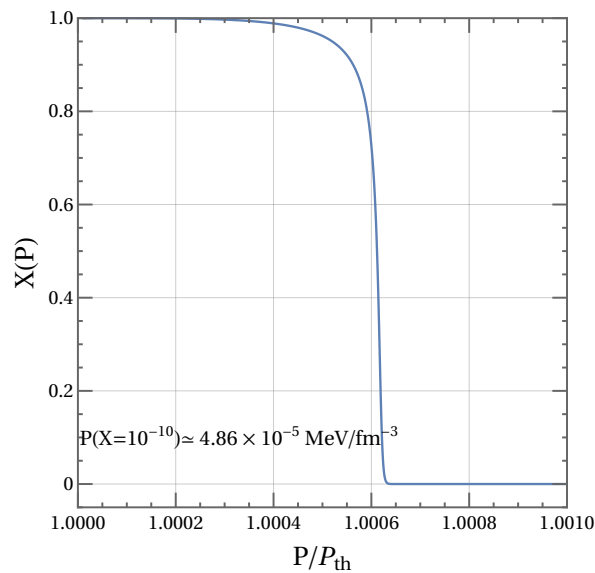


Figure 4.25: Solution to the stationary form of the continuity equation for parent proton number $Z_0 = 22$.

The range of pressure for the layer is: $[4.82 \times 10^{-5} - 4.86 \times 10^{-5}] \text{ MeV/fm}^{-3}$.

The layer of electron captures is non negligible for the reaction with parent proton number $Z_0 = 26$, and is relatively thinner for the reaction with parent proton number $Z_0 = 22$.

The steepness of the decrease of X can be anticipated from the reaction rate formula. The constant quantity $1/\tau_{\text{ec}}$ presented in Eq. (4.72), Eq. (4.74), and Eq. (4.76) established from experimental data on β^- -decay reactions, dictates the pressure derivative in the continuity equation (4.107): the larger this quantity, the steeper the decrease of X .

It is interesting to note that the absolute thickness of the electron capture layers are quite similar for the three shells we study. For $Z_0 = 26$, $Z_0 = 24$ and $Z_0 = 22$, this layer is of the order of 10^{-7} MeV/fm³ in pressure thickness. In terms of mass of the layer which can be calculated from Eq. (4.9), it corresponds to approximately $10^{-8} M_{\odot}$. The number of baryons in the layer of electron captures are also approximately the same for all three shells studied.

Now let us discuss the heat release associated to those results: in the following, we assume that the stationary solution prevails during the whole of the active accretion. From Eq. (4.103), the dependence on the pressure of the heating rate \dot{q} implies that reactions triggered deeper in the layer, release more heat. Therefore, the thicker the layer of electron captures, the larger the heat release. In Fig. 4.26, we present the heating rate per unit volume, as a function of the pressure in the star for $Z_0 = 26$ and $Z_0 = 22$. To assess the role of the pressure dependence on the heating rate per unit volume, we also represent the value of the heating rate for $q = q_{\text{instan}}$; note that this is not the heating rate per unit volume for the instantaneous approach, as the heat should entirely be released at the pressure threshold.

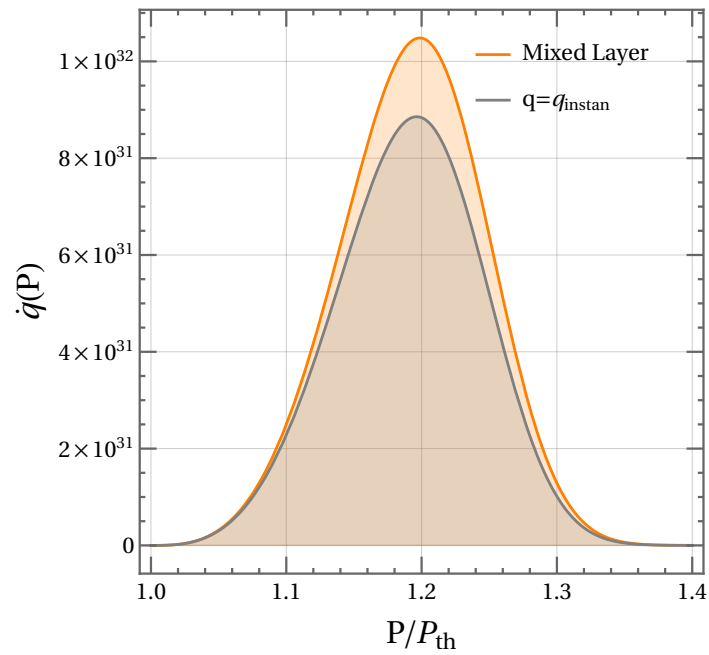
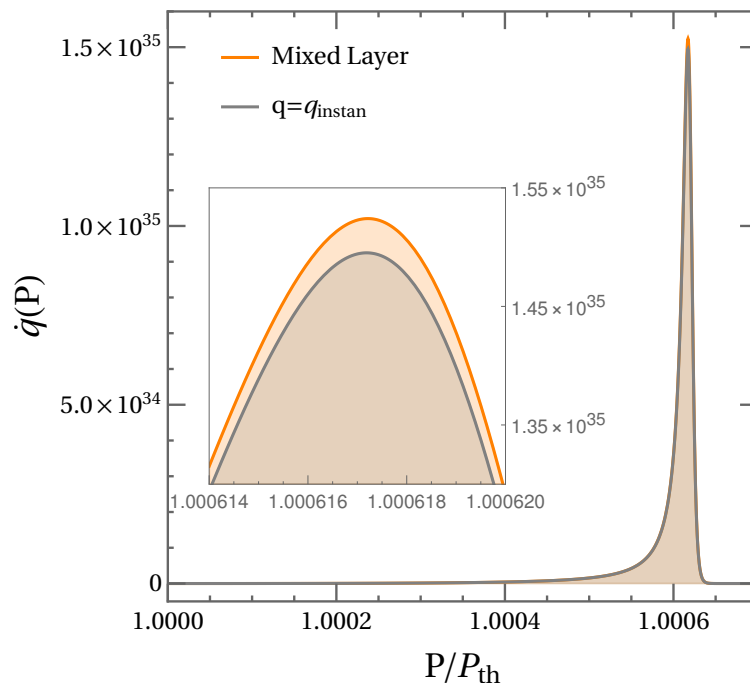
(a) $Z_0 = 26$ (b) $Z_0 = 22$

Figure 4.26: Heating rate per volume \dot{q} as a function of the pressure in the crust for the parent nuclei with proton number $Z_0 = 26$ and $Z_0 = 22$.

From Fig. 4.26a and Fig 4.26b, we can conclude the following:

- The heating rate per volume peaks to a higher value for the reaction with parent proton

number $Z_0 = 22$ than for $Z_0 = 26$: this can be explained by the value of the heat release per nucleus, which is higher for deeper shells.

- The pressure dependence affects the heating rate relatively more for the reaction with parent proton number $Z_0 = 26$ than $Z_0 = 22$: the thickness of the layer capture is relatively thicker for $Z_0 = 26$ than for $Z_0 = 22$, therefore, nuclei can go through the reaction deeper in the shell, and release more heat. It is also interesting to note that in Fig. 4.26a, while the $q = q_{\text{instan}}$ approach has the shape of a perfectly symmetric Gaussian, our mixed layer approach is ever so slightly asymmetric.

In the stationary approach to the equation, we can estimate the total heat release.

- For $Z_0 = 26$: in the instantaneous approach, 38.91 keV per accreted nucleon is released, and in the mixed layer approach, 50 keV per accreted nucleon is released; this is equivalent to a $\sim 30\%$ increase of the heat release in the mixed layer approach.
- For $Z_0 = 24$: in the instantaneous approach, 41.81 keV per accreted nucleon is released, and in the mixed layer approach, 47.21 keV per accreted nucleon is released; this is equivalent to a $\sim 13\%$ increase of the heat release in the mixed layer approach.
- For $Z_0 = 22$: in the instantaneous approach 33.96 keV per accreted nucleon is released, and in the mixed layer approach 38.26 keV per accreted nucleon is released; this is equivalent to a $\sim 11\%$ increase in the mixed layer approach.

In overall, the heat release in the first few shells of the outer crust of accreting neutron stars is affected by the treatment of electron capture's kinetics. The thicker the layer of electron capture, the larger the heat release.

4.3.5 Solution to the full continuity equation

To solve the full continuity equation, we specify an accretion cycle of four years of active accretion with a 0.2 years onset and offset, followed by forty years of quiescence. In addition to the boundary condition $X(t, P = P_{\text{th}}) = 1$, an initial condition is required to solve the equation: we choose $X(t = 0, P) = 1$, a condition that shall have no consequence after the first accretion cycle. In the following, results are presented for the second cycle: active accretion starts at 44 years and ends at 48 years, and is followed by quiescence until the next cycle starts at 88 years.

The solution for the active phase of the second cycle is presented in Fig. 4.27 as a contour representation of the two variable solution $X(t, P)$, for the parent proton number $Z_0 = 26$. During the onset of accretion, *i.e.* between 44 years and 44.2 years, the value of the accretion rate is not large enough to increase the profile of $X(t, P)$ which remains at its pre-active phase level. When the accretion rate peaks at its maximum value, around 0.7 years are required to reach the stationary profile: from 0.2 to 0.7 years, the time derivative and the pressure derivative of Eq. (4.97) battle one another, the pressure derivative increasingly dominating the time derivative, until the latter can be completely neglected at 0.7 years. The stationary

profile continues until the offset of the active phase is triggered at 47.8 years. The total heat released during the active phase is 41 keV per accreted nucleon for the first four years of the cycle, which corresponds to an increase of around 7% compared to the instantaneous approach.

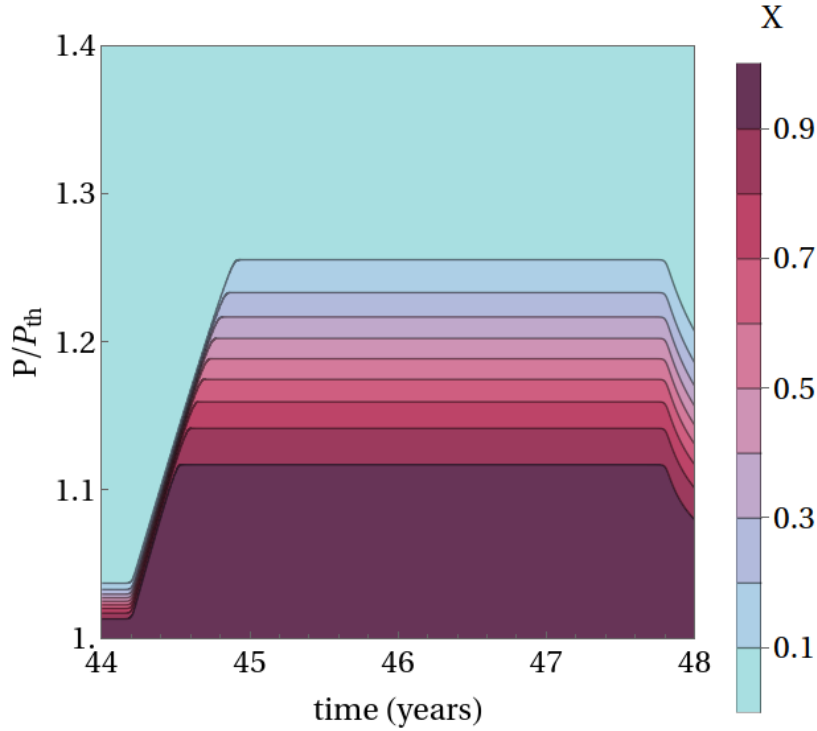


Figure 4.27: Solution $X(t, P)$ of the continuity equation during the active phase of the second cycle for the reaction with parent proton number $Z_0 = 26$.

Contrary to the instantaneous approach, reactions can also occur during the quiescence phase; from the solution established at the end of the active phase $X(t = 48, P)$, the following differential equation must be solved

$$\tau_{\text{ec}} \frac{\partial}{\partial t} \ln(nX) = - \left[\mathcal{F}(\bar{E}_F(P)) - \mathcal{F}(\bar{W}) \right]. \quad (4.108)$$

The solution of the mixed layer approach during the quiescence phase is presented in Fig. 4.28. The total heat released during the quiescence phase is 4.1 keV per accreted nucleon. During one cycle (active phase and quiescence), a total energy of approximately 45 keV per accreted nucleon is released, *i.e.* an 18% increase from the instantaneous approach.

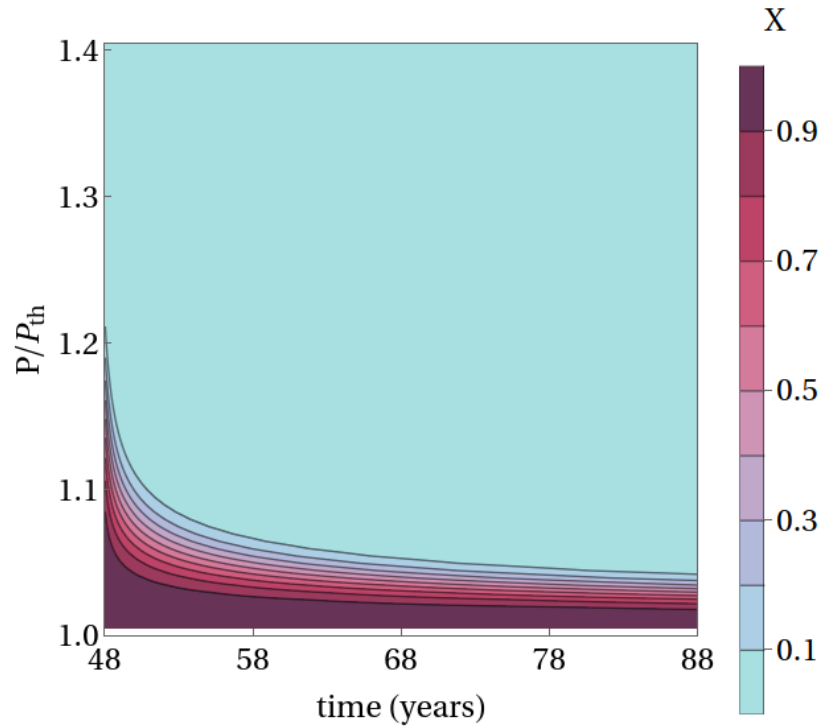


Figure 4.28: Solution $X(t, P)$ of the continuity equation during the quiescence phase of the second cycle for the reaction with parent proton number $Z_0 = 26$.

The solution $X(t, P)$ at the end of the quiescence phase is not step like: the cycles of accretion are not completely independent. The quiescence time required for the solution $X(t, P)$ to reach a profile which is at most 1% of the thickness of the stationary solution is of the order of a few hundred years.

The heat released during one cycle of accretion depends on the active phase, and whether or not it is long enough to reach the stationary profile. In Fig. 4.29, we present the contour representation of $X(t, P)$ during two cycles of 0.2 years of active accretion followed by 2 years of quiescence. The stationary profile is not reached before the accretion stops; the quiescence is not long enough to ensure that the profile at the start of the next cycle is step-like. The total heat released per accreted nucleon during one cycle is 43.39 keV, which is equivalent to an 11% increase from the instantaneous approach. Reaching the stationary profile is therefore very important to attain a large heat release; this stationary profile is reached as fast as the electron capture timescale τ_{ec} will allow.

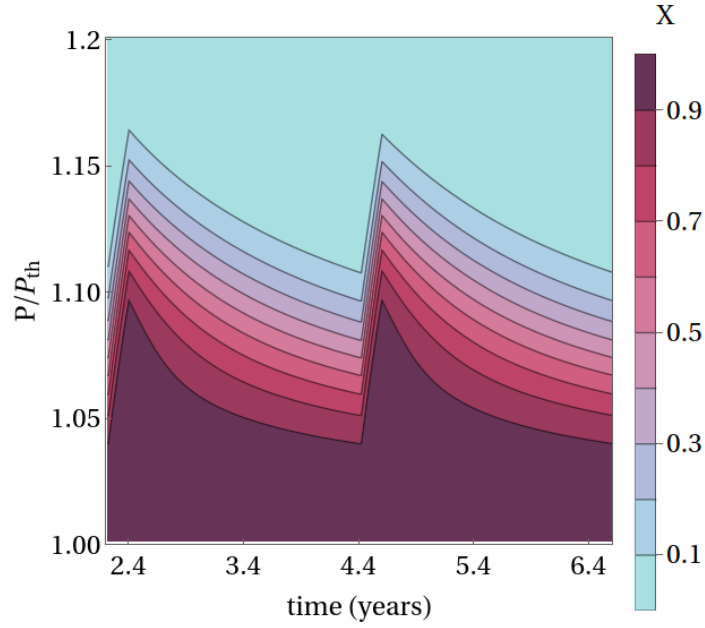


Figure 4.29: Solution $X(t, P)$ of the continuity equation for the reaction with parent proton number $Z_0 = 26$ for two accretion cycles of 0.2 years of active accretion followed by 2 years of quiescence.

Finally, the accretion rate influences the heat release. We present the stationary solution, as well as the solution $X(t, P)$ to the continuity equation for the cycle of 4 years of active accretion followed by 40 years of quiescence with a peak accretion rate of $10^{-10} M_\odot$ per year, respectively in Fig. 4.30a and Fig. 4.30b. Although the times for active accretion and quiescence are the same as the first accretion scenario studied in this section, the lower value of the accretion rate leads to a smaller layer of electron captures in the stationary case. When the full continuity equation is solved, we can see that the stationary solution is not reached during the active phase. The heat released associated this scenario is 45.73 keV in our approach and 44.41 keV in the instantaneous approach. We can conclude that even though reaching the stationary profile increases the heat release more significantly, even small layers of electron captures lead to an increase in the heat release compared to the instantaneous approach.

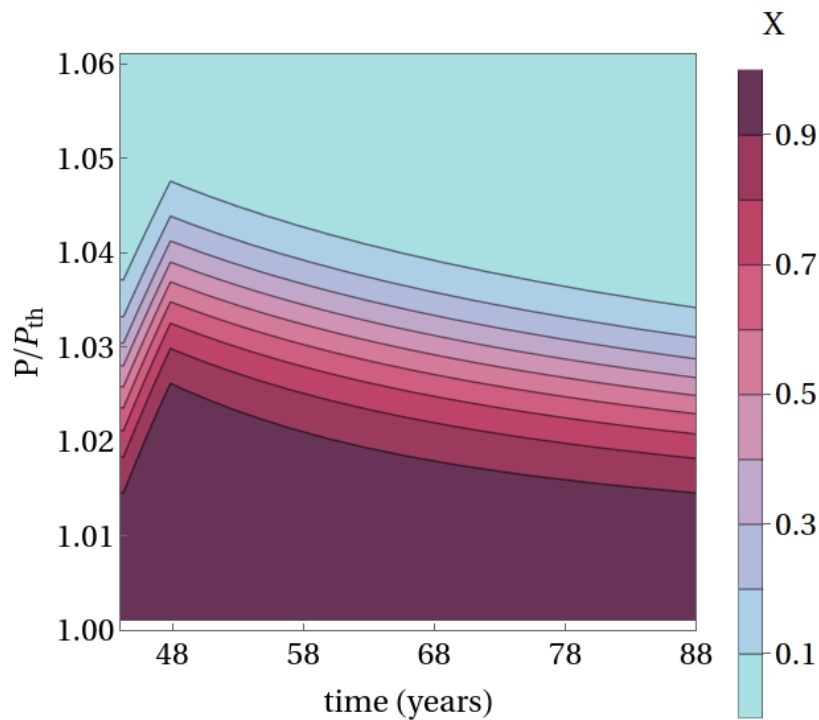
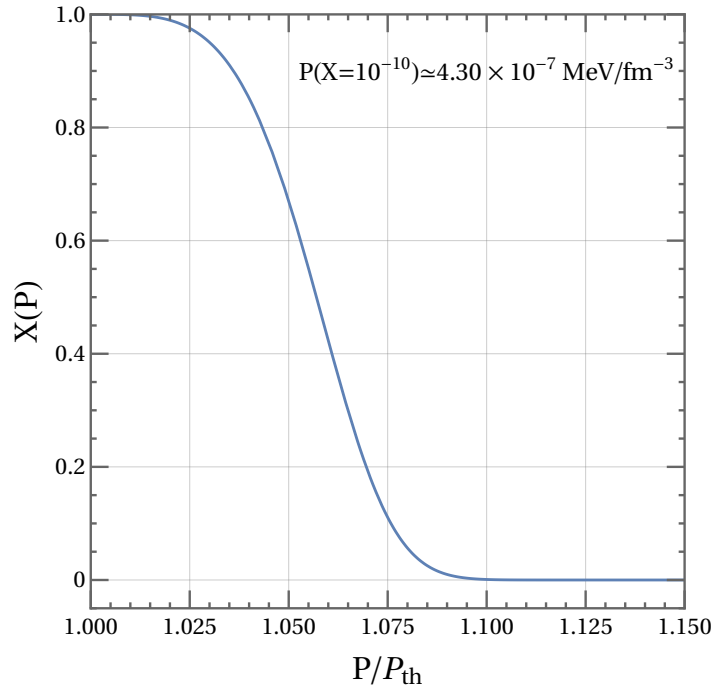


Figure 4.30: Solution X of the continuity equation for the reaction with parent proton number $Z_0 = 26$ for an accretion cycle of 4 years of active accretion followed by 40 years of quiescence, with a peak accretion rate of $10^{-10} M_{\odot}$ per year.

Overall, the instantaneous approach to electron captures in accreting neutron stars underestimates the heat release in the shallowest shells of the outer crust; for example, taking

into account the layer of electron capture $^{56}\text{Fe} \rightarrow ^{56}\text{Mn}^*$ leads to an 20% increase of the heat release in the shell. Including the reaction rate of electron captures in the study of deep crustal heating leads to a pressure dependent heat release, which has most of its effect when the layer with a mixture of parent and grand-daughter nuclei is large. In this approach, heat is also released during the quiescence phase.

The heat release increase found in the mixed layer approach leads us to discuss an important mystery of X-ray transient thermal relaxation: the shallow heating. The cooling data suggests that the shallowest parts of the crust is missing heat sources to explain the thermal relaxation of accreting neutron stars. The amount of heat required depends on the source and ranges from 0.1 MeV to 10 MeV, see [Ootes et al. \[2016\]](#), [Chamel et al. \[2020\]](#). Some mechanisms that could explain shallow heating were explored, for example, convection in the envelope or differential rotation can lead to an increase of the heat in the shallowest part of the star, but not to the extent of the shallow heating mystery, see [Medin and Cumming \[2015\]](#). It is also possible to partially explain shallow heating by varying the initial temperature and superfluidity of neutron stars, as well as the accretion rate of the binary, see [Ootes et al. \[2016\]](#). In the context of layers of electron captures, although the increase of heat release in the shallowest shells of the crust in our study is significant, it is still not sufficient to explain the shallow heating phenomenon observed in X-ray transient thermal relaxation.

5 Modified Urca neutrino emission at finite temperature

Emitted in the core and in the crust of neutron stars through a large number of processes, neutrinos are crucial actors of neutron star cooling. As they move in the star with a mean free path that depends on the age of the neutron star, they take away energy from the interior of the star. The role of neutrino emission processes in cooling, particularly concerning processes in the core, has been confirmed by X-ray observations of the thermal relaxation of neutron stars. This chapter focuses on one neutrino emission process, that involves both weak interaction and strong interaction: the Modified Urca process.

In the following, we present the derivation of the neutrino emissivity of the Modified Urca process, which plays an important role in the cooling of "adult" neutron stars, as well as neutron stars in temperature dependent stages (proto-neutron star or merger). In section 5.1, we introduce the Direct and Modified Urca processes, and present an overview of the previously established neutrino emissivity calculations for the Modified Urca process. The theoretical framework for our derivation is introduced in section 5.2. The hadronic part of the process is derived in details in section 5.3. In section 5.4, details on the numerical method used to compute the hadronic part of the process are given, and results are presented in section 5.5.

Contents

5.1	Direct and Modified Urca processes	153
5.1.1	The Direct Urca process	153
5.1.2	The Direct Urca threshold	154
5.1.3	State of the art of Modified Urca derivations	155
5.2	Modified Urca neutrino opacity at finite temperature	157
5.3	Hadronic part of the Modified Urca process	169
5.3.1	Derivation of the spin and isospin terms	169
5.3.1.1	Self-energy correction	170
5.3.1.2	Vertex corrections	176

5.3.2	The hadronic polarization function treated in the Matsubara formalism	179
5.4	Numerical treatment of the momenta integrations with the Monte-Carlo method	182
5.5	Results of the Monte-Carlo integration for the hadronic part of Modified Urca	185
5.5.1	Numerical divergence above the Direct Urca threshold	185
5.5.2	The vector contribution	188
5.5.3	The role of the denominator of \mathcal{N} functions	190
5.5.4	Modified Urca suppression above the Direct Urca threshold	192

5.1 Direct and Modified Urca processes

In this section, the Direct Urca and Modified Urca processes are introduced. First, the Direct Urca process is presented. A simple estimation of the Direct Urca process's kinetics for degenerate fermions is briefly discussed. The Modified Urca process is introduced, and a quick overview of already available calculations for the Modified Urca neutrino emissivity is presented. For an extensive discussion of the Direct Urca and Modified Urca process and their role in neutron star cooling, we refer to [Yakovlev et al. \[2001\]](#).

5.1.1 The Direct Urca process

As a fast cooling process, the Direct Urca (DUrca) process [[Lattimer et al., 1991](#)] plays a crucial role in neutron star's thermal relaxation. The Direct Urca process corresponds to the following set of reactions

$$\begin{cases} B_1 \leftrightarrow B_2 + l^\pm + \bar{\nu}_l^\pm, \\ B_2 + l^\pm \leftrightarrow B_1 + \nu_{l^\pm}, \end{cases}$$

with l designating a lepton either negatively or positively charged and ν_l its corresponding neutrino such that $\nu_l = \nu_{l^-} = \bar{\nu}_{l^+}$ and $\bar{\nu}_l = \bar{\nu}_{l^-} = \nu_{l^+}$. In this reaction, B_1 and B_2 designate two baryons of opposite isospin quantum number. Direct Urca is mediated by the weak interaction.

Depending on the leptons and baryons present in the core of neutron stars, the Direct Urca process can involve many different particles. In the following, we present a few of them:

- neutrons, protons and electrons/positrons

$$\begin{cases} n \leftrightarrow p + e^- + \bar{\nu}_e, \\ p + e^- \leftrightarrow n + \nu_e, \end{cases} \quad \begin{cases} p \leftrightarrow n + e^+ + \nu_e, \\ n + e^+ \leftrightarrow p + \bar{\nu}_e, \end{cases}$$

In this chapter, we shall focus on reactions involving these particles.

- neutrons, protons and muons μ^-/μ^+

$$\begin{cases} n \leftrightarrow p + \mu^- + \bar{\nu}_\mu, \\ p + \mu^- \leftrightarrow n + \nu_\mu, \end{cases} \quad \begin{cases} p \leftrightarrow n + \mu^+ + \nu_\mu, \\ n + \mu^+ \leftrightarrow p + \bar{\nu}_\mu, \end{cases}$$

- protons, leptons and neutral charge hyperon Λ :

$$\begin{cases} \Lambda \leftrightarrow p + l^- + \bar{\nu}_{l^-}, \\ p + l^- \leftrightarrow \Lambda + \nu_{l^-}, \end{cases}$$

- neutrons, leptons and charged hyperon Σ^\pm :

$$\begin{cases} \Sigma^\pm \leftrightarrow n + l^\pm + \bar{\nu}_{l^\pm} , \\ n + l^\pm \leftrightarrow \Sigma^\pm + \nu_{l^\pm} , \end{cases}$$

- leptons, charged hyperons Σ^\pm and neutral charge hyperons Λ and Σ^0 :

$$\begin{cases} \Sigma^\pm \leftrightarrow \Lambda + l^\pm + \bar{\nu}_{l^\pm} , \\ \Lambda + l^\pm \leftrightarrow \Sigma^\pm + \nu_{l^\pm} , \end{cases} \quad \begin{cases} \Sigma^\pm \leftrightarrow \Sigma^0 + l^\pm + \bar{\nu}_{l^\pm} , \\ \Sigma^0 + l^\pm \leftrightarrow \Sigma^\pm + \nu_{l^\pm} . \end{cases}$$

The above mentioned reactions can be classified in terms of the efficiency of the neutrino emission. To do so, a factor normalized to the nuclear Direct Urca process is introduced in [Prakash et al. \[1992\]](#) and discussed in [Providência et al. \[2019\]](#).

5.1.2 The Direct Urca threshold

Depending on the equation of state and the mass of the neutron star, the Direct Urca process does not systematically occur in the core; we refer to the discussion in section [3.3.2](#) for equations of state which allow the Direct Urca process at zero temperature. There are conditions for the kinetics of the particles involved which forbid this reaction from proceeding. The conservation of energy and momentum of particles in play leads to a threshold above which this reaction is permitted and below which it is not. The Direct Urca threshold can be easily assessed at zero temperature for a process with degenerate nucleons and electrons from the derivation presented in [Shapiro and Teukolsky \[1986\]](#).

The process must respect the following conservation laws

- the conservation of the momentum p of particles in play

$$|\vec{p}_n| \leq |\vec{p}_p| + |\vec{p}_{e^-}| , \quad (5.1)$$

if we consider that the neutrinos escape immediately after being emitted,

- the charge conservation¹:

$$n_{e^-} = n_p \quad \rightarrow \quad |\vec{p}_n| \leq 2|\vec{p}_p| , \quad (5.2)$$

with n_{e^-} and n_p the electron and proton densities respectively. From the assumption that particles are on their Fermi surface, we obtain

$$y_p \geq \frac{n_p}{n_p + n_n} = 1/9 , \quad (5.3)$$

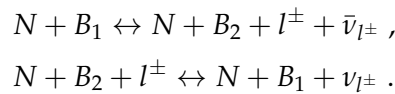
¹The charge conservation should include considerations of muons even if they do not take part in the reaction, but they are neglected here.

with y_p the proton fraction.

The Direct Urca reactions are allowed only if the proton fraction is sufficiently high. In conditions for which the Direct Urca process is not allowed, the kinetics of the weak interaction can be "saved" by adding a spectator nucleon in the so-called Modified Urca process.

5.1.3 State of the art of Modified Urca derivations

The Modified Urca (MUrca) process is permitted below the DUrca threshold by the presence of a spectator baryon N . The spectator transfers energy *via* the strong interaction to baryons B_1 and B_2 which are involved in the Urca part mediated by the weak interaction



This set of reactions was first discussed in [Chiu and Salpeter \[1964\]](#). If the process occurs with a neutron as a spectator baryon, it is referred to as the MUrca neutron branch, and the process with a proton as a spectator baryon is referred to as the MUrca proton branch. In this reaction, both the weak interaction and the strong interaction are in play. Contrary to the Direct Urca which is a fast cooling process, the Modified Urca process is considered to be a slow cooling process [[Page, 2009](#)].

Let us give a quick overview of the state of the art of Modified Urca neutrino emissivity calculations. The pioneer study is that of [Friman and Maxwell \[1979\]](#), in which the neutron branch of the reaction is treated for cold matter at β -equilibrium. The strong interaction is approximated to be mediated by the exchange of one free pion, corrected to include a Fermi liquid contribution resulting from short range correlations. Nucleons are treated as non-relativistic degenerate particles such that they are on their Fermi surface. The nucleon propagator is the first order of an expansion in the nucleon mass. The weak interaction is treated in the non-relativistic approximation, and the momentum of neutrinos is neglected compared with that of electrons and nucleons. And finally, the function expressing the conservation of momenta only includes the conservation of neutron momentum. The MUrca proton branch was treated by [Yakovlev and Levenfish \[1995\]](#) in the same framework. This approach is revised in [Yakovlev et al. \[2001\]](#) for the neutron and proton branch.

In medium effects brought forth by the neutron star medium are discussed *e.g.* in [Blaschke et al. \[1995\]](#) using the T -matrix method. The neutrino emissivity of the Modified Urca process is not computed because authors focus on the Bremsstrahlung process, but they conclude that including *in medium* effects should reduce the neutrino mean free path for any process concerned by neutron-neutron interaction (and by extension, by neutron-proton interaction). Collective effects in the context of *in medium* One Pion Exchange (OPE) are discussed in [Senatorov and Voskresensky \[1987\]](#) and references therein; loop effects on the strong interaction and resonances are also discussed, see [Voskresensky \[2001\]](#) for a review.

Shternin et al. [2018] took into account *in medium* effects on the nucleon's energy in the framework of the quasi-particle approximation. In their study, the authors treat nucleons as non-relativistic particles on their Fermi surfaces; the nucleon propagator includes effective masses and chemical potentials. *In medium* nucleon scattering is treated in the framework of the non-relativistic Bruckner–Hartree–Fock theory (with a G -matrix) for β -equilibrated matter. The authors conclude that including *in medium* effects directly in the propagator of nucleons results in an increased MUrca rate for high mass neutron stars.

In Alford and Harris [2018], the authors focus on the role of finite temperature effects in an effort to accurately compute Urca neutrino emission processes for the merger of neutron stars, and to study the conditions for achieving β -equilibrium. They emphasize that during the merger, neutron star matter is heated such that neutrinos are not trapped in some regions of the star, and the full neutrino transport must be solved, with the help of a finite temperature equation of state.

In all previously mentioned calculations of the Modified Urca neutrino emissivity, one point has not been fully addressed: the role of momentum transfer and the full momentum dependence of the matrix element. Moreover, we intend to address the Modified Urca process at finite temperature without considering particles on their Fermi surface. In the next section, we present the detailed derivation of the neutrino emissivity of this process at finite temperature, by taking the following approximations

- nucleons are non-relativistic,
- the strong interaction is represented by a One-Pion-Exchange matrix,
- we use a perturbative approach, in which the propagator of nucleons is not dressed in the derivation, and we propose a correction to this approximation in section 5.5.1 of this chapter.

5.2 Modified Urca neutrino opacity at finite temperature

Similarly to the Direct Urca process presented in section 5.1.1, the Modified Urca process operates on nucleons, electrons, positrons, muons and hyperons. In the following, we focus on the Modified Urca process involving nucleons n (neutron), p (proton), charged leptons e^- (electron), e^+ (positron), and electronic neutrino ν_e , anti-neutrino $\bar{\nu}_e$.

$$\begin{cases} N + n \leftrightarrow N + p + e^- + \bar{\nu}_e, \\ N + p + e^- \leftrightarrow N + n + \nu_e, \end{cases} \quad (5.4)$$

$$\begin{cases} N + p \leftrightarrow N + n + e^+ + \nu_e, \\ N + n + e^+ \leftrightarrow N + p + \bar{\nu}_e. \end{cases} \quad (5.5)$$

The (anti-)neutrino emissivity is the integral of the change over time in the distribution function of (anti-)neutrinos. The quantities of interest for our derivation are therefore

$$\frac{\partial}{\partial t} \mathcal{F}_{\nu_e} \quad \text{and} \quad \frac{\partial}{\partial t} \mathcal{F}_{\bar{\nu}_e}, \quad (5.6)$$

with \mathcal{F}_{ν_e} and $\mathcal{F}_{\bar{\nu}_e}$ the distribution function of electronic neutrinos and anti-neutrinos. The (anti-)neutrino opacity which has the dimension of an inverse length can be derived from the quantity $1/c \partial_t \mathcal{F}_{\nu_e/\bar{\nu}_e}$, for details see [Pascal et al. \[2022\]](#). The opacity is particularly interesting if the distribution of neutrinos over time is not constant, *i.e.* when the (anti-)neutrino's mean free path changes. Integrated over the four-momentum of (anti-)neutrinos, it corresponds to a variation of (anti-)neutrino number with time, *i.e.* the emissivity of neutrinos.

While Quantum Field Theory has been very successful in predicting properties of the Standard Model particles, it does so at zero-temperature. Fortunately, Thermal Quantum Field Theory offers a framework to design the thermal Green's function whose explicit expression depends on the choice of integration contour relating the initial and final time. To calculate the emissivity of the reaction, we use two different but equivalent formalisms:

- The real-time Schwinger-Keldysh [[Kadanoff et al., 1963](#)] formalism: the real axis is included in the contour treated separately for advanced and retarded times, and a "ghost" unphysical field must be treated alongside the physical one, which involves treating double the number of fields and operators. This approach is used for the lepton part of the study.
- The Matsubara formalism [[Matsubara, 1955](#)]: the time is replaced by a purely imaginary quantity which assumes discrete values and is proportional to the inverse of the temperature. An analytical continuation is required, for more details see Appendix B. The hadron part of our study is treated with this approach for convenience.

For a detailed review of both formalisms, we refer to [Lundberg and Pasechnik \[2021\]](#).

In the real-time formalism, the Green's function of leptons close to equilibrium corresponds to the superposition of the forward and reverse Green's functions respectively denoted $G_l^>$ and $G_l^<$, and defined as

$$iG_l^> = \frac{\pi}{\mathcal{E}_l} (\not{p} + m_l) \left((1 - \mathcal{F}_l) \delta(p_0 - \mathcal{E}_l) - \mathcal{F}_l \delta(p_0 + \mathcal{E}_l) \right), \quad (5.7)$$

$$iG_l^< = -\frac{\pi}{\mathcal{E}_l} (\not{p} + m_l) \left(\mathcal{F}_l \delta(p_0 - \mathcal{E}_l) - (1 - \mathcal{F}_l) \delta(p_0 + \mathcal{E}_l) \right); \quad (5.8)$$

with:

- p the lepton four-momentum,
- the Dirac operator notation $\not{p} = \gamma^\alpha p_\alpha$ using the Dirac γ matrices,
- \mathcal{E}_l the energy of the lepton,
- m_l the mass of the lepton.

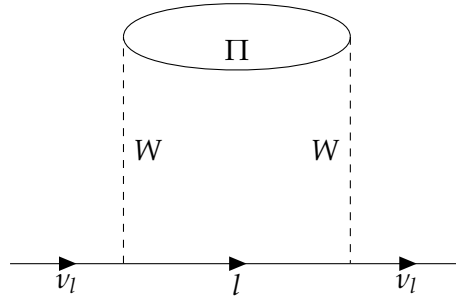


Figure 5.1: Diagram of the (anti-)neutrinos self-energy in the MURca process; the hadronic part of the diagram is accounted for by the polarization function Π , and the weak interaction mediated by the boson W is represented in dashed lines.

The second quantity crucial to assess the change in the (anti-)neutrino distribution is their self-energy, *i.e.* how the energy of (anti-)neutrinos is affected by the reaction it is involved in. The self-energy of (anti-)neutrinos denoted Σ_ν is represented as a diagram in Fig. 5.1. In the real-time formalism, the expression of the forward and reverse self-energy of neutrinos is given by

$$i \Sigma_\nu^{>/<} = \frac{G_F^2 V_{ud}^2}{2} \int \frac{d^4 p}{(2\pi)^4} \gamma^\alpha (1 - \gamma^5) G^{>/<}(p) \gamma^\beta (1 - \gamma^5) \Pi_{\alpha\beta}^{</>}(Q), \quad (5.9)$$

with Π a tensor related to hadrons of the process, which we also refer to as the hadron polarisation function. Q is the four-momentum of the weak boson, and $G(p)$ is the Green's function of the charged lepton. The constants that appear in the following derivation are taken from Zyla and et al. [2020], or the website of the Particle Data Group [Workman and et al., 2022]. G_F is the Fermi coupling constant in MeV^{-2} ; the propagator of the weak boson is hidden in this constant (the moment of the weak boson is neglected with respect to its mass). V_{ud} is the up/down component of the electroweak Cabibbo-Kobayashi-Maskawa mixing matrix [Cabibbo, 1963, Kobayashi and Maskawa, 1973] which enters the coupling between

the quarks and the weak boson. Performing the integral over the zeroth component of the charged lepton's momentum, the Dirac δ -function in Eq. (5.7) and Eq. (5.8) ensures that the particles are on-shell *i.e.* that particles follow the conservation laws of momentum, and are therefore real particles (as opposed to virtual particles).

In the following, electronic neutrinos and anti-neutrinos are denoted ν and $\bar{\nu}$. The self-energy of electronic neutrinos can be rewritten as

$$\Sigma_\nu^> = -\frac{G_F^2 V_{ud}^2}{2} \int \frac{d^3\vec{p}}{(2\pi)^4} \frac{\pi}{\mathcal{E}_e} \left((1 - \mathcal{F}_{e^-}) \gamma_\alpha (1 - \gamma_5) (\not{p}_- + m_e) \gamma_\beta (1 - \gamma_5) \Pi^{<:\alpha\beta}(Q_-) \right. \\ \left. - \mathcal{F}_{e^+} \gamma_\alpha (1 - \gamma_5) (\not{p}_+ + m_e) \gamma_\beta (1 - \gamma_5) \Pi^{<:\alpha\beta}(Q_+) \right), \quad (5.10)$$

$$\Sigma_\nu^{<} = \frac{G_F^2 V_{ud}^2}{2} \int \frac{d^3\vec{p}}{(2\pi)^4} \frac{\pi}{\mathcal{E}_e} \left(\mathcal{F}_{e^-} \gamma_\alpha (1 - \gamma_5) (\not{p}_- + m_e) \gamma_\beta (1 - \gamma_5) \Pi^{>:\alpha\beta}(Q_-) \right. \\ \left. - (1 - \mathcal{F}_{e^+}) \gamma_\alpha (1 - \gamma_5) (\not{p}_+ + m_e) \gamma_\beta (1 - \gamma_5) \Pi^{>:\alpha\beta}(Q_+) \right), \quad (5.11)$$

with \mathcal{E}_e the energy of the charged lepton. The notation \not{p}_+ and \not{p}_- corresponds to the four-momenta of the charged leptons respectively positively and negatively charged. A similar notation is used for the weak boson four-momentum Q which also depends on the four-momenta of the charged lepton; expression for those quantities are defined later on in this section. The Fermi distribution of the electrons and positrons are denoted \mathcal{F}_{e^-} and \mathcal{F}_{e^+} respectively.

The time variation of the (anti-)neutrino distribution function can be obtained from the kinetic equation for reverse and forward Green's function

$$i \frac{\partial^\lambda}{\partial X} \text{Tr} [\gamma_\lambda G_\nu^{</>}(X, p_\nu)] = - \text{Tr} [G_\nu^{>/<}(X, p_\nu) \Sigma_\nu^{</>} - \Sigma_\nu^{>/<} G_\nu^{</>}(X, p_\nu)], \quad (5.12)$$

with X the space-time domain. A few words can be said about these equations:

- The reverse and forward kinetics equation are equivalent because

$$\text{Tr}[G_\nu^{>} \Sigma_\nu^{<}] = \text{Tr}[\Sigma_\nu^{<} G_\nu^{>}] \quad \text{and} \quad \text{Tr}[G_\nu^{<} \Sigma_\nu^{>}] = \text{Tr}[\Sigma_\nu^{>} G_\nu^{<}]. \quad (5.13)$$

- The trace on the right hand side can be separated into two parts: leptons are involved in a loop (in the Feynman diagram sense), nucleons are also involved in a loop, but there is no loop connecting the hadron and lepton parts, only the weak boson acts as a mediator. This leads us to define the lepton tensor²

$$L_{\alpha\beta} = \text{Tr} \left[(\gamma_\mu p^\mu + m_{l^\pm}) \gamma_\alpha (1 - \gamma_5) \gamma_\lambda q^\lambda \gamma_\beta (1 - \gamma_5) \right] \\ = 8(p_\alpha q_\beta + q_\alpha p_\beta + p \cdot q g_{\alpha\beta} - i \epsilon_{\rho\lambda\alpha\beta} p^\rho q^\lambda), \quad (5.14)$$

²Traces and commutation properties of Dirac matrices were used.

with q the four-momentum of (anti-)neutrinos, $g_{\alpha\beta}$ the metric of the system (later on chosen to be Minkowski), and ϵ the Levi-Civita tensor³.

- The neutrino Green's function includes Dirac δ -functions to ensure that (anti-)neutrinos are real particles. Similarly to what was introduced for charged leptons, after integrating Eq. (5.12) on both sides over the zero component of the neutrino momentum, the neutrinos have been put on-shell.

We introduce the notation $[L\Pi^{>/<}(Q)]$ to designate the contraction with respect to indices α and β of the lepton and hadron tensors

$$[L\Pi^{>/<}(Q)] \triangleq L_{\alpha\beta}\Pi^{\alpha\beta}. \quad (5.15)$$

We introduce the index notation to the contraction to designate which reaction is studied, and rewrite

$$\begin{aligned} \frac{\partial}{\partial t} \left[(1 - \mathcal{F}_\nu) + \mathcal{F}_{\bar{\nu}} \right] &= i \frac{G_F^2 V_{ud}^2}{16} \int \frac{d^3\vec{p}}{(2\pi)^3} \frac{1}{\mathcal{E}_e \mathcal{E}_\nu} \\ &\times \left((1 - \mathcal{F}_{e^-})(1 - \mathcal{F}_{\bar{\nu}}) [L\Pi^{<}(Q)]^{[e^-\bar{\nu}]} - \mathcal{F}_{e^-} \mathcal{F}_{\bar{\nu}} [L\Pi^{>}(Q)]^{[e^-\bar{\nu}]} \right. \\ &\quad + \mathcal{F}_{e^-} (1 - \mathcal{F}_\nu) [L\Pi^{>}(Q)]^{[e^-\nu]} - (1 - \mathcal{F}_{e^-}) \mathcal{F}_\nu [L\Pi^{<}(Q)]^{[e^-\nu]} \\ &\quad - (1 - \mathcal{F}_{e^+})(1 - \mathcal{F}_\nu) [L\Pi^{>}(Q)]^{[e^+\nu]} + \mathcal{F}_{e^+} \mathcal{F}_\nu [L\Pi^{<}(Q)]^{[e^+\nu]} \\ &\quad \left. - \mathcal{F}_{e^+} (1 - \mathcal{F}_{\bar{\nu}}) [L\Pi^{<}(Q)]^{[e^+\bar{\nu}]} + (1 - \mathcal{F}_{e^+}) \mathcal{F}_{\bar{\nu}} [L\Pi^{>}(Q)]^{[e^+\bar{\nu}]} \right), \end{aligned} \quad (5.16)$$

with \mathcal{E}_ν the energy of neutrinos. In this expression, all processes of Eq. (5.4) and Eq. (5.5) are represented: terms proportional to the distribution function correspond to incoming particles, and terms proportional to $(1 - \text{distribution function})$ correspond to outgoing particles.

To simplify the treatment of Eq. (5.16), we implement the approximation that neutrinos and anti-neutrinos are treated independently: no interaction between neutrinos and anti-neutrinos, nor neutrino oscillations are taken into account. Moreover, the forward and reverse hadron polarisation tensors are related to the retarded polarisation tensor denoted $\Pi^{\alpha\beta}$ according to

$$\begin{aligned} \Pi^{\alpha\beta;>} &= -2i(1 + n_{\text{BE}}(Q_0)) \text{Im} \Pi^{\alpha\beta}(Q), \\ \Pi^{\alpha\beta;<} &= -2in_{\text{BE}}(Q_0) \text{Im} \Pi^{\alpha\beta}(Q), \end{aligned}$$

with the boson distribution function denoted n_{BE} , and Q_0 the energy of the weak boson (or zero component of the four-momentum). The time derivative of the distribution function of

³Let us note that the first two terms of the lepton tensor are symmetric together, the term with the metric is also symmetric, and the last term is anti-symmetric.

(anti-)neutrinos finally writes as

$$\begin{aligned} \frac{\partial \mathcal{F}_\nu}{\partial t} = & -\frac{G_F^2 V_{ud}^2}{8} \int \frac{d^3 \vec{p}}{(2\pi)^3} \frac{1}{\mathcal{E}_e \mathcal{E}_\nu} \left((1 + n_{\text{BE}}(Q_0^{[e^- \nu]})) \mathcal{F}_{e^-} (1 - \mathcal{F}_\nu) [L \text{Im} \Pi(Q)]^{[e^- \nu]} \right. \\ & - n_{\text{BE}}(Q_0^{[e^- \nu]}) (1 - \mathcal{F}_{e^-}) \mathcal{F}_\nu [L \text{Im} \Pi(Q)]^{[e^- \nu]} \\ & - (1 + n_{\text{BE}}(Q_0^{[e^+ \nu]})) (1 - \mathcal{F}_{e^+}) (1 - \mathcal{F}_\nu) [L \text{Im} \Pi(Q)]^{[e^+ \nu]} \\ & \left. + n_{\text{BE}}(Q_0^{[e^+ \nu]}) \mathcal{F}_{e^+} \mathcal{F}_\nu [L \text{Im} \Pi(Q)]^{[e^+ \nu]} \right), \end{aligned} \quad (5.17)$$

$$\begin{aligned} \frac{\partial \mathcal{F}_{\bar{\nu}}}{\partial t} = & \frac{G_F^2 V_{ud}^2}{8} \int \frac{d^3 \vec{p}}{(2\pi)^3} \frac{1}{\mathcal{E}_e \mathcal{E}_{\bar{\nu}}} \left(n_{\text{BE}}(Q_0^{[e^- \bar{\nu}]}) (1 - \mathcal{F}_{e^-}) (1 - \mathcal{F}_{\bar{\nu}}) [L \text{Im} \Pi(Q)]^{[e^- \bar{\nu}]} \right. \\ & - (1 + n_{\text{BE}}(Q_0^{[e^- \bar{\nu}]}) \mathcal{F}_{e^-} \mathcal{F}_{\bar{\nu}} [L \text{Im} \Pi(Q)]^{[e^- \bar{\nu}]} \\ & - n_{\text{BE}}(Q_0^{[e^+ \bar{\nu}]}) \mathcal{F}_{e^+} (1 - \mathcal{F}_{\bar{\nu}}) [L \text{Im} \Pi(Q)]^{[e^+ \bar{\nu}]} \\ & \left. + (1 + n_{\text{BE}}(Q_0^{[e^+ \bar{\nu}]}) (1 - \mathcal{F}_{e^+}) \mathcal{F}_{\bar{\nu}} [L \text{Im} \Pi(Q)]^{[e^+ \bar{\nu}]} \right). \end{aligned} \quad (5.18)$$

This derivation is intended to provide results that can be used in a neutrino transport solver for proto-neutron stars such as presented in [Pascal et al. \[2022\]](#): the distribution function of the (anti-)neutrinos is calculated. Therefore, as is presented for Direct Urca calculations in [Oertel et al. \[2020\]](#), we shall focus on computing each factor proportional to $\mathcal{F}_{\nu/\bar{\nu}}$ and $(1 - \mathcal{F}_{\nu/\bar{\nu}})$ in Eq. (5.17) and Eq. (5.18). The final form of the integrals accounting for the eight reactions studied are given by:

- For the first set of reactions, which corresponds to a modified neutron decay and its inverse

$$N + p + e^- + \bar{\nu} \rightarrow N + n, \quad (5.19)$$

$$N + n \rightarrow N + p + e^- + \bar{\nu}, \quad (5.20)$$

represented in Fig. 5.2, gives

$$I_1 = -\frac{G_F^2 V_{ud}^2}{8(2\pi)^3} \int \frac{d^3 \vec{p}}{\mathcal{E}_e \mathcal{E}_\nu} (1 + n_{\text{BE}}(Q_0)) \mathcal{F}_{e^-} [L \text{Im} \Pi(Q)]^{[e^- \bar{\nu}]}, \quad (5.21)$$

$$I_2 = \frac{G_F^2 V_{ud}^2}{8(2\pi)^3} \int \frac{d^3 \vec{p}}{\mathcal{E}_e \mathcal{E}_\nu} n_{\text{BE}}(Q_0) (1 - \mathcal{F}_{e^-}) [L \text{Im} \Pi(Q)]^{[e^- \bar{\nu}]}. \quad (5.22)$$

At this point, a choice must be made in how the diagram is drawn around the weak boson. We choose the convention that the weak boson is oriented from left to right in the diagram of the Modified Urca process. If we choose to align the neutrino along the

z axis such that the angle (\vec{p}, \vec{q}) is denoted θ_e , the conservation of four-momenta gives

$$\begin{cases} |\vec{Q}|^2 = |\vec{p}|^2 + |\vec{q}|^2 + 2 \cos(\theta_e) |\vec{p}| |\vec{q}| , \\ Q_0 = \mathcal{E}_e - \mu_e + |\vec{q}| + \mu_\nu , \\ Q_0^{\min} = m_e - \mu_e + |\vec{q}| + \mu_\nu , \end{cases} \quad (5.23)$$

with Q_0^{\min} the minimum value of the energy of the weak boson, and μ_e and μ_ν the chemical potential of electrons and neutrinos.

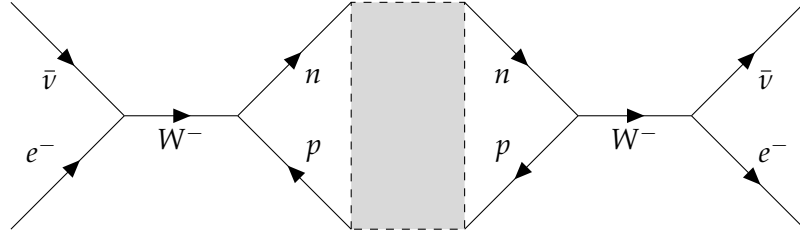


Figure 5.2: Diagram of reactions presented in Eq. (5.19) (on the left) and Eq. (5.20) (on the right). The strong interaction part of the diagram is represented in grey.

- For the second set of reactions which corresponds to a modified electron capture and its inverse

$$N + p + e^- \rightarrow N + n + \nu , \quad (5.24)$$

$$N + n + \nu \rightarrow N + p + e^- , \quad (5.25)$$

represented in Fig. 5.3, gives

$$I_3 = -\frac{G_F^2 V_{ud}^2}{8(2\pi)^3} \int \frac{d^3 \vec{p}}{\mathcal{E}_e \mathcal{E}_\nu} (1 + n_{\text{BE}}(Q_0)) \mathcal{F}_{e^-} [L \text{Im} \Pi(Q)]^{[e^- \nu]} , \quad (5.26)$$

$$I_4 = \frac{G_F^2 V_{ud}^2}{8(2\pi)^3} \int \frac{d^3 \vec{p}}{\mathcal{E}_e \mathcal{E}_\nu} n_{\text{BE}}(Q_0) (1 - \mathcal{F}_{e^-}) [L \text{Im} \Pi(Q)]^{[e^- \nu]} . \quad (5.27)$$

Through the conservation of four-momenta

$$\begin{cases} |\vec{Q}|^2 = |\vec{p}|^2 + |\vec{q}|^2 - 2 \cos(\theta_e) |\vec{p}| |\vec{q}| , \\ Q_0 = \mathcal{E}_e - \mu_e - |\vec{q}| + \mu_\nu , \\ Q_0^{\min} = m_e - \mu_e - |\vec{q}| + \mu_\nu . \end{cases} \quad (5.28)$$

- For the third set of reactions which corresponds to a modified positron capture and its inverse

$$N + n + e^+ \rightarrow N + p + \bar{\nu} , \quad (5.29)$$

$$N + p + \bar{\nu} \rightarrow N + n + e^+ , \quad (5.30)$$

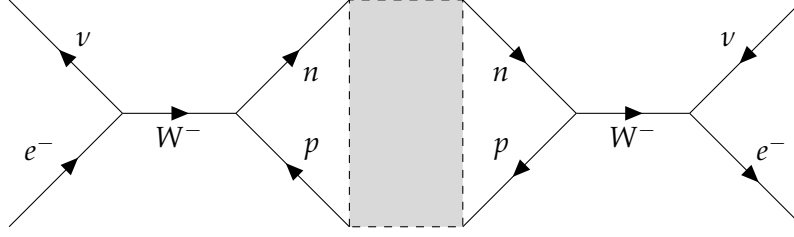


Figure 5.3: Diagram of reactions presented in Eq. (5.24) (on the left) and Eq. (5.25) (on the right).

represented in Fig. 5.4, gives

$$I_5 = -\frac{G_F^2 V_{ud}^2}{8(2\pi)^3} \int \frac{d^3\vec{p}}{\mathcal{E}_e \mathcal{E}_\nu} n_{\text{BE}}(Q_0) \mathcal{F}_{e^+} [L \text{Im} \Pi(Q)]^{[e^+\bar{\nu}]}, \quad (5.31)$$

$$I_6 = \frac{G_F^2 V_{ud}^2}{8(2\pi)^3} \int \frac{d^3\vec{p}}{\mathcal{E}_e \mathcal{E}_\nu} (1 + n_{\text{BE}}(Q_0)) (1 - \mathcal{F}_{e^+}) [L \text{Im} \Pi(Q)]^{[e^+\bar{\nu}]}, \quad (5.32)$$

Through the conservation of four-momenta

$$\begin{cases} |\vec{Q}|^2 = |\vec{p}|^2 + |\vec{q}|^2 - 2 \cos(\theta_e) |\vec{p}| |\vec{q}|, \\ Q_0 = -\mathcal{E}_e - \mu_e + |\vec{q}| + \mu_\nu, \\ Q_0^{\text{max}} = -m_e - \mu_e + |\vec{q}| + \mu_\nu, \end{cases} \quad (5.33)$$

with Q_0^{max} the maximum value of the energy of the weak boson

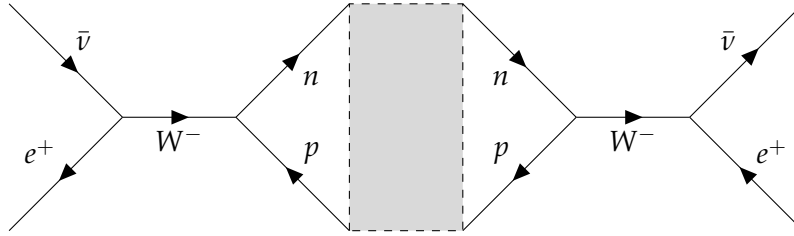


Figure 5.4: Diagram of reactions presented in Eq. (5.29) (on the right) and Eq. (5.30) (on the left).

- For the fourth set of reactions which corresponds to a modified proton decay and its inverse

$$N + p \rightarrow N + n + e^+ + \nu, \quad (5.34)$$

$$N + n + e^+ + \nu \rightarrow N + p. \quad (5.35)$$

represented in Fig. 5.5, gives

$$I_7 = -\frac{G_F^2 V_{ud}^2}{8(2\pi)^3} \int \frac{d^3\vec{p}}{\mathcal{E}_e \mathcal{E}_\nu} n_{\text{BE}}(Q_0) (1 - \mathcal{F}_{e^+}) [L \text{Im} \Pi(Q)]^{[e^+\nu]}, \quad (5.36)$$

$$I_8 = \frac{G_F^2 V_{ud}^2}{8(2\pi)^3} \int \frac{d^3\vec{p}}{\mathcal{E}_e \mathcal{E}_\nu} (1 + n_{\text{BE}}(Q_0)) \mathcal{F}_{e^+} [L \text{Im} \Pi(Q)]^{[e^+\nu]}, \quad (5.37)$$

Through the conservation of four-momenta

$$\begin{cases} |\vec{Q}|^2 = |\vec{p}|^2 + |\vec{q}|^2 + 2 \cos(\theta_e) |\vec{p}| |\vec{q}|, \\ Q_0 = -\mathcal{E}_e - \mu_e - |\vec{q}| + \mu_\nu, \\ Q_0^{\max} = -m_e - \mu_e - |\vec{q}| + \mu_\nu. \end{cases} \quad (5.38)$$

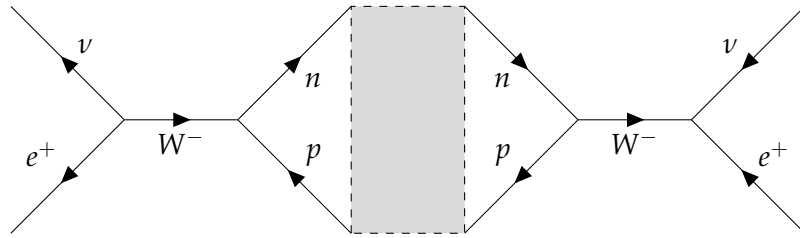


Figure 5.5: Diagram of reactions presented in Eq. (5.34) (on the right) and Eq. (5.35) (on the left).

Let us note that for cold matter neutron stars, the neutrinos escape immediately after being emitted such that reactions presented in Eq. (5.20), Eq. (5.25), Eq. (5.30) and Eq. (5.35) can be disregarded. However, this is not the case for proto-neutron stars, in regions where neutrinos are trapped [Pons et al., 1998].

In the remaining part of this chapter, results are presented only for the hadronic part of the Modified Urca process. The hadronic polarization function $\Pi^{\alpha\beta}$ depends on the four-momentum of the weak boson (Q_0, \vec{Q}), which is different for each of the eight reactions presented in Fig. 5.2, Fig. 5.3, Fig. 5.4 and Fig. 5.5. Results in section 5.5 are presented only for the electronic capture and its inverse (see Eq. (5.24) and Eq. (5.25)) to which corresponds a specific \vec{Q} ; the value of the weak boson energy Q_0 is an input of the function $\Pi^{\alpha\beta}(Q_0, \vec{Q})$ in the presentation of our results. We will show in section 5.5.2 that the location of the hadronic polarization function maxima is not significantly affected by the value of \vec{Q} .

We present in Fig. 5.6 and Fig. 5.7 the different regions of Q_0 for which each of the eight reactions considered above is favored by the presence of charged leptons in the medium. In this figure, we present the incoming and outgoing electron and positron distribution functions \mathcal{F}_{e^-} , \mathcal{F}_{e^+} , $(1 - \mathcal{F}_{e^-})$ and $(1 - \mathcal{F}_{e^+})$, as a function of Q_0 . The energy of neutrinos is $E_\nu = |\vec{q}| = 10$ MeV. Values of the chemical potentials of the leptons are extracted from the equation of state RG(SLy4)⁴ as can be found in the database [CompOSE CompOSE \[2022\]](#); all results in this chapter are established using this equation of state. Results are given for different values of the temperature (5 and 30 MeV) and of the baryonic density n_B (10^{-5} and 0.3 fm^{-3}). The electron fraction is fixed at 0.3: although the positron and electron abundances depend on y_e , the reasoning presented in the following is the same for a different value of the charged lepton fraction.

⁴RG(SLy4) is a three parameter equation of state; it depends on the baryonic density, but also on the temperature and the electron fraction.

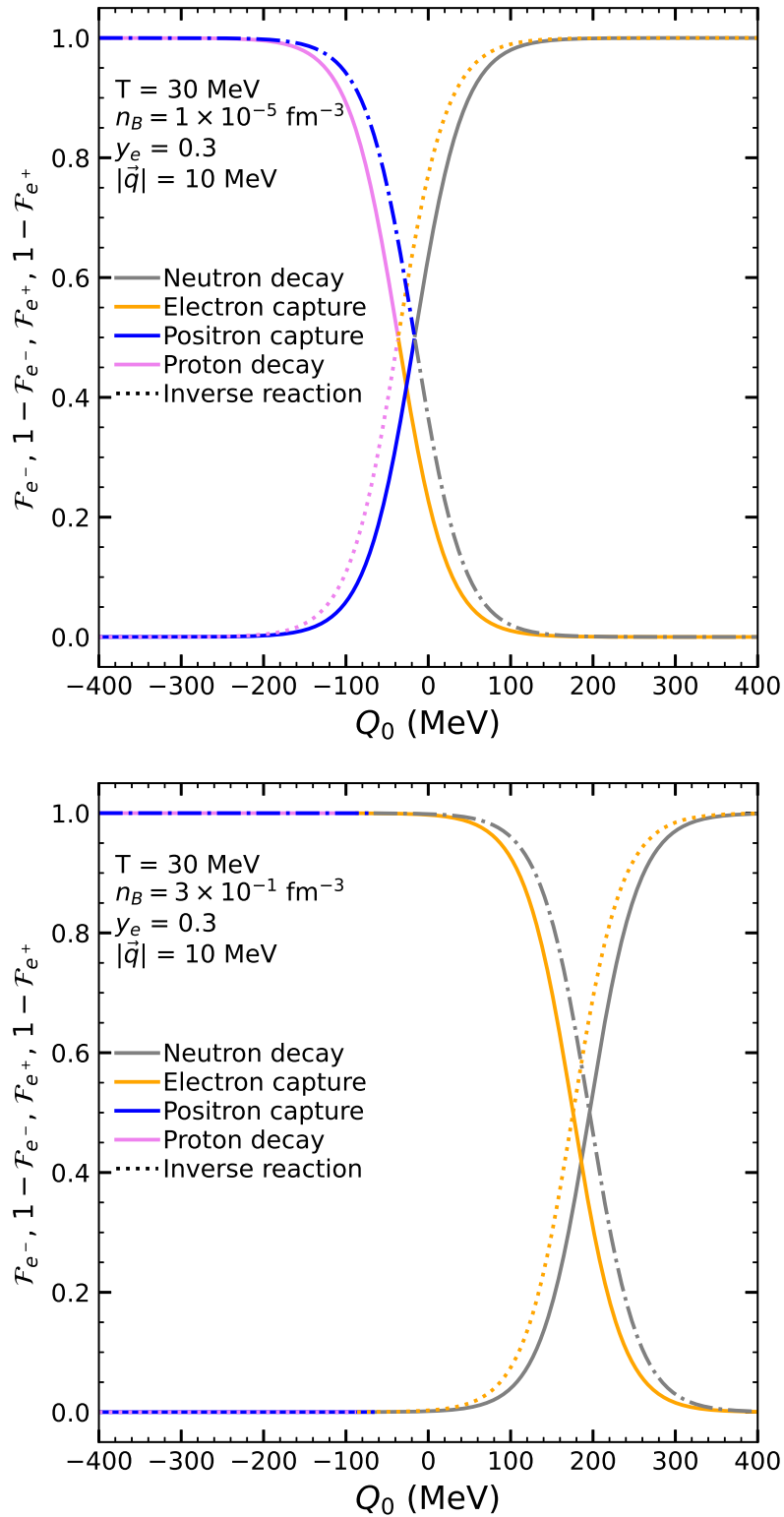


Figure 5.6: Fermi distribution of incoming \mathcal{F} and outgoing $(1 - \mathcal{F})$ electrons e^- and positrons e^+ as a function of the energy of the weak boson Q_0 , at temperature $T = 30$ MeV, for the eight reactions studied in this chapter.

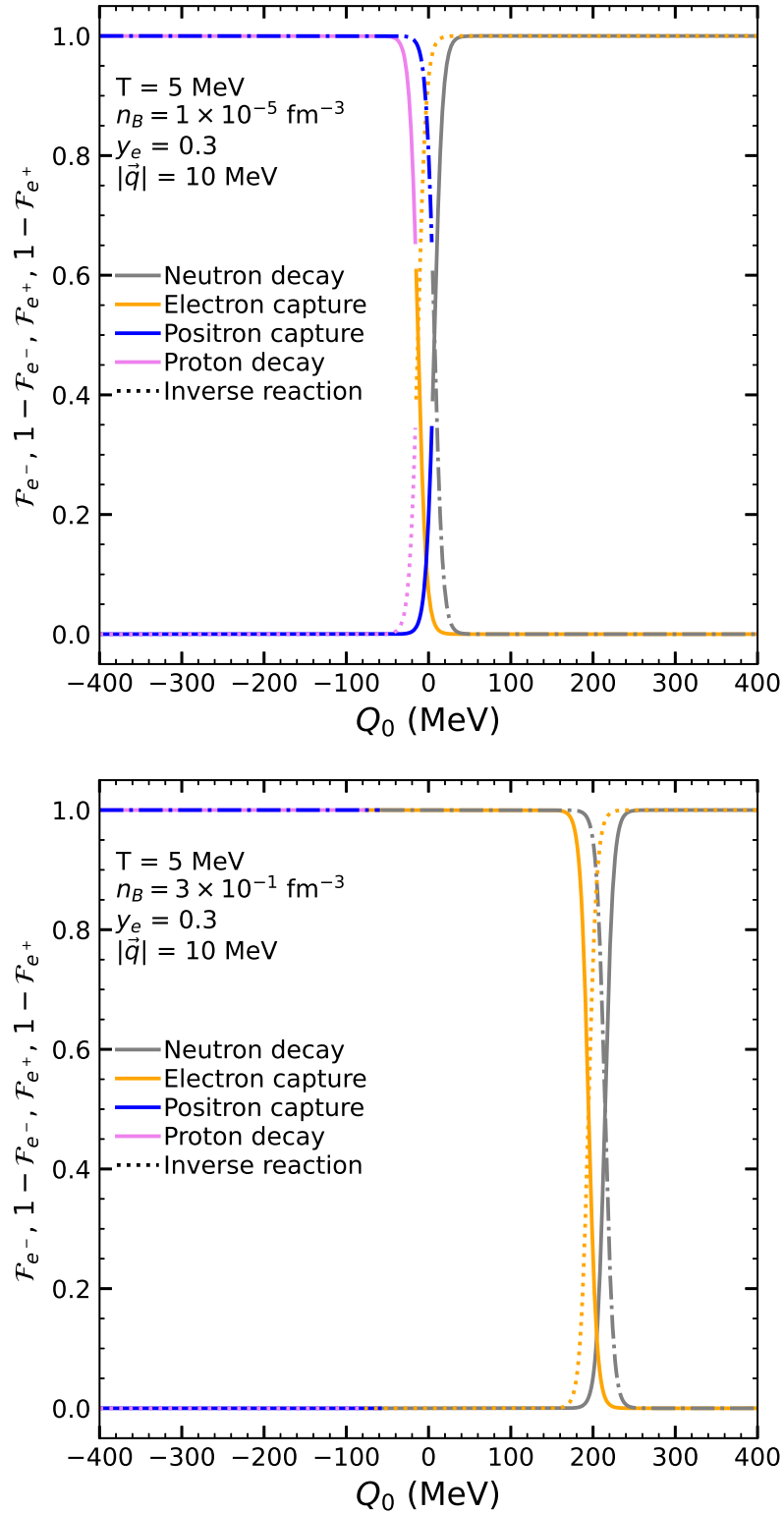


Figure 5.7: Fermi distribution of incoming \mathcal{F} and outgoing $(1 - \mathcal{F})$ electrons e and positrons \bar{e} as a function of the energy of the weak boson Q_0 , at temperature $T = 5 \text{ MeV}$, for the eight reactions studied in this chapter.

If the distribution functions of charged leptons is close to zero, the phase factor inhibits the reaction, whereas if the distribution function is large the reaction is favored.

Let us present the results for one example at high temperature (30 MeV) and high density (0.3 fm^{-3}), as is presented in the lower plot of Fig. 5.6. The inverse neutron decay and electron captures (in orange and grey plain lines) are favored from a minimum value $Q_0 = -71.4 \text{ MeV}$ and $Q_0 = -81.5 \text{ MeV}$ respectively. In the range $Q_0 = [-81.5; -71.4] \text{ MeV}$, the electron capture is favored and not the inverse neutron decay. Note that when the inverse neutron decay is favored, it always dominates the electron capture. For electronic reaction, between $Q_0 = Q_0^{\min}$ and $Q_0 \simeq 50 \text{ MeV}$, only the electron capture and inverse neutron decay are favored; for larger values of Q_0 , the Fermi distribution of their inverse reaction evolves from zero to one, whereas the neutron decay and electron capture Fermi distributions evolve from one to zero. In other words, we can distinguish the following domains:

- for $Q_0 = [Q_0^{\min}; 50 \text{ MeV}]$, the electron captures and inverse neutron decays are favored, but not the inverse electron captures and neutron decays;
- for $Q_0 \simeq [50; 300] \text{ MeV}$ electron captures, inverse electron captures, neutron decays and inverse neutron decays are all favored;
- for $Q_0 > 300 \text{ MeV}$, only the inverse electron captures and the neutron decays are favored.

With respect to positronic reactions, the conditions are such that Q_0 is small. Only the positron captures and inverse proton decays are favored, and not the inverse positron captures and proton decays for any value of Q_0 . This result can be anticipated by defining $a \in [0; 1]$ the value that the distribution of positron should reach; let's take the example of the proton decay

$$n_F(\mathcal{E}_e + \mu_e) \geq a \quad \Leftrightarrow \quad Q_0 \geq \mu_\nu - |\vec{q}| - T \ln \left(\frac{1-a}{a} \right). \quad (5.39)$$

By imposing the limit that the Fermi distribution of positrons must be under the value a for values of Q_0 under the maximum value of Q_0 , we can establish the limit

$$m_e + \mu_e < T \ln \left(\frac{1-a}{a} \right). \quad (5.40)$$

Under the conditions $T = 30 \text{ MeV}$, $n_B = 0.3 \text{ fm}^{-3}$ and $y_e = 0.3$, the chemical potential of electrons is 262.66 MeV . Assuming that the Fermi distribution of positrons must be above the value $a = 0.2$, we have

$$T \ln \left(\frac{1-a}{a} \right) = 41.59 \text{ MeV} \quad \text{and} \quad m_e + \mu_e = 263.17 \text{ MeV}, \quad (5.41)$$

such that the inequality presented in Eq. (5.40) does not hold. Another way to anticipate this result is to realize that the neutrino energy $|\vec{q}|$ must be negative for the Fermi distribution of positrons to be above $a = 0.2$, which makes no physical sense.

Similarly, we can discuss results at high temperature and low density (10^{-5} fm^{-3}) from the upper plot of Fig. 5.6. There are the following domains

- the inverse positron capture and proton decay are favored for $Q_0 = [-400 : -180] \text{ MeV}$,
- the positron capture, proton decay, inverse proton decay and inverse positron capture are favored for $Q_0 = [-180 : -40] \text{ MeV}$,
- for $Q_0 = [-40 : -10] \text{ MeV}$, only the captures and their inverse are favored,
- for $Q_0 = [-10 : 100] \text{ MeV}$, the neutron decay, inverse neutron decay, electron capture and inverse electron capture are favored,
- for $Q_0 = [100 : 400] \text{ MeV}$ the neutron decay and inverse electron capture are favored.

On the one hand, we note that results of Fig. 5.6 and Fig. 5.7 for low density present a region where the Fermi distribution of leptons change from the favoring of positronic reactions to electronic reactions, centered around the zero value of Q_0 . Indeed, at low densities, the chemical potential of electrons and neutrinos are small, therefore Q_0^{max} for positronic reactions and Q_0^{min} for electronic reactions are relatively small. For low densities, the region where electronic reactions and positronic reaction are favored is small, and proton decay and neutron decay are both inhibited (and similarly for their inverse). On the other hand, for high densities there are domains of Q_0 in which all reactions are favored. Those regions are rather large at high temperature (Fig. 5.6) because the Fermi distribution function is not steep, and rather small at low temperature because the Fermi distribution function is steep.

Although Fig. 5.6 and Fig. 5.7 are helpful to understand the regions where each reaction is favored, we shall abandon studying the lepton part of the Modified Urca process from now on. In this manuscript, numerical results are restricted to the hadronic part of the Modified Urca process. The next section focuses on the derivation of the imaginary part of the retarded polarisation function which describes the hadronic part entering the MURca rate calculation.

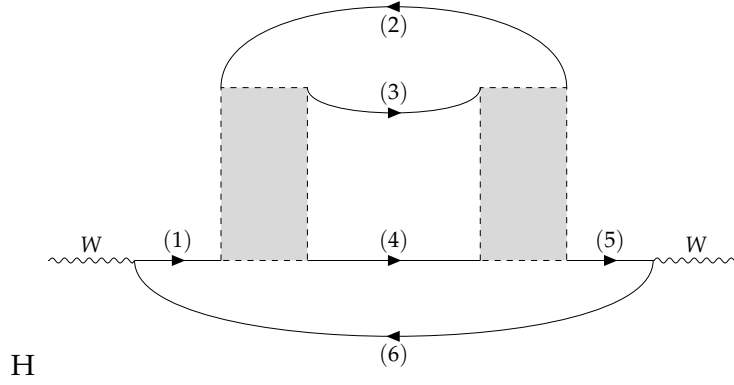


Figure 5.8: Diagram of the first self-energy correction to the weak boson in the MUrca process. The strong interaction matrix is represented in grey with dashed contours. This diagram is equivalent to diagram (3a) in [Bacca et al. \[2012\]](#).

5.3 Hadronic part of the Modified Urca process

The hadronic current denoted j_c^μ presents a vector part and axial vector part such that

$$j_c^\mu = \bar{\psi}_h \gamma^\mu (C_V - C_A \gamma_5) \psi_h, \quad (5.42)$$

with C_A and C_V the coupling constants for the charged current respectively [[Horowitz and Pérez-García, 2003](#)]. In the following, the derivation of the hadronic part is presented as a correction to the weak boson self-energy.

5.3.1 Derivation of the spin and isospin terms

The hadronic polarisation function, denoted $\Pi^{\alpha\beta}$, for the Modified Urca process corresponds to how the strong interaction affects the weak interaction part of the process; it can be separated into

- the corrections to the nucleon propagators associated with the weak boson self-energy,
- and the corrections to the nucleon-nucleon- weak boson vertex.

The retarded hadronic polarisation function can be written as

$$\Pi^{\alpha\beta}(Q) = \left(\prod_{j=1}^4 \int \frac{d^4 p_j}{(2\pi)^4} \right) \sum_X I_X X_{\text{spin}}^{\alpha\beta}(Q) \delta^4(p_1 + p_2 - p_3 - p_4), \quad (5.43)$$

with j the index of the nucleon, and $X = D_{a,b,c,d}, E_{a,b,c,d}, V_{1a,b,c,d}, V_{2a,b,c,d}, V_{3a,b,c,d}$ presented in the following.

5.3.1.1 Self-energy correction

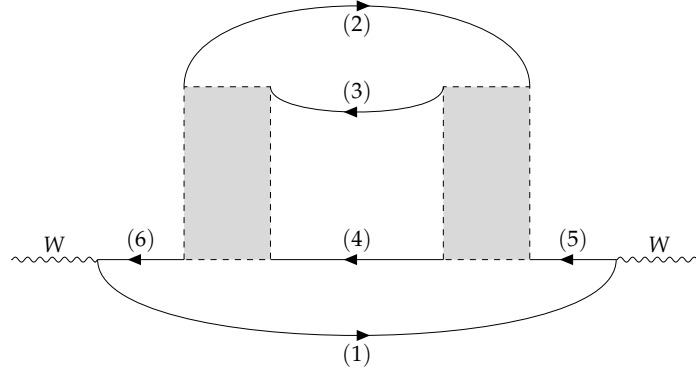


Figure 5.9: Diagram of the second self-energy correction to the weak boson in the MURca process. This diagram is equivalent to diagram (3b) in [Bacca et al. \[2012\]](#).

There are two diagrams of self-energy, presented in Fig. 5.8 and Fig. 5.9, respectively denoted D and E . In order to collect all contributions of those diagrams, one must think of the different ways the strong interaction can couple the nucleons in play. By naming all vertices of the diagram, four self-energy contributions can be listed

$$\begin{cases} D_1^{\alpha\beta} \\ D_2^{\alpha\beta} \\ D_3^{\alpha\beta} \\ D_4^{\alpha\beta} \end{cases} = \Gamma_{\pm;ba}^{\alpha} \Gamma_{\mp;cd}^{\beta} S^{am}(p_1) S^{et}(p_2) S^{vf}(p_3) S^{ng}(p_4) S^{hc}(p_5) S^{db}(p_6) \quad (5.44)$$

$$\times \begin{cases} T_{mn;tv}(p_1, p_4; p_2, p_3) T_{gh;fe}(p_4, p_5; p_3, p_2) \\ T_{mv;tn}(p_1, p_3; p_2, p_4) T_{ge;fh}(p_4, p_2; p_3, p_5) \\ T_{mn;tv}(p_1, p_4; p_2, p_3) T_{ge;fh}(p_4, p_2; p_3, p_5) \\ T_{mv;tn}(p_1, p_3; p_2, p_4) T_{gh;fe}(p_4, p_5; p_3, p_2) \end{cases}, \quad (5.45)$$

$$\begin{cases} E_1^{\alpha\beta} \\ E_2^{\alpha\beta} \\ E_3^{\alpha\beta} \\ E_4^{\alpha\beta} \end{cases} = \Gamma_{\pm;ab}^{\alpha} \Gamma_{\mp;dc}^{\beta} S^{bd}(p_1) S^{tg}(p_2) S^{hv}(p_3) S^{fn}(p_4) S^{ce}(p_5) S^{ma}(p_6) \quad (5.46)$$

$$\times \begin{cases} T_{mn;tv}(p_6, p_4; p_2, p_3) T_{gh;fe}(p_2, p_3; p_4, p_5) \\ T_{mv;tn}(p_6, p_3; p_2, p_4) T_{ge;fh}(p_2, p_5; p_4, p_3) \\ T_{mn;tv}(p_6, p_4; p_2, p_3) T_{ge;fh}(p_2, p_5; p_4, p_3) \\ T_{mv;tn}(p_6, p_3; p_2, p_4) T_{gh;fe}(p_2, p_3; p_4, p_5) \end{cases}. \quad (5.47)$$

Each diagram represented in Fig. 5.8 and Fig. 5.9 leads to four sub-diagrams related to the different combinations of the strong nucleon-nucleon interaction matrix; the sub-diagrams are presented in Fig. 5.10 and Fig. 5.11 for the diagrams D and E respectively.

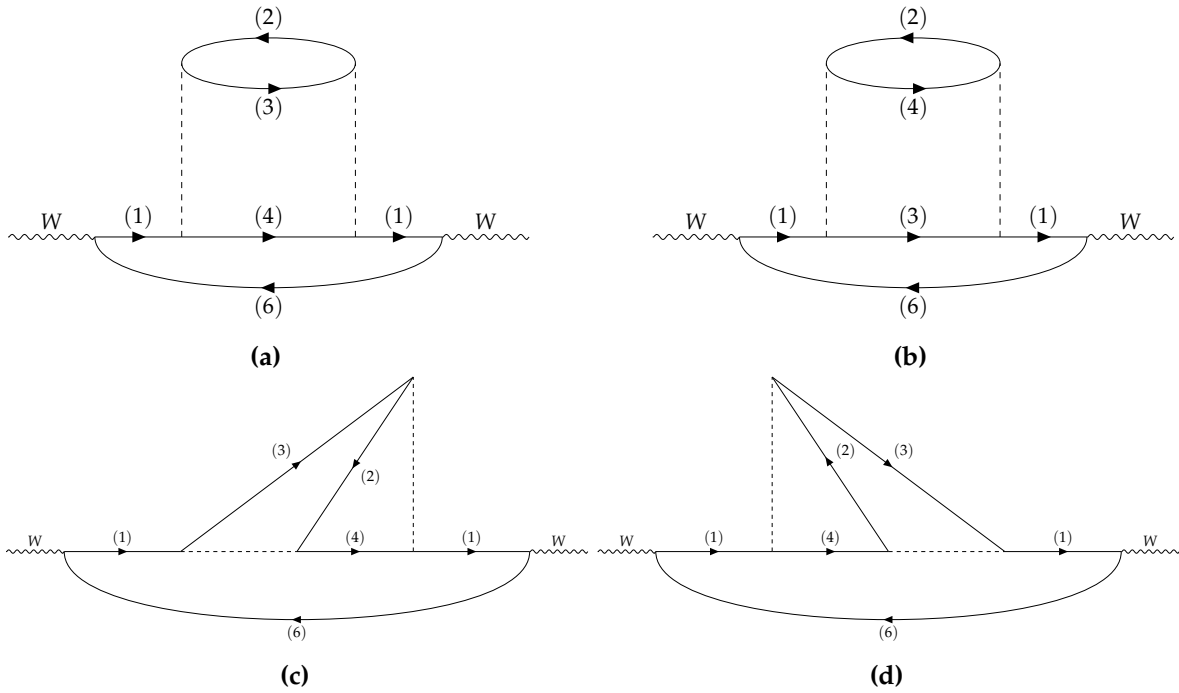


Figure 5.10: Feynman representation of the first self-energy sub-diagrams, within the One-Pion-Exchange approximation. Dashed lines represent a pion, and plain lines represent a nucleon.

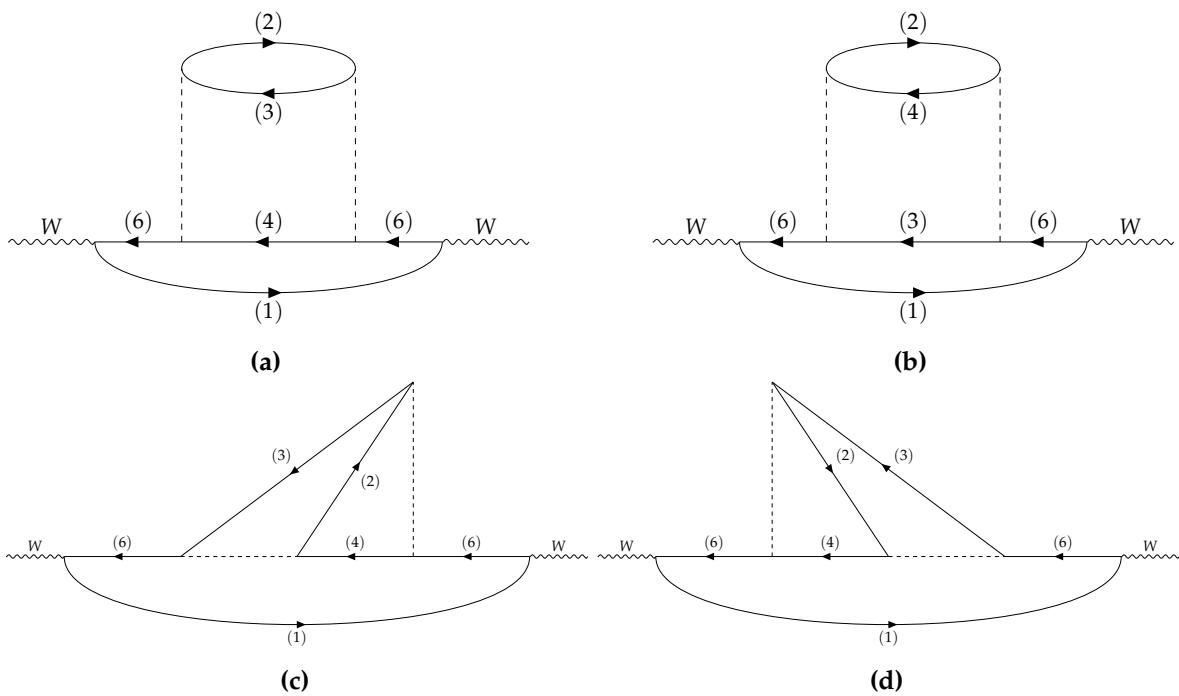


Figure 5.11: Feynman representation of the second self-energy sub-diagrams, within the One-Pion-Exchange approximation. Dashed lines represent a pion, and plain lines represent a nucleon.

Let us detail the quantities introduced. Γ expresses the vertex between the weak boson and nucleon-nucleon coupling

$$\Gamma_{\pm,ab}^{\mu} = [\gamma^{\mu}(c_V - c_A\gamma^5)\tau_{\pm}]_{ab} \quad \text{and} \quad \tau_{\pm} = \frac{1}{2}(\tau^1 \pm \tau^2), \quad (5.48)$$

with γ and τ respectively the Dirac and Pauli matrices for isospin, and $C_A \simeq 1.267$ and $C_V \simeq 1$ the axial and vector coupling constants. The weak interaction imposes that particles (1) and (6) in Fig. 5.10 or Fig. 5.11 are of opposite isospin nature: if nucleon (1) is a neutron, then nucleon (6) is a proton and *vice-versa*. This is equivalent to saying that a τ^+ at the vertex implies an incoming nucleon with isospin $-1/2$ and an outgoing nucleon with isospin $+1/2$, whereas a τ^- at the vertex implies an incoming nucleon with isospin $+1/2$ and an outgoing nucleon with isospin $-1/2$.

T is the strong interaction matrix, which we choose to express in the One-Pion-Exchange (OPE) approximation: the interaction between two nucleons is mediated by the exchange of a pion π^{\pm} or π^0 . The matrix T is the product of:

- the pion-nucleon-nucleon vertex⁵

$$\frac{f_{\pi NN}}{m_{\pi}} \gamma^5 \gamma^{\mu} k_{\mu} \tau^{\alpha}, \quad (5.49)$$

with k the four-momentum of the pion, m_{π} the pion mass, $f_{\pi NN}$ the coupling constant of the OPE strong interaction,

- the propagator of the pion:

$$\frac{1}{k^2 - m_{\pi}^2}. \quad (5.50)$$

This quantity can be expressed in terms of the outgoing/ingoing four-momenta of the nucleons involved with the pion

$$T_{ab;cd}(p_1, p_3; p_2, p_4) = \frac{\left(\frac{f_{\pi NN}}{m_{\pi}}\right)^2}{(p_3 - p_1)^2 - m_{\pi}^2} \left(-\gamma^5 \gamma^{\mu} (p_3 - p_1)_{\mu} \tau^i\right)_{ab} \left(\gamma^5 \gamma^{\nu} (p_4 - p_2)_{\nu} \tau_i\right)_{cd}. \quad (5.51)$$

The strong interaction in the OPE approximation can either be:

- mediated by π^0 : nucleons (1) and (4) in Fig. 5.10 are of the same isospin nature (either both neutrons or both protons), then so are (2) and (3),
- mediated by π^{\pm} : nucleons (1) and (4) are of different nature, then so are (2) and (3).

⁵Giving the physical sense of the isospin, we use latin indices for the (1,2,3) components of the Pauli matrix τ , contrary to the derivation for the spin for which greek indices are used for the components (0,1,2,3).

Last (but not least) quantity to be introduced is the nucleon propagator S ; we project it in isospin space with the isoscalar S_S and isovector S_V propagators

$$S = S_S + \tau^3 S_V \quad \text{with} \quad S_S = \frac{S_n + S_p}{2} \quad \text{and} \quad S_V = \frac{S_n - S_p}{2}; \quad (5.52)$$

S_n and S_p are the relativistic proton and neutron fermionic propagators

$$S_x(l) = \frac{\gamma^\alpha l_{\alpha;x} + m_x^*}{k_{0;x}^2 - \mathcal{E}_{k;x}^2}, \quad (5.53)$$

with m^* the effective mass of the particle, $x = \{n, p\}$ the isospin nature of the nucleon. In the following, for nucleons (1), (2), (3), (4), (5) and (6) it will respectively be denoted x, y, z, u, v and w ; the isospin sign of nucleons is denoted s with $s = 1$ for neutrons and $s = -1$ for protons. The isospin nature of the six nucleons depends on whether a τ^+ or a τ^- are chosen in the left hand side and right hand side of the diagram; in the following, we refer to this convention as the vertex combination. Exchanging the τ^+ to a τ^- and the τ^- to a τ^+ , or in other words exchanging the vertex combination, simply inverts the isospin nature of the incoming and outgoing nucleons involved in the weak boson vertex; as such, the isospin sign of all six nucleons in play will be opposite for the complementary vertex combination.

Because spin and isospin spaces are orthogonal, the derivation can be conducted separately for the spin and isospin part. We choose to neglect the time component of the pion four-momentum and define the spin quantities

$$\bar{T}_{ab} = \begin{pmatrix} C_V \\ -C_A \vec{\sigma} \end{pmatrix}_{ab}, \quad \bar{T}_{ab}(p_1, p_2) = \frac{f_{\pi NN}}{m_\pi} \sqrt{\frac{1}{(\vec{p}_2 - \vec{p}_1)^2 + m_\pi^2}} [\sigma^i (p_2 - p_1)_i]_{ab}; \quad (5.54)$$

the quantity \bar{T} is related to the strong interaction matrix according to

$$T_{ab;cd}(p_1, p_2; p_3, p_4) = \bar{T}_{ab}(p_1, p_2) \bar{T}_{cd}(p_3, p_4) \quad (5.55)$$

We choose to treat nucleons as non-relativistic particles and redefine the energy and propagator of nucleons such that

$$\mathcal{E}_{\vec{l};x} = \frac{\vec{l} \cdot \vec{l}}{2m_x^*} + m_x^*, \quad S_x^{ab}(l) = \frac{\delta^{ab}}{l_{0;x} - \mathcal{E}_{\vec{l};x}}, \quad (5.56)$$

with δ^{ab} the Kröneckel- δ in spin space. In Eq. (5.44), traces immediately appear *via* the contraction of indices involved in loops of nucleons in the diagrams: this corresponds to the trace presented in the kinetics equation Eq. (5.12) which appears naturally from the nucleon loops in the hadronic part of the process.

By conservation of four-momentum, $S_1 = S_5$ for the first self-energy diagram, and $S_6 = S_5$ for the second self-energy diagram, such that the different terms of the self-energy

corrections write as

$$\begin{cases} D_1^{\alpha\beta} \\ D_2^{\alpha\beta} \\ D_3^{\alpha\beta} \\ D_4^{\alpha\beta} \end{cases} = \frac{1}{64} \sum_{x,y,z,u,w} S_x^2(p_1) S_y(p_2) S_z(p_3) S_u(p_4) S_w(p_6) \begin{cases} D_{1;\text{iso}} D_{1;\text{spin}}^{\alpha\beta} \\ D_{2;\text{iso}} D_{2;\text{spin}}^{\alpha\beta} \\ D_{3;\text{iso}} D_{3;\text{spin}}^{\alpha\beta} \\ D_{4;\text{iso}} D_{4;\text{spin}}^{\alpha\beta} \end{cases}, \quad (5.57)$$

$$\begin{cases} E_1^{\alpha\beta} \\ E_2^{\alpha\beta} \\ E_3^{\alpha\beta} \\ E_4^{\alpha\beta} \end{cases} = \frac{1}{64} \sum_{x,y,z,u,w} S_x(p_1) S_y(p_2) S_z(p_3) S_u(p_4) S_w^2(p_6) \begin{cases} E_{1;\text{iso}} E_{1;\text{spin}}^{\alpha\beta} \\ E_{2;\text{iso}} E_{2;\text{spin}}^{\alpha\beta} \\ E_{3;\text{iso}} E_{3;\text{spin}}^{\alpha\beta} \\ E_{4;\text{iso}} E_{4;\text{spin}}^{\alpha\beta} \end{cases}. \quad (5.58)$$

and the four-momenta of nucleons in play are presented in Table. 5.1.

Nucleon	four-momentum	
	D	E
(1)	p_1	p_1
(2)	p_2	p_2
(3)	p_3	p_3
(4)	$p_1 + p_2 - p_3$	$p_1 - Q + p_2 - p_3$
(5)	p_1	$p_1 - Q$
(6)	$p_1 - Q$	$p_1 - Q$

Table 5.1: Conservation of four-momenta of nucleons of the self-energy corrections to MUrca.

On the one hand, let us treat the isospin part of the first diagram of the self-energy corrections. We chose to present the derivation for the nucleon-weak boson vertex combination with a τ^+ on the left hand side of the diagram, and a τ^- on the right hand side of the diagram. As was discussed above, choosing the other vertex combination only means that all nucleons in play have opposite isospin quantum number, or in other words, that protons are changed into neutrons and *vice-versa*. In the chosen convention, the isospin part is given by the following traces

$$D_{1;\text{iso}} = \text{Tr} \left[\tau^+ (1 + s_x \tau^3) \tau^i (1 + s_u \tau^3) \tau^j (1 + s_x \tau^3) \tau^- (1 + s_w \tau^3) \right] \text{Tr} \left[(1 + s_y \tau^3) \tau_i (1 + s_z \tau^3) \tau_j \right], \quad (5.59)$$

$$D_{2;\text{iso}} = \text{Tr} \left[\tau^+ (1 + s_x \tau^3) \tau^i (1 + s_z \tau^3) \tau^j (1 + s_x \tau^3) \tau^- (1 + s_w \tau^3) \right] \text{Tr} \left[(1 + s_y \tau^3) \tau_i (1 + s_u \tau^3) \tau_j \right], \quad (5.60)$$

$$D_{3;\text{iso}} = \text{Tr} \left[\tau^+ (1 + s_x \tau^3) \tau^i (1 + s_z \tau^3) \tau^j (1 + s_y \tau^3) \tau_i (1 + s_u \tau^3) \tau_j (1 + s_x \tau^3) \tau^- (1 + s_w \tau^3) \right], \quad (5.61)$$

$$D_{4;\text{iso}} = \text{Tr} \left[\tau^+ (1 + s_x \tau^3) \tau^i (1 + s_u \tau^3) \tau^j (1 + s_y \tau^3) \tau_i (1 + s_z \tau^3) \tau_j (1 + s_x \tau^3) \tau^- (1 + s_w \tau^3) \right]. \quad (5.62)$$

After operating the isospin traces with the *Mathematica* algebra software, we operate the sum over the nucleon isospin nature to define the quantity I :

$$\begin{aligned} \begin{cases} I_{D1} \\ I_{D2} \\ I_{D3} \\ I_{D4} \end{cases} &= \frac{1}{64} \sum_{x,y,z,u,w} S_x^2(p_1) S_y(p_2) S_z(p_3) S_u(p_4) S_w(p_6) \times \begin{cases} D_{1,\text{iso}}^{i,j} \\ D_{2,\text{iso}}^{i,j} \\ D_{3,\text{iso}}^{i,j} \\ D_{4,\text{iso}}^{i,j} \end{cases} \quad (5.63) \\ &= \begin{cases} S_p(p_1)^2 \left[S_p(p_2) S_p(p_3) S_p(p_4) + S_n(p_2) \left(4S_p(p_3) S_n(p_4) + S_n(p_3) S_p(p_4) \right) \right] S_n(p_6) \\ S_p(p_1)^2 \left[S_p(p_2) S_p(p_3) S_p(p_4) + S_n(p_2) \left(4S_n(p_3) S_p(p_4) + S_p(p_3) S_n(p_4) \right) \right] S_n(p_6) \\ S_p(p_1)^2 \left[S_p(p_2) S_p(p_3) S_p(p_4) - 2S_n(p_2) \left(S_p(p_3) S_n(p_4) + S_n(p_3) S_p(p_4) \right) \right] S_n(p_6) \\ S_p(p_1)^2 \left[S_p(p_2) S_p(p_3) S_p(p_4) - 2S_n(p_2) \left(S_p(p_3) S_n(p_4) + S_n(p_3) S_p(p_4) \right) \right] S_n(p_6) \end{cases} \end{aligned}$$

and similarly for the second diagram of the self-energy correction

$$\begin{aligned} \begin{cases} I_{E1} \\ I_{E2} \\ I_{E3} \\ I_{E4} \end{cases} &= \frac{1}{64} \sum_{x,y,z,u,w} S_x(p_1) S_y(p_2) S_z(p_3) S_u(p_4) S_w^2(p_6) \times \begin{cases} E_{1,\text{iso}}^{i,j} \\ E_{2,\text{iso}}^{i,j} \\ E_{3,\text{iso}}^{i,j} \\ E_{4,\text{iso}}^{i,j} \end{cases} \quad (5.64) \\ &= \begin{cases} S_p(p_1) \left[S_n(p_2) S_n(p_3) S_n(p_4) + S_p(p_2) \left(4S_n(p_3) S_p(p_4) + S_p(p_3) S_n(p_4) \right) \right] S_n^2(p_6) \\ S_p(p_1) \left[S_n(p_2) S_n(p_3) S_n(p_4) + S_p(p_2) \left(4S_n(p_3) S_p(p_4) + S_p(p_3) S_n(p_4) \right) \right] S_n^2(p_6) \\ S_p(p_1) \left[S_n(p_2) S_n(p_3) S_n(p_4) - 2S_p(p_2) \left(S_n(p_3) S_p(p_4) + S_p(p_3) S_n(p_4) \right) \right] S_n^2(p_6) \\ S_p(p_1) \left[S_n(p_2) S_n(p_3) S_n(p_4) - 2S_p(p_2) \left(S_n(p_3) S_p(p_4) + S_p(p_3) S_n(p_4) \right) \right] S_n^2(p_6) \end{cases} \end{aligned}$$

On the other hand, let us treat the spin part of the self-energy corrections

$$D_{1,\text{spin}}^{\alpha\beta} = \text{Tr} \left[\bar{\Gamma}^\mu \bar{T}(p_1, p_4) \bar{T}(p_4, p_1) \bar{\Gamma}^\nu \right] \text{Tr} \left[\bar{T}(p_2, p_3) \bar{T}(p_3, p_2) \right], \quad (5.65)$$

$$D_{2,\text{spin}}^{\alpha\beta} = \text{Tr} \left[\bar{\Gamma}^\mu \bar{T}(p_1, p_3) \bar{T}(p_3, p_1) \bar{\Gamma}^\nu \right] \text{Tr} \left[\bar{T}(p_2, p_4) \bar{T}(p_4, p_2) \right], \quad (5.66)$$

$$D_{3,\text{spin}}^{\alpha\beta} = \text{Tr} \left[\bar{\Gamma}^\mu \bar{T}(p_1, p_3) \bar{T}(p_3, p_2) \bar{T}(p_2, p_4) \bar{T}(p_4, p_1) \bar{\Gamma}^\nu \right], \quad (5.67)$$

$$D_{4,\text{spin}}^{\alpha\beta} = \text{Tr} \left[\bar{\Gamma}^\mu \bar{T}(p_1, p_4) \bar{T}(p_4, p_2) \bar{T}(p_2, p_3) \bar{T}(p_3, p_1) \bar{\Gamma}^\nu \right], \quad (5.68)$$

$$E_{1,\text{spin}}^{\alpha\beta} = \text{Tr} \left[\bar{\Gamma}^\nu \bar{T}(p_6, p_4) \bar{T}(p_4, p_6) \bar{\Gamma}^\mu \right] \text{Tr} \left[\bar{T}(p_2, p_3) \bar{T}(p_3, p_2) \right], \quad (5.69)$$

$$E_{2,\text{spin}}^{\alpha\beta} = \text{Tr} \left[\bar{\Gamma}^\nu \bar{T}(p_6, p_3) \bar{T}(p_3, p_6) \bar{\Gamma}^\mu \right] \text{Tr} \left[\bar{T}(p_2, p_4) \bar{T}(p_4, p_2) \right], \quad (5.70)$$

$$E_{3,\text{spin}}^{\alpha\beta} = \text{Tr} \left[\bar{\Gamma}^\nu \bar{T}(p_6, p_4) \bar{T}(p_4, p_2) \bar{T}(p_2, p_3) \bar{T}(p_3, p_6) \bar{\Gamma}^\mu \right], \quad (5.71)$$

$$E_{4,\text{spin}}^{\alpha\beta} = \text{Tr} \left[\bar{\Gamma}^\nu \bar{T}(p_6, p_3) \bar{T}(p_3, p_2) \bar{T}(p_2, p_4) \bar{T}(p_4, p_6) \bar{\Gamma}^\mu \right]. \quad (5.72)$$

The traces operated on the spin Pauli matrices include terms related to the weak boson vertex $\bar{\Gamma}$ and the strong interaction matrices \bar{T} but not the nucleon propagator thanks to the

Kronecker- δ in spin space appearing in the non-relativistic approach of the nucleon propagator. The spin 4×4 matrix $X_{\text{spin}}^{\alpha\beta}$ can be decomposed into vector (proportional to C_V^2), axial (proportional to C_A^2) and cross (proportional to $C_A C_V$) terms such that

$$X_{\text{spin}}^{\alpha\beta} = \begin{pmatrix} \sim C_V^2 & \sim C_A C_V & \sim C_A C_V & \sim C_A C_V \\ \sim C_A C_V & \sim C_A^2 & \sim C_A^2 & \sim C_A^2 \\ \sim C_A C_V & \sim C_A^2 & \sim C_A^2 & \sim C_A^2 \\ \sim C_A C_V & \sim C_A^2 & \sim C_A^2 & \sim C_A^2 \end{pmatrix} = \begin{pmatrix} X_{C_V} & X_{C_V C_A}^i \\ X_{C_V C_A}^j & X_{C_A}^{ij} \end{pmatrix}, \quad (5.73)$$

with the indices i , and j accounting for the space components. The detailed expression of the spin part is presented in Appendix A. The axial terms can be presented using two different projections

- terms projected on δ^{ij} and terms projected on $Q^i Q^j / |\vec{Q}|^2$, as is the case in Appendix A;
- terms projected along the transverse projector $\delta^{ij} - Q^i Q^j / |\vec{Q}|^2$ and on the longitudinal projector $Q^i Q^j / |\vec{Q}|^2$, as will be used to present the results.

5.3.1.2 Vertex corrections

Three contributions to the vertex correction, denoted in the following V_1 , V_2 and V_3 and presented in Fig. 5.12, Fig. 5.13 and Fig. 5.14 respectively, must be taken into account. It is easily noticeable that vertex contributions 1 and 2 correspond exactly to the same integrated contribution, such that we shall present the derivation only for V_2 . The conservation of four-momenta for the three vertex contributions is presented in Table 5.2.

Nucleon	four-momentum		
	V_1	V_2	V_3
(1)	p_1	p_1	p_1
(2)	p_2	p_2	p_2
(3)	p_3	p_3	p_3
(4)	$p_1 + p_2 - p_3$	$p_1 + p_2 - p_3$	$p_1 + p_2 - p_3$
(5)	$p_1 - Q$	$p_1 - Q$	$p_1 - Q$
(6)	$p_1 - Q + p_2 - p_3$	$p_3 - Q$	$p_2 + Q$

Table 5.2: Conservation of four-momenta of nucleons in the vertex contributions to MURca.

For diagrams V_2 and V_3 , we can distinguish four different ways the strong interaction can couple nucleons in play per diagram, such that

$$\begin{cases} V_{2a}^{\alpha\beta} \\ V_{2b}^{\alpha\beta} \\ V_{2c}^{\alpha\beta} \\ V_{2d}^{\alpha\beta} \end{cases} = \frac{1}{64} \sum_{x,y,z,u,v,w} S_x(p_1) S_y(p_2) S_z(p_3) S_u(p_4) S_v(p_5) S_w(p_6) \begin{cases} V_{2a;iso} V_{2a;spin}^{\alpha\beta} \\ V_{2b;iso} V_{2b;spin}^{\alpha\beta} \\ V_{2c;iso} V_{2c;spin}^{\alpha\beta} \\ V_{2d;iso} V_{2d;spin}^{\alpha\beta} \end{cases},$$

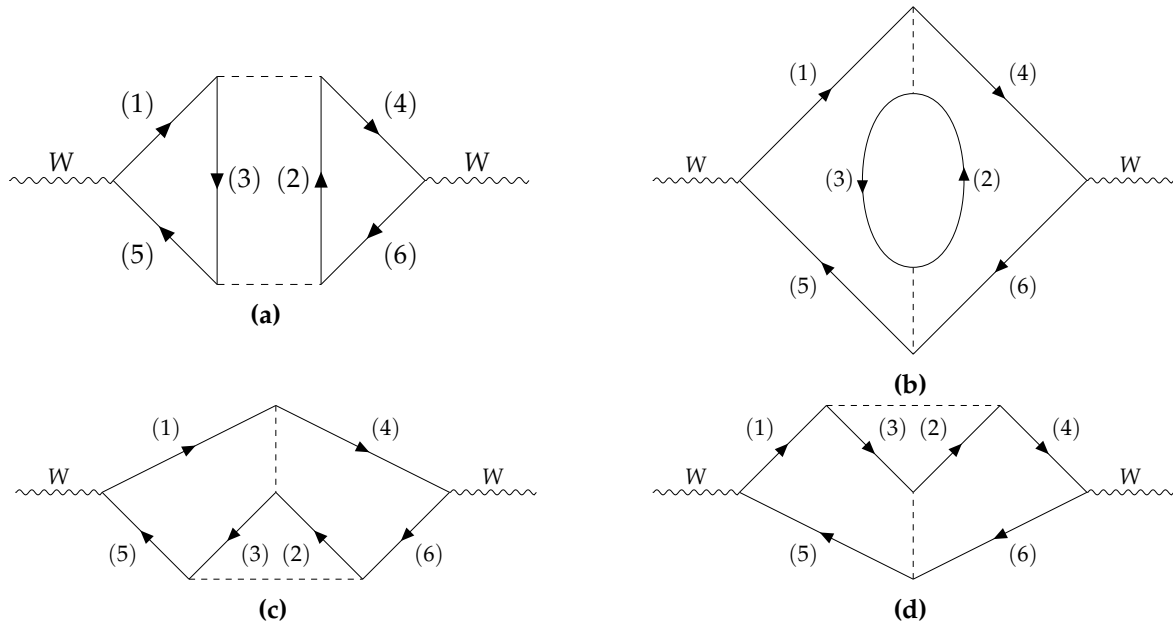


Figure 5.12: Diagrams of the first vertex correction of MURca denoted V_1 , corresponding to diagram (3d) in [Bacca et al. \[2012\]](#).

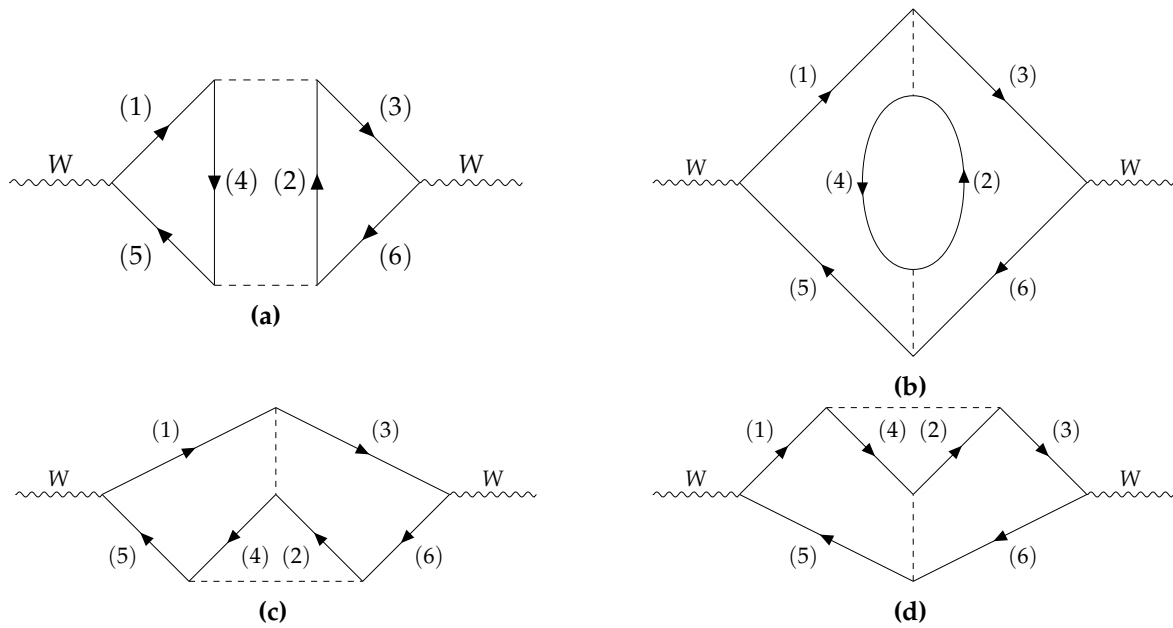


Figure 5.13: Diagrams of the second vertex correction of MURca denoted V_2 , corresponding to diagram (3e) in [Bacca et al. \[2012\]](#).

$$\begin{cases} V_{3a}^{\alpha\beta} \\ V_{3b}^{\alpha\beta} \\ V_{3c}^{\alpha\beta} \\ V_{3d}^{\alpha\beta} \end{cases} = \frac{1}{64} \sum_{x,y,z,u,v,w} S_x(p_1) S_y(p_2) S_z(p_3) S_u(p_4) S_v(p_5) S_w(p_6) \begin{cases} V_{3a;iso} V_{3a;spin}^{\alpha\beta} \\ V_{3b;iso} V_{3b;spin}^{\alpha\beta} \\ V_{3c;iso} V_{3c;spin}^{\alpha\beta} \\ V_{3d;iso} V_{3d;spin}^{\alpha\beta} \end{cases} ,$$

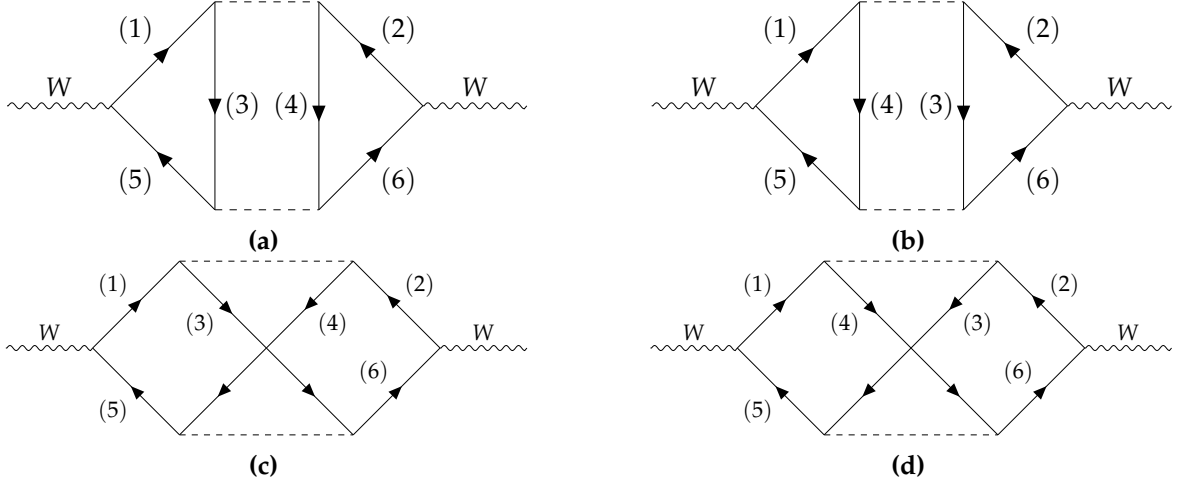


Figure 5.14: Diagrams of the third vertex correction of MURca denoted V_3 , corresponding to diagram (3c) in [Bacca et al. \[2012\]](#).

On the one hand, let us treat the isospin part of the V_2 and V_3 contributions, again presented for a τ^+ nucleon-weak boson vertex on the left of the diagram, and a τ^- nucleon-weak boson vertex on the right of the diagram. For the contribution V_2

$$\begin{cases} I_{V2a} &= 2S_p(p_1) [S_p(p_2)S_p(p_4) + S_n(p_2)S_n(p_4)] S_p(p_3)S_n(p_5)S_n(p_6) , \\ I_{V2b} &= -S_p(p_1) [S_p(p_2)S_p(p_4) + S_n(p_2)S_n(p_4)] S_p(p_3)S_n(p_5)S_n(p_6) , \\ I_{V2c} &= S_p(p_1) [2S_p(p_2)S_p(p_4) - S_n(p_2)S_n(p_4)] S_p(p_3)S_n(p_5)S_n(p_6) , \\ I_{V2d} &= S_p(p_1) [2S_n(p_2)S_n(p_4) - S_p(p_2)S_p(p_4)] S_p(p_3)S_n(p_5)S_n(p_6) , \end{cases} \quad (5.74)$$

and for the contribution V_3

$$\begin{cases} I_{V3a} &= -2S_p(p_1)S_n(p_2) [S_n(p_3)S_p(p_4) + S_p(p_3)S_n(p_4)] S_n(p_5)S_p(p_6) , \\ I_{V3b} &= -2S_p(p_1)S_n(p_2) [S_n(p_3)S_p(p_4) + S_p(p_3)S_n(p_4)] S_n(p_5)S_p(p_6) , \\ I_{V3c} &= S_p(p_1)S_n(p_2) [4S_n(p_3)S_p(p_4) + S_p(p_3)S_n(p_4)] S_n(p_5)S_p(p_6) , \\ I_{V3d} &= S_p(p_1)S_n(p_2) [4S_p(p_3)S_n(p_4) + S_n(p_3)S_p(p_4)] S_n(p_5)S_p(p_6) . \end{cases} \quad (5.75)$$

On the other hand, we treat the spin part of the V_2 and V_3 contributions

$$V_{2a;spin}^{\alpha\beta} = \text{Tr} [\bar{\Gamma}^\alpha \bar{T}(p_1, p_4) \bar{T}(p_4, p_5)] \text{Tr} [\bar{\Gamma}^\beta \bar{T}(p_6, p_2) \bar{T}(p_2, p_3)] , \quad (5.76)$$

$$V_{2b;spin}^{\alpha\beta} = \text{Tr} [\bar{\Gamma}^\alpha \bar{T}(p_1, p_3) \bar{\Gamma}^\beta \bar{T}(p_6, p_5)] \text{Tr} [\bar{T}(p_2, p_4) \bar{T}(p_4, p_2)] , \quad (5.77)$$

$$V_{2c;spin}^{\alpha\beta} = \text{Tr} [\bar{\Gamma}^\alpha \bar{T}(p_1, p_3) \bar{\Gamma}^\beta \bar{T}(p_6, p_2) \bar{T}(p_2, p_4) \bar{T}(p_4, p_5)] , \quad (5.78)$$

$$V_{2d;spin}^{\alpha\beta} = \text{Tr} [\bar{\Gamma}^\alpha \bar{T}(p_1, p_4) \bar{T}(p_4, p_2) \bar{T}(p_2, p_3) \bar{\Gamma}^\beta \bar{T}(p_6, p_5)] , \quad (5.79)$$

$$V_{3a;spin}^{\alpha\beta} = \text{Tr} [\bar{\Gamma}^\alpha \bar{T}(p_1, p_3) \bar{T}(p_3, p_5)] \text{Tr} [\bar{\Gamma}^\beta \bar{T}(p_2, p_4) \bar{T}(p_4, p_6)] , \quad (5.80)$$

$$V_{3b;spin}^{\alpha\beta} = \text{Tr} [\bar{\Gamma}^\alpha \bar{T}(p_1, p_4) \bar{T}(p_4, p_5)] \text{Tr} [\bar{\Gamma}^\beta \bar{T}(p_2, p_3) \bar{T}(p_3, p_6)] , \quad (5.81)$$

$$V_{3c;spin}^{\alpha\beta} = \text{Tr} \left[\bar{\Gamma}^\alpha \bar{T}(p_1, p_3) \bar{T}(p_3, p_6) \bar{\Gamma}^\beta \bar{T}(p_2, p_4) \bar{T}(p_4, p_5) \right], \quad (5.82)$$

$$V_{3d;spin}^{\alpha\beta} = \text{Tr} \left[\bar{\Gamma}^\alpha \bar{T}(p_1, p_4) \bar{T}(p_4, p_6) \bar{\Gamma}^\beta \bar{T}(p_2, p_3) \bar{T}(p_3, p_5) \right]; \quad (5.83)$$

details are presented in Appendix A.

5.3.2 The hadronic polarization function treated in the Matsubara formalism

In Eq. (5.43), the conservation of four-momentum in the hadronic part of the diagrams introduces the Dirac δ -function, which can reduce the number of integrals to operate

$$\Pi^{\alpha\beta}(Q) = \left(\prod_{j=1}^4 \int \frac{d^4 p_j}{(2\pi)^4} \right) \sum_X I_X X_{\text{spin}}^{\alpha\beta}(Q) \delta^4(p_1 + p_2 - p_3 - p_4). \quad (5.84)$$

Because we neglect the time component of the pion, only the isospin part of the derivation is concerned with the integral over the time component of the four-momenta. The four dimensional integrals over the nucleon four-momenta can be replaced by three dimensional integrals and summed *via* the Matsubara formalism. In this formalism, an analytical continuation is used, and thankfully the expression is simple enough that this continuation can be performed. We introduce the Matsubara frequencies denoted ω (for details, see Appendix B), and the time component of the nucleon with four-momentum l such that

$$l_{0,x} = i\omega + \mu_x^*, \quad (5.85)$$

with μ^* the effective chemical potential of the nucleon of isospin nature x ; including the chemical potential of particles allows us to include *in medium* effects. The integral is transformed such that

$$\frac{1}{2\pi} \int d^4 k \rightarrow \frac{1}{\beta} \sum_{\omega_l} \int d^3 k, \quad (5.86)$$

with β the inverse of the temperature. By introducing the Matsubara frequencies, the nucleon propagator takes the form

$$S_x^{ab}(l) = \frac{\delta^{ab}}{i\omega - \tilde{\mathcal{E}}_{l;x} + i\eta}, \quad \text{with} \quad \tilde{\mathcal{E}}_{l;x} = \mathcal{E}(\vec{l}) - \mu_x^*, \quad (5.87)$$

and with η a small quantity permitting the analytical continuation for a retarded function; in practice, we operate an analytical continuation of Q_0 from a bosonic frequency. We denote ω_1, ω_2 and ω_3 the Matsubara frequencies referring to p_1, p_2 and p_3 respectively. The retarded hadronic polarisation function can therefore be written as

$$\Pi^{\alpha\beta}(Q) = \left(\prod_{j=1}^3 \int \frac{d^3 \vec{p}_j}{(2\pi)^3} \right) \int \frac{d^3 p_4}{(2\pi)^4} \delta^3(\vec{p}_1 + \vec{p}_2 - \vec{p}_3 - \vec{p}_4) \sum_X \left(\frac{1}{\beta^3} \sum_{\omega_1} \sum_{\omega_2} \sum_{\omega_3} I_X \right) X_{\text{spin}}^{\alpha\beta}, \quad (5.88)$$

The sum operated over Matsubara frequencies introduces distribution functions denoted n_F and n_{BE} , respectively for the Fermi distribution and the Bose-Einstein distribution. Details on the derivation of the sum over Matsubara frequencies are given in Appendix B; the MATHEMATICA package `MatsubaraSum` is also a very useful tool to rapidly compute those sums. Using Table 5.1 and Table 5.2, the sums are given by

$$\begin{aligned} \frac{1}{\beta^3} \sum_{\omega_1} \sum_{\omega_2} \sum_{\omega_3} I_X &= \frac{1}{\beta^3} \sum_{\{x,y,z,u,v,w\}=\text{iso}} \left[\sum_{\omega_1} \sum_{\omega_2} \sum_{\omega_3} S_x(p_1) S_y(p_2) S_z(p_3) S_u(p_4) S_v(p_5) S_w(p_6) \right]_X \\ &\equiv \sum_{\text{iso}} \mathcal{M}_X, \end{aligned} \quad (5.89)$$

with the sum over isospin indices given by Eq. (5.63), Eq. (5.74) and Eq. (5.75). Details on the derivation of the \mathcal{M} functions are given in Appendix C. In our derivation, only the imaginary part of the retarded polarization function is of interest, such that

$$\begin{aligned} \text{Im } \Pi^{\alpha\beta}(Q) &= \left(\prod_{j=1}^3 \int \frac{d^3 \vec{p}_j}{(2\pi)^3} \right) \int \frac{d^3 p_4}{(2\pi)^4} \sum_{\text{iso}} \delta^3(\vec{p}_1 + \vec{p}_2 - \vec{p}_3 - \vec{p}_4) \left(\text{Im } \mathcal{M}_D \sum_{X=D,1,2,3,4} X_{\text{spin}}^{\alpha\beta} \right. \\ &\quad \left. + \text{Im } \mathcal{M}_E \sum_{X=E,1,2,3,4} X_{\text{spin}}^{\alpha\beta} + 2 \text{Im } \mathcal{M}_{V_2} \sum_{X=a,b,c,d} V_{2X,\text{spin}}^{\alpha\beta} + \text{Im } \mathcal{M}_{V_3} \sum_{X=a,b,c,d} V_{3X,\text{spin}}^{\alpha\beta} \right) \end{aligned} \quad (5.90)$$

with $\text{Im } \mathcal{M}_D$, $\text{Im } \mathcal{M}_E$, $\text{Im } \mathcal{M}_{V_2}$ and $\text{Im } \mathcal{M}_{V_3}$ explicitly given in Appendix C.

Taking the imaginary part of the \mathcal{M} functions introduces a Dirac δ -function similar to a conservation of the time component of the four-momentum (energy) of particles. Let us note that it is an additional Dirac δ -function that reduces one more integral in the imaginary part of the retarded polarization function, not to be confused with the Dirac δ -function used in Eq. (5.88). Taking the imaginary part of the \mathcal{M} functions puts the particles on their mass shell. Let us introduce the notation

$$\mathcal{G}(\alpha, \beta, \gamma, \delta) = n_F(\alpha) n_F(\beta) (1 - n_F(\gamma)) (1 - n_F(\delta)) - (1 - n_F(\alpha)) (1 - n_F(\beta)) n_F(\gamma) n_F(\delta), \quad (5.91)$$

and

$$\mathcal{N}_D = \pi \frac{\mathcal{G}(\tilde{\mathcal{E}}_{\vec{p}_6;w}, \tilde{\mathcal{E}}_{\vec{p}_2;y}, \tilde{\mathcal{E}}_{\vec{p}_3;z}, \tilde{\mathcal{E}}_{\vec{p}_4;u})}{(\tilde{\mathcal{E}}_{\vec{p}_1;x} + \tilde{\mathcal{E}}_{\vec{p}_2;y} - \tilde{\mathcal{E}}_{\vec{p}_3;z} - \tilde{\mathcal{E}}_{\vec{p}_4;u})^2}, \quad (5.92)$$

$$\mathcal{N}_E = \pi \frac{\mathcal{G}(\tilde{\mathcal{E}}_{\vec{p}_1;x}, \tilde{\mathcal{E}}_{\vec{p}_2;y}, \tilde{\mathcal{E}}_{\vec{p}_3;z}, \tilde{\mathcal{E}}_{\vec{p}_4;u})}{(\tilde{\mathcal{E}}_{\vec{p}_6;w} + \tilde{\mathcal{E}}_{\vec{p}_2;y} - \tilde{\mathcal{E}}_{\vec{p}_3;z} - \tilde{\mathcal{E}}_{\vec{p}_4;u})^2}, \quad (5.93)$$

$$\mathcal{N}_{V_2}^{(1)} = -\pi \frac{\mathcal{G}(\tilde{\mathcal{E}}_{\vec{p}_5;v}, \tilde{\mathcal{E}}_{\vec{p}_2;y}, \tilde{\mathcal{E}}_{\vec{p}_3;z}, \tilde{\mathcal{E}}_{\vec{p}_4;u})}{(\tilde{\mathcal{E}}_{\vec{p}_5;v} + \tilde{\mathcal{E}}_{\vec{p}_2;y} - \tilde{\mathcal{E}}_{\vec{p}_4;u} - \tilde{\mathcal{E}}_{\vec{p}_6;w})(\tilde{\mathcal{E}}_{\vec{p}_1;x} + \tilde{\mathcal{E}}_{\vec{p}_2;y} - \tilde{\mathcal{E}}_{\vec{p}_3;z} - \tilde{\mathcal{E}}_{\vec{p}_4;u})}, \quad (5.94)$$

$$\mathcal{N}_{V_2}^{(1)} = \pi \frac{\mathcal{G}(\tilde{\mathcal{E}}_{\vec{p}_1;x}, \tilde{\mathcal{E}}_{\vec{p}_2;y}, \tilde{\mathcal{E}}_{\vec{p}_4;u}, \tilde{\mathcal{E}}_{\vec{p}_6;w})}{(\tilde{\mathcal{E}}_{\vec{p}_5;v} + \tilde{\mathcal{E}}_{\vec{p}_2;y} - \tilde{\mathcal{E}}_{\vec{p}_4;u} - \tilde{\mathcal{E}}_{\vec{p}_6;w})(\tilde{\mathcal{E}}_{\vec{p}_1;x} + \tilde{\mathcal{E}}_{\vec{p}_2;y} - \tilde{\mathcal{E}}_{\vec{p}_3;z} - \tilde{\mathcal{E}}_{\vec{p}_4;u})}, \quad (5.95)$$

$$\mathcal{N}_{V_3}^{(1)} = -\pi \frac{\mathcal{G}(\tilde{\mathcal{E}}_{\vec{p}_1;x}, \tilde{\mathcal{E}}_{\vec{p}_6;w}, \tilde{\mathcal{E}}_{\vec{p}_3;z}, \tilde{\mathcal{E}}_{\vec{p}_4;u})}{(\tilde{\mathcal{E}}_{\vec{p}_3;z} + \tilde{\mathcal{E}}_{\vec{p}_4;u} - \tilde{\mathcal{E}}_{\vec{p}_5;v} - \tilde{\mathcal{E}}_{\vec{p}_6;w})(\tilde{\mathcal{E}}_{\vec{p}_1;x} + \tilde{\mathcal{E}}_{\vec{p}_2;y} - \tilde{\mathcal{E}}_{\vec{p}_3;z} - \tilde{\mathcal{E}}_{\vec{p}_4;u})}, \quad (5.96)$$

$$\mathcal{N}_{V_3}^{(1)} = \pi \frac{\mathcal{G}(\tilde{\mathcal{E}}_{\vec{p}_2;y}, \tilde{\mathcal{E}}_{\vec{p}_5;v}, \tilde{\mathcal{E}}_{\vec{p}_3;z}, \tilde{\mathcal{E}}_{\vec{p}_4;u})}{(\tilde{\mathcal{E}}_{\vec{p}_3;z} + \tilde{\mathcal{E}}_{\vec{p}_4;u} - \tilde{\mathcal{E}}_{\vec{p}_5;v} - \tilde{\mathcal{E}}_{\vec{p}_6;w})(\tilde{\mathcal{E}}_{\vec{p}_1;x} + \tilde{\mathcal{E}}_{\vec{p}_2;y} - \tilde{\mathcal{E}}_{\vec{p}_3;z} - \tilde{\mathcal{E}}_{\vec{p}_4;u})}; \quad (5.97)$$

later on referred to as the \mathcal{N} functions. Once summed over the different diagrams, the \mathcal{N} functions correspond to the matrix element of the reaction multiplied by the distribution functions of incoming and outgoing particles with the propagator of what we call the intermediary particles. Intermediary particles are particles that would lead to Direct Urca cuts correcting the dominant Direct Urca contribution in the diagrams drawn in section 5.3.1; note that the Direct Urca cuts were neglected when we established the \mathcal{N} functions in Appendix C, because we present the derivation for the Modified Urca process only. The \mathcal{N} functions can be easily deduced by cutting the diagrams presented in Fig. 5.10, Fig. 5.11, Fig. 5.13 and Fig. 5.14 either vertically or with diagonals. The imaginary part of the retarded polarization function can be expressed as

$$\begin{aligned} \text{Im } \Pi^{\alpha\beta}(Q) &= \left(\prod_{j=1}^3 \int \frac{d^3 \vec{p}_j}{(2\pi)^3} \right) \int \frac{d^3 p_4}{(2\pi)^4} \sum_{\text{iso}} \delta^3(\vec{p}_1 + \vec{p}_2 - \vec{p}_3 - \vec{p}_4) \\ &\times \left(\delta(\tilde{\mathcal{E}}_{\vec{p}_6;w} + \tilde{\mathcal{E}}_{\vec{p}_2;y} + Q_0 - \tilde{\mathcal{E}}_{\vec{p}_3;z} - \tilde{\mathcal{E}}_{\vec{p}_4;u}) \mathcal{N}_D \sum_X X_{\text{spin}}^{\alpha\beta} \right. \\ &\delta(\tilde{\mathcal{E}}_{\vec{p}_1;x} + \tilde{\mathcal{E}}_{\vec{p}_2;y} - Q_0 - \tilde{\mathcal{E}}_{\vec{p}_3;z} - \tilde{\mathcal{E}}_{\vec{p}_4;u}) \mathcal{N}_E \sum_X X_{\text{spin}}^{\alpha\beta} \\ &+ 2 \left[\delta(\tilde{\mathcal{E}}_{\vec{p}_5;v} + \tilde{\mathcal{E}}_{\vec{p}_2;y} + Q_0 - \tilde{\mathcal{E}}_{\vec{p}_3;z} - \tilde{\mathcal{E}}_{\vec{p}_4;u}) \mathcal{N}_{V_2}^{(1)} \right. \\ &\quad \left. + \delta(\tilde{\mathcal{E}}_{\vec{p}_1;x} + \tilde{\mathcal{E}}_{\vec{p}_2;y} - Q_0 - \tilde{\mathcal{E}}_{\vec{p}_4;u} - \tilde{\mathcal{E}}_{\vec{p}_6;w}) \mathcal{N}_{V_2}^{(2)} \right] \sum_{X=a,b,c,d} V_{2X,\text{spin}}^{\alpha\beta} \\ &+ \left[\delta(\tilde{\mathcal{E}}_{\vec{p}_6;w} + \tilde{\mathcal{E}}_{\vec{p}_1;x} - Q_0 - \tilde{\mathcal{E}}_{\vec{p}_3;z} - \tilde{\mathcal{E}}_{\vec{p}_4;u}) \mathcal{N}_{V_3}^{(1)} \right. \\ &\quad \left. + \delta(\tilde{\mathcal{E}}_{\vec{p}_5;v} + \tilde{\mathcal{E}}_{\vec{p}_2;y} + Q_0 - \tilde{\mathcal{E}}_{\vec{p}_3;z} - \tilde{\mathcal{E}}_{\vec{p}_4;u}) \mathcal{N}_{V_3}^{(2)} \right] \sum_{X=a,b,c,d} V_{3X,\text{spin}}^{\alpha\beta} \Big). \quad (5.98) \end{aligned}$$

In Appendix C, we present the details of a change of variables to reduce the number of integrals with the help of the Dirac δ -functions. Numerical results associated to the expression of the imaginary part of the hadronic polarization function are presented in the next section.

5.4 Numerical treatment of the momenta integrations with the Monte-Carlo method

At this stage of the derivation, we are left with an integration of dimension eight, which is operated in spherical coordinates such that the norm, and altitude and azimuthal angles for the momentum of particles are the variables to integrate over. To treat this integral, we use the Monte-Carlo integration numerical recipe [Metropolis, 1985]. The use of the Monte-Carlo integration is warranted because we know the behavior of all particles in play, or in other words the integrand. We want to treat the variables that are the momenta of independent particles in the Modified Urca diagrams, as random quantities such that the result can be interpreted as a probabilistic entity numerically solvable.

A simple first approach to the Monte-Carlo integration technique would be to generate N number of the random variable x in the domain $[a, b]$ along a uniform probability density such that

$$I = \int_a^b f(x)dx = \frac{b-a}{N} \sum_{i=1}^N f(x_i) . \quad (5.99)$$

A uniform probability density is constant such that all random generation of the variable x has the same probability in the domain $[a, b]$. Such sampling is called elementary. However, imagine that you know that in a part of the domain the integrand is very small: a uniform sampling allocates too many points to a part of the integral that is small and virtually does not matter, and too few points to a part of the integrand which dominates the value of the integral; the convergence of the numerical integration is therefore rather slow.

Therefore, we turn to a biased Monte-Carlo method called importance sampling: random sampling follows a non-uniform distribution denoted ρ which we know how to analytically integrate. The integration can be estimated according to

$$I = \int \frac{f(x)}{\rho(x)} \rho(x) dx = \frac{b-a}{N} \sum_{i=1}^N \frac{f(z_i)}{\rho(z_i)} , \quad (5.100)$$

with z the random variable sampled with the density probability ρ and $b-a$ the interval of the non-uniform sampling. To sample N variables according to the density probability ρ , one can use the formula linking two variables z and x following the density probability $\rho(z)$ and $\omega(x)$ respectively

$$\rho(z)dz = \omega(x)dx . \quad (5.101)$$

Let us give a simple example of an integral which resemble the one we want to discuss in Modified Urca calculations but with a smaller number of variables. The density of particle i denoted n_i is calculated from the expression

$$n_i = \frac{2}{(2\pi)^3 \hbar c} \int_0^\infty dp \int_0^\pi d\theta \int_0^{2\pi} d\phi p^2 n_F(\mathcal{E}_p - \mu_i) \sin(\phi) \quad (5.102)$$

$$= \frac{\sqrt{2}}{\pi^2 \hbar c} (m_i^* T)^{3/2} \int_0^\infty dx \frac{\sqrt{x}}{1 + e^{x-\eta_i}} , \quad (5.103)$$

with $x = p^2/(2mT)$, $\eta_i = (\mu_i^* - m_i^*)/T$, m_i^* the effective mass of the particle, μ_i^* the effective chemical potential of the particle and T the temperature. The density of particles can be extracted from an equation of state, and we present this example for the equation of state (RG)SLy4. The integral over dx is not trivial analytically, therefore we shall treat it with a Monte-Carlo method with random sampling.

Let us choose the non-uniform distribution for the variable x to be

$$\rho(x) = \frac{A}{1 + e^{x-\eta}}, \quad (5.104)$$

with A a constant to be determined by ensuring that the distribution (density probability) is normalized⁶

$$\int_0^\infty \rho(x) dx \equiv 1 \quad \rightarrow \quad A \left[-\ln(1 + e^{\eta-x}) \right]_0^\infty = 1 \quad \leftrightarrow \quad A = \frac{1}{\ln(1 + e^\eta)}. \quad (5.105)$$

We denote x the variable distributed uniformly such that

$$z = \eta - \ln\left(e^{-x/A} (1 + e^\eta) - 1\right). \quad (5.106)$$

Results of this integration are presented in Fig. 5.15 as the absolute difference between the value extracted from the (RG)SLy4, and the one calculated from the elementary Monte-Carlo and random-sampling Monte-Carlo, as a function of the number of points. We present results at temperature $T = 4.7$ MeV, baryon density $n_B = 0.2$ fm⁻³ and electron fraction $y_e = 0.3$. The random-sampling method converges much quicker than the elementary method.

⁶This allows us to randomly throw x between 0 and 1 and not care further for boundaries of the integral.

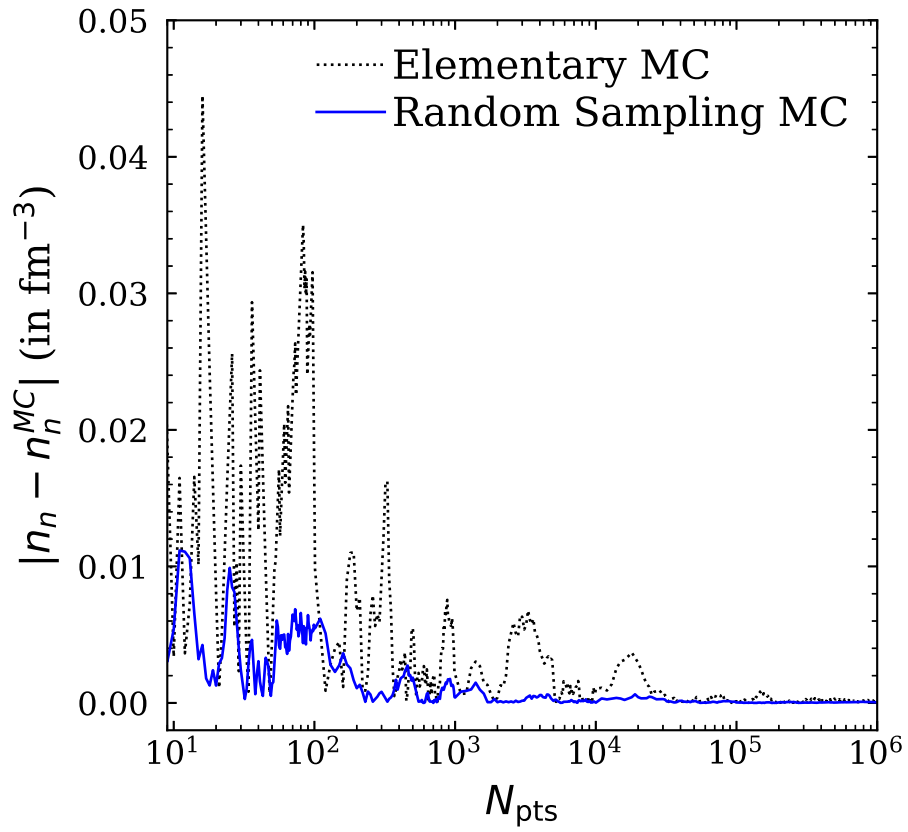


Figure 5.15: Absolute difference between the exact value for the neutron density in EoS (RG)SLy4 and the calculation by Monte-Carlo with elementary and random sampling method, at $T \sim 4.7$ MeV, $n_B \sim 0.2$ fm $^{-4}$ and $y_e \sim 0.3$.

5.5 Results of the Monte-Carlo integration for the hadronic part of Modified Urca

The results presented in this section are focused on the hadronic polarization function. Establishing the Modified Urca neutrino emissivity requires treating the lepton part of the process, which is beyond the scope of this manuscript. Our goal is to discuss our results for the hadronic part of the diagrams, and how it will affect the neutrino emissivity of this process.

5.5.1 Numerical divergence above the Direct Urca threshold

The \mathcal{N} functions described in section 5.3.2 can be rewritten using the conservation of energy as follows

$$\mathcal{N}_D = \pi \frac{\mathcal{G}(\tilde{\mathcal{E}}_{\vec{p}_6;w}, \tilde{\mathcal{E}}_{\vec{p}_2;y}, \tilde{\mathcal{E}}_{\vec{p}_3;z}, \tilde{\mathcal{E}}_{\vec{p}_4;u})}{(\tilde{\mathcal{E}}_{\vec{p}_1;x} - \tilde{\mathcal{E}}_{\vec{p}_6;w} - Q_0)^2}, \quad (5.107)$$

$$\mathcal{N}_E = \pi \frac{\mathcal{G}(\tilde{\mathcal{E}}_{\vec{p}_1;x}, \tilde{\mathcal{E}}_{\vec{p}_2;y}, \tilde{\mathcal{E}}_{\vec{p}_3;z}, \tilde{\mathcal{E}}_{\vec{p}_4;u})}{(\tilde{\mathcal{E}}_{\vec{p}_6;x} - \tilde{\mathcal{E}}_{\vec{p}_1;w} + Q_0)^2}, \quad (5.108)$$

$$\mathcal{N}_{V_2}^{(1)} = -\pi \frac{\mathcal{G}(\tilde{\mathcal{E}}_{\vec{p}_5;v}, \tilde{\mathcal{E}}_{\vec{p}_2;y}, \tilde{\mathcal{E}}_{\vec{p}_3;z}, \tilde{\mathcal{E}}_{\vec{p}_4;u})}{(\tilde{\mathcal{E}}_{\vec{p}_5;v} - \tilde{\mathcal{E}}_{\vec{p}_1;x} + Q_0)(\tilde{\mathcal{E}}_{\vec{p}_6;w} - \tilde{\mathcal{E}}_{\vec{p}_3;z} + Q_0)}, \quad (5.109)$$

$$\mathcal{N}_{V_2}^{(1)} = \pi \frac{\mathcal{G}(\tilde{\mathcal{E}}_{\vec{p}_1;x}, \tilde{\mathcal{E}}_{\vec{p}_2;y}, \tilde{\mathcal{E}}_{\vec{p}_4;u}, \tilde{\mathcal{E}}_{\vec{p}_6;w})}{(\tilde{\mathcal{E}}_{\vec{p}_5;v} - \tilde{\mathcal{E}}_{\vec{p}_1;x} + Q_0)(\tilde{\mathcal{E}}_{\vec{p}_6;w} - \tilde{\mathcal{E}}_{\vec{p}_3;z} + Q_0)}, \quad (5.110)$$

$$\mathcal{N}_{V_3}^{(1)} = -\pi \frac{\mathcal{G}(\tilde{\mathcal{E}}_{\vec{p}_1;x}, \tilde{\mathcal{E}}_{\vec{p}_6;w}, \tilde{\mathcal{E}}_{\vec{p}_3;z}, \tilde{\mathcal{E}}_{\vec{p}_4;u})}{(\tilde{\mathcal{E}}_{\vec{p}_2;y} - \tilde{\mathcal{E}}_{\vec{p}_6;w} + Q_0)(\tilde{\mathcal{E}}_{\vec{p}_1;x} - \tilde{\mathcal{E}}_{\vec{p}_5;v} - Q_0)}, \quad (5.111)$$

$$\mathcal{N}_{V_3}^{(1)} = \pi \frac{\mathcal{G}(\tilde{\mathcal{E}}_{\vec{p}_2;y}, \tilde{\mathcal{E}}_{\vec{p}_5;v}, \tilde{\mathcal{E}}_{\vec{p}_3;z}, \tilde{\mathcal{E}}_{\vec{p}_4;u})}{(\tilde{\mathcal{E}}_{\vec{p}_2;y} - \tilde{\mathcal{E}}_{\vec{p}_6;w} + Q_0)(\tilde{\mathcal{E}}_{\vec{p}_1;x} - \tilde{\mathcal{E}}_{\vec{p}_5;v} - Q_0)}. \quad (5.112)$$

The energy of the weak boson Q_0 is fixed by the weak interaction part of the diagram, *i.e.* by the energies of the leptons involved in the reaction. Close and beyond the threshold of the Direct Urca process, which exact location in terms of Q_0 is extracted from the Direct Urca calculations [Oertel et al., 2020, Pascal et al., 2022], the \mathcal{N} functions present a pole. This translates into numerical divergence of the integration. There are jumps in the Monte-Carlo integral, and the convergence is impossible. In Eq. (5.107), Eq. (5.108), Eq. (5.109), Eq. (5.110), Eq. (5.111) and Eq. (5.112), the denominator includes only intermediary particles (particles that corresponds to the Direct Urca cuts in the diagrams drawn in section 5.3.1⁷). For conditions of the weak boson energy Q_0 and momentum \vec{Q} which are below the DUrca threshold, the denominator of the \mathcal{N} functions can never reach zero, as the conditions of the Direct Urca process are not allowed: below the DUrca threshold, the Modified Urca calculations

⁷Direct Urca cuts were neglected when we established the \mathcal{N} functions from the Matsubara sums, because we presented the derivation for the Modified Urca process only.

do not diverge. However, the numerical divergence can appear close and beyond the DUrca threshold.

This is illustrated in Fig. 5.16, in which we present the imaginary part of the hadronic polarization function of the first self-energy diagram, for different values of the number of points in the Monte-Carlo integration. Results are presented for a temperature $T = 10$ MeV, a baryonic density $n_B = 0.2 \text{ fm}^{-3}$, and an electron fraction $y_e = 0.3$.

- In the top of this figure, the conditions for the leptonic part of the reaction are below the DUrca threshold of the reaction $(Q_{0,\text{th}}, |\vec{Q}|_{\text{th}}) \simeq (-45, 19)$ MeV. In this case, the numerical method converges well to a value around nine. We can note that the curve stops before 3×10^4 points: that means that for almost half of the points of the integration, the kinematics conditions randomly thrown for the nucleon's momenta do not permit the reaction, such that the Heaviside function in Eq. (C.18) of the Appendix leads to zero.
- In the bottom figure, the conditions for the leptonic part of the reaction are above the DUrca threshold. It is clear from the scale on the y axis that the jumps lead to numerical divergence. Moreover from the last jump around 10^4 points to the last point for an integration with 5×10^5 points, the curve is slowly decreasing, suggesting that the convergence is not reached.

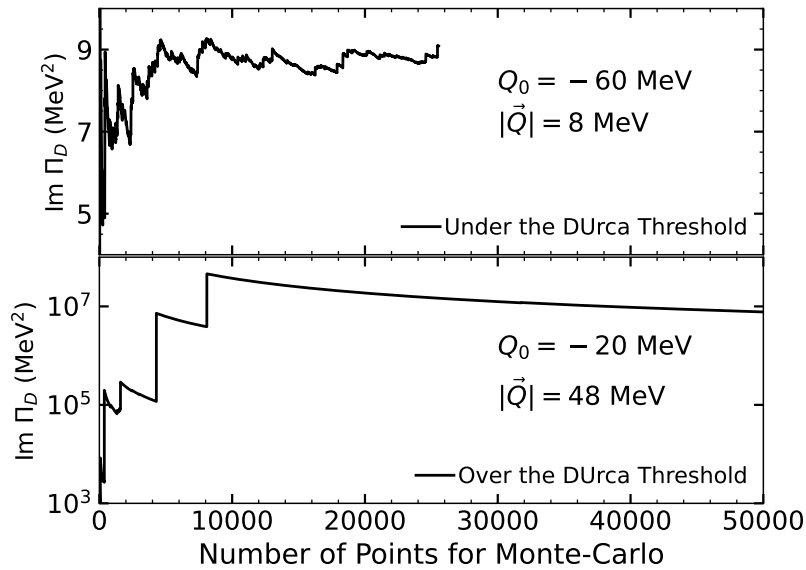


Figure 5.16: Imaginary part of the hadronic polarization function for the first self-energy diagram $\text{Im } \Pi_D$, as a function of the number of points in the Monte-Carlo integration.

The emergence of this numerical divergence beyond the Direct Urca process threshold can be explained from an approximation taken in Eq. (5.56), when we established the propagator of the nucleons. Strictly, the nucleon propagator in spectral representation is defined

by the formula

$$S_x^{ab}(k) = -\frac{1}{\pi} \int d\Omega \frac{\text{Im } S_x(\Omega, \vec{k})}{k_0 - \Omega} \delta^{ab}, \quad (5.113)$$

with k the four-momentum of the nucleon, and k_0 its time component. The variable Ω can be understood as the energy states of the particle within the propagator with a weight given by $\text{Im } S$. For bare nucleons, the quantity in the numerator $\text{Im } S_x(\Omega, \vec{k})$ is reduced to a Dirac δ -function $\delta(\Omega - \omega)$; in this case, the nucleon propagator only has the Krönecker- δ δ^{ab} in the numerator after the integration is operated. This is the approach that we have chosen from Eq. (5.56) until the end of the derivation.

Now, let us try to dress the nucleons *a posteriori* of the derivation. Because the numerical challenge is focused on the denominator of the \mathcal{N} functions, we dress nucleon propagators only for the intermediary particles of the diagrams. The sums over Matsubara frequencies leading to the function \mathcal{G} in Eq. (5.107), Eq. (5.108), Eq. (5.109), Eq. (5.110), Eq. (5.111) and Eq. (5.112) are not affected by our treatment of dressed nucleons: indeed, the function \mathcal{G} does not include intermediary particles. For example, for the vertex diagram V_2 , one of the terms of the imaginary part of the \mathcal{N} function presented in Eq. (5.109) and Eq. (5.98), when taking into account the dressed nature of intermediary particles can be rewritten as

$$\text{Im } \mathcal{M} = -\frac{1}{\pi} \mathcal{G}(\tilde{\mathcal{E}}_{\vec{p}_5;v}, \tilde{\mathcal{E}}_{\vec{p}_2;y}, \tilde{\mathcal{E}}_{\vec{p}_3;z}, \tilde{\mathcal{E}}_{\vec{p}_4;u}) \int d\Omega_1 \int d\Omega_6 \delta(\tilde{\mathcal{E}}_{\vec{p}_5;v} + \tilde{\mathcal{E}}_{\vec{p}_2;y} + Q_0 - \tilde{\mathcal{E}}_{\vec{p}_3;z} - \tilde{\mathcal{E}}_{\vec{p}_4;u})$$

$$\frac{1}{(\Omega_1 - \tilde{\mathcal{E}}_{\vec{p}_5;v} - Q_0)(\Omega_6 - \tilde{\mathcal{E}}_{\vec{p}_3;z} + Q_0)} \frac{\text{Im } \Sigma_1}{(\Omega_1 - \tilde{\mathcal{E}}_{\vec{p}_1;x})^2 + \text{Im } \Sigma_1^2} \frac{\text{Im } \Sigma_6}{(\Omega_1 - \tilde{\mathcal{E}}_{\vec{p}_6;w})^2 + \text{Im } \Sigma_6^2}.$$
(5.114)

with particles (1) and (6) the intermediary nucleons associated to the variables Ω_1 and Ω_6 respectively. The quantities $\text{Im } \Sigma_1$ and $\text{Im } \Sigma_6$ designate the self-energy of the intermediary nucleons (1) and (6).

For our calculation to be complete, we should know the functions $\text{Im } \Sigma(k_0, \vec{k})$, but we do not. One way would be to solve a self-consistent equation for these functions. In [Hannestad and Raffelt \[1998\]](#), the authors have used a sum rule to evaluate the functions of the particles self-energy. In [Bacca et al. \[2012\]](#), the authors present results for pure neutron matter, which does not allow for the Modified Urca process. For our calculations, the following approximation is taken: $\text{Im } \Sigma_1$ and $\text{Im } \Sigma_6$ are both constant quantities. In that framework, we can rewrite

$$\text{Im } \mathcal{M} = -\frac{1}{\pi} \mathcal{G}(\tilde{\mathcal{E}}_{\vec{p}_5;v}, \tilde{\mathcal{E}}_{\vec{p}_2;y}, \tilde{\mathcal{E}}_{\vec{p}_3;z}, \tilde{\mathcal{E}}_{\vec{p}_4;u}) \delta(\tilde{\mathcal{E}}_{\vec{p}_5;v} + \tilde{\mathcal{E}}_{\vec{p}_2;y} + Q_0 - \tilde{\mathcal{E}}_{\vec{p}_3;z} - \tilde{\mathcal{E}}_{\vec{p}_4;u})$$

$$\frac{\tilde{\mathcal{E}}_{\vec{p}_1;x} - \tilde{\mathcal{E}}_{\vec{p}_5;v} - Q_0}{(\tilde{\mathcal{E}}_{\vec{p}_1;x} - \tilde{\mathcal{E}}_{\vec{p}_5;v} - Q_0)^2 + \Gamma_1^2} \frac{\tilde{\mathcal{E}}_{\vec{p}_6;w} - \tilde{\mathcal{E}}_{\vec{p}_3;z} + Q_0}{(\tilde{\mathcal{E}}_{\vec{p}_6;w} - \tilde{\mathcal{E}}_{\vec{p}_3;z} + Q_0)^2 + \Gamma_6^2},$$
(5.115)

with Γ_1 and Γ_6 the constant for the self-energy of intermediary nucleons. A similar formula can be established for the self-energy diagram and the other vertex diagrams. In the following, Γ_i are parameters of our calculations and results.

The parameters Γ_i and their role in avoiding numerical divergence in the polarization function was discussed in [Hannestad and Raffelt \[1998\]](#). Unless otherwise stipulated, results are presented for $\Gamma_i = 10$. This value allowed us to avoid the numerical divergence close to and beyond the threshold of the Direct Urca process, while not polluting the results below the threshold. To be clear, the results presented in the following well below the DUrca threshold do not depend on the value of Γ_i ; on the other hand, results presented around and beyond the DUrca threshold depend on Γ_i , and should be taken with extreme caution. When results beyond the DUrca threshold will be discussed, our intent is to present general trends and not exact calculations.

In overall, our derivation of the Modified Urca hadronic polarization function in Thermal Quantum Field theory allows us to establish calculations at finite temperatures. However, our treatment of the nucleon propagators in the perturbative theory of Feynman diagrams, in which the Direct Urca is the one particle-one hole order in the perturbation, and Modified Urca is the two particles-two holes, leads to issues for Modified Urca calculations close and beyond the DUrca threshold. The role of the bareness of the nucleon propagators in the calculations of the Modified Urca process implies that a careful calculation of the nucleon's self-energy must be established to have an exact value of the parameter (function) Γ_i . This is however beyond the scope of this manuscript.

5.5.2 The vector contribution

The role of the vector contribution in the neutral current of the weak interaction is discussed in [Timmermans et al. \[2002\]](#). In this paper, the authors propose the soft Bremsstrahlung theorem: the vector part of the neutral weak current vanishes for a "soft" process, *i.e.* when the momentum of the weak boson is negligible. In [Friman and Maxwell \[1979\]](#), both the Bremsstrahlung and Modified Urca reactions are discussed. They found, phenomenologically, that in the One Pion Exchange approximation, the vector part of the weak interaction vanishes for the Bremsstrahlung process. In this paper, the authors use a particularly simplistic form of the nucleon propagator in the Modified Urca process. However, it is not true to consider that the vector part of the charged weak current vanishes per definition. For example, in [Yakovlev et al. \[2001\]](#), the authors present the derivation of the vector contribution in Eq. (136), but do not discuss its value beyond the [Friman and Maxwell \[1979\]](#) approximation. In the following, the vector part is treated as completely as the axial part.

In [Fig.5.17](#), we present the vector, axial longitudinal and axial transverse parts of the imaginary part of the hadronic polarization function for the modified electron capture presented in Eq. (5.24). In this figure, results are presented with the coupling constants set as $C_V = C_A = 1$; such will be the case for all the results of this section. The temperature, baryonic density and electron fraction are selected to be 10 MeV, 0.2 fm^{-3} and 0.3 respectively. For the lepton part of the reaction, the neutrino energy is chosen to be 5 MeV. The energy of the weak boson Q_0 ranges from its minimum value defined by Eq. (5.28), to zero. The space component of the weak boson is selected by calculating the electron momentum from the

value of Q_0 , and finding the maximum value $|\vec{Q}|_{\max}$ determined by electron and neutrino momenta with aligned directions.

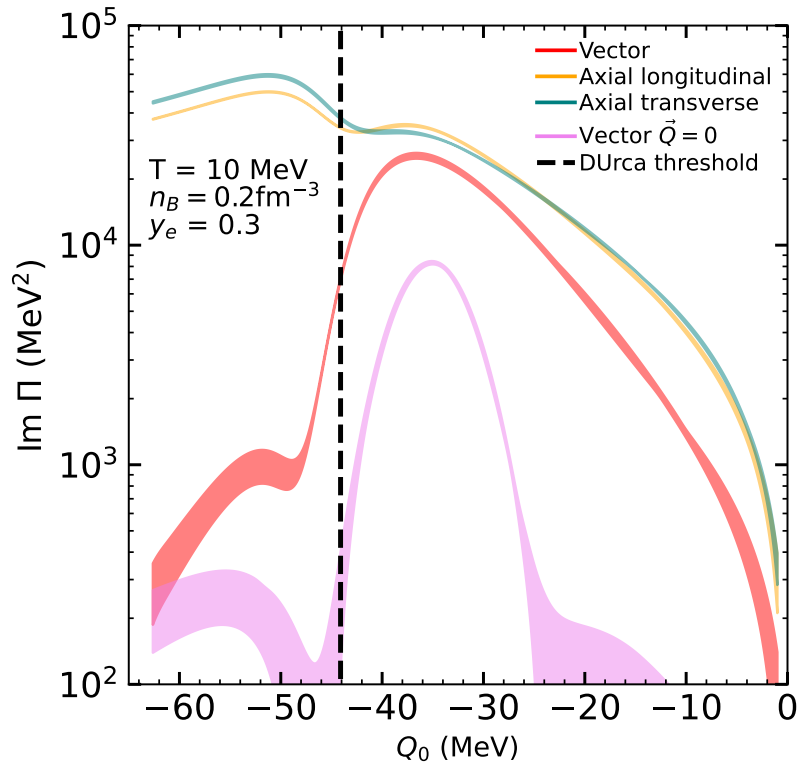


Figure 5.17: Vector and axial part of the imaginary part of the hadronic polarization function $\text{Im } \Pi$ as a function of the energy of the weak boson Q_0 . The space momentum of the weak boson is chosen to be $\vec{Q} = \vec{Q}_{\max}$ except for the curve representing the vector contribution for $\vec{Q} = 0$. The Monte Carlo integration is performed with 5×10^4 points, and the band for each curve represent an estimation of the error for this number of points.

First, let us discuss the results presented in Fig. 5.17 below the DUrca threshold (represented as a dashed black line in the figure). The vector part of the Modified Urca process represented in red in the figure, is much smaller than the axial parts such that neglecting it with respect to the axial longitudinal and axial transverse part is reasonable. It is however not zero, as it would be for the Bremsstrahlung process. The vector part calculated with the momentum of the weak boson set to zero is represented in the figure in violet. It is much smaller than the vector part calculated for $\vec{Q} = \vec{Q}_{\max}$, but still not zero. From this, we can also conclude that the value of \vec{Q} does not affect the maximum of the hadronic polarization function. Let us note that the error of the Monte-Carlo method represented as bands in the figure is similar for vector and axial parts, only the logarithmic scale of the y axis seems to enlarge it.

With respect to the results close and beyond the DUrca threshold, the vector and axial part seem to be much more of the same order. This can be explained because the results beyond the DUrca threshold depend on Γ_i . Therefore, the different terms of the imaginary part

of the hadronic polarization function are dominated by the denominator which is subject to numerical divergence, and not by the element matrix of the reaction.

5.5.3 The role of the denominator of \mathcal{N} functions

In our study, the denominator in Eq. (5.107), Eq. (5.108), Eq. (5.109), Eq. (5.110), Eq. (5.111) and Eq. (5.112), referred to in the following as the "full denominator", include the effective masses and chemical potential of the intermediary particles. In the work of Friman and Maxwell [1979], Yakovlev and Levenfish [1995], Yakovlev et al. [2001], Alford and Harris [2018], the denominator is reduced to the energy of the electrons. *In-medium* effects are therefore only taken into account in the energy of the nucleons that appear in the distribution functions of \mathcal{G} . To assess the role of the denominator in the hadronic polarization function, we compute our results with the full denominator in the \mathcal{N} functions, and also by reducing the denominator to the square of the electron energy E_e^2 . Results in Fig. 5.18 are only presented below the DUrca threshold. We also present results for the calculation operated with the denominator Q_0^2 , as is presented in Bacca et al. [2012].

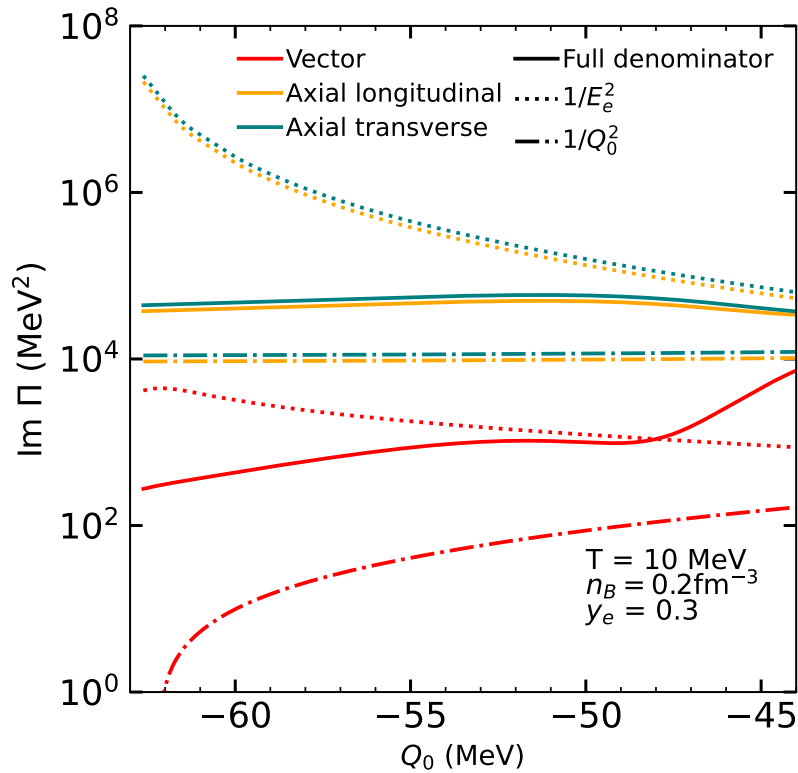


Figure 5.18: Vector and axial parts of the imaginary part of the hadronic polarization function $\text{Im } \Pi$ as a function of the energy of the weak boson Q_0 , calculated with a 5×10^4 points Monte-Carlo method. Results are presented for our calculation (full denominator), and by replacing the denominator by the energy of the electrons ($1/E_e^2$) and by the energy of the weak boson ($1/Q_0^2$).

From Fig. 5.18, we compare results from calculations with the full denominator and the denominator E_e^2 :

- In the case of the denominator E_e^2 , the axial and vector terms have a very large value close to the minimum value of the energy of the weak boson. At $Q_0 = Q_0^{\min}$, the energy of the electrons is reduced to their mass, such that the denominator is small and the result for the imaginary part of the hadronic polarization function is large.
- Calculations with the full denominator present values which are much smaller than for the denominator E_e^2 : for the axial terms, there is an order of magnitude and a half of difference. Moreover, for the denominator E_e^2 , the axial terms present a trend of decrease which can be grossly associated to a square function, thus suggesting that the denominator plays an important role (more important than the matrix element) in the results.

The results for the imaginary part of the hadronic polarization function with a denominator Q_0^2 seem to underestimate the value of the hadronic polarization function. Note that the condition of the temperature, density and electron fraction presented in Fig. 5.18 correspond to low values of the weak boson energy in the range between the minimum energy of the weak boson and the DUrca threshold. The differences between the full denominator approach and the one with the denominator Q_0^2 would not be as exacerbated if the DUrca threshold is close to zero.

In [Shternin et al. \[2018\]](#), the role of the denominator of the \mathcal{N} functions is discussed in section 2.1. The authors estimate analytically the enhancement factor that appears when including the nucleon *in medium* energy in the denominator of the \mathcal{N} functions compared to the simple approach of $1/E_e^2$. They also discuss the pole that appears in the denominator and conclude that it leads to an enhancement of the results close to the DUrca threshold. In our approach with the full denominator, we have introduced the quantity Γ_i to avoid the divergence that is related to this pole. In order to assess the enhancement discussed in [Shternin et al. \[2018\]](#), we present results of calculations with $\Gamma_i = 0$ in Fig. 5.19. The divergence related to the pole in the denominator of the \mathcal{N} functions is clear. The enhancement of the Modified Urca hadronic polarization function occurs close to the DUrca threshold. This is no longer the case when the Γ_i is introduced, as is presented in Fig. 5.18: considering dressed nucleons therefore avoids this enhancement.

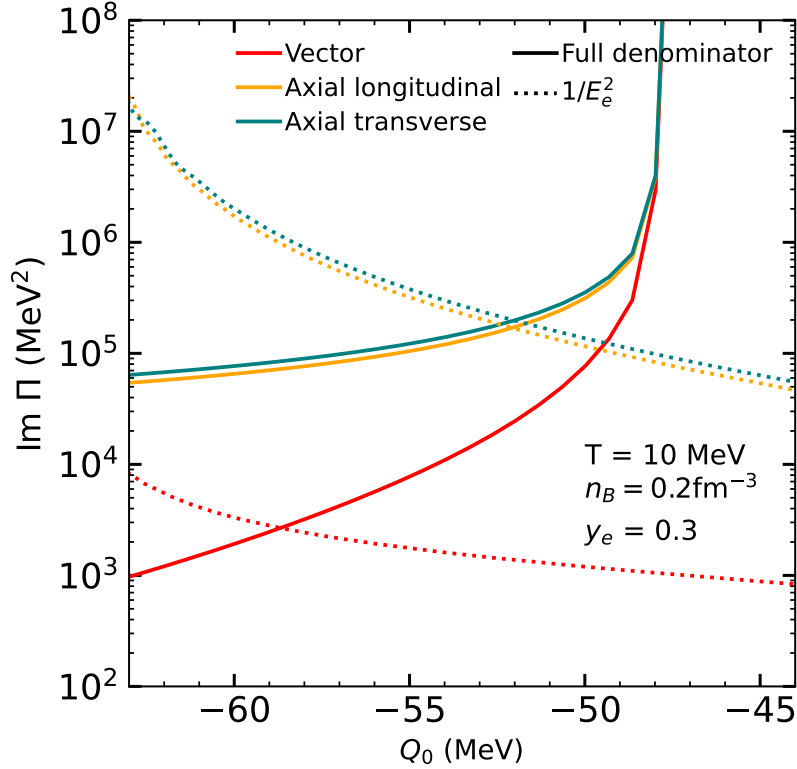


Figure 5.19: Vector and axial contributions to the imaginary part of the hadronic polarization function Π as a function of the energy of the weak boson Q_0 with the parameters $\Gamma_i = 0$, calculated with a 5×10^4 points Monte-Carlo method. Results are presented for our calculation (full denominator) and by replacing the denominator by the energy of the electrons ($1/E_e^2$).

5.5.4 Modified Urca suppression above the Direct Urca threshold

Let us now discuss the Modified Urca calculations close to and above the DUrca threshold. In [Yakovlev et al. \[2001\]](#), [Schmitt and Shternin \[2018\]](#), simple formulas for the neutrino emissivity of the Direct Urca and Modified Urca processes are presented. For example, the neutrino emissivity of the Direct Urca process denoted Q^{Du} is presented in Eq. (120) of [Yakovlev et al. \[2001\]](#) and the neutrino emissivity of the Modified Urca process denoted Q^{Mu} is presented in Eq. (140) of [Yakovlev et al. \[2001\]](#). It is important to note that those formulas are established for strongly degenerate electrons and nucleons, such that particles are on their Fermi surfaces. This is an approach which is valid in the low temperature and high density regime, later on referred to as LtHd. From the formulas presented in [Yakovlev et al. \[2001\]](#), we can establish an approximation of the ratio between the neutrino emissivity of the Modified Urca process and the Direct Urca process in the LtHd regime

$$\frac{Q^{\text{Mu}}}{Q^{\text{Du}}} \simeq 2 \times 10^{-6} \left(\frac{T}{10^9 \text{K}} \right)^2 \frac{(m_n^*)^2}{m_n m_p}, \quad (5.116)$$

with m_n^* the effective mass of neutrons. This ratio is small, such that the Modified Urca process can be neglected with respect to the Direct Urca process once the latter is kinematically

allowed. The Direct Urca process is referred to as fast cooling process, whereas the Modified Urca process is referred to as a slow cooling process. In other words, the Modified Urca process is suppressed above the DURca threshold, to the point that there is no need to compute the Modified Urca process beyond the DURca threshold.

Now let us make a crude approximation of the ratio between the neutrino emissivity of the Modified Urca and Direct Urca processes outside of the above mentioned regime, *i.e.* for high temperatures and low density. The integrand related to the hadronic part for the Direct Urca and Modified Urca processes are denoted I^{Du} and I^{Mu} respectively. While the Direct Urca process involves one incoming particle and one outgoing particle, the Modified Urca process involves two incoming particles and two outgoing particles, such that

$$I^{\text{Mu}} \propto \frac{(m_1^* T)^{3/2} (m_2^* T)^{3/2} (m_3^* T)^{3/2}}{(2\pi^2)^3} n_1 n_3 (1 - n_2) (1 - n_4), \quad (5.117)$$

$$I^{\text{Du}} \propto \frac{(m_1^* T)^{3/2}}{2\pi^2} n_1 (1 - n_2), \quad (5.118)$$

with m_i^* the effective mass of the nucleon i . We remind that n_i is the Fermi distribution of particle i and is given by

$$n_i = \frac{1}{1 + e^{\beta \epsilon_i - \eta_i}}, \quad (5.119)$$

with $\eta_i = (\mu_i^* - m_i^*)/T$ and ϵ_i the energy of the particle. In Fig. 5.20 and Fig. 5.21, the quantities η_n (for neutrons) and η_p (for protons) are presented as a function of the temperature T and the baryonic density n_B ; the calculations were established only for $\eta_i \leq 300$, which explains the white areas in the lower right corners of the figures.

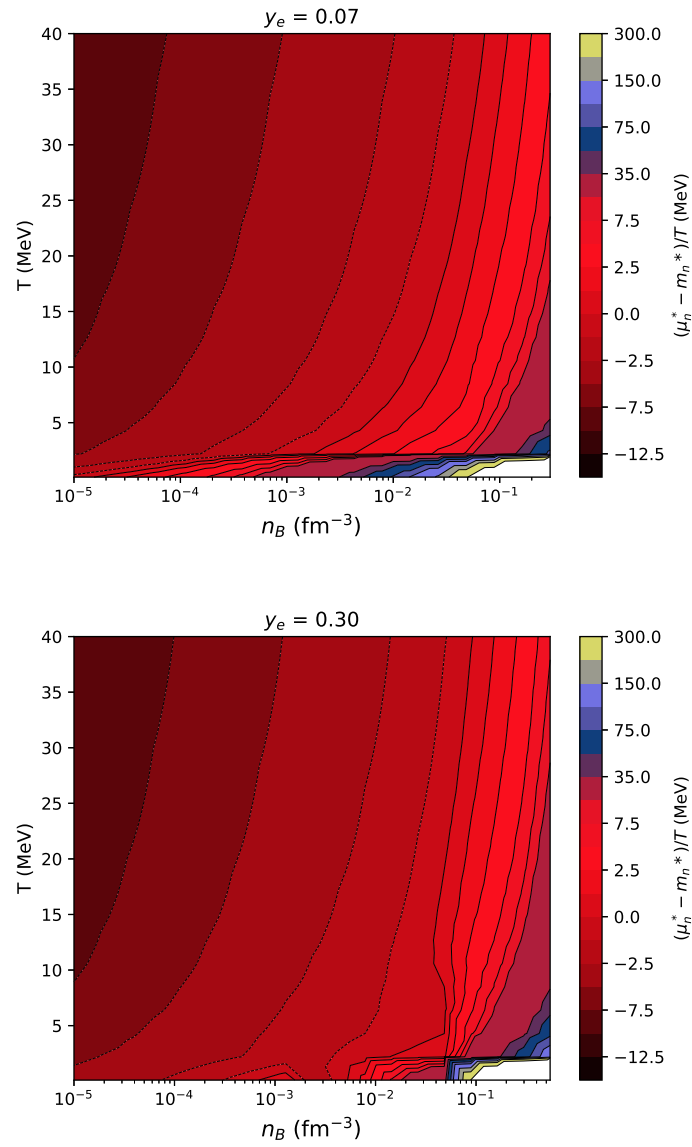


Figure 5.20: Contour representation of the quantity $\eta_n = (\mu_n^* - m_n^*)/T$ as a function of the temperature T and baryonic density n_B , for the electron fractions $y_e = 0.07$ and $y_e = 0.3$.

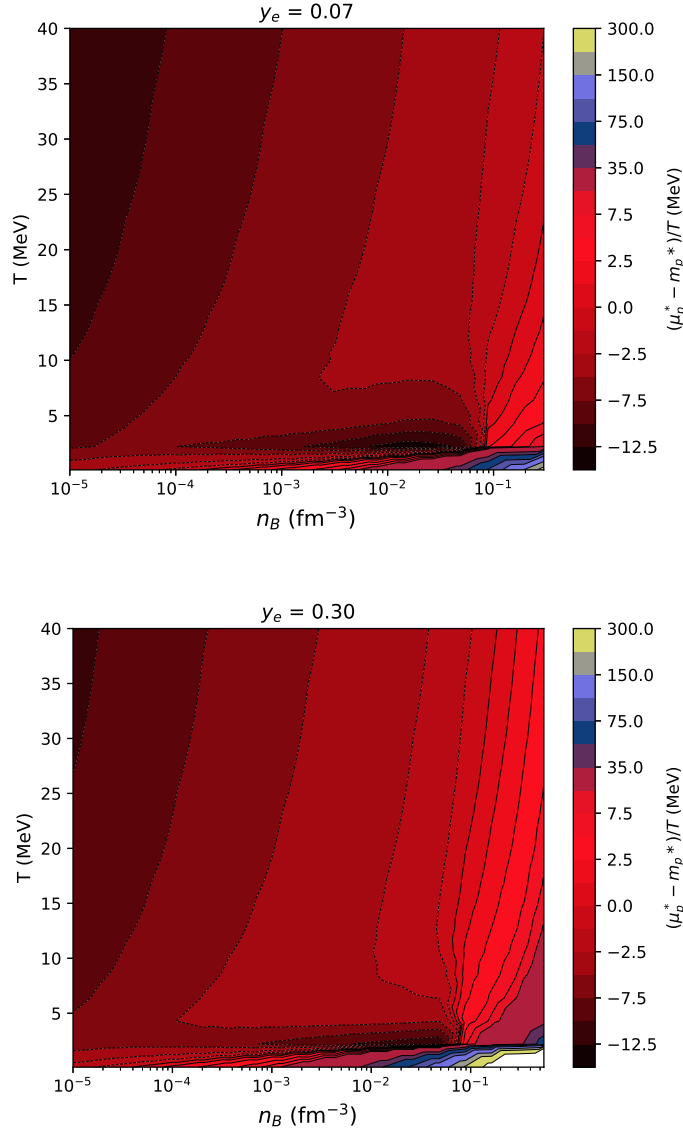


Figure 5.21: Contour representation of the quantity $\eta_p = (\mu_p^* - m_p^*)/T$ as a function of the temperature T and baryonic density n_B , for the electron fractions $y_q = 0.07$ and $y_q = 0.3$.

In the high temperature and low density regime, later on referred to as HtLd, η_n and η_p are negative or small. The quantity $e^{-\eta}$ is sufficiently large so that the Fermi distribution can be approximated to be

$$n_i^{\text{HtLd}} = e^{-\beta\epsilon_i} e^{\eta_i}. \quad (5.120)$$

In the HtLd regime, the Fermi distribution can be neglected with respect to 1, such that the ratio of the Modified Urca and Direct Urca integrand presented in Eq. (5.117) and Eq. (5.118) can be approximated by

$$\frac{I^{\text{Mu}}}{I^{\text{Du}}} \propto e^{\eta_i} \frac{(m_2^* T)^{3/2} (m_3^* T)^{3/2}}{(2\pi^2)^2} e^{-\beta\epsilon_i} \quad (5.121)$$

The exponential factor e^{η_i} gives us an indication of the order of magnitude of the ratio

$I^{\text{Mu}}/I^{\text{Du}}$. Using results presented in Fig. 5.20 and Fig. 5.21, we can anticipate the following

- In the HtLd regime, *i.e.* the upper left corner of the figures, the factor e^{η_i} is very small, such that the Modified Urca should be suppressed relative to the Direct Urca process.
- In the figures, the quantity η_i can be around zero, such that the exponential e^{η_i} would be equal to one. Let us note that in this case, the approximation is strictly speaking no longer valid, but we will keep it here for the purpose of a rough estimation. If the $\int e^{-\beta\epsilon_i} d\epsilon$ is approximated to be one, the Modified Urca and Direct Urca process are of the same order of magnitude for $e^{\eta_i} \sim 1$, *i.e.* close to the zero contour line in the figures. We can deduce that there might be a temperature and density regime in the vicinity of the zero contour line of Fig. 5.20 and Fig. 5.21, for which the Modified Urca process is not suppressed compared to the Direct Urca process. This regime shall be referred to as the moderate regime, as it refers to densities around 10^{-2} fm^{-3} and temperatures above a few MeV.
- In the LtHd regime, *i.e.* the lower right corner of the figures, our approximation of the Fermi distribution is no longer valid. The estimation of the ratio $I^{\text{Mu}}/I^{\text{Du}}$ can be estimated from the approach taken in Yakovlev et al. [2001]: the Modified Urca process is suppressed with respect to the Direct Urca process.

To illustrate the different regimes of Modified Urca suppression with respect to the Direct Urca process, we present results for the imaginary part of the hadronic polarization function for various temperatures, baryonic densities and electron fractions. In Fig. 5.22, results are presented for a temperature of 30 MeV; in Fig. 5.23, results are presented for a temperature of 5 MeV.

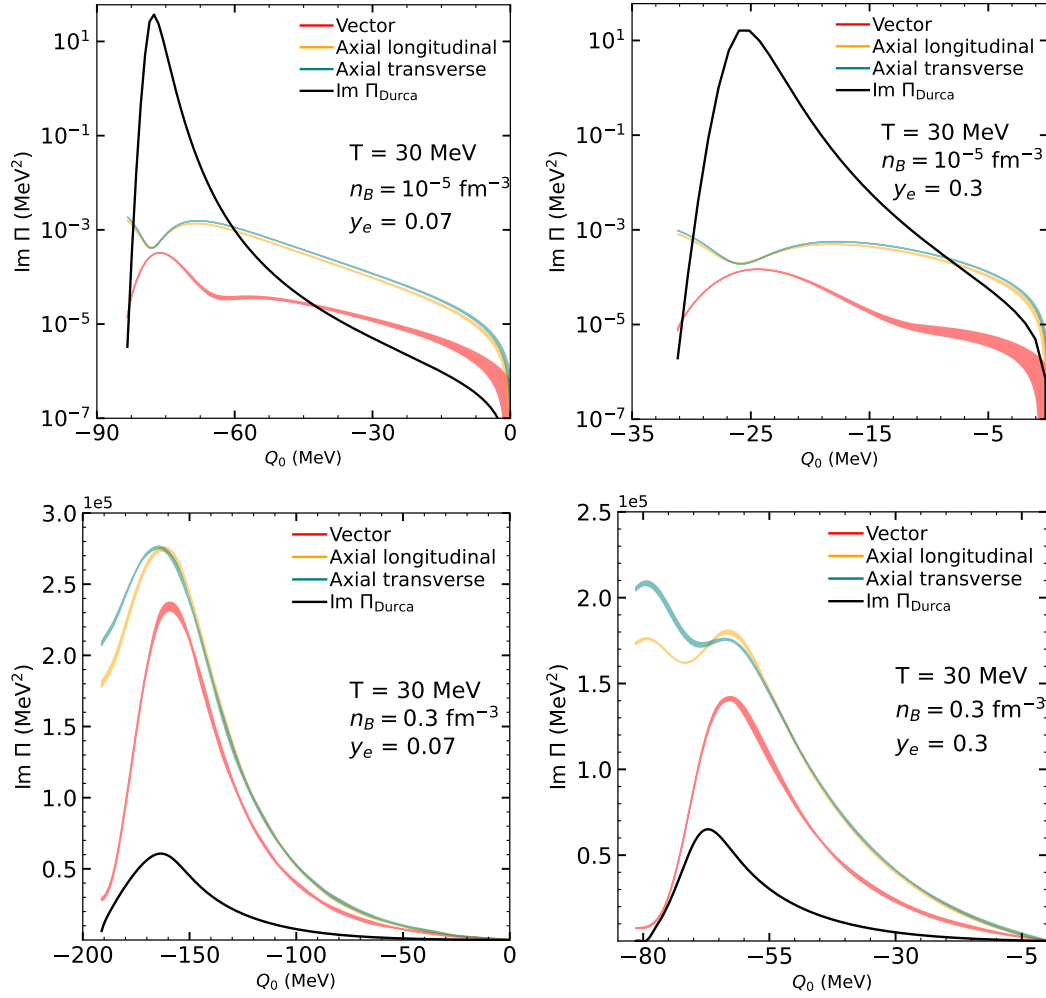


Figure 5.22: Comparison between the MURca vector and axial terms of the imaginary part of the hadronic polarization function, and the imaginary part of the hadronic polarization function of the DURca process, at high temperature $T = 30$ MeV, with $\Gamma_i = 10$. The Monte-Carlo integration is operated with 5×10^4 points.

On the one hand, in the HtLd regime ($T = 30$ MeV and $n_B = 10^{-5} \text{ fm}^{-3}$) presented in the upper plots of Fig. 5.22, the Direct Urca process dominates the Modified Urca process by several orders of magnitude, as is suggested in the upper left corner of Fig. 5.20 and Fig. 5.21. Note that from Fig. 5.22, the trend of which reaction dominates the other is similar for the two values of the electron fraction $y_e = 0.07$ or $y_e = 0.3$; for that reason, only one value of the electron fraction is presented per temperature and baryonic density conditions in the remaining figures. This suppression is also illustrated in the left plot of Fig. 5.23: the temperature is not particularly high ($T = 5$ MeV) but the baryonic density is low ($n_B = 10^{-4}$), and the contour lines in those conditions follows that of the HtLd regime presented in Fig. 5.20 and Fig. 5.21.

On the other hand, in the moderate regime which is represented in the lower plots of Fig. 5.22 ($T = 30$ MeV and $n_B = 0.3 \text{ fm}^{-3}$) or in the right plot of Fig. 5.23 ($T = 5$ MeV and

$n_B = 0.3 \text{ fm}^{-3}$), the Modified Urca dominates the Direct Urca process by a factor of two to four, or in other words, both processes are of the same order.

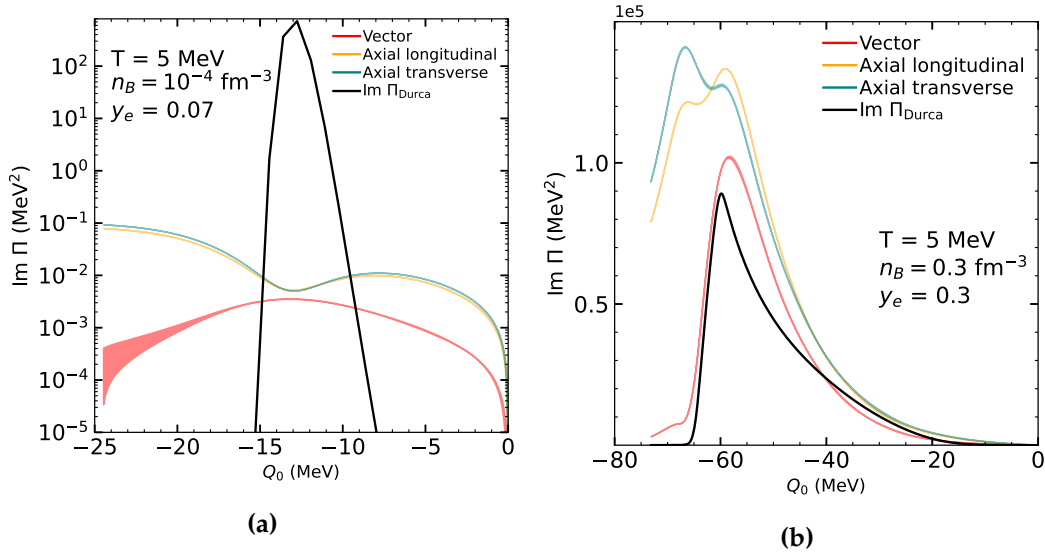


Figure 5.23: Comparison between the MURca vector and axial terms of the imaginary part of the hadronic polarization function, and the imaginary part of the hadronic polarization function of the DURca process, at temperature $T = 5 \text{ MeV}$. The parameter Γ_i are selected to be five. The Monte-Carlo integration is operated with 5×10^5 points.

In overall, we can distinguish three different regimes for the Modified Urca process: it is suppressed with respect to the Direct Urca process in the low temperature and high density regime, as well as the high temperature and low density regime. Our results, however, indicate that there is a moderate regime in which the Direct Urca and Modified Urca process are of the same order, or in other words for which

$$\frac{I^{\text{Mu}}}{I^{\text{Du}}} \simeq 1. \quad (5.122)$$

The approach to Modified Urca suppression can be discussed for the next order reaction. Our derivation for the Modified Urca process is treated with a perturbative approach: the first order corresponds to the Direct Urca process (vertical cuts in the diagrams presented for example in Fig. 5.10), and the second order to the Modified Urca process. Our results show that the Modified Urca is not necessarily suppressed beyond the DURca threshold in the moderate regime. Moreover, for such conditions the Modified Urca process seems to dominate by a factor of ~ 3 the Direct Urca process, which means that the second order in the perturbation is higher than the first. At this point, in order for the perturbative theory to converge, we must ensure that a factor suppresses the higher order terms in front of the first order term. In the same spirit as Eq. (5.121), the third order in the perturbative theory (the Modified Modified Urca process) will introduce an additional factor e^{η_i} . In the HtLd regime, the suppression is now proportional to $(e^{\eta_i})^2$ such that the Modified Modified Urca process would be suppressed with respect to the Modified Urca process. In the moderate

regime however, the perturbative approach is not assured to converge because $(e^{\eta_i})^2 \sim 1$. This probable lack of convergence shows again that in the moderate regime the perturbative approach has limits.

Let us quickly go back to the domain of occurrence of electronic and positronic reactions presented in Fig. 5.6 and Fig. 5.7 of section 5.2. From the lower right plot of Fig. 5.22 presented for $T = 30$ MeV, $n_B = 0.3$ fm $^{-3}$ and $y_e = 0.3$, it can be seen that the axial parts of the hadronic polarization function have their maxima at two values of the weak boson energy $Q_0 \simeq -80$ and $Q_0 \simeq -60$. From Fig. 5.6, we can conclude that for the maximum at $Q_0 \simeq -80$ the modified electron capture dominates the Direct Urca for these conditions of temperature, density and electron fraction. In the assumption that the maxima of the hadronic function is not strongly affected by the quantity \vec{Q} , we can also state that the Modified inverse positron capture dominates the Direct Urca reaction. For the maximum value at $Q_0 \simeq -60$, the electron capture and inverse neutron decay dominate the Direct Urca processes. Similarly, we can conclude from the plot on the right hand side of Fig. 5.23 and the lower plot of Fig. 5.7 which presents a maximum of the hadronic polarization function in the interval $Q_0 = [-70 : -60]$ MeV for $T = 5$ MeV, $n_B = 0.3$ fm $^{-3}$ and $y_e = 0.3$, that the Modified electron captures and inverse positron decays dominate the Direct Urca in the assumption that the hadronic polarization function maximum does not depend on \vec{Q} .

In conclusion, we have presented the calculation of the imaginary part of the hadronic polarization function for the Modified Urca process involving electrons, protons and nucleons. We do so at finite temperature and alleviate the commonly used approximations of Fermi surface, and simple intermediary propagator denominator. In our approach, the intermediary nucleons are dressed using a parameter which we chose to be constant, but should ideally be consistently calculated from the self-energy of nucleons; this is however beyond the scope of this manuscript. By extending the approximation to the Fermi distribution of nucleons in the high temperature regime, we put into light a moderate regime in which the Modified Urca process could be of the same order as the Direct Urca process, above the DUrca threshold. Our results are presented for various conditions of temperature, density and electronic fraction. We can distinguish three regimes:

- the low temperature and high density regime in which the Modified Urca process is suppressed,
- the high temperature and low density regime in which the Modified Urca process is suppressed,
- a moderate regime for which the difference of the effective chemical potential and the effective mass of nucleons over the temperature are close to zero: the Modified Urca process might not be suppressed.

These new findings for the Modified Urca process might be relevant for the cooling of proto-neutron stars or the neutrino emission from a binary merger remnant, or in other

words, for finite temperature neutron stars. Work to include the leptonic part in the calculation to obtain the neutrino emission rates is in progress.

6 Conclusion and perspectives

During my PhD studies, I explored different aspects of ultra dense matter and how it affects neutron star modelling.

I evaluated the impact of non-unified constructions of catalyzed matter equations of state on the modelling of neutron star's macroscopic parameters. By reconstructing non-unified equations of state that can be found in the literature, I evaluated the relative error on the mass, the radius, the tidal deformability and the moment of inertia with respect to unified constructions. This error is not negligible in the prospect of current and future detections of neutron star's observables, which leads us to conclude that unified constructions, or at least smartly constructed non-unified equations of state, are important to explore ultra dense matter properties. Non-unified equations of state have an impact on the precision of some relations between macroscopic parameters that depend only slightly on the equation of state, also referred to as quasi-universal relations. In order to provide accurate relations for neutron star modelling, fits for quasi-universal relations based on a variety of unified and modern equation of state should be established, for example with the set of equations of state discussed in this manuscript. It would also be interesting to explore this universality beyond the framework of general relativity, and establish those fits in alternative theories of gravitation; this would allow to get a better understanding of the underlying physics leading to this quasi-universality.

I also worked on establishing analytical representations of modern equations of state for neutron star modelling based on more than fifty unified models. The parameters for the piecewise polytropic fits are publicly available. In the future, I will work as a member of the Virgo group LUTH/Caen, in collaboration with members of the Ligo scientific collaboration, on implementing unified equations of state, in the form of tables or analytical representations, into the simulation tool of the LVK collaboration *LalSuite*. Within the LUTH/Caen group, I will also work on revising Bayesian analysis for neutron star matter using unified constructions of the equation of state prior, and assess how non-unified constructions impact what can be learned on ultra dense matter properties from astrophysical data; for example, how non-unified constructions impact the neutron star radius value extracted from gravitational wave data for the tidal deformability.

The thermal relaxation of transient accreting sources can help us explore the composition of the crust of neutron stars. I established the equation of state, the composition and the heat deposition in the crust of accreting neutron stars for sources which have accreted only small amounts of matter, or in other words beyond the fully accreted crust approximation.

The heat sources of the original crust under the compression provided by accreted material is not negligible with respect to the heat sources of the accreted material part of the crust. The properties of the compressed crust are also very different than that of a fully accreted crust. The next step of this study would be to evaluate the thermal relaxation of a neutron star with a partially accreted crust using the relativistic equations of cooling and transport that are coded for example by Dany Page [Page, 2006] or Morgane Fortin [Fortin, 2020]. However, a reevaluation of the partially accreted crust's equation of state and composition must be made by including the neutron diffusion by hand, or by stepping outside of the single nucleus model.

I also evaluated the impact of the kinetics of electron captures on the heat release in the crust of accreting neutron stars. It was shown for a few shells in the outermost part of the outer crust that the layers of electron captures have an impact on heat release that can be as high as 20%. The absolute thickness of the layer of electron captures being approximately the same for all three shells that were studied, the thickness of those layers for deeper shells in the crust should be evaluated to check whether it is the same throughout the whole crust. In that case, it would allow for a simple approximation of the reaction rate correction to the accreting crust heat deposition. To push this study beyond the three shallowest shells of the crust, an analytical estimation of the reaction thresholds is required, whereas this quantity was extracted from measurements of atomic masses in this manuscript.

Neutrino emission processes play a crucial role in the thermal evolution of neutron stars at different stages of their life. Therefore, it is important to establish accurate calculations of the neutrino emissivity for finite temperature stars. I focused on the neutrino emission of the Modified Urca process, which includes the presence of a spectator nucleon. By setting the derivation in a perturbative approach based on Thermal Quantum Field theory, I established the full derivation of the hadronic part of the Modified Urca process. The approximation of Fermi surface for the nucleons and of a simple nucleon propagator for intermediary particles were removed, and it was shown that the latter has an impact on the value of the hadronic polarization function. A simple approximation of the ratio between the emissivity of the Direct Urca and the Modified Urca processes using the effective mass and chemical potential of nucleons was established. This put into light the possible existence of different regimes of suppression of one process with respect to the other, which depends on the temperature and on the density. The perturbative approach chosen to derive the neutrino emissivity leads to an enhancement of the rate close to and above the Direct Urca threshold. We have introduced a quasi-particle width for the intermediate propagators to avoid the numerical divergence related to the enhancement, however the results depend on that parameter. To provide accurate calculations, the self-energies of the intermediary nucleons, which were reduced to a constant for the parameter in our study should be carefully assessed. If the non-suppression of the Modified Urca process with respect to the Direct Urca process is confirmed, our results will be interesting for proto-neutron star cooling, and in general for finite temperature neutron stars. The leptonic part of the process will also be computed to provide results for the neutrino emissivity of the reaction at finite temperature.

A Details for the spin part of the Modified Urca derivation

In this Appendix, we present details of the derivation of the spin part of the hadronic polarization function, which are not presented in the main text of Chapter 5.

The space momentum of the six nucleons in play define the pion space momentum denoted k . We introduce the following notation

$$\vec{k}_1 = \vec{p}_4 - \vec{p}_1, \quad (\text{A.1})$$

$$\vec{k}'_1 = \vec{p}_4 - \vec{p}_6, \quad (\text{A.2})$$

$$\vec{k}_2 = \vec{p}_3 - \vec{p}_1, \quad (\text{A.3})$$

$$\vec{k}'_2 = \vec{p}_3 - \vec{p}_6, \quad (\text{A.4})$$

$$\vec{k}_3 = \vec{p}_5 - \vec{p}_3, \quad (\text{A.5})$$

$$\vec{k}_4 = \vec{p}_5 - \vec{p}_4. \quad (\text{A.6})$$

For the first self-energy diagram, the different components of the spin tensor are presented, and details about the projection on the different components of the weak boson four-momentum Q are given. For the other diagrams, we present directly the results projected on Q .

A.1 Self-energy contributions

$$D_{1;\text{spin}}^{00} = \left(\frac{f_\pi}{m_\pi} \right)^4 \frac{4\vec{k}_1^4 C_V^2}{(\vec{k}_1^2 + m_\pi^2)^2}, \quad E_{1;\text{spin}}^{00} = \left(\frac{f_\pi}{m_\pi} \right)^4 \frac{4\vec{k}'_1{}^4 C_V^2}{(\vec{k}'_1{}^2 + m_\pi^2)^2} \quad (\text{A.7})$$

$$D_{1;\text{spin}}^{ij} = \left(\frac{f_\pi}{m_\pi} \right)^4 \frac{4\vec{k}_1^4 C_A^2}{(\vec{k}_1^2 + m_\pi^2)^2} \delta^{ij}, \quad E_{1;\text{spin}}^{ij} = \left(\frac{f_\pi}{m_\pi} \right)^4 \frac{4\vec{k}'_1{}^4 C_A^2}{(\vec{k}'_1{}^2 + m_\pi^2)^2} \delta^{ij} \quad (\text{A.8})$$

$$D_{1;\text{spin}}^{i0} = D_{1;\text{spin}}^{0j} = E_{1;\text{spin}}^{i0} = E_{1;\text{spin}}^{0j} = 0, \quad (\text{A.9})$$

$$D_{2;\text{spin}}^{00} = \left(\frac{f_\pi}{m_\pi} \right)^4 \frac{4\vec{k}_2^4 C_V^2}{(\vec{k}_2^2 + m_\pi^2)^2}, \quad E_{2;\text{spin}}^{00} = \left(\frac{f_\pi}{m_\pi} \right)^4 \frac{4\vec{k}'_2{}^4 C_V^2}{(\vec{k}'_2{}^2 + m_\pi^2)^2} \quad (\text{A.10})$$

$$D_{2;\text{spin}}^{ij} = \left(\frac{f_\pi}{m_\pi} \right)^4 \frac{4\vec{k}_2^4 C_A^2}{(\vec{k}_2^2 + m_\pi^2)^2} \delta^{ij}, \quad E_{2;\text{spin}}^{ij} = \left(\frac{f_\pi}{m_\pi} \right)^4 \frac{4\vec{k}'_2{}^4 C_A^2}{(\vec{k}'_2{}^2 + m_\pi^2)^2} \delta^{ij} \quad (\text{A.11})$$

$$D_{2;\text{spin}}^{i0} = D_{2;\text{spin}}^{0j} = E_{2;\text{spin}}^{i0} = E_{2;\text{spin}}^{0j} = 0, \quad (\text{A.12})$$

$$D_{3;\text{spin}}^{00} = \left(\frac{f_\pi}{m_\pi}\right)^4 \frac{2C_V^2 [2(\vec{k}_1 \cdot \vec{k}_2)^2 - \vec{k}_1^2 \vec{k}_2^2]}{(\vec{k}_1^2 + m_\pi^2)(\vec{k}_2^2 + m_\pi^2)} = D_{4;\text{spin}}^{00}, \quad (\text{A.13})$$

$$E_{3;\text{spin}}^{00} = \left(\frac{f_\pi}{m_\pi}\right)^4 \frac{2C_V^2 [2(\vec{k}'_1 \cdot \vec{k}'_2)^2 - \vec{k}'_1{}^2 \vec{k}'_2{}^2]}{(\vec{k}'_1{}^2 + m_\pi^2)(\vec{k}'_2{}^2 + m_\pi^2)} = E_{4;\text{spin}}^{00}, \quad (\text{A.14})$$

$$D_{3;\text{spin}}^{ij} = \left(\frac{f_\pi}{m_\pi}\right)^4 \frac{2C_A^2 [(2(\vec{k}_1 \cdot \vec{k}_2)^2 - \vec{k}_1^2 \vec{k}_2^2) \delta^{ij} - 2\vec{k}_1 \cdot \vec{k}_2 (k_1^i k_2^j - k_1^j k_2^i)]}{(\vec{k}_1^2 + m_\pi^2)(\vec{k}_2^2 + m_\pi^2)} = D_{4;\text{spin}}^{ij}, \quad (\text{A.15})$$

$$E_{3;\text{spin}}^{ij} = \left(\frac{f_\pi}{m_\pi}\right)^4 \frac{2C_A^2 [(2(\vec{k}'_1 \cdot \vec{k}'_2)^2 - \vec{k}'_1{}^2 \vec{k}'_2{}^2) \delta^{ij} - 2\vec{k}'_1 \cdot \vec{k}'_2 (k_1^i k_2^j - k_1^j k_2^i)]}{(\vec{k}'_1{}^2 + m_\pi^2)(\vec{k}'_2{}^2 + m_\pi^2)} = E_{4;\text{spin}}^{ij}, \quad (\text{A.16})$$

$$D_{3;\text{spin}}^{i0} = -\left(\frac{f_\pi}{m_\pi}\right)^4 \frac{4iC_A C_V \vec{k}_1 \cdot \vec{k}_2 (k_1 \wedge k_2)^i}{(\vec{k}_1^2 + m_\pi^2)(\vec{k}_2^2 + m_\pi^2)} = -D_{4;\text{spin}}^{i0}, \quad (\text{A.17})$$

$$E_{3;\text{spin}}^{i0} = -\left(\frac{f_\pi}{m_\pi}\right)^4 \frac{4iC_A C_V \vec{k}'_1 \cdot \vec{k}'_2 (k'_1 \wedge k'_2)^i}{(\vec{k}'_1{}^2 + m_\pi^2)(\vec{k}'_2{}^2 + m_\pi^2)} = -E_{4;\text{spin}}^{i0}, \quad (\text{A.18})$$

$$D_{3;\text{spin}}^{0j} = -\left(\frac{f_\pi}{m_\pi}\right)^4 \frac{4iC_A C_V \vec{k}_1 \cdot \vec{k}_2 (k_1 \wedge k_2)^j}{(\vec{k}_1^2 + m_\pi^2)(\vec{k}_2^2 + m_\pi^2)} = -D_{4;\text{spin}}^{0j}, \quad (\text{A.19})$$

$$E_{3;\text{spin}}^{0j} = -\left(\frac{f_\pi}{m_\pi}\right)^4 \frac{4iC_A C_V \vec{k}'_1 \cdot \vec{k}'_2 (k'_1 \wedge k'_2)^j}{(\vec{k}'_1{}^2 + m_\pi^2)(\vec{k}'_2{}^2 + m_\pi^2)} = -E_{4;\text{spin}}^{0j}. \quad (\text{A.20})$$

The cross and axial components of the spin matrix present a dependence on the different component of the pion three-momentum (k^i, k^j). We operate a projection on the four-momentum Q of the weak boson in order to express the spin 4×4 matrix as

$$\begin{aligned} X_{C_A}^{ij} &= X_\delta \delta^{ij} + X_{Q^i Q^j} Q^i Q^j, & X_{C_A}^{ij} \delta_{ij} &= 3X_\delta + X_{Q^i Q^j} \vec{Q}^2, \\ X_{C_V C_A}^{i0} &= X_{Q^i} Q^i, & X_{C_A}^{ij} \frac{Q_i Q_j}{\vec{Q}^2} &= X_\delta + X_{Q^i Q^j} \vec{Q}^2, \\ X_{C_V C_A}^{0j} &= X_{Q^j} Q^j, & X_{C_V C_A}^{i0} \frac{Q_i}{\vec{Q}^2} &= X_{Q^i}, \\ & & X_{C_V C_A}^{0j} \frac{Q_j}{\vec{Q}^2} &= X_{Q^j}, \end{aligned} \quad \text{using} \quad (\text{A.21})$$

with X_δ , $X_{Q^i Q^j}$, X_{Q^i} and X_{Q^j} functions to be determined. After explicitly operating this projection, we obtain for the first self-energy diagram

$$D_{3;\delta} = \left(\frac{f_\pi}{m_\pi}\right)^4 \frac{2}{(\vec{k}_1^2 + m_\pi^2)(\vec{k}_2^2 + m_\pi^2)} C_A^2 [2(\vec{k}_1 \cdot \vec{k}_2)^2 - \vec{k}_1^2 \vec{k}_2^2] = D_{4;\delta}, \quad (\text{A.22})$$

$$D_{3;Q^i Q^j} = D_{4;Q^i Q^j} = 0, \quad (\text{A.23})$$

$$D_{3;Q^i} = -D_{4;Q^i} = \left(\frac{f_\pi}{m_\pi}\right)^4 \frac{-4i}{(\vec{k}_1^2 + m_\pi^2)(\vec{k}_2^2 + m_\pi^2)} C_A C_V \vec{k}_1 \cdot \vec{k}_2 \frac{(\vec{k}_1 \wedge \vec{k}_2) \cdot \vec{Q}}{\vec{Q}^2}, \quad (\text{A.24})$$

$$D_{3;Q^j} = -D_{4;Q^j} = -\left(\frac{f_\pi}{m_\pi}\right)^4 \frac{4i}{(\vec{k}_1^2 + m_\pi^2)(\vec{k}_2^2 + m_\pi^2)} C_A C_V \vec{k}_1 \cdot \vec{k}_2 \frac{(\vec{k}_1 \wedge \vec{k}_2) \cdot \vec{Q}}{\vec{Q}^2}, \quad (\text{A.25})$$

and similarly for the second self-energy diagram.

A.2 Vertex V_2

$$V_{2a;spin}^{00} = \left(\frac{f_\pi}{m_\pi} \right)^4 \frac{4C_V^2}{(\vec{k}_1^2 + m_\pi^2)(\vec{k}_4^2 + m_\pi^2)} (\vec{k}_1 \cdot \vec{k}_4)^2, \quad (\text{A.26})$$

$$V_{2a;\delta} = \left(\frac{f_\pi}{m_\pi} \right)^4 \frac{C_A^2}{(\vec{k}_1^2 + m_\pi^2)(\vec{k}_4^2 + m_\pi^2)} f_1(\vec{k}_1, \vec{k}_4), \quad (\text{A.27})$$

$$V_{2a;Q^i Q^j} = \left(\frac{f_\pi}{m_\pi} \right)^4 \frac{C_A^2}{(\vec{k}_1^2 + m_\pi^2)(\vec{k}_4^2 + m_\pi^2)} g_1(\vec{k}_1, \vec{k}_4), \quad (\text{A.28})$$

$$V_{2a;Q^i} = \left(\frac{f_\pi}{m_\pi} \right)^4 \frac{4iC_A C_V}{(\vec{k}_1^2 + m_\pi^2)(\vec{k}_4^2 + m_\pi^2)} \vec{k}_1 \cdot \vec{k}_4 \frac{\vec{k}_1 \wedge \vec{k}_4}{\vec{Q}^2}, \quad (\text{A.29})$$

$$V_{2a;Q^i} = - \left(\frac{f_\pi}{m_\pi} \right)^4 \frac{4iC_A C_V}{(\vec{k}_1^2 + m_\pi^2)(\vec{k}_4^2 + m_\pi^2)} \vec{k}_1 \cdot \vec{k}_4 \frac{\vec{k}_1 \wedge \vec{k}_4}{\vec{Q}^2}, \quad (\text{A.30})$$

$$V_{2b;spin}^{00} = \left(\frac{f_\pi}{m_\pi} \right)^4 \frac{4C_V^2}{(\vec{k}_2^2 + m_\pi^2)^2} \vec{k}_2^4, \quad (\text{A.31})$$

$$V_{2b;\delta} = - \left(\frac{f_\pi}{m_\pi} \right)^4 \frac{4C_A^2}{(\vec{k}_2^2 + m_\pi^2)^2} \frac{\vec{k}_2^2 (\vec{Q} \cdot \vec{k}_2)^2}{\vec{Q}^2}, \quad (\text{A.32})$$

$$V_{2b;Q^i Q^j} = \left(\frac{f_\pi}{m_\pi} \right)^4 \frac{4C_A^2}{(\vec{k}_2^2 + m_\pi^2)^2} \frac{3\vec{k}_2^2 (\vec{Q} \cdot \vec{k}_2)^2 - \vec{Q}^2 \vec{k}_2^4}{\vec{Q}^4}, \quad (\text{A.33})$$

$$V_{2b;Q^i} = V_{2b;Q^j} = 0, \quad (\text{A.34})$$

$$V_{2c;spin}^{00} = \left(\frac{f_\pi}{m_\pi} \right)^4 \frac{2C_V^2}{(\vec{k}_2^2 + m_\pi^2)(\vec{k}_4^2 + m_\pi^2)} [2(\vec{k}_2 \cdot \vec{k}_4)^2 - \vec{k}_2^2 \vec{k}_4^2], \quad (\text{A.35})$$

$$V_{2c;\delta} = \left(\frac{f_\pi}{m_\pi} \right)^4 \frac{C_A^2}{(\vec{k}_2^2 + m_\pi^2)(\vec{k}_4^2 + m_\pi^2)} f_2(\vec{k}_2, \vec{k}_4), \quad (\text{A.36})$$

$$V_{2c;Q^i Q^j} = \left(\frac{f_\pi}{m_\pi} \right)^4 \frac{C_A^2}{(\vec{k}_2^2 + m_\pi^2)(\vec{k}_4^2 + m_\pi^2)} g_2(\vec{k}_2, \vec{k}_4), \quad (\text{A.37})$$

$$V_{2c;Q^i} = \left(\frac{f_\pi}{m_\pi} \right)^4 \frac{4iC_A C_V}{(\vec{k}_2^2 + m_\pi^2)(\vec{k}_4^2 + m_\pi^2)} \vec{k}_2 \cdot \vec{k}_4 \frac{(\vec{k}_2 \wedge \vec{k}_4) \cdot \vec{Q}}{\vec{Q}^2}, \quad (\text{A.38})$$

$$V_{2c;Q^i} = - \left(\frac{f_\pi}{m_\pi} \right)^4 \frac{4iC_A C_V}{(\vec{k}_2^2 + m_\pi^2)(\vec{k}_4^2 + m_\pi^2)} \vec{k}_2 \cdot \vec{k}_4 \frac{(\vec{k}_2 \wedge \vec{k}_4) \cdot \vec{Q}}{\vec{Q}^2}, \quad (\text{A.39})$$

$$V_{2d;spin}^{00} = \left(\frac{f_\pi}{m_\pi} \right)^4 \frac{2C_V^2}{(\vec{k}_1^2 + m_\pi^2)(\vec{k}_2^2 + m_\pi^2)} [2(\vec{k}_1 \cdot \vec{k}_2)^2 - \vec{k}_1^2 \vec{k}_2^2], \quad (\text{A.40})$$

$$V_{2d;\delta} = \left(\frac{f_\pi}{m_\pi} \right)^4 \frac{C_A^2}{(\vec{k}_1^2 + m_\pi^2)(\vec{k}_2^2 + m_\pi^2)} f_2(\vec{k}_2, \vec{k}_1), \quad (\text{A.41})$$

$$V_{2d;Q^i Q^j} = \left(\frac{f_\pi}{m_\pi} \right)^4 \frac{C_A^2}{(\vec{k}_1^2 + m_\pi^2)(\vec{k}_2^2 + m_\pi^2)} g_2(\vec{k}_2, \vec{k}_1), \quad (\text{A.42})$$

$$V_{2d;Q^i} = - \left(\frac{f_\pi}{m_\pi} \right)^4 \frac{4iC_A C_V}{(\vec{k}_1^2 + m_\pi^2)(\vec{k}_2^2 + m_\pi^2)} \vec{k}_1 \cdot \vec{k}_2 \frac{(\vec{k}_2 \wedge \vec{k}_1) \cdot \vec{Q}}{\vec{Q}^2}, \quad (\text{A.43})$$

$$V_{2d;Q^i} = \left(\frac{f_\pi}{m_\pi} \right)^4 \frac{4iC_A C_V}{(\vec{k}_1^2 + m_\pi^2)(\vec{k}_2^2 + m_\pi^2)} \vec{k}_1 \cdot \vec{k}_2 \frac{(\vec{k}_2 \wedge \vec{k}_1) \cdot \vec{Q}}{\vec{Q}^2}, \quad (\text{A.44})$$

with the following functions defined as

$$f_1(\vec{k}_a, \vec{k}_b) = -2 \frac{2(\vec{Q} \cdot \vec{k}_a)(\vec{Q} \cdot \vec{k}_b)(\vec{k}_a \cdot \vec{k}_b) - \vec{k}_a^2(\vec{Q} \cdot \vec{k}_b)^2 - \vec{k}_b^2(\vec{Q} \cdot \vec{k}_a)^2}{\vec{Q}^2}, \quad (\text{A.45})$$

$$f_2(\vec{k}_a, \vec{k}_b) = -2 \frac{\vec{Q} \cdot \vec{k}_a [2\vec{k}_a \cdot \vec{k}_b \vec{Q} \cdot \vec{k}_b - \vec{k}_b^2 \vec{Q} \cdot \vec{k}_a]}{\vec{Q}^2}, \quad (\text{A.46})$$

$$g_1(\vec{k}_a, \vec{k}_b) = 2 \frac{6(\vec{Q} \cdot \vec{k}_a)(\vec{Q} \cdot \vec{k}_b)(\vec{k}_a \cdot \vec{k}_b) - 3[\vec{k}_a^2(\vec{Q} \cdot \vec{k}_b)^2 + \vec{k}_b^2(\vec{Q} \cdot \vec{k}_a)^2]}{\vec{Q}^4} + 4 \frac{\vec{k}_a^2 \vec{k}_b^2 - (\vec{k}_a \cdot \vec{k}_b)^2}{\vec{Q}^2}, \quad (\text{A.47})$$

$$g_2(\vec{k}_a, \vec{k}_b) = 2 \frac{6(\vec{Q} \cdot \vec{k}_a)(\vec{Q} \cdot \vec{k}_b)(\vec{k}_a \cdot \vec{k}_b) - 3\vec{k}_b^2(\vec{Q} \cdot \vec{k}_a)^2}{\vec{Q}^4} - 2 \frac{2(\vec{k}_a \cdot \vec{k}_b)^2 - \vec{k}_a^2 \vec{k}_b^2}{\vec{Q}^2}. \quad (\text{A.48})$$

A.3 Vertex V_3

After introducing the function

$$f_3(\vec{k}_a, \vec{k}_b) = 2 \frac{2(\vec{Q} \cdot \vec{k}_a)(\vec{Q} \cdot \vec{k}_b)(\vec{k}_b \cdot \vec{k}_a) - \vec{k}_a^2((\vec{Q} \cdot \vec{k}_b)^2 - \vec{Q}^2 \vec{k}_b^2) - \vec{k}_b^2(\vec{Q} \cdot \vec{k}_a)^2}{\vec{Q}^2}, \quad (\text{A.49})$$

the spin part gives

$$V_{3a;spin}^{00} = \left(\frac{f_\pi}{m_\pi} \right)^4 \frac{4C_V^2}{(\vec{k}_2^2 + m_\pi^2)(\vec{k}_3^2 + m_\pi^2)} (\vec{k}_2 \cdot \vec{k}_3)^2, \quad (\text{A.50})$$

$$V_{3a;\delta} = - \left(\frac{f_\pi}{m_\pi} \right)^4 \frac{C_A^2}{(\vec{k}_2^2 + m_\pi^2)(\vec{k}_3^2 + m_\pi^2)} f_1(\vec{k}_2, \vec{k}_3), \quad (\text{A.51})$$

$$V_{3a;Q^i Q^j} = - \left(\frac{f_\pi}{m_\pi} \right)^4 \frac{C_A^2}{(\vec{k}_2^2 + m_\pi^2)(\vec{k}_3^2 + m_\pi^2)} g_1(\vec{k}_2, \vec{k}_3), \quad (\text{A.52})$$

$$V_{3a;Q^i} = \left(\frac{f_\pi}{m_\pi} \right)^4 \frac{4iC_A C_V}{(\vec{k}_2^2 + m_\pi^2)(\vec{k}_3^2 + m_\pi^2)} \vec{k}_2 \cdot \vec{k}_3 \frac{(\vec{k}_2 \wedge \vec{k}_3) \cdot \vec{Q}}{\vec{Q}^2}, \quad (\text{A.53})$$

$$V_{3a;Q^j} = \left(\frac{f_\pi}{m_\pi} \right)^4 \frac{4iC_V C_A}{(\vec{k}_2^2 + m_\pi^2)(\vec{k}_3^2 + m_\pi^2)} \vec{k}_2 \cdot \vec{k}_3 \frac{(\vec{k}_2 \wedge \vec{k}_3) \cdot \vec{Q}}{\vec{Q}^2}, \quad (\text{A.54})$$

$$V_{3b;spin}^{00} = \left(\frac{f_\pi}{m_\pi} \right)^4 \frac{4C_V^2}{(\vec{k}_1^2 + m_\pi^2)(\vec{k}_4^2 + m_\pi^2)} (\vec{k}_1 \cdot \vec{k}_4)^2, \quad (\text{A.55})$$

$$V_{3b;\delta} = - \left(\frac{f_\pi}{m_\pi} \right)^4 \frac{C_A^2}{(\vec{k}_1^2 + m_\pi^2)(\vec{k}_4^2 + m_\pi^2)} f_1(\vec{k}_1, \vec{k}_4), \quad (\text{A.56})$$

$$V_{3b;Q^i Q^j} = - \left(\frac{f_\pi}{m_\pi} \right)^4 \frac{C_A^2}{(\vec{k}_1^2 + m_\pi^2)(\vec{k}_4^2 + m_\pi^2)} g_1(\vec{k}_1, \vec{k}_4), \quad (\text{A.57})$$

$$V_{3b;Q^i} = \left(\frac{f_\pi}{m_\pi} \right)^4 \frac{4iC_A C_V}{(\vec{k}_1^2 + m_\pi^2)(\vec{k}_4^2 + m_\pi^2)} \vec{k}_1 \cdot \vec{k}_4 \frac{(\vec{k}_1 \wedge \vec{k}_4) \cdot \vec{Q}}{\vec{Q}^2}, \quad (\text{A.58})$$

$$V_{3b;Q^i} = \left(\frac{f_\pi}{m_\pi}\right)^4 \frac{4iC_A C_V}{(\vec{k}_1^2 + m_\pi^2)(\vec{k}_4^2 + m_\pi^2)} \vec{k}_1 \cdot \vec{k}_4 \frac{(\vec{k}_1 \wedge \vec{k}_4) \cdot \vec{Q}}{\vec{Q}^2}, \quad (\text{A.59})$$

$$V_{3c;spin}^{00} = \left(\frac{f_\pi}{m_\pi}\right)^4 \frac{2C_V^2}{(\vec{k}_2^2 + m_\pi^2)(\vec{k}_4^2 + m_\pi^2)} [2(\vec{k}_2 \cdot \vec{k}_4)^2 - \vec{k}_2^2 \vec{k}_4^2], \quad (\text{A.60})$$

$$V_{3c;\delta} = \left(\frac{f_\pi}{m_\pi}\right)^4 \frac{C_A^2}{(\vec{k}_2^2 + m_\pi^2)(\vec{k}_4^2 + m_\pi^2)} f_3(\vec{k}_2, \vec{k}_4), \quad (\text{A.61})$$

$$V_{3c;Q^i Q^j} = -\left(\frac{f_\pi}{m_\pi}\right)^4 \frac{C_A^2}{(\vec{k}_2^2 + m_\pi^2)(\vec{k}_4^2 + m_\pi^2)} g_1(\vec{k}_2, \vec{k}_4), \quad (\text{A.62})$$

$$V_{3c;Q^i} = \frac{4iC_V C_A}{(\vec{k}_2^2 + m_\pi^2)(\vec{k}_4^2 + m_\pi^2)} \vec{k}_2 \cdot \vec{k}_4 \frac{(\vec{k}_2 \wedge \vec{k}_4) \cdot \vec{Q}}{\vec{Q}^2}, \quad (\text{A.63})$$

$$V_{3c;Q^j} = \left(\frac{f_\pi}{m_\pi}\right)^4 \frac{4iC_V C_A}{(\vec{k}_2^2 + m_\pi^2)(\vec{k}_4^2 + m_\pi^2)} \vec{k}_2 \cdot \vec{k}_4 \frac{(\vec{k}_2 \wedge \vec{k}_4) \cdot \vec{Q}}{\vec{Q}^2}, \quad (\text{A.64})$$

$$V_{3d;spin}^{00} = \left(\frac{f_\pi}{m_\pi}\right)^4 \frac{2C_V^2}{(\vec{k}_1^2 + m_\pi^2)(\vec{k}_3^2 + m_\pi^2)} [2(\vec{k}_1 \cdot \vec{k}_3)^2 - \vec{k}_1^2 \vec{k}_3^2], \quad (\text{A.65})$$

$$V_{3d;\delta} = \left(\frac{f_\pi}{m_\pi}\right)^4 \frac{C_A^2}{(\vec{k}_1^2 + m_\pi^2)(\vec{k}_3^2 + m_\pi^2)} f_3(\vec{k}_1, \vec{k}_3), \quad (\text{A.66})$$

$$V_{3d;Q^i Q^j} = -\left(\frac{f_\pi}{m_\pi}\right)^4 \frac{C_A^2}{(\vec{k}_1^2 + m_\pi^2)(\vec{k}_3^2 + m_\pi^2)} g_1(\vec{k}_1, \vec{k}_3), \quad (\text{A.67})$$

$$V_{3d;Q^i} = \left(\frac{f_\pi}{m_\pi}\right)^4 \frac{4iC_V C_A}{(\vec{k}_1^2 + m_\pi^2)(\vec{k}_3^2 + m_\pi^2)} \vec{k}_1 \cdot \vec{k}_3 \frac{(\vec{k}_1 \wedge \vec{k}_3) \cdot \vec{Q}}{\vec{Q}^2}, \quad (\text{A.68})$$

$$V_{3d;Q^j} = \left(\frac{f_\pi}{m_\pi}\right)^4 \frac{4iC_V C_A}{(\vec{k}_1^2 + m_\pi^2)(\vec{k}_3^2 + m_\pi^2)} \vec{k}_1 \cdot \vec{k}_3 \frac{(\vec{k}_1 \wedge \vec{k}_3) \cdot \vec{Q}}{\vec{Q}^2}. \quad (\text{A.69})$$

B Details on the Matsubara sums

In this Appendix, we present details on the Matsubara sums used to establish the hadronic polarization function of the Modified Urca process, which are not presented in the main text of Chapter 5.

Matsubara frequencies are oftentimes introduced in the finite temperature formalism to substitute the time component integral of the four-momentum to a sum in complex plane in which Fermi and Bose-Einstein distributions of particles appear.

B.1 Use of Residue theorem in sums on the imaginary axis

Oftentimes, a four dimensional integral over momentum k noted d^4k may be written as $\frac{1}{\beta} \sum_n \int d^3\vec{k}$ with $\beta = T^{-1}$ corresponding to the inverse temperature. By introducing Matsubara frequencies in the time component of the quadrimomentum, one can operate sums using the Residue theorem and eliminate the time component integral.

Let us go through one example in details, that corresponds to one of the sums for the the self-energy of weak boson in the Modified Urca process

$$\frac{1}{\beta} \sum_n \frac{1}{i\omega_n - \omega} \frac{1}{i\omega_n - (i\omega_m + \mu_{\vec{p}-\vec{q}}^{s_x})} \hat{=} \frac{1}{\beta} \sum_n f(i\omega_n) , \quad (\text{B.1})$$

with $\omega_n = 2n\pi/\beta$ ($n \in \mathbb{Z}$) a boson frequency. The Bose-Einstein distribution n_{BE} has one pole which results in the residue $\frac{1}{\beta}$ such that one can write

$$\frac{1}{\beta} \sum_n f(i\omega_n) = \frac{1}{2\pi i} \oint_{\mathcal{C}} f(z) n_{BE}(z) dz . \quad (\text{B.2})$$

The function f presents two poles, one on the real axis and one in the complex plane; because poles are off the imaginary axis, the Residue theorem can be applied

$$\frac{1}{2\pi i} \oint_{\mathcal{C}} f(z) n_{BE}(z) dz = \sum_n \text{Res}(n_{BE}(z_n)) f(z_n) . \quad (\text{B.3})$$

The two poles of function f pertain to two residues

$$\text{Res}_f(z \rightarrow \omega) = \lim_{z \rightarrow \omega} \frac{n_{BE}(\omega)}{z - (i\omega_m + \mu_{\vec{p}-\vec{q}}^{s_x})} = \frac{n_{BE}(\omega)}{\omega - (i\omega_m + \mu_{\vec{p}-\vec{q}}^{s_x})} , \quad (\text{B.4})$$

$$\text{Res}_f(z \rightarrow i\omega_m + \mu_{\vec{p}-\vec{q}}^{s_x}) = \lim_{z \rightarrow i\omega_m + \mu_{\vec{p}-\vec{q}}^{s_x}} \frac{n_{BE}(i\omega_m + \mu_{\vec{p}-\vec{q}}^{s_x})}{z - \omega} = \frac{n_{BE}(i\omega_m + \mu_{\vec{p}-\vec{q}}^{s_x})}{i\omega_m + \mu_{\vec{p}-\vec{q}}^{s_x} - \omega}, \quad (\text{B.5})$$

and our sum over bosonic Matsubara frequencies renders

$$\frac{1}{\beta} \sum_n \frac{1}{i\omega_n - \omega} \frac{1}{i\omega_n - (i\omega_m + \mu_{\vec{p}-\vec{q}}^{s_x})} = \frac{n_{BE}(i\omega_m + \mu_{\vec{p}-\vec{q}}^{s_x}) - n_{BE}(\omega)}{i\omega_m + \mu_{\vec{p}-\vec{q}}^{s_x} - \omega}. \quad (\text{B.6})$$

Same reasoning can be applied for fermionic frequency in which case the Fermi distribution is used; note that its residue with fermionic frequency $\omega_m = (2n + 1)\pi/\beta$ is $-1/\beta$.

B.2 Properties of Bose-Einstein and Fermi distributions

In the following, the notation ω_m designates a fermion frequency and ω_n a boson frequency. There are a series of simplification properties involving boson n_{BE} and fermion n_F distributions

$$\begin{cases} n_{BE}(z) = \frac{1}{e^{\beta z} - 1}, \\ n_F(z) = \frac{1}{e^{\beta z} + 1}. \end{cases} \quad (\text{B.7})$$

First, some properties related to negative arguments of the distribution functions

$$n_{BE}(-\omega) = -[1 + n_{BE}(\omega)], \quad (\text{B.8})$$

$$n_F(-\omega) = [1 - n_F(\omega)]. \quad (\text{B.9})$$

With regards to relations related to the fermion or boson distributions, for an even frequency ω_e and an odd one ω_o (both can be the sum of several frequencies) give the rules

$$n_{BE}(i\omega_o + \mu) = -n_F(\mu), \quad (\text{B.10})$$

$$n_{BE}(i\omega_e + \mu) = n_{BE}(\mu), \quad (\text{B.11})$$

$$n_F(i\omega_e + \mu) = n_F(\mu), \quad (\text{B.12})$$

$$n_F(i\omega_o + \mu) = -n_{BE}(\mu). \quad (\text{B.13})$$

With regards to simplifications with the Fermi distribution of three elements

$$n_F(\omega_a + \omega_b - \omega_c)(1 - n_F(\omega_a)) \quad (\text{B.14})$$

$$= (1 - n_F(\omega_a + \omega_b + \omega_c))n_F(\omega_a), \quad (\text{B.15})$$

from which we establish the following expressions

$$n_{BE}(\omega_1 - \omega_2)[n_F(\omega_1) - n_F(\omega_2)] = n_F(\omega_1)[1 - n_F(\omega_2)], \quad (\text{B.16})$$

$$[1 - n_F(\omega_1)]n_F(\omega_2) = (n_F(\omega_2) - n_F(\omega_1))[1 + n_{BE}(\omega_1 - \omega_2)], \quad (\text{B.17})$$

$$n_F(\omega_1)n_F(\omega_2) = [1 - n_F(\omega_1) - n_F(\omega_2)]n_{BE}(\omega_1 + \omega_2). \quad (\text{B.18})$$

C Expression for the \mathcal{M} functions

In this Appendix, we present details on the change of variables to operate the reduction of integrals for the Modified Urca process numerical integration of Chapter 5.

C.1 Direct and exchange diagram

The square of the nucleon propagator of particle (1) will introduce the derivative of a distribution function. We are interested in the Modified Urca reaction when the Direct Urca is no longer available, therefore Direct Urca corrections of the vertex are neglected, which reduces the expression to

$$\mathcal{M}_D = \frac{1}{(\tilde{\mathcal{E}}_{\vec{p}_1+\vec{p}_2-\vec{p}_3;u} - \tilde{\mathcal{E}}_{\vec{p}_1;x} - \tilde{\mathcal{E}}_{\vec{p}_2;y} + \tilde{\mathcal{E}}_{\vec{p}_3;z})^2 (\tilde{\mathcal{E}}_{\vec{p}_1+\vec{p}_2-\vec{p}_3;u} - \tilde{\mathcal{E}}_{\vec{p}_2;y} + \tilde{\mathcal{E}}_{\vec{p}_3;z} - \tilde{\mathcal{E}}_{\vec{p}_1-\vec{Q};w} - Q_0 - i\eta)} \times \left(n_F(\tilde{\mathcal{E}}_{\vec{p}_2;y}) n_F(\tilde{\mathcal{E}}_{\vec{p}_1-\vec{Q};w}) (1 - n_F(\tilde{\mathcal{E}}_{\vec{p}_3;z})) (1 - n_F(\tilde{\mathcal{E}}_{\vec{p}_1+\vec{p}_2-\vec{p}_3;u})) - (1 - n_F(\tilde{\mathcal{E}}_{\vec{p}_2;y})) (1 - n_F(\tilde{\mathcal{E}}_{\vec{p}_1-\vec{Q};w})) n_F(\tilde{\mathcal{E}}_{\vec{p}_3;z}) n_F(\tilde{\mathcal{E}}_{\vec{p}_1+\vec{p}_2-\vec{p}_3;u}) \right). \quad (\text{C.1})$$

Only the imaginary part of the hadron polarisation function is of interest. From the spin contribution of the direct diagram, only the cross terms of E_1 and E_2 have imaginary parts; however, they vanish once those terms are summed. Note that the cross terms imaginary parts all vanish once contracted to the lepton tensor (which has symmetric and anti-symmetric parts); this can be verified analytical for the second vertex diagram and numerically for the third. Therefore, only the imaginary part of the \mathcal{M} functions will count in the analytical continuation. According to the Sokhotski-Plemelj theorem,

$$\lim_{\eta \rightarrow 0} \frac{1}{x + i\eta} = -i\pi\delta(x) + \mathcal{P}, \quad (\text{C.2})$$

$$\lim_{\eta \rightarrow 0} \frac{1}{x - i\eta} = i\pi\delta(x) + \mathcal{P} \quad (\text{C.3})$$

with \mathcal{P} the Cauchy principle value; taking the imaginary part of the \mathcal{M} function, we obtain

$$\text{Im } \mathcal{M}_D = \pi \frac{\delta(\tilde{\mathcal{E}}_{\vec{p}_1+\vec{p}_2-\vec{p}_3;u} - \tilde{\mathcal{E}}_{\vec{p}_2;y} + \tilde{\mathcal{E}}_{\vec{p}_3;z} - \tilde{\mathcal{E}}_{\vec{p}_1-\vec{Q};w} - Q_0)}{(\tilde{\mathcal{E}}_{\vec{p}_1+\vec{p}_2-\vec{p}_3;u} - \tilde{\mathcal{E}}_{\vec{p}_1;x} - \tilde{\mathcal{E}}_{\vec{p}_2;y} + \tilde{\mathcal{E}}_{\vec{p}_3;z})^2} \times \left(n_F(\tilde{\mathcal{E}}_{\vec{p}_1-\vec{Q};w}) n_F(\tilde{\mathcal{E}}_{\vec{p}_2;y}) (1 - n_F(\tilde{\mathcal{E}}_{\vec{p}_3;z})) (1 - n_F(\tilde{\mathcal{E}}_{\vec{p}_1+\vec{p}_2-\vec{p}_3;u})) \right) \quad (\text{C.4})$$

$$- (1 - n_F(\tilde{\mathcal{E}}_{\vec{p}_1 - \vec{Q}; w})) (1 - n_F(\tilde{\mathcal{E}}_{\vec{p}_2; y})) n_F(\tilde{\mathcal{E}}_{\vec{p}_3; z}) n_F(\tilde{\mathcal{E}}_{\vec{p}_1 + \vec{p}_2 - \vec{p}_3; u}) \Big).$$

C.2 Second vertex diagram

After introducing the Matsubara frequencies

$$\mathcal{M}_{V_2} = \frac{1}{\beta^3} \sum_{m_1} \sum_{m_2} \sum_{m_3} \frac{1}{i\omega_{m_1} - \tilde{\mathcal{E}}_{\vec{p}_1; x}} \frac{1}{i\omega_{m_2} - \tilde{\mathcal{E}}_{\vec{p}_2; y}} \frac{1}{i\omega_{m_3} - \tilde{\mathcal{E}}_{\vec{p}_3; z}} \frac{1}{i\omega_{m_1} + i\omega_{m_2} - i\omega_{m_3} - \tilde{\mathcal{E}}_{\vec{p}_1 + \vec{p}_2 - \vec{p}_3; u}} \times \frac{1}{i\omega_{m_1} - Q_0 - i\eta - \tilde{\mathcal{E}}_{\vec{p}_1 - \vec{Q}; v}} \frac{1}{i\omega_{m_3} - Q_0 - i\eta - \tilde{\mathcal{E}}_{\vec{p}_3 - \vec{Q}; w}}, \quad (\text{C.5})$$

such that for Direct Urca neglected terms

$$\mathcal{M}_{V_2} = \frac{1}{(\tilde{\mathcal{E}}_{\vec{p}_2; y} - \tilde{\mathcal{E}}_{\vec{p}_1 + \vec{p}_2 - \vec{p}_3; u} + \tilde{\mathcal{E}}_{\vec{p}_1 - \vec{Q}; v} - \tilde{\mathcal{E}}_{\vec{p}_3 - \vec{Q}; w})(\tilde{\mathcal{E}}_{\vec{p}_1; x} + \tilde{\mathcal{E}}_{\vec{p}_2; y} - \tilde{\mathcal{E}}_{\vec{p}_3; z} - \tilde{\mathcal{E}}_{\vec{p}_1 + \vec{p}_2 - \vec{p}_3; u})} \times \left(\frac{1}{Q_0 + i\eta + \tilde{\mathcal{E}}_{\vec{p}_2; y} - \tilde{\mathcal{E}}_{\vec{p}_3; z} - \tilde{\mathcal{E}}_{\vec{p}_1 + \vec{p}_2 - \vec{p}_3; u} + \tilde{\mathcal{E}}_{\vec{p}_1 - \vec{Q}; v}} n_F(\tilde{\mathcal{E}}_{\vec{p}_2; y}) n_F(\tilde{\mathcal{E}}_{\vec{p}_1 - \vec{Q}; v}) (1 - n_F(\tilde{\mathcal{E}}_{\vec{p}_3; z})) (1 - n_F(\tilde{\mathcal{E}}_{\vec{p}_1 + \vec{p}_2 - \vec{p}_3; u})) - n_F(\tilde{\mathcal{E}}_{\vec{p}_3; z}) n_F(\tilde{\mathcal{E}}_{\vec{p}_1 + \vec{p}_2 - \vec{p}_3; u}) (1 - n_F(\tilde{\mathcal{E}}_{\vec{p}_2; y})) (1 - n_F(\tilde{\mathcal{E}}_{\vec{p}_1 - \vec{Q}; v})) \right) - \frac{1}{Q_0 + i\eta - \tilde{\mathcal{E}}_{\vec{p}_1; x} - \tilde{\mathcal{E}}_{\vec{p}_2; y} + \tilde{\mathcal{E}}_{\vec{p}_1 + \vec{p}_2 - \vec{p}_3; u} + \tilde{\mathcal{E}}_{\vec{p}_3 - \vec{Q}; w}} n_F(\tilde{\mathcal{E}}_{\vec{p}_1; x}) n_F(\tilde{\mathcal{E}}_{\vec{p}_2; y}) (1 - n_F(\tilde{\mathcal{E}}_{\vec{p}_1 + \vec{p}_2 - \vec{p}_3; u})) (1 - n_F(\tilde{\mathcal{E}}_{\vec{p}_3 - \vec{Q}; w})) - n_F(\tilde{\mathcal{E}}_{\vec{p}_1 + \vec{p}_2 - \vec{p}_3; u}) n_F(\tilde{\mathcal{E}}_{\vec{p}_3 - \vec{Q}; w}) (1 - n_F(\tilde{\mathcal{E}}_{\vec{p}_1; x})) (1 - n_F(\tilde{\mathcal{E}}_{\vec{p}_2; y})) \Big), \quad (\text{C.6})$$

which imaginary part gives

$$\text{Im } \mathcal{M}_{V_2} = -\pi \frac{1}{(\tilde{\mathcal{E}}_{\vec{p}_2; y} - \tilde{\mathcal{E}}_{\vec{p}_1 + \vec{p}_2 - \vec{p}_3; u} + \tilde{\mathcal{E}}_{\vec{p}_1 - \vec{Q}; v} - \tilde{\mathcal{E}}_{\vec{p}_3 - \vec{Q}; w})(\tilde{\mathcal{E}}_{\vec{p}_1; x} + \tilde{\mathcal{E}}_{\vec{p}_2; y} - \tilde{\mathcal{E}}_{\vec{p}_3; z} - \tilde{\mathcal{E}}_{\vec{p}_1 + \vec{p}_2 - \vec{p}_3; u})} \times \left(\delta(Q_0 + \tilde{\mathcal{E}}_{\vec{p}_2; y} - \tilde{\mathcal{E}}_{\vec{p}_3; z} - \tilde{\mathcal{E}}_{\vec{p}_1 + \vec{p}_2 - \vec{p}_3; u} + \tilde{\mathcal{E}}_{\vec{p}_1 - \vec{Q}; v}) \left[n_F(\tilde{\mathcal{E}}_{\vec{p}_2; y}) n_F(\tilde{\mathcal{E}}_{\vec{p}_1 - \vec{Q}; v}) (1 - n_F(\tilde{\mathcal{E}}_{\vec{p}_3; z})) (1 - n_F(\tilde{\mathcal{E}}_{\vec{p}_1 + \vec{p}_2 - \vec{p}_3; u})) - n_F(\tilde{\mathcal{E}}_{\vec{p}_3; z}) n_F(\tilde{\mathcal{E}}_{\vec{p}_1 + \vec{p}_2 - \vec{p}_3; u}) (1 - n_F(\tilde{\mathcal{E}}_{\vec{p}_2; y})) (1 - n_F(\tilde{\mathcal{E}}_{\vec{p}_1 - \vec{Q}; v})) \right] - \delta(Q_0 - \tilde{\mathcal{E}}_{\vec{p}_1; x} - \tilde{\mathcal{E}}_{\vec{p}_2; y} + \tilde{\mathcal{E}}_{\vec{p}_1 + \vec{p}_2 - \vec{p}_3; u} + \tilde{\mathcal{E}}_{\vec{p}_3 - \vec{Q}; w}) \left[n_F(\tilde{\mathcal{E}}_{\vec{p}_1; x}) n_F(\tilde{\mathcal{E}}_{\vec{p}_2; y}) (1 - n_F(\tilde{\mathcal{E}}_{\vec{p}_1 + \vec{p}_2 - \vec{p}_3; u})) (1 - n_F(\tilde{\mathcal{E}}_{\vec{p}_3 - \vec{Q}; w})) - n_F(\tilde{\mathcal{E}}_{\vec{p}_1 + \vec{p}_2 - \vec{p}_3; u}) n_F(\tilde{\mathcal{E}}_{\vec{p}_3 - \vec{Q}; w}) (1 - n_F(\tilde{\mathcal{E}}_{\vec{p}_1; x})) (1 - n_F(\tilde{\mathcal{E}}_{\vec{p}_2; y})) \right] \Big). \quad (\text{C.7})$$

C.3 Third vertex diagram

After introducing the Matsubara frequencies

$$\mathcal{M}_{V_3} = \sum_{m_1} \sum_{m_2} \sum_{m_3} \frac{1}{i\omega_{m_1} - \tilde{\mathcal{E}}_{\vec{p}_1;x}} \frac{1}{i\omega_{m_2} - \tilde{\mathcal{E}}_{\vec{p}_2;y}} \frac{1}{i\omega_{m_3} - \tilde{\mathcal{E}}_{\vec{p}_3;z}} \frac{1}{i\omega_{m_1} + i\omega_{m_2} - i\omega_{m_3} - \tilde{\mathcal{E}}_{\vec{p}_1+\vec{p}_2-\vec{p}_3;u}} \times \frac{1}{i\omega_{m_1} - Q_0 - i\eta - \tilde{\mathcal{E}}_{\vec{p}_1-\vec{Q};v}} \frac{1}{i\omega_{m_2} + Q_0 + i\eta - \tilde{\mathcal{E}}_{\vec{p}_2+\vec{Q};w}}, \quad (\text{C.8})$$

such that for neglected Direct Urca contributions

$$\mathcal{M}_{V_3} = \frac{1}{(\tilde{\mathcal{E}}_{\vec{p}_3;z} + \tilde{\mathcal{E}}_{\vec{p}_1+\vec{p}_2-\vec{p}_3;u} - \tilde{\mathcal{E}}_{\vec{p}_1-\vec{Q};v} - \tilde{\mathcal{E}}_{\vec{p}_2+\vec{Q};w})(\tilde{\mathcal{E}}_{\vec{p}_1;x} + \tilde{\mathcal{E}}_{\vec{p}_2;y} - \tilde{\mathcal{E}}_{\vec{p}_3;z} - \tilde{\mathcal{E}}_{\vec{p}_1+\vec{p}_2-\vec{p}_3;u})} \times \left(\frac{1}{Q_0 + i\eta - \tilde{\mathcal{E}}_{\vec{p}_1;x} + \tilde{\mathcal{E}}_{\vec{p}_3;z} + \tilde{\mathcal{E}}_{\vec{p}_1+\vec{p}_2-\vec{p}_3;u} - \tilde{\mathcal{E}}_{\vec{p}_2+\vec{Q};w}} \right. \\ \left. n_F(\tilde{\mathcal{E}}_{\vec{p}_1;x}) n_F(\tilde{\mathcal{E}}_{\vec{p}_2+\vec{Q};w}) (1 - n_F(\tilde{\mathcal{E}}_{\vec{p}_3;z})) (1 - n_F(\tilde{\mathcal{E}}_{\vec{p}_1+\vec{p}_2-\vec{p}_3;u})) \right. \\ \left. - n_F(\tilde{\mathcal{E}}_{\vec{p}_3;z}) n_F(\tilde{\mathcal{E}}_{\vec{p}_1+\vec{p}_2-\vec{p}_3;u}) (1 - n_F(\tilde{\mathcal{E}}_{\vec{p}_1;x})) (1 - n_F(\tilde{\mathcal{E}}_{\vec{p}_2+\vec{Q};w})) \right) \\ - \frac{1}{Q_0 + i\eta + \tilde{\mathcal{E}}_{\vec{p}_2;y} - \tilde{\mathcal{E}}_{\vec{p}_3;z} - \tilde{\mathcal{E}}_{\vec{p}_1+\vec{p}_2-\vec{p}_3;u} + \tilde{\mathcal{E}}_{\vec{p}_1-\vec{Q};v}} \quad (\text{C.9})$$

$$\left. n_F(\tilde{\mathcal{E}}_{\vec{p}_2;y}) n_F(\tilde{\mathcal{E}}_{\vec{p}_1-\vec{Q};v}) (1 - n_F(\tilde{\mathcal{E}}_{\vec{p}_3;z})) (1 - n_F(\tilde{\mathcal{E}}_{\vec{p}_1+\vec{p}_2-\vec{p}_3;u})) \right. \\ \left. - n_F(\tilde{\mathcal{E}}_{\vec{p}_3;z}) n_F(\tilde{\mathcal{E}}_{\vec{p}_1+\vec{p}_2-\vec{p}_3;u}) (1 - n_F(\tilde{\mathcal{E}}_{\vec{p}_2;y})) (1 - n_F(\tilde{\mathcal{E}}_{\vec{p}_1-\vec{Q};v})) \right), \quad (\text{C.10})$$

which imaginary part renders

$$\text{Im } \mathcal{M}_{V_3} = -\pi \frac{1}{(\tilde{\mathcal{E}}_{\vec{p}_3;z} + \tilde{\mathcal{E}}_{\vec{p}_1+\vec{p}_2-\vec{p}_3;u} - \tilde{\mathcal{E}}_{\vec{p}_1-\vec{Q};v} - \tilde{\mathcal{E}}_{\vec{p}_2+\vec{Q};w})(\tilde{\mathcal{E}}_{\vec{p}_1;x} + \tilde{\mathcal{E}}_{\vec{p}_2;y} - \tilde{\mathcal{E}}_{\vec{p}_3;z} - \tilde{\mathcal{E}}_{\vec{p}_1+\vec{p}_2-\vec{p}_3;u})} \times \left(\delta(Q_0 - \tilde{\mathcal{E}}_{\vec{p}_1;x} + \tilde{\mathcal{E}}_{\vec{p}_3;z} + \tilde{\mathcal{E}}_{\vec{p}_1+\vec{p}_2-\vec{p}_3;u} - \tilde{\mathcal{E}}_{\vec{p}_2+\vec{Q};w}) \left[\right. \right. \\ \left. \left. n_F(\tilde{\mathcal{E}}_{\vec{p}_1;x}) n_F(\tilde{\mathcal{E}}_{\vec{p}_2+\vec{Q};w}) (1 - n_F(\tilde{\mathcal{E}}_{\vec{p}_3;z})) (1 - n_F(\tilde{\mathcal{E}}_{\vec{p}_1+\vec{p}_2-\vec{p}_3;u})) \right. \right. \\ \left. \left. - n_F(\tilde{\mathcal{E}}_{\vec{p}_3;z}) n_F(\tilde{\mathcal{E}}_{\vec{p}_1+\vec{p}_2-\vec{p}_3;u}) (1 - n_F(\tilde{\mathcal{E}}_{\vec{p}_1;x})) (1 - n_F(\tilde{\mathcal{E}}_{\vec{p}_2+\vec{Q};w})) \right] \right. \\ \left. - \delta(Q_0 + \tilde{\mathcal{E}}_{\vec{p}_2;y} - \tilde{\mathcal{E}}_{\vec{p}_3;z} - \tilde{\mathcal{E}}_{\vec{p}_1+\vec{p}_2-\vec{p}_3;u} + \tilde{\mathcal{E}}_{\vec{p}_1-\vec{Q};v}) \left[\right. \right. \\ \left. \left. n_F(\tilde{\mathcal{E}}_{\vec{p}_2;y}) n_F(\tilde{\mathcal{E}}_{\vec{p}_1-\vec{Q};v}) (1 - n_F(\tilde{\mathcal{E}}_{\vec{p}_3;z})) (1 - n_F(\tilde{\mathcal{E}}_{\vec{p}_1+\vec{p}_2-\vec{p}_3;u})) \right. \right. \\ \left. \left. - n_F(\tilde{\mathcal{E}}_{\vec{p}_3;z}) n_F(\tilde{\mathcal{E}}_{\vec{p}_1+\vec{p}_2-\vec{p}_3;u}) (1 - n_F(\tilde{\mathcal{E}}_{\vec{p}_2;y})) (1 - n_F(\tilde{\mathcal{E}}_{\vec{p}_1-\vec{Q};v})) \right] \right). \quad (\text{C.11})$$

C.4 Center of mass change in variables

C.4.1 Details for the first self-energy correction

We intend to apply the Dirac δ -functions in the expression

$$\begin{aligned} \text{Im} \Pi_D^{\alpha\beta}(Q) = & \left(\prod_{j=1}^3 \int \frac{d^3 \vec{p}_j}{(2\pi)^3} \right) \int \frac{d^3 p_4}{(2\pi)^4} \sum_{\text{iso}} \delta^3(\vec{p}_1 + \vec{p}_2 - \vec{p}_3 - \vec{p}_4) \\ & \times \delta(\tilde{\mathcal{E}}_{\vec{p}_6;w} + \tilde{\mathcal{E}}_{\vec{p}_2;y} + Q_0 - \tilde{\mathcal{E}}_{\vec{p}_3;z} - \tilde{\mathcal{E}}_{\vec{p}_4;u}) \mathcal{M}_D \sum_X X_{\text{spin}}^{\alpha\beta} \end{aligned} \quad (\text{C.12})$$

Let us assume that we intend to eliminate the integral over particles (3) and (4), the following change in variables can be introduced:

- the total masses $M = m_3 + m_4$ with m_3 and m_4 the masses of particles (3) and (4) respectively,

- the reduced mass

$$\eta = \frac{m_3 m_4}{m_3 + m_4}, \quad (\text{C.13})$$

- the speed of the center of mass

$$\vec{V} = \frac{\vec{p}_3 + \vec{p}_4}{m_3 + m_4}, \quad (\text{C.14})$$

- and the relative speed

$$\vec{v} = \frac{\vec{p}_3}{m_3} - \frac{\vec{p}_4}{m_4}, \quad (\text{C.15})$$

such that

$$\vec{p}_3 = m_3 \vec{V} + \eta \vec{v}. \quad (\text{C.16})$$

The Jacobian matrix of the change in variable we want to operate is

$$J = \begin{pmatrix} m_3 & \zeta \\ m_4 & -\zeta \end{pmatrix}, \quad (\text{C.17})$$

By introducing the change of variable related to the center of mass between two nucleons, we can write the imaginary part of the retarded function

$$\begin{aligned} \text{Im} \Pi_D^{\alpha\beta}(Q) = & \frac{\eta^2}{(2\pi)^{13}} \int d|\vec{p}_1| \int d\theta_1 \int d\phi_1 \int d|\vec{p}_2| \int d\theta_2 \int d\phi_2 \int d\theta_v \int d\phi_v \\ & \times |\vec{p}_1|^2 |\vec{p}_2|^2 \sin(\theta_1) \sin(\theta_2) \sin(\theta_v) \sum_{\text{iso}} \mathcal{M}_D \sum_X X_{\text{spin}}^{\alpha\beta} \\ & \times \sqrt{\frac{2}{\eta} \left(A_D(\vec{p}_1, \vec{p}_2) - \frac{(\vec{p}_1 + \vec{p}_2)^2}{2M} \right)} \Theta \left(A_D(\vec{p}_1, \vec{p}_2) - \frac{(\vec{p}_1 + \vec{p}_2)^2}{2M} \right), \end{aligned} \quad (\text{C.18})$$

with

$$A_D(\vec{p}_1, \vec{p}_2) = \tilde{\mathcal{E}}_{\vec{p}_1 - \vec{Q}; w} + \tilde{\mathcal{E}}_{\vec{p}_2; y} + Q_0 - m_3 - m_4 + \mu_3 + \mu_4, \quad (\text{C.19})$$

and

$$\mathcal{M}_D = -\pi \frac{\mathcal{G}(\tilde{\mathcal{E}}_{\vec{p}_6; w}, \tilde{\mathcal{E}}_{\vec{p}_2; y}, \tilde{\mathcal{E}}_{\vec{p}_3; z}, \tilde{\mathcal{E}}_{\vec{p}_4; u})}{(\tilde{\mathcal{E}}_{\vec{p}_1; x} - \tilde{\mathcal{E}}_{\vec{p}_1 - \vec{Q}; w} - Q_0)^2}. \quad (\text{C.20})$$

$$(\text{C.21})$$

Similarly, if we choose to eliminate the integrals over particles (1) and (2), the retarded polarization function for the self-energy correction is given by

$$\begin{aligned} \text{Im } \Pi_D^{\alpha\beta}(Q) &= \frac{\zeta^2}{(2\pi)^{13}} \int d|\vec{p}_3| \int d\theta_3 \int d\phi_3 \int d|\vec{p}_4| \int d\theta_4 \int d\phi_4 \int d\theta_v \int d\phi_v \\ &\times |\vec{p}_3|^2 |\vec{p}_4|^2 \sin(\theta_3) \sin(\theta_4) \sin(\theta_v) \sum_{\text{iso}} \mathcal{M}_D \sum_X X_{\text{spin}}^{\alpha\beta} \\ &\times \sqrt{\frac{2}{\zeta} \left(B_D(\vec{p}_3, \vec{p}_4) - \frac{(\vec{p}_3 + \vec{p}_4 - \vec{Q})^2}{2\tilde{M}} \right)} \Theta \left(B_D(\vec{p}_3, \vec{p}_4) - \frac{(\vec{p}_3 + \vec{p}_4 - \vec{Q})^2}{2\tilde{M}} \right), \end{aligned} \quad (\text{C.22})$$

with $\tilde{M} = m_2 + m_6$, $\zeta = m_2 m_6 / (m_2 + m_6)$ and

$$B_D(\vec{p}_3, \vec{p}_4) = \tilde{\mathcal{E}}_{\vec{p}_3; z} + \tilde{\mathcal{E}}_{\vec{p}_4; u} - Q_0 - m_6 - m_2 + \mu_6 + \mu_2. \quad (\text{C.23})$$

Although it might seem redundant to present results which are equivalent whether we eliminate the integrals over particles (1) and (2) or (3) and (4), both expressions are useful for a method of importance sampling in the numerical integration.

C.4.2 Expression for the second self-energy correction

The retarded polarization function of the second self-energy correction can either be written as

- if we eliminate the integrals over particles (3) and (4)

$$\begin{aligned} \text{Im } \Pi_D^{\alpha\beta}(Q) &= \frac{\eta^2}{(2\pi)^{13}} \int d|\vec{p}_1| \int d\theta_1 \int d\phi_1 \int d|\vec{p}_2| \int d\theta_2 \int d\phi_2 \int d\theta_v \int d\phi_v \\ &\times |\vec{p}_1|^2 |\vec{p}_2|^2 \sin(\theta_1) \sin(\theta_2) \sin(\theta_v) \sum_{\text{iso}} \mathcal{M}_D \sum_X X_{\text{spin}}^{\alpha\beta} \\ &\times \sqrt{\frac{2}{\eta} \left(A_D(\vec{p}_1, \vec{p}_2) - \frac{(\vec{p}_1 + \vec{p}_2 + \vec{Q})^2}{2M} \right)} \Theta \left(A_D(\vec{p}_1, \vec{p}_2) - \frac{(\vec{p}_1 + \vec{p}_2 + \vec{Q})^2}{2M} \right), \end{aligned} \quad (\text{C.24})$$

with

$$A_D(\vec{p}_1, \vec{p}_2) = \tilde{\mathcal{E}}_{\vec{p}_1; x} + \tilde{\mathcal{E}}_{\vec{p}_2; y} + Q_0 - m_3 - m_4 + \mu_3 + \mu_4, \quad (\text{C.25})$$

- if we eliminate the integrals over particles (1) and (2)

$$\begin{aligned} \text{Im } \Pi_D^{\alpha\beta}(Q) &= \frac{\zeta^2}{(2\pi)^{13}} \int d|\vec{p}_3| \int d\theta_3 \int d\phi_3 \int d|\vec{p}_4| \int d\theta_4 \int d\phi_4 \int d\theta_v \int d\phi_v \\ &\times |\vec{p}_3|^2 |\vec{p}_4|^2 \sin(\theta_3) \sin(\theta_4) \sin(\theta_v) \sum_{\text{iso}} \mathcal{M}_D \sum_X X_{\text{spin}}^{\alpha\beta} \\ &\times \sqrt{\frac{2}{\zeta} \left(B_D(\vec{p}_3, \vec{p}_4) - \frac{(\vec{p}_3 + \vec{p}_4 - \vec{Q})^2}{2\tilde{M}} \right)} \Theta \left(B_D(\vec{p}_3, \vec{p}_4) - \frac{(\vec{p}_3 + \vec{p}_4 - \vec{Q})^2}{2\tilde{M}} \right), \end{aligned} \quad (\text{C.26})$$

with $\tilde{M} = m_2 + m_6$, $\zeta = m_2 m_6 / (m_2 + m_6)$ and

$$B_D(\vec{p}_3, \vec{p}_4) = \tilde{\mathcal{E}}_{\vec{p}_3,z} + \tilde{\mathcal{E}}_{\vec{p}_4,u} - Q_0 - m_6 - m_2 + \mu_6 + \mu_2. \quad (\text{C.27})$$

C.4.3 Expression for the second vertex

The retarded polarization function of the second vertex correction can either be written as

- if we eliminate the integrals over particles (3) and (4)

$$\begin{aligned} \text{Im } \Pi_{V_2}^{\alpha\beta}(Q) &= \frac{1}{(2\pi)^{13}} \int d|\vec{p}_1| \int d\theta_1 \int d\phi_1 \int d|\vec{p}_2| \int d\theta_2 \int d\phi_2 \int d\theta_v \int d\phi_v \\ &\times |\vec{p}_1|^2 |\vec{p}_2|^2 \sin(\theta_1) \sin(\theta_2) \sin(\theta_v) \sum_{\text{iso}} \sum_{X=a,b,c,d} V_{2X,\text{spin}}^{\alpha\beta} \\ &\times \left[\left(\eta^{(1)} \right)^2 \sqrt{\frac{2}{\eta^{(1)}} \left(A_{V_2}^{(1)} - \frac{(\vec{p}_1 + \vec{p}_2)^2}{2M^{(1)}} \right)} \Theta \left(A_{V_2}^{(1)} - \frac{(\vec{p}_1 + \vec{p}_2)^2}{2M^{(1)}} \right) \mathcal{M}_{V_2}^{(1)} \right. \\ &\left. + \left(\eta^{(2)} \right)^2 \sqrt{\frac{2}{\eta^{(2)}} \left(A_{V_2}^{(2)} - \frac{(\vec{p}_1 + \vec{p}_2)^2}{2M^{(2)}} \right)} \Theta \left(A_{V_2}^{(2)} - \frac{(\vec{p}_1 + \vec{p}_2)^2}{2M^{(2)}} \right) \mathcal{M}_{V_2}^{(2)} \right] \end{aligned} \quad (\text{C.28})$$

with

$$M^{(1)} = m_3 + m_4, \eta^{(1)} = \frac{m_3 m_4}{m_3 + m_4}, M^{(2)} = m_6 + m_4, \eta^{(2)} = \frac{m_6 m_4}{m_6 + m_4} \quad (\text{C.29})$$

$$A_{V_2}^{(1)}(\vec{p}_1, \vec{p}_2) = \tilde{\mathcal{E}}_{\vec{p}_1 - \vec{Q},v} + \tilde{\mathcal{E}}_{\vec{p}_2,y} + Q_0 - m_3 - m_4 + \mu_3 + \mu_4, \quad (\text{C.30})$$

$$A_{V_2}^{(2)}(\vec{p}_1, \vec{p}_2) = \tilde{\mathcal{E}}_{\vec{p}_1,x} + \tilde{\mathcal{E}}_{\vec{p}_2,y} - Q_0 - m_6 - m_4 + \mu_6 + \mu_4, \quad (\text{C.31})$$

and

$$\mathcal{M}_{V_2}^{(1)} = -\pi \frac{\mathcal{G}(\tilde{\mathcal{E}}_{\vec{p}_5,v}, \tilde{\mathcal{E}}_{\vec{p}_2,y}, \tilde{\mathcal{E}}_{\vec{p}_3,z}, \tilde{\mathcal{E}}_{\vec{p}_4,u})}{(\tilde{\mathcal{E}}_{\vec{p}_3 - \vec{Q},w} - \tilde{\mathcal{E}}_{\vec{p}_3,z} + Q_0)(\tilde{\mathcal{E}}_{\vec{p}_1 - \vec{Q},v} - \tilde{\mathcal{E}}_{\vec{p}_1,x} + Q_0)} \quad (\text{C.32})$$

$$\mathcal{M}_{V_2}^{(1)} = \pi \frac{\mathcal{G}(\tilde{\mathcal{E}}_{\vec{p}_1,x}, \tilde{\mathcal{E}}_{\vec{p}_2,y}, \tilde{\mathcal{E}}_{\vec{p}_4,u}, \tilde{\mathcal{E}}_{\vec{p}_6,w})}{(\tilde{\mathcal{E}}_{\vec{p}_3 - \vec{Q},w} - \tilde{\mathcal{E}}_{\vec{p}_3,z} + Q_0)(\tilde{\mathcal{E}}_{\vec{p}_1 - \vec{Q},v} - \tilde{\mathcal{E}}_{\vec{p}_1,x} + Q_0)} \quad (\text{C.33})$$

- or if we eliminate the integrals over particles (1) and (2)

$$\begin{aligned} \text{Im } \Pi_{V_2}^{\alpha\beta}(Q) &= \frac{1}{(2\pi)^{13}} \int d|\vec{p}_3| \int d\theta_3 \int d\phi_3 \int d|\vec{p}_4| \int d\theta_4 \int d\phi_4 \int d\theta_v \int d\phi_v \quad (\text{C.34}) \\ &\times |\vec{p}_3|^2 |\vec{p}_4|^2 \sin(\theta_3) \sin(\theta_4) \sin(\theta_v) \sum_{\text{iso}} \sum_{X=a,b,c,d} V_{2X,\text{spin}}^{\alpha\beta} \\ &\times \left[\left(\zeta^{(1)} \right)^2 \sqrt{\frac{2}{\zeta^{(1)}} \left(A_{V_2}^{(1)} - \frac{(\vec{p}_3 + \vec{p}_4 + \vec{Q})^2}{2\tilde{M}^{(1)}} \right)} \Theta \left(A_{V_2}^{(1)} - \frac{(\vec{p}_3 + \vec{p}_4 + \vec{Q})^2}{2\tilde{M}^{(1)}} \right) \mathcal{M}_{V_2}^{(1)} \right. \\ &\left. + \left(\zeta^{(2)} \right)^2 \sqrt{\frac{2}{\zeta^{(2)}} \left(A_{V_2}^{(2)} - \frac{(\vec{p}_3 + \vec{p}_4)^2}{2\tilde{M}^{(2)}} \right)} \Theta \left(A_{V_2}^{(2)} - \frac{(\vec{p}_3 + \vec{p}_4)^2}{2\tilde{M}^{(2)}} \right) \mathcal{M}_{V_2}^{(2)} \right] \end{aligned}$$

with

$$\tilde{M}^{(1)} = m_5 + m_2, \zeta^{(1)} = \frac{m_5 m_2}{m_5 + m_2}, \tilde{M}^{(2)} = m_1 + m_2, \zeta^{(2)} = \frac{m_1 m_2}{m_1 + m_2} \quad (\text{C.35})$$

$$A_{V_2}^{(1)}(\vec{p}_3, \vec{p}_4) = \tilde{\mathcal{E}}_{\vec{p}_3,z} + \tilde{\mathcal{E}}_{\vec{p}_4,u} - Q_0 - m_5 - m_2 + \mu_5 + \mu_2, \quad (\text{C.36})$$

$$A_{V_2}^{(2)}(\vec{p}_3, \vec{p}_4) = \tilde{\mathcal{E}}_{\vec{p}_4,u} + \tilde{\mathcal{E}}_{\vec{p}_3-\vec{Q},w} + Q_0 - m_1 - m_2 + \mu_1 + \mu_2. \quad (\text{C.37})$$

C.4.4 Expression for the third vertex

The retarded polarization function of the third vertex correction can either be written as

- if we eliminate the integrals over particles (3) and (4)

$$\begin{aligned} \text{Im } \Pi_{V_3}^{\alpha\beta}(Q) &= \frac{1}{(2\pi)^{13}} \int d|\vec{p}_1| \int d\theta_1 \int d\phi_1 \int d|\vec{p}_2| \int d\theta_2 \int d\phi_2 \int d\theta_v \int d\phi_v \quad (\text{C.38}) \\ &\times |\vec{p}_1|^2 |\vec{p}_2|^2 \sin(\theta_1) \sin(\theta_2) \sin(\theta_v) \sum_{\text{iso}} \sum_{X=a,b,c,d} V_{3X,\text{spin}}^{\alpha\beta} \\ &\times \left[\eta^2 \sqrt{\frac{2}{\eta} \left(A_{V_3}^{(1)} - \frac{(\vec{p}_1 + \vec{p}_2)^2}{2M} \right)} \Theta \left(A_{V_3}^{(1)} - \frac{(\vec{p}_1 + \vec{p}_2)^2}{2M} \right) \mathcal{M}_{V_3}^{(1)} \right. \\ &\left. + \eta^2 \sqrt{\frac{2}{\eta} \left(A_{V_2}^{(2)} - \frac{(\vec{p}_1 + \vec{p}_2)^2}{2M} \right)} \Theta \left(A_{V_3}^{(2)} - \frac{(\vec{p}_1 + \vec{p}_2)^2}{2M} \right) \mathcal{M}_{V_3}^{(2)} \right] \end{aligned}$$

with

$$M = m_3 + m_4, \eta = \frac{m_3 m_4}{m_3 + m_4}, \quad (\text{C.39})$$

$$A_{V_3}^{(1)} = \tilde{\mathcal{E}}_{\vec{p}_1,x} + \tilde{\mathcal{E}}_{\vec{p}_2+\vec{Q},w} - Q_0 - m_3 - m_4 + \mu_3 + \mu_4, \quad (\text{C.40})$$

$$A_{V_3}^{(2)} = \tilde{\mathcal{E}}_{\vec{p}_1-\vec{Q},v} + \tilde{\mathcal{E}}_{\vec{p}_2,y} + Q_0 - m_3 - m_4 + \mu_3 + \mu_4, \quad (\text{C.41})$$

and

$$\mathcal{M}_{V_3}^{(1)} = -\pi \frac{\mathcal{G}(\tilde{\mathcal{E}}_{\vec{p}_1;x}, \tilde{\mathcal{E}}_{\vec{p}_6;w}, \tilde{\mathcal{E}}_{\vec{p}_3;z}, \tilde{\mathcal{E}}_{\vec{p}_4;u})}{(\tilde{\mathcal{E}}_{\vec{p}_1-\vec{Q},v} - \tilde{\mathcal{E}}_{\vec{p}_1;x} + Q_0)(\tilde{\mathcal{E}}_{\vec{p}_2+\vec{Q},w} - \tilde{\mathcal{E}}_{\vec{p}_2,y} - Q_0)} \quad (\text{C.42})$$

$$\mathcal{M}_{V_3}^{(1)} = \pi \frac{\mathcal{G}(\tilde{\mathcal{E}}_{\vec{p}_2;y}, \tilde{\mathcal{E}}_{\vec{p}_5;v}, \tilde{\mathcal{E}}_{\vec{p}_3;z}, \tilde{\mathcal{E}}_{\vec{p}_4;u})}{(\tilde{\mathcal{E}}_{\vec{p}_1-\vec{Q};v} - \tilde{\mathcal{E}}_{\vec{p}_1;x} + Q_0)(\tilde{\mathcal{E}}_{\vec{p}_2+\vec{Q};w} - \tilde{\mathcal{E}}_{\vec{p}_2;y} - Q_0)}. \quad (\text{C.43})$$

- or if we eliminate the integrals over particles (1) and (2)

$$\begin{aligned} \text{Im} \Pi_{V_3}^{\alpha\beta}(Q) &= \frac{1}{(2\pi)^{13}} \int d|\vec{p}_3| \int d\theta_3 \int d\phi_3 \int d|\vec{p}_4| \int d\theta_4 \int d\phi_4 \int d\theta_v \int d\phi_v \quad (\text{C.44}) \\ &\times |\vec{p}_3|^2 |\vec{p}_4|^2 \sin(\theta_3) \sin(\theta_4) \sin(\theta_v) \sum_{\text{iso}} \sum_{X=a,b,c,d} V_{3X,\text{spin}}^{\alpha\beta} \\ &\times \left[\left(\eta^{(1)} \right)^2 \sqrt{\frac{2}{\eta^{(1)}} \left(A_{V_3}^{(1)} - \frac{(\vec{p}_3 + \vec{p}_4 + \vec{Q})^2}{2M^{(1)}} \right)} \Theta \left(A_{V_3}^{(1)} - \frac{(\vec{p}_3 + \vec{p}_4 + \vec{Q})^2}{2M^{(1)}} \right) \mathcal{M}_{V_2}^{(1)} \right. \\ &\left. + \left(\eta^{(2)} \right)^2 \sqrt{\frac{2}{\eta^{(2)}} \left(A_{V_3}^{(2)} - \frac{(\vec{p}_3 + \vec{p}_4 - \vec{Q})^2}{2M^{(2)}} \right)} \Theta \left(A_{V_3}^{(2)} - \frac{(\vec{p}_3 + \vec{p}_4 - \vec{Q})^2}{2M^{(2)}} \right) \mathcal{M}_{V_3}^{(2)} \right] \end{aligned}$$

with

$$M^{(1)} = m_6 + m_1, \eta^{(1)} = \frac{m_6 m_1}{m_6 + m_1}, M^{(2)} = m_5 + m_2, \eta^{(2)} = \frac{m_5 m_2}{m_5 + m_2} \quad (\text{C.45})$$

$$A_{V_3}^{(1)} = \tilde{\mathcal{E}}_{\vec{p}_3;z} + \tilde{\mathcal{E}}_{\vec{p}_4;u} + Q_0 - m_6 - m_1 + \mu_6 + \mu_1, \quad (\text{C.46})$$

$$A_{V_3}^{(2)} = \tilde{\mathcal{E}}_{\vec{p}_3;z} + \tilde{\mathcal{E}}_{\vec{p}_4;u} - Q_0 - m_5 - m_2 + \mu_5 + \mu_2. \quad (\text{C.47})$$

Bibliography

- L. Suleiman, M. Fortin, J. L. Zdunik, and P. Haensel. Influence of the crust on the neutron star macrophysical quantities and universal relations. *Physical Review C*, 104(1):015801, July 2021. doi: 10.1103/PhysRevC.104.015801.
- L. Suleiman, M. Fortin, J. L. Zdunik, and C. Providência. Polytopic fits of modern and unified equations of state. *Physical Review C*, 106(3):035805, September 2022a. doi: 10.1103/PhysRevC.106.035805.
- L. Suleiman, J. L. Zdunik, P. Haensel, and M. Fortin. Partially accreted crusts of neutron stars. *Astronomy & Astrophysics*, 662:A63, June 2022b. doi: 10.1051/0004-6361/202243040.
- J. Chadwick. Possible Existence of a Neutron. *Nature*, 129(3252):312, February 1932. doi: 10.1038/129312a0.
- L. D. Landau. On the Theory of Stars. *Physikalische Zeitschrift Sowjetunion*, page 285, February 1932.
- D. G. Yakovlev, P. Haensel, G. Baym, and C. Pethick. Lev Landau and the concept of neutron stars. *Physics Uspekhi*, 56(3):289-295, March 2013. doi: 10.3367/UFNe.0183.201303f.0307.
- W. Baade and F. Zwicky. Remarks on Super-Novae and Cosmic Rays. *Physical Review*, 46(1):76-77, July 1934a. doi: 10.1103/PhysRev.46.76.2.
- W. Baade and F. Zwicky. On Super-novae. *Proceedings of the National Academy of Science*, 20(5):254-259, May 1934b. doi: 10.1073/pnas.20.5.254.
- W. Baade and F. Zwicky. Cosmic Rays from Super-novae. *Proceedings of the National Academy of Science*, 20(5):259-263, May 1934c. doi: 10.1073/pnas.20.5.259.
- R. C. Tolman. Static Solutions of Einstein's Field Equations for Spheres of Fluid. *Physical Review*, 55(4):364-373, February 1939. doi: 10.1103/PhysRev.55.364.
- J. R. Oppenheimer and G. M. Volkoff. On Massive Neutron Cores. *Physical Review*, 55(4):374-381, February 1939. doi: 10.1103/PhysRev.55.374.
- A. G. Cameron. Neutron Star Models. *Astrophysical Journal*, 130:884, November 1959. doi: 10.1086/146780.
- V. A. Ambartsumyan and G. S. Saakyan. The Degenerate Superdense Gas of Elementary Particles. *Soviet Astronomy AJ*, 37:193, January 1960.

- A. Hewish, S. J. Bell, J. D. H. Pilkington, P. F. Scott, and R. A. Collins. Observation of a Rapidly Pulsating Radio Source. *Nature*, 217(5130):709–713, February 1968. doi: 10.1038/217709a0.
- Nobel Prize Outreach AB. The Nobel Prize in Physics 1974. *NobelPrize.org*, October 2022. URL <https://www.nobelprize.org/prizes/physics/1974/summary/>.
- V. Radhakrishnan and R. N. Manchester. Detection of a Change of State in the Pulsar PSR 0833-45. *Nature*, 222(5190):228–229, April 1969. doi: 10.1038/222228a0.
- P. E. Boynton, III Groth, E. J., R. B. Partridge, and David T. Wilkinson. Precision Measurement of the Frequency Decay of the Crab Nebula Pulsar, NP 0532. *The Astrophysical Journal, Letters*, 157:L197, September 1969. doi: 10.1086/180418.
- T. Gold. Rotating Neutron Stars as the Origin of the Pulsating Radio Sources. *Nature*, 218(5143):731–732, May 1968. doi: 10.1038/218731a0.
- V. Radhakrishnan and G. Srinivasan. On the origin of the recently discovered ultra-rapid pulsar. *Current Science*, 51:1096–1099, December 1982.
- R. Nan, D. Li, C. Jin, Q. Wang, L. Zhu, W. Zhu, H. Zhang, Y. Yue, and Le. Qian. The Five-Hundred Aperture Spherical Radio Telescope (fast) Project. *International Journal of Modern Physics D*, 20(6):989–1024, January 2011. doi: 10.1142/S0218271811019335.
- A. Watts and et al. Probing the neutron star interior and the Equation of State of cold dense matter with the SKA. In *Advancing Astrophysics with the Square Kilometre Array (AASKA14)*, page 43, April 2015.
- M. Kramer and et al. Strong-Field Gravity Tests with the Double Pulsar. *Physical Review X*, 11(4):041050, October 2021. doi: 10.1103/PhysRevX.11.041050.
- F. Jansen and et al. XMM-Newton observatory. I. The spacecraft and operations. *Astronomy & Astrophysics*, 365:L1–L6, January 2001. doi: 10.1051/0004-6361:20000036.
- Martin C. Weisskopf, Harvey D. Tananbaum, Leon P. Van Speybroeck, and Stephen L. O’Dell. Chandra X-ray Observatory (CXO): overview. In Joachim E. Truemper and Bernd Aschenbach, editors, *X-Ray Optics, Instruments, and Missions III*, volume 4012 of *Society of Photo-Optical Instrumentation Engineers (SPIE) Conference Series*, pages 2–16, July 2000. doi: 10.1117/12.391545.
- F. A. Harrison and et al. The Nuclear Spectroscopic Telescope Array (NuSTAR) High-energy X-Ray Mission. *Astrophysical Journal*, 770(2):103, June 2013. doi: 10.1088/0004-637X/770/2/103.
- Keith C. Gendreau, Zaven Arzoumanian, and Takashi Okajima. The Neutron star Interior Composition ExploreR (NICER): an Explorer mission of opportunity for soft x-ray timing

- spectroscopy. In *Space Telescopes and Instrumentation 2012: Ultraviolet to Gamma Ray*, volume 8443 of *Society of Photo-Optical Instrumentation Engineers (SPIE) Conference Series*, page 844313, September 2012. doi: 10.1117/12.926396.
- Anna L. Watts and et al. Dense matter with eXTP. *Science China Physics, Mechanics, and Astronomy*, 62(2):29503, February 2019. doi: 10.1007/s11433-017-9188-4.
- S. Hauf, M. Kuster, M. G. Pia, D. H. H. Hoffmann, P. Lang, S. Neff, A. Stefanescu, and L. Strüder. Background simulations of the wide field imager of the ATHENA X-ray observatory. In *2011 IEEE Nuclear Science Symposium Conference Record*, pages 1239–1243, 2011. doi: 10.1109/NSSMIC.2011.6154609.
- Albert Einstein. The Foundation of the General Theory of Relativity. *Annalen Phys.*, 49(7): 769–822, 1916. doi: 10.1002/andp.19163540702.
- B. P. Abbott and et al. Observation of Gravitational Waves from a Binary Black Hole Merger. *Physical Review Letters*, 116(6):061102, February 2016. doi: 10.1103/PhysRevLett.116.061102.
- B. P. Abbott, LIGO Scientific Collaboration, Virgo Collaboration, Kagra Collaboration, and et al. Prospects for observing and localizing gravitational-wave transients with Advanced LIGO, Advanced Virgo and KAGRA. *Living Reviews in Relativity*, 23(1):3, September 2020a. doi: 10.1007/s41114-020-00026-9.
- A. Le Tiec and M. Casals. Spinning Black Holes Fall in Love. *Physical Review Letters*, 126(13): 131102, April 2021. doi: 10.1103/PhysRevLett.126.131102.
- B. P. Abbott, LIGO Scientific Collaboration, and Virgo Collaboration and et al. GW170817: Observation of Gravitational Waves from a Binary Neutron Star Inspiral. *Physical Review Letters*, 119(16):161101, October 2017. doi: 10.1103/PhysRevLett.119.161101.
- B. P. Abbott and et al. GW190425: Observation of a Compact Binary Coalescence with Total Mass $\sim 3.4 M_{\odot}$. *The Astrophysical Journal Letters*, 892(1):L3, March 2020. doi: 10.3847/2041-8213/ab75f5.
- R. Abbott, LIGO Scientific Collaboration, and Virgo Collaboration and et al. GW190814: Gravitational Waves from the Coalescence of a 23 Solar Mass Black Hole with a 2.6 Solar Mass Compact Object. *The Astrophysical Journal Letters*, 896(2):L44, June 2020b. doi: 10.3847/2041-8213/ab960f.
- R. Abbott, LIGO Scientific Collaboration, Virgo Collaboration, and KAGRA Collaboration and et al. Observation of Gravitational Waves from Two Neutron Star-Black Hole Coalescences. *The Astrophysical Journal Letters*, 915(1):L5, July 2021. doi: 10.3847/2041-8213/ac082e.
- B. P. Abbott, LIGO Scientific Collaboration, Virgo Collaboration, Kagra Collaboration, and et al. Prospects for observing and localizing gravitational-wave transients with Advanced

- LIGO, Advanced Virgo and KAGRA. *Living Reviews in Relativity*, 21(1):3, April 2018. doi: 10.1007/s41114-018-0012-9.
- M. Maggiore and et al. Science case for the Einstein telescope. *Journal of Cosmology and Astroparticle Physics*, 2020(03):050–050, March 2020. ISSN 1475-7516. doi: 10.1088/1475-7516/2020/03/050. URL <http://dx.doi.org/10.1088/1475-7516/2020/03/050>.
- M. Evans and et al. A Horizon Study for Cosmic Explorer: Science, Observatories, and Community. *arXiv e-prints*, art. arXiv:2109.09882, September 2021.
- H. A. Bethe, G. E. Brown, J. Applegate, and J. M. Lattimer. Equation of state in the gravitational collapse of stars. *Nuclear Physics A*, 324(2-3):487–533, July 1979. doi: 10.1016/0375-9474(79)90596-7.
- S. Chandrasekhar. The Maximum Mass of Ideal White Dwarfs. *The Astrophysical Journal*, 74: 81, July 1931. doi: 10.1086/143324.
- H.T. Janka. Explosion Mechanisms of Core-Collapse Supernovae. *Annual Review of Nuclear and Particle Science*, 62(1):407–451, November 2012. doi: 10.1146/annurev-nucl-102711-094901.
- H. Th. Janka, K. Langanke, A. Marek, G. Martínez-Pinedo, and B. Müller. Theory of core-collapse supernovae. *Physics Reports*, 442(1-6):38–74, April 2007. doi: 10.1016/j.physrep.2007.02.002.
- R. Diehl and et al. Radioactive ^{26}Al from massive stars in the Galaxy. *Nature*, 439(7072): 45–47, January 2006. doi: 10.1038/nature04364.
- S.Z. Li, Y.W. Yu, and Y. Huang. SN 1054: A pulsar-powered supernova? *Research in Astronomy and Astrophysics*, 15(11):1823, November 2015. doi: 10.1088/1674-4527/15/11/005.
- A. Arcones and F. K. Thielemann. Neutrino-driven wind simulations and nucleosynthesis of heavy elements. *Journal of Physics G Nuclear Physics*, 40(1):013201, January 2013. doi: 10.1088/0954-3899/40/1/013201.
- S. Woosley and H. T. Janka. The physics of core-collapse supernovae. *Nature Physics*, 1(3): 147–154, December 2005. doi: 10.1038/nphys172.
- M. Prakash, I. Bombaci, M. Prakash, P. J. Ellis, J. M. Lattimer, and R. Knorren. Composition and structure of protoneutron stars. *Physics Report*, 280:1–77, January 1997. doi: 10.1016/S0370-1573(96)00023-3.
- A. Pascal, J. Novak, and M. Oertel. Proto-neutron star evolution with improved charged-current neutrino-nucleon interactions. *Monthly Notices of the Royal Astronomical Society*, 511(1):356–370, March 2022. doi: 10.1093/mnras/stac016.
- P. Haensel, A. Y. Potekhin, and D. G. Yakovlev. *Neutron Stars 1 : Equation of State and Structure*, volume 326. Springer Science & Business Media, 2007, 2007a.

- J. R. Fuentes, C. M. Espinoza, A. Reisenegger, B. Shaw, B. W. Stappers, and A. G. Lyne. The glitch activity of neutron stars (Corrigendum). *Astronomy & Astrophysics*, 618:C1, October 2018. doi: 10.1051/0004-6361/201731519e.
- D. G. Ravenhall, C. J. Pethick, and J. R. Wilson. Structure of Matter below Nuclear Saturation Density. *Physical Review Letters*, 50(26):2066–2069, June 1983. doi: 10.1103/PhysRevLett.50.2066.
- H. Dinh Thi, A. F. Fantina, and F. Gulminelli. Properties of pasta phases in catalyzed neutron stars. *arXiv e-prints*, art. arXiv:2206.07969, June 2022.
- S. Typel and et al. CompOSE Reference Manual. *arXiv e-prints*, art. arXiv:2203.03209, March 2022.
- M. Oertel, M. Hempel, T. Klähn, and S. Typel. Equations of state for supernovae and compact stars. *Reviews of Modern Physics*, 89(1):015007, January 2017. doi: 10.1103/RevModPhys.89.015007.
- M. Dutra, O. Lourenço, S. S. Avancini, B. V. Carlson, A. Delfino, D. P. Menezes, C. Providência, S. Typel, and J. R. Stone. Relativistic mean-field hadronic models under nuclear matter constraints. *Physical Review C*, 90(5):055203, November 2014. doi: 10.1103/PhysRevC.90.055203.
- B. K. Agrawal. Asymmetric nuclear matter and neutron skin in an extended relativistic mean-field model. *Physical Review C*, 81(3):034323, March 2010. doi: 10.1103/PhysRevC.81.034323.
- S. Typel, G. Röpke, T. Klähn, D. Blaschke, and H. H. Wolter. Composition and thermodynamics of nuclear matter with light clusters. *Physical Review C*, 81(1):015803, January 2010. doi: 10.1103/PhysRevC.81.015803.
- G. A. Lalazissis, T. Nikšić, D. Vretenar, and P. Ring. New relativistic mean-field interaction with density-dependent meson-nucleon couplings. *Physical Review C*, 71(2):024312, February 2005. doi: 10.1103/PhysRevC.71.024312.
- T. Gaitanos, M. Di Toro, S. Typel, V. Baran, C. Fuchs, V. Greco, and H. H. Wolter. On the Lorentz structure of the symmetry energy. *Nuclear Physics A*, 732:24–48, February 2004. doi: 10.1016/j.nuclphysa.2003.12.001.
- W.C. Chen and J. Piekarewicz. Building relativistic mean field models for finite nuclei and neutron stars. *Physical Review C*, 90(4):044305, October 2014. doi: 10.1103/PhysRevC.90.044305.
- R. Negreiros, L. Tolos, M. Centelles, A. Ramos, and V. Dexheimer. Cooling of Small and Massive Hyperonic Stars. *The Astrophysical Journal*, 863(1):104, August 2018. doi: 10.3847/1538-4357/aad049.

- N. K. Glendenning and S. A. Moszkowski. Reconciliation of neutron-star masses and binding of the Lambda in hypernuclei. *Physical Review Letters*, 67:2414–1417, October 1991. doi: 10.1103/PhysRevLett.67.2414.
- B. D. Lackey, M. Nayyar, and B. J. Owen. Observational constraints on hyperons in neutron stars. *Phys. Rev. D*, 73(2):024021, January 2006. doi: 10.1103/PhysRevD.73.024021.
- C. J. Horowitz and J. Piekarewicz. Neutron Star Structure and the Neutron Radius of ^{208}Pb . *Physical Review Letters*, 86(25):5647–5650, June 2001. doi: 10.1103/PhysRevLett.86.5647.
- G. A. Lalazissis, J. König, and P. Ring. New parametrization for the Lagrangian density of relativistic mean field theory. *Physical Review C*, 55(1):540–543, January 1997. doi: 10.1103/PhysRevC.55.540.
- Y. Sugahara and H. Toki. Relativistic mean-field theory for unstable nuclei with non-linear σ and ω terms. *Nuclear Physics A*, 579(3):557–572, October 1994. doi: 10.1016/0375-9474(94)90923-7.
- C. Providência and A. Rabhi. Interplay between the symmetry energy and the strangeness content of neutron stars. *Physical Review C*, 87(5):055801, May 2013. doi: 10.1103/PhysRevC.87.055801.
- T. H. R. Skyrme. CVII. The nuclear surface. *Philosophical Magazine*, 1(11):1043–1054, November 1956. doi: 10.1080/14786435608238186.
- K. A. Brueckner, C. A. Levinson, and H. M. Mahmoud. Two-Body Forces and Nuclear Saturation. I. Central Forces. *Physical Review*, 95(1):217–228, July 1954. doi: 10.1103/PhysRev.95.217.
- N. Chamel, S. Goriely, and J. M. Pearson. Further explorations of Skyrme-Hartree-Fock-Bogoliubov mass formulas. XI. Stabilizing neutron stars against a ferromagnetic collapse. *Physical Review C*, 80(6):065804, December 2009. doi: 10.1103/PhysRevC.80.065804.
- S. Goriely, N. Chamel, and J. M. Pearson. Further explorations of Skyrme-Hartree-Fock-Bogoliubov mass formulas. XII. Stiffness and stability of neutron-star matter. *Physical Review C*, 82(3):035804, September 2010. doi: 10.1103/PhysRevC.82.035804.
- S. Goriely, N. Chamel, and J. M. Pearson. Further explorations of Skyrme-Hartree-Fock-Bogoliubov mass formulas. XIII. The 2012 atomic mass evaluation and the symmetry coefficient. *Physical Review C*, 88(2):024308, August 2013. doi: 10.1103/PhysRevC.88.024308.
- Eric Chabanat. *Interactions effectives pour des conditions extrêmes d'isospin*. PhD thesis, Université Claude Bernard Lyon-1, 43 Bs du 11 Novembre 1918, 69622 Villeurbanne, Cedex, France, March 1995.
- F. Douchin and P. Haensel. A unified equation of state of dense matter and neutron star structure. *Astronomy & Astrophysics*, 380:151–167, December 2001. doi: 10.1051/0004-6361:20011402.

- E. Chabanat, P. Bonche, P. Haensel, J. Meyer, and R. Schaeffer. A skyrme parametrization from subnuclear to neutron star densities part ii. nuclei far from stabilities. *Nuclear Physics A*, 635(1):231–256, 1998. ISSN 0375-9474. doi: [https://doi.org/10.1016/S0375-9474\(98\)00180-8](https://doi.org/10.1016/S0375-9474(98)00180-8). URL <https://www.sciencedirect.com/science/article/pii/S0375947498001808>.
- B. K. Agrawal, S. Shlomo, and V. Kim Au. Determination of the parameters of a Skyrme type effective interaction using the simulated annealing approach. *Physical Review C*, 72(1):014310, July 2005. doi: 10.1103/PhysRevC.72.014310.
- J. Friedrich and P. G. Reinhard. Skyrme-force parametrization: Least-squares fit to nuclear ground-state properties. *Physical Review C*, 33(1):335–351, January 1986. doi: 10.1103/PhysRevC.33.335.
- H. S. Köhler. Skyrme force and the mass formula. *Nuclear Physics A*, 258(2):301–316, February 1976. doi: 10.1016/0375-9474(76)90008-7.
- B. K. Agrawal, S. Shlomo, and V. Kim Au. Nuclear matter incompressibility coefficient in relativistic and nonrelativistic microscopic models. *Physical Review C*, 68(3):031304(R), September 2003. doi: 10.1103/PhysRevC.68.031304.
- L. Bennour, P. H. Heenen, P. Bonche, J. Dobaczewski, and H. Flocard. Charge distributions of ^{208}Pb , ^{206}Pb , and ^{205}Tl and the mean-field approximation. *Physical Review C*, 40(6):2834–2839, December 1989. doi: 10.1103/PhysRevC.40.2834.
- P. G. Reinhard, D. J. Dean, W. Nazarewicz, J. Dobaczewski, J. A. Maruhn, and M. R. Strayer. Shape coexistence and the effective nucleon-nucleon interaction. *Physical Review C*, 60(1):014316, July 1999. doi: 10.1103/PhysRevC.60.014316.
- P. G. Reinhard and H. Flocard. Nuclear effective forces and isotope shifts. *Nuclear Physics A*, 584(3):467–488, February 1995. doi: 10.1016/0375-9474(94)00770-N.
- W. Nazarewicz, J. Dobaczewski, T. R. Werner, J. A. Maruhn, P. G. Reinhard, K. Rutz, C. R. Chinn, A. S. Umar, and M. R. Strayer. Structure of proton drip-line nuclei around doubly magic ^{48}Ni . *Physical Review C*, 53(2):740–751, February 1996. doi: 10.1103/PhysRevC.53.740.
- J. W. Negele and D. Vautherin. Neutron star matter at sub-nuclear densities. *Nuclear Physics A*, 207(2):298–320, June 1973. doi: 10.1016/0375-9474(73)90349-7.
- F. Douchin and P. Haensel. Inner edge of neutron-star crust with SLy effective nucleon-nucleon interactions. *Physics Letters B*, 485(1-3):107–114, July 2000. doi: 10.1016/S0370-2693(00)00672-9.
- S. S. Avancini, L. Brito, J. R. Marinelli, D. P. Menezes, M. M. W. de Moraes, C. Providência, and A. M. Santos. Nuclear “pasta” phase within density dependent hadronic models. *Physical Review C*, 79(3):035804, March 2009. doi: 10.1103/PhysRevC.79.035804.

- G. Taranto, M. Baldo, and G. F. Burgio. Selecting microscopic equations of state. *Physical Review C*, 87(4):045803, April 2013. doi: 10.1103/PhysRevC.87.045803.
- B. K. Sharma, M. Centelles, X. Viñas, M. Baldo, and G. F. Burgio. Unified equation of state for neutron stars on a microscopic basis. *Astronomy & Astrophysics*, 584:A103, December 2015. doi: 10.1051/0004-6361/201526642.
- C. Drischler, J. W. Holt, and C. Wellenhofer. Chiral Effective Field Theory and the High-Density Nuclear Equation of State. *Annual Review of Nuclear and Particle Science*, 71:403–432, September 2021. doi: 10.1146/annurev-nucl-102419-041903.
- Isaac Vidaña. Hyperons in Finite and Infinite Nuclear Systems. *Universe*, 7(10):376, October 2021. doi: 10.3390/universe7100376.
- I. Bednarek, P. Haensel, J. L. Zdunik, M. Bejger, and R. Mańka. Hyperons in neutron-star cores and a $2 M_{\odot}$ pulsar. *Astronomy & Astrophysics*, 543:A157, July 2012. doi: 10.1051/0004-6361/201118560.
- Debarati Chatterjee and Isaac Vidaña. Do hyperons exist in the interior of neutron stars? *European Physical Journal A*, 52:29, February 2016. doi: 10.1140/epja/i2016-16029-x.
- Isaac Vidaña. Hyperons and neutron stars. *Nuclear Physics A*, 914:367–376, September 2013. doi: 10.1016/j.nuclphysa.2013.01.015.
- M. Fortin, S. S. Avancini, C. Providência, and I. Vidaña. Hypernuclei and massive neutron stars. *Physical Review C*, 95(6):065803, June 2017. doi: 10.1103/PhysRevC.95.065803.
- M. Fortin, A. R. Raduta, S. Avancini, and C. Providência. Relativistic hypernuclear compact stars with calibrated equations of state. *Physical Review D*, 101(3):034017, February 2020. doi: 10.1103/PhysRevD.101.034017.
- C. Providência, M. Fortin, H. Pais, and A. Rabhi. Hyperonic stars and the symmetry energy. *Frontiers in Astronomy and Space Sciences*, 6:13, March 2019. doi: 10.3389/fspas.2019.00013.
- D. Blaschke and N. Chamel. *Phases of Dense Matter in Compact Stars*, pages 337–400. Springer International Publishing, Cham, 2018. ISBN 978-3-319-97616-7. doi: 10.1007/978-3-319-97616-7_7. URL https://doi.org/10.1007/978-3-319-97616-7_7.
- R. C. Pereira, P. Costa, and C. Providência. Two-solar-mass hybrid stars: A two model description using the Nambu-Jona-Lasinio quark model. *Physical Review D*, 94(9):094001, November 2016. doi: 10.1103/PhysRevD.94.094001.
- M. Ferreira, R. C. Pereira, and C. Providência. Neutron stars with large quark cores. *Physical Review D*, 101(12):123030, June 2020. doi: 10.1103/PhysRevD.101.123030.
- Márcio Ferreira, Renan Câmara Pereira, and Constança Providência. Hybrid stars with large strange quark cores constrained by GW170817. *Physical Review D*, 103(12):123020, June 2021. doi: 10.1103/PhysRevD.103.123020.

- C. Maieron, M. Baldo, G. F. Burgio, and H. J. Schulze. Hybrid stars with the color dielectric and the MIT bag models. *Physical Review D*, 70(4):043010, August 2004. doi: 10.1103/PhysRevD.70.043010.
- H. Chen, M. Baldo, G. F. Burgio, and H. J. Schulze. Hybrid stars with the Dyson-Schwinger quark model. *Physical Review D*, 84(10):105023, November 2011. doi: 10.1103/PhysRevD.84.105023.
- G. F. Burgio, H. J. Schulze, I. Vidaña, and J. B. Wei. Neutron stars and the nuclear equation of state. *Progress in Particle and Nuclear Physics*, 120:103879, September 2021. doi: 10.1016/j.pnpnp.2021.103879.
- M. Wang, G. Audi, A. H. Wapstra, F. G. Kondev, M. MacCormick, X. Xu, and B. Pfeiffer. The Ame2012 atomic mass evaluation. *Chinese Physics C*, 36(12):003, December 2012. doi: 10.1088/1674-1137/36/12/003.
- M. Wang, G. Audi, F. G. Kondev, W. J. Huang, S. Naimi, and Xing Xu. The AME2016 atomic mass evaluation (II). Tables, graphs and references. *Chinese Physics C*, 41(3):030003, March 2017. doi: 10.1088/1674-1137/41/3/030003.
- M. Wang, W. J. Huang, F. G. Kondev, G. Audi, and S. Naimi. The AME 2020 atomic mass evaluation (II). Tables, graphs and references. *Chinese Physics C*, 45(3):030003, March 2021a. doi: 10.1088/1674-1137/abddaf.
- D. S. Ahn and et al. Location of the Neutron Dripline at Fluorine and Neon. *Physical Review Letter*, 123(21):212501, November 2019. doi: 10.1103/PhysRevLett.123.212501.
- M. B. Tsang and et al. Constraints on the symmetry energy and neutron skins from experiments and theory. *Physical Review C*, 86(1):015803, July 2012. doi: 10.1103/PhysRevC.86.015803.
- P. Möller, W. D. Myers, H. Sagawa, and S. Yoshida. New Finite-Range Droplet Mass Model and Equation-of-State Parameters. *Physical Review Letters*, 108(5):052501, February 2012. doi: 10.1103/PhysRevLett.108.052501.
- P. Danielewicz. Surface symmetry energy. *Nuclear Physics A*, 727(3):233–268, November 2003. doi: 10.1016/j.nuclphysa.2003.08.001.
- P. Danielewicz and J. Lee. Symmetry energy II: Isobaric analog states. *Nuclear Physics A*, 922:1–70, February 2014. doi: 10.1016/j.nuclphysa.2013.11.005.
- M. Kortelainen, T. Lesinski, J. Moré, W. Nazarewicz, J. Sarich, N. Schunck, M. V. Stoitsov, and S. Wild. Nuclear energy density optimization. *Physical Review C*, 82(2):024313, August 2010. doi: 10.1103/PhysRevC.82.024313.
- M. B. Tsang, Yingxun Zhang, P. Danielewicz, M. Famiano, Zhuxia Li, W. G. Lynch, and A. W. Steiner. Constraints on the Density Dependence of the Symmetry Energy. *Physical Review Letters*, 102(12):122701, March 2009. doi: 10.1103/PhysRevLett.102.122701.

- C. J. Horowitz, K. S. Kumar, and R. Michaels. Electroweak measurements of neutron densities in CREX and PREX at JLab, USA. *European Physical Journal A*, 50:48, February 2014. doi: 10.1140/epja/i2014-14048-3.
- D. Adhikari, et al., and PREX Collaboration. Accurate Determination of the Neutron Skin Thickness of ^{208}Pb through Parity-Violation in Electron Scattering. *Physical Review Letters*, 126(17):172502, April 2021. doi: 10.1103/PhysRevLett.126.172502.
- D. Adhikari and et al. Precision Determination of the Neutral Weak Form Factor of ^{48}Ca . *arXiv e-prints*, art. arXiv:2205.11593, May 2022.
- L. W. Chen, C. M. Ko, B. A. Li, and J. Xu. Density slope of the nuclear symmetry energy from the neutron skin thickness of heavy nuclei. *Physical Review C*, 82(2):024321, August 2010. doi: 10.1103/PhysRevC.82.024321.
- B. T. Reed, F. J. Fattoyev, C. J. Horowitz, and J. Piekarewicz. Implications of PREX-2 on the Equation of State of Neutron-Rich Matter. *Physical Review Letters*, 126(17):172503, April 2021. doi: 10.1103/PhysRevLett.126.172503.
- E. Yüksel and N. Paar. Implications of parity-violating electron scattering experiments on ^{48}Ca (CREX) and ^{208}Pb (PREX-II) for nuclear energy density functionals. *arXiv e-prints*, art. arXiv:2206.06527, June 2022.
- U. Garg and G. Colò. The compression-mode giant resonances and nuclear incompressibility. *Progress in Particle and Nuclear Physics*, 101:55–95, July 2018. doi: 10.1016/j.pnpnp.2018.03.001.
- C. Drischler, R. J. Furnstahl, J. A. Melendez, and D. R. Phillips. How Well Do We Know the Neutron-Matter Equation of State at the Densities Inside Neutron Stars? A Bayesian Approach with Correlated Uncertainties. *Physical Review Letters*, 125(20):202702, November 2020. doi: 10.1103/PhysRevLett.125.202702.
- L. Trippa, G. Colò, and E. Vigezzi. Giant dipole resonance as a quantitative constraint on the symmetry energy. *Physical Review C*, 77(6):061304(R), June 2008. doi: 10.1103/PhysRevC.77.061304.
- S. Gandolfi, A. Gezerlis, and J. Carlson. Neutron Matter from Low to High Density. *Annual Review of Nuclear and Particle Science*, 65(1):303–328, October 2015. doi: 10.1146/annurev-nucl-102014-021957.
- E. Chabanat, P. Bonche, P. Haensel, J. Meyer, and R. Schaeffer. A skyrme parametrization from subnuclear to neutron star densities. *Nuclear Physics A*, 627(4):710–746, 1997. ISSN 0375-9474. doi: [https://doi.org/10.1016/S0375-9474\(97\)00596-4](https://doi.org/10.1016/S0375-9474(97)00596-4). URL <https://www.sciencedirect.com/science/article/pii/S0375947497005964>.
- P. Danielewicz and J. Lee. Symmetry energy i: Semi-infinite matter. *Nuclear Physics A*, 818(1-2):36–96, February 2009. ISSN 0375-9474. doi: 10.1016/j.nuclphysa.2008.11.007. URL <http://dx.doi.org/10.1016/j.nuclphysa.2008.11.007>.

- A. Einstein. Die Feldgleichungen der Gravitation. *Sitzungsberichte der Königlich Preußischen Akademie der Wissenschaften (Berlin)*, pages 844–847, January 1915.
- S. L. Shapiro and S. A. Teukolsky. *Black Holes, White Dwarfs and Neutron Stars: The Physics of Compact Objects*. Wiley, 1983, 1986.
- P. Haensel, A. Y. Potekhin, and D. G. Yakovlev. *Neutron Stars 1 : Equation of State and Structure*, volume 326. Springer, 2007b.
- Paulo Freire. Pulsar mass measurements and tests of general relativity, 2021. URL https://www3.mpifr-bonn.mpg.de/staff/pfreire/NS_masses.html.
- F. Özel and P. Freire. Masses, radii, and the equation of state of neutron stars. *Annual Review of Astronomy and Astrophysics*, 54(1):401–440, Sep 2016. ISSN 1545-4282. doi: 10.1146/annurev-astro-081915-023322. URL <http://dx.doi.org/10.1146/annurev-astro-081915-023322>.
- J. Alsing, H. O. Silva, and E. Berti. Evidence for a maximum mass cut-off in the neutron star mass distribution and constraints on the equation of state. *Monthly Notices of the Royal Astronomical Society*, 478(1):1377–1391, July 2018. doi: 10.1093/mnras/sty1065.
- James M. Lattimer. The Nuclear Equation of State and Neutron Star Masses. *Annual Review of Nuclear and Particle Science*, 62(1):485–515, November 2012. doi: 10.1146/annurev-nucl-102711-095018.
- The LIGO Scientific Collaboration, the Virgo Collaboration, the KAGRA Collaboration, and et al. GWTC-3: Compact Binary Coalescences Observed by LIGO and Virgo During the Second Part of the Third Observing Run. *arXiv e-prints*, art. arXiv:2111.03606, November 2021.
- C. W. Misner, K. S. Thorne, and J. A. Wheeler. *Gravitation*. Freeman & Co. 1973, 1973.
- Z. Arzoumanian and et al. The NANOGrav 11-year data set: High-precision timing of 45 millisecond pulsars. *The Astrophysical Journal Supplement Series*, 235(2):37, April 2018. doi: 10.3847/1538-4365/aab5b0. URL <https://doi.org/10.3847/1538-4365/aab5b0>.
- R. W. Romani, D. Kandel, A. V. Filippenko, T. G. Brink, and W. Zheng. PSR J0952-0607: The Fastest and Heaviest Known Galactic Neutron Star. *The Astrophysical Journal Letters*, 934(2):L17, August 2022. doi: 10.3847/2041-8213/ac8007.
- H. T. Cromartie, E. Fonseca, S. M. Ransom, P. B. Demorest, Z. Arzoumanian, H. Blumer, P. R. Brook, M. E. DeCesar, T. Dolch, J. A. Ellis, and et al. Relativistic Shapiro delay measurements of an extremely massive millisecond pulsar. *Nature Astronomy*, 4(1):72–76, September 2019. ISSN 2397-3366. doi: 10.1038/s41550-019-0880-2. URL <http://dx.doi.org/10.1038/s41550-019-0880-2>.

- E. Fonseca and et al. Refined Mass and Geometric Measurements of the High-mass PSR J0740+6620. *Astrophysical Journal, Letters*, 915(1):L12, July 2021. doi: 10.3847/2041-8213/ac03b8.
- J. M. Lattimer and M. Prakash. Neutron Star Structure and the Equation of State. *Astrophysical Journal*, 550(1):426–442, March 2001. doi: 10.1086/319702.
- Riley T. E. and et al. A NICER View of PSR J0030+0451: Millisecond Pulsar Parameter Estimation. *The Astrophysical Journal*, 887(1):L21, dec 2019. doi: 10.3847/2041-8213/ab481c. URL <https://doi.org/10.3847/2041-8213/ab481c>.
- M. C. Miller and et al. PSR J0030+0451 Mass and Radius from NICER Data and Implications for the Properties of Neutron Star Matter. *Astrophysical Journal, Letters*, 887(1):L24, December 2019. doi: 10.3847/2041-8213/ab50c5.
- T. E. Riley and et al. A NICER View of the Massive Pulsar PSR J0740+6620 Informed by Radio Timing and XMM-Newton Spectroscopy. *Astrophysical Journal, Letters*, 918(2):L27, September 2021. doi: 10.3847/2041-8213/ac0a81.
- M. C. Miller, F. K. Lamb, A. J. Dittmann, S. Bogdanov, Z. Arzoumanian, K. C. Gendreau, S. Guillot, W. C. G. Ho, J. M. Lattimer, M. Loewenstein, S. M. Morsink, P. S. Ray, M. T. Wolff, C. L. Baker, T. Cazeau, S. Manthripragada, C. B. Markwardt, T. Okajima, S. Pollard, I. Cognard, H. T. Cromartie, E. Fonseca, L. Guillemot, M. Kerr, A. Parthasarathy, T. T. Pennucci, S. Ransom, and I. Stairs. The Radius of PSR J0740+6620 from NICER and XMM-Newton Data. *Astrophysical Journal, Letters*, 918(2):L28, September 2021. doi: 10.3847/2041-8213/ac089b.
- A. Yu Potekhin. Atmospheres and radiating surfaces of neutron stars. *Physics Uspekhi*, 57(8): 735-770, August 2014. doi: 10.3367/UFNe.0184.201408a.0793.
- K. Yagi and N. Yunes. Approximate universal relations for neutron stars and quark stars. *Physics Reports*, 681:1–72, April 2017. doi: 10.1016/j.physrep.2017.03.002.
- A. W. Steiner, J. M. Lattimer, and E. F. Brown. The Neutron Star Mass-Radius Relation and the Equation of State of Dense Matter. *Astrophysical Journal, Letters*, 765(1):L5, March 2013. doi: 10.1088/2041-8205/765/1/L5.
- S. Guillot, Mathieu Servillat, N. A. Webb, and R. E. Rutledge. Measurement of the Radius of Neutron Stars with High Signal-to-noise Quiescent Low-mass X-Ray Binaries in Globular Clusters. *Astrophysical Journal*, 772(1):7, July 2013. doi: 10.1088/0004-637X/772/1/7.
- P. Haensel, J. L. Zdunik, M. Bejger, and J. M. Lattimer. Keplerian frequency of uniformly rotating neutron stars and strange stars. *Astronomy and Astrophysics*, 502(2):605–610, August 2009. doi: 10.1051/0004-6361/200811605.
- J. B. Hartle. Slowly Rotating Relativistic Stars. I. Equations of Structure. *The Astrophysical Journal*, 150:1005, December 1967. doi: 10.1086/149400.

- E. Gourgoulhon, P. Grandclément, J. A. Marck, J. Novak, and K. Taniguchi. LORENE: Spectral methods differential equations solver. Astrophysics Source Code Library, record ascl:1608.018, August 2016.
- P. Haensel, M. Bejger, M. Fortin, and L. Zdunik. Rotating neutron stars with exotic cores: masses, radii, stability. *European Physical Journal A*, 52:59, March 2016. doi: 10.1140/epja/i2016-16059-4.
- S. K. Greif, K. Hebeler, J. M. Lattimer, C. J. Pethick, and A. Schwenk. Equation of state constraints from nuclear physics, neutron star masses, and future moment of inertia measurements. *The Astrophysical Journal*, 901(2):155, October 2020. ISSN 1538-4357. doi: 10.3847/1538-4357/abaf55. URL <http://dx.doi.org/10.3847/1538-4357/abaf55>.
- J. M. Lattimer and B. F. Schutz. Constraining the equation of state with moment of inertia measurements. *The Astrophysical Journal*, 629(2):979–984, Aug 2005. ISSN 1538-4357. doi: 10.1086/431543. URL <http://dx.doi.org/10.1086/431543>.
- M. A. McLaughlin, F. Camilo, M. Burgay, N. D’Amico, B. C. Joshi, M. Kramer, D. R. Lorimer, A. G. Lyne, R. N. Manchester, and A. Possenti. X-ray emission from the double pulsar system j0737-3039. *The Astrophysical Journal*, 605(1):L41–L44, Mar 2004. ISSN 1538-4357. doi: 10.1086/392511. URL <http://dx.doi.org/10.1086/392511>.
- H. O. Silva, A. M. Holgado, A. Cárdenas-Avendaño, and N. Yunes. Astrophysical and Theoretical Physics Implications from Multimessenger Neutron Star Observations. *Physical Review Letters*, 126(18):181101, May 2021. doi: 10.1103/PhysRevLett.126.181101.
- T. Damour and A. Nagar. Relativistic tidal properties of neutron stars. *Physical Review D*, 80(8):084035, October 2009. doi: 10.1103/PhysRevD.80.084035.
- T. Hinderer. Tidal Love Numbers of Neutron Stars. *Astrophysical Journal*, 677(2):1216–1220, April 2008. doi: 10.1086/533487.
- M. Fortin, G. Taranto, G. F. Burgio, P. Haensel, H. J. Schulze, and J. L. Zdunik. Thermal states of neutron stars with a consistent model of interior. *Monthly Notices of the Royal Astronomical Society*, 475(4):5010–5022, April 2018. doi: 10.1093/mnras/sty147.
- J. M. Lattimer, C. J. Pethick, M. Prakash, and P. Haensel. Direct URCA process in neutron stars. *Physical Review Letters*, 66(21):2701–2704, May 1991. doi: 10.1103/PhysRevLett.66.2701.
- M. Fortin, A. R. Raduta, S. Avancini, and C. Providência. Thermal evolution of relativistic hyperonic compact stars with calibrated equations of state. *Physical Review D*, 103(8):083004, April 2021. doi: 10.1103/PhysRevD.103.083004.
- Jacob Golomb and Colm Talbot. Hierarchical Inference of Binary Neutron Star Mass Distribution and Equation of State with Gravitational Waves. *Astrophysical Journal*, 926(1):79, February 2022. doi: 10.3847/1538-4357/ac43bc.

- Salvatore Vitale, Davide Gerosa, Will M. Farr, and Stephen R. Taylor. Inferring the properties of a population of compact binaries in presence of selection effects. *arXiv e-prints*, art. arXiv:2007.05579, July 2020.
- C. A. Raithel and F. Özel. Measurement of the Nuclear Symmetry Energy Parameters from Gravitational-wave Events. *Astrophysical Journal*, 885(2):121, November 2019. doi: 10.3847/1538-4357/ab48e6.
- H. Güven, K. Bozkurt, E. Khan, and J. Margueron. Multimessenger and multiphysics Bayesian inference for the GW170817 binary neutron star merger. *Physical Review C*, 102(1):015805, July 2020. doi: 10.1103/PhysRevC.102.015805.
- T. Malik, N. Alam, M. Fortin, C. Providência, B. K. Agrawal, T. K. Jha, Bharat Kumar, and S. K. Patra. GW170817: Constraining the nuclear matter equation of state from the neutron star tidal deformability. *Phys. Rev. C*, 98(3):035804, September 2018. doi: 10.1103/PhysRevC.98.035804.
- Reed Essick, Philippe Landry, Achim Schwenk, and Ingo Tews. Detailed examination of astrophysical constraints on the symmetry energy and the neutron skin of ^{208}Pb with minimal modeling assumptions. *Physical Review C*, 104(6):065804, December 2021. doi: 10.1103/PhysRevC.104.065804.
- R. Somasundaram, C. Drischler, I. Tews, and J. Margueron. Constraints on the nuclear symmetry energy from asymmetric-matter calculations with chiral NN and 3N interactions. *Physical Review C*, 103(4):045803, April 2021. doi: 10.1103/PhysRevC.103.045803.
- M. Al-Mamun, A. W. Steiner, J. Nättilä, J. Lange, R. O’Shaughnessy, I. Tews, S. Gandolfi, C. Heinke, and S. Han. Combining Electromagnetic and Gravitational-Wave Constraints on Neutron-Star Masses and Radii. *Physical Review Letters*, 126(6):061101, February 2021. doi: 10.1103/PhysRevLett.126.061101.
- T. Malik and C. Providência. Bayesian inference of signatures of hyperons inside neutron stars. *Physical Review D*, 106(6):063024, September 2022. doi: 10.1103/PhysRevD.106.063024.
- S. Ghosh, B. K. Pradhan, D. Chatterjee, and J. Schaffner-Bielich. Multi-Physics Constraints at Different Densities to Probe Nuclear Symmetry Energy in Hyperonic Neutron Stars. *Frontiers in Astronomy and Space Sciences*, 9:864294, March 2022. doi: 10.3389/fspas.2022.864294.
- C.Y. Tsang, M.B. Tsang, Pawel Danielewicz, F.J. Fattoyev, and W.G. Lynch. Insights on skyrme parameters from gw170817. *Physics Letters B*, 796:1–5, 2019. ISSN 0370-2693. doi: <https://doi.org/10.1016/j.physletb.2019.05.055>. URL <https://www.sciencedirect.com/science/article/pii/S0370269319304575>.
- H. Pais and C. Providência. Vlasov formalism for extended relativistic mean field models: The crust-core transition and the stellar matter equation of state. *Physical Review C*, 94(1),

- Jul 2016. ISSN 2469-9993. doi: 10.1103/physrevc.94.015808. URL <http://dx.doi.org/10.1103/PhysRevC.94.015808>.
- K. Oyamatsu and K. Iida. Symmetry energy at subnuclear densities and nuclei in neutron star crusts. *Physical Review C*, 75(1), Jan 2007. ISSN 1089-490X. doi: 10.1103/physrevc.75.015801. URL <http://dx.doi.org/10.1103/PhysRevC.75.015801>.
- C. Ducoin, J. Margueron, C. Providência, and I. Vidaña. Core-crust transition in neutron stars: Predictivity of density developments. *Phys. Rev. C*, 83(4):045810, April 2011. doi: 10.1103/PhysRevC.83.045810.
- Jérôme Margueron, Rudiney Hoffmann Casali, and Francesca Gulminelli. Equation of state for dense nucleonic matter from metamodeling. II. Predictions for neutron star properties. *Physical Review C*, 97(2):025806, February 2018. doi: 10.1103/PhysRevC.97.025806.
- M. Fortin, C. Providência, Ad. R. Raduta, F. Gulminelli, J. L. Zdunik, P. Haensel, and M. Bejger. Neutron star radii and crusts: Uncertainties and unified equations of state. *Physical Review C*, 94(3):035804, September 2016. doi: 10.1103/PhysRevC.94.035804.
- F. Grill, H. Pais, C. Providência, I. Vidaña, and S. S. Avancini. Equation of state and thickness of the inner crust of neutron stars. *Phys. Rev. C*, 90(4):045803, October 2014. doi: 10.1103/PhysRevC.90.045803.
- S. B. Rüster, M. Hempel, and J. Schaffner-Bielich. Outer crust of nonaccreting cold neutron stars. *Phys. Rev. C*, 73(3):035804, March 2006. doi: 10.1103/PhysRevC.73.035804.
- G. Baym, C. Pethick, and P. Sutherland. The Ground State of Matter at High Densities: Equation of State and Stellar Models. *The Astrophysical Journal*, 170:299, December 1971. doi: 10.1086/151216.
- P. Haensel and B. Pichon. Experimental nuclear masses and the ground state of cold dense matter. *Astronomy & Astrophysics*, 283(1):313–318, March 1994.
- J. M. Pearson, N. Chamel, A. Y. Potekhin, A. F. Fantina, C. Ducoin, A. K. Dutta, and S. Goriely. Unified equations of state for cold non-accreting neutron stars with Brussels-Montreal functionals - I. Role of symmetry energy. *Monthly Notices of the Royal Astronomical Society*, 481(3):2994–3026, December 2018. doi: 10.1093/mnras/sty2413.
- F. Gulminelli and Ad. R. Raduta. Unified treatment of subsaturation stellar matter at zero and finite temperature. *Physical Review C*, 92(5):055803, November 2015. doi: 10.1103/PhysRevC.92.055803.
- Xavier Viñas, Claudia Gonzalez-Boquera, Mario Centelles, Chiranjib Mondal, and Luis M. Robledo. Unified equation of state for neutron stars based on the gogny interaction. *Symmetry*, 13(9), 2021. ISSN 2073-8994. doi: 10.3390/sym13091613. URL <https://www.mdpi.com/2073-8994/13/9/1613>.

- Vishal Parmar, H. C. Das, Ankit Kumar, M. K. Sharma, and S. K. Patra. Crustal properties of a neutron star within an effective relativistic mean-field model. *Physical Review D*, 105(4):043017, February 2022. doi: 10.1103/PhysRevD.105.043017.
- A. F. Fantina, N. Chamel, J. M. Pearson, and S. Goriely. Neutron star properties with unified equations of state of dense matter. *Astronomy & Astrophysics*, 559:A128, November 2013. doi: 10.1051/0004-6361/201321884.
- J. L. Zdunik, M. Fortin, and P. Haensel. Neutron star properties and the equation of state for the core. *Astronomy & Astrophysics*, 599:A119, March 2017. doi: 10.1051/0004-6361/201629975.
- M. Dutra, O. Lourenço, J. S. Sá Martins, A. Delfino, J. R. Stone, and P. D. Stevenson. Skyrme interaction and nuclear matter constraints. *Physical Review C*, 85(3):035201, March 2012. doi: 10.1103/PhysRevC.85.035201.
- C. A. Raithel, F. Özel, and D. Psaltis. Tidal Deformability from GW170817 as a Direct Probe of the Neutron Star Radius. *Astrophys. J. Letters*, 857(2):L23, April 2018. doi: 10.3847/2041-8213/aabcbf.
- K. Yagi and N. Yunes. I-love-q: Unexpected universal relations for neutron stars and quark stars. *Science*, 341(6144):365–368, Jul 2013. ISSN 1095-9203. doi: 10.1126/science.1236462. URL <http://dx.doi.org/10.1126/science.1236462>.
- G. Shen, C. J. Horowitz, and S. Teige. New equation of state for astrophysical simulations. *Physical Review C*, 83(3):035802, March 2011. doi: 10.1103/PhysRevC.83.035802.
- A. Akmal, V. R. Pandharipande, and D. G. Ravenhall. Equation of state of nucleon matter and neutron star structure. *Physical Review C*, 58(3):1804–1828, September 1998. doi: 10.1103/PhysRevC.58.1804.
- A. Maselli, V. Cardoso, V. Ferrari, L. Gualtieri, and P. Pani. Equation-of-state-independent relations in neutron stars. *Phys. Rev. D*, 88(2):023007, July 2013. doi: 10.1103/PhysRevD.88.023007.
- A. W. Steiner, J. M. Lattimer, and E. F. Brown. Neutron star radii, universal relations, and the role of prior distributions. *European Physical Journal A*, 52:18, February 2016. doi: 10.1140/epja/i2016-16018-1.
- C. Breu and L. Rezzolla. Maximum mass, moment of inertia and compactness of relativistic stars. *Mon. Not. Roy. Astron. Soc.*, 459(1):646–656, June 2016. doi: 10.1093/mnras/stw575.
- T. Zhao and J. M. Lattimer. Tidal deformabilities and neutron star mergers. *Phys. Rev. D*, 98(6):063020, September 2018. doi: 10.1103/PhysRevD.98.063020.
- J. B. Wei, A. Figura, G. F. Burgio, H. Chen, and H. J. Schulze. Neutron star universal relations with microscopic equations of state. *Journal of Physics G Nuclear Physics*, 46(3):034001, March 2019. doi: 10.1088/1361-6471/aaf95c.

- A. R. Raduta, M. Oertel, and A. Sedrakian. Proto-neutron stars with heavy baryons and universal relations. *Monthly Notices of the Royal Astronomical Society*, 499(1):914–931, November 2020. doi: 10.1093/mnras/staa2491.
- S. Khadkikar, A. R. Raduta, M. Oertel, and A. Sedrakian. Maximum mass of compact stars from gravitational wave events with finite-temperature equations of state. *Physical Review C*, 103(5):055811, May 2021. doi: 10.1103/PhysRevC.103.055811.
- K. Yagi, L. C. Stein, G. Pappas, N. Yunes, and T. A. Apostolatos. Why i-love-q: Explaining why universality emerges in compact objects. *Physical Review D*, 90(6), Sep 2014. ISSN 1550-2368. doi: 10.1103/physrevd.90.063010. URL <http://dx.doi.org/10.1103/PhysRevD.90.063010>.
- Y.-H. Sham, T. K. Chan, L.-M. Lin, and P. T. Leung. Unveiling the universality of i-love-q relations. *The Astrophysical Journal*, 798(2):121, January 2015. ISSN 1538-4357. doi: 10.1088/0004-637x/798/2/121. URL <http://dx.doi.org/10.1088/0004-637X/798/2/121>.
- D. A. Godzieba, R. Gamba, D. Radice, and S. Bernuzzi. Updated universal relations for tidal deformabilities of neutron stars from phenomenological equations of state. *Physical Review D*, 103(6):063036, March 2021. doi: 10.1103/PhysRevD.103.063036.
- J. S. Read, B. D. Lackey, B. J. Owen, and J. L. Friedman. Constraints on a phenomenologically parametrized neutron-star equation of state. *Phys. Rev. D*, 79(12):124032, June 2009. doi: 10.1103/PhysRevD.79.124032.
- L. Baiotti. Gravitational waves from neutron star mergers and their relation to the nuclear equation of state. *Progress in Particle and Nuclear Physics*, 109:103714, Nov 2019. ISSN 0146-6410. doi: 10.1016/j.ppnp.2019.103714. URL <http://dx.doi.org/10.1016/j.ppnp.2019.103714>.
- L. Lindblom. Causal representations of neutron-star equations of state. *Physical Review D*, 97(12):123019, June 2018. doi: 10.1103/PhysRevD.97.123019.
- S. De, D. Finstad, J. M. Lattimer, D. A. Brown, E. Berger, and C. M. Biwer. Tidal Deformabilities and Radii of Neutron Stars from the Observation of GW170817. *Physical Review Letters*, 121(9):091102, August 2018. doi: 10.1103/PhysRevLett.121.091102.
- R. E. Rutledge, L. Bildsten, E. F. Brown, G. G. Pavlov, V. E. Zavlin, and G. Ushomirsky. Crustal Emission and the Quiescent Spectrum of the Neutron Star in KS 1731-260. *The Astrophysical Journal*, 580(1):413–422, November 2002. doi: 10.1086/342745.
- E. M. Cackett, R. Wijnands, M. Linares, J. M. Miller, J. Homan, and W. H. G. Lewin. Cooling of the quasi-persistent neutron star X-ray transients KS 1731-260 and MXB 1659-29. *Monthly Notices of the Royal Astronomical Society*, 372(1):479–488, October 2006. doi: 10.1111/j.1365-2966.2006.10895.x.
- R. Wijnands, N. Degenaar, and D. Page. Cooling of Accretion-Heated Neutron Stars. *Journal of Astrophysics and Astronomy*, 38(3):49, September 2017. doi: 10.1007/s12036-017-9466-5.

- N. Degenaar, R. Wijnands, A. Bahramian, G. R. Sivakoff, C. O. Heinke, E. F. Brown, J. K. Fridriksson, J. Homan, E. M. Cackett, A. Cumming, J. M. Miller, D. Altamirano, and D. Pooley. Neutron star crust cooling in the Terzan 5 X-ray transient Swift J174805.3-244637. *Monthly Notices of the Royal Astronomical Society*, 451(2):2071–2081, August 2015. doi: 10.1093/mnras/stv1054.
- T. M. Tauris, M. Kramer, and N. Langer. Recycling Pulsars: spins, masses and ages. In Joeri van Leeuwen, editor, *Neutron Stars and Pulsars: Challenges and Opportunities after 80 years*, volume 291, pages 137–140, March 2013. doi: 10.1017/S1743921312023393.
- A G Suvorov and A Melatos. Recycled pulsars with multipolar magnetospheres from accretion-induced magnetic burial. *Monthly Notices of the Royal Astronomical Society*, 499(3):3243–3254, Oct 2020. ISSN 1365-2966. doi: 10.1093/mnras/staa3132.
- L. Bildsten. Thermonuclear Burning on Rapidly Accreting Neutron Stars. In R. Buccheri, J. van Paradijs, and A. Alpar, editors, *The Many Faces of Neutron Stars.*, volume 515 of *NATO Advanced Study Institute (ASI) Series C*, page 419, January 1998.
- A. Parikh, J. José, G. Sala, and C. Iliadis. Nucleosynthesis in type I X-ray bursts. *Progress in Particle and Nuclear Physics*, 69:225–253, March 2013. doi: 10.1016/j.pnpnp.2012.11.002.
- Z. Meisel, A. Deibel, L. Keek, P. Shternin, and J. Elfritz. Nuclear physics of the outer layers of accreting neutron stars. *Journal of Physics G Nuclear Physics*, 45(9):093001, September 2018. doi: 10.1088/1361-6471/aad171.
- N. Chamel and P. Haensel. Physics of neutron star crusts. *Living Reviews in Relativity*, 11(1), December 2008. ISSN 1433-8351. doi: 10.12942/lrr-2008-10. URL <http://dx.doi.org/10.12942/lrr-2008-10>.
- P. Haensel and J. L. Zdunik. Models of crustal heating in accreting neutron stars. *Astronomy & Astrophysics*, 480(2):459–464, March 2008. doi: 10.1051/0004-6361:20078578.
- A. F. Fantina, J. L. Zdunik, N. Chamel, J. M. Pearson, P. Haensel, and S. Goriely. Crustal heating in accreting neutron stars from the nuclear energy-density functional theory. I. Proton shell effects and neutron-matter constraint. *Astronomy & Astrophysics*, 620:A105, December 2018. doi: 10.1051/0004-6361/201833605.
- A. Y. Potekhin and G. Chabrier. Crust structure and thermal evolution of neutron stars in soft X-ray transients. *Astronomy & Astrophysics*, 645:A102, January 2021. doi: 10.1051/0004-6361/202039006.
- N. N. Shchekilin, M. E. Gusakov, and A. I. Chugunov. Accreting neutron stars: heating of the upper layers of the inner crust. *Monthly Notices of the Royal Astronomical Society*, 515(1):L6–L10, September 2022. doi: 10.1093/mnrasl/slac059.
- D. G. Yakovlev, L. Gasques, and M. Wiescher. Pycnonuclear burning of ^{34}Ne in accreting neutron stars. *Monthly Notices of the Royal Astronomical Society*, 371(3):1322–1326, September 2006. doi: 10.1111/j.1365-2966.2006.10753.x.

- F. D. Mackie and G. Baym. Compressible liquid drop nuclear model and mass formula. *nphysa*, 285(2):332–348, July 1977. doi: 10.1016/0375-9474(77)90256-1.
- A. F. Fantina, J. L. Zdunik, N. Chamel, J. M. Pearson, L. Suleiman, and S. Goriely. Accreting neutron stars from the nuclear energy-density functional theory. II. Equation of state and global properties. *Astronomy & Astrophysics*, 665:A74, September 2022. doi: 10.1051/0004-6361/202243715.
- E. F. Brown, L. Bildsten, and R. E. Rutledge. Crustal heating and quiescent emission from transiently accreting neutron stars. *"Astrophysical Journal"*, 504(2):L95–L98, Sep 1998. ISSN 0004-637X. doi: 10.1086/311578. URL <http://dx.doi.org/10.1086/311578>.
- E. F. Brown and A. Cumming. Mapping crustal heating with the cooling light curves of quasi-persistent transients. *"Astrophysical Journal"*, 698(2):1020–1032, May 2009. ISSN 1538-4357. doi: 10.1088/0004-637x/698/2/1020. URL <http://dx.doi.org/10.1088/0004-637X/698/2/1020>.
- A. Bonanno and V. Urpin. IGR J17480-2446: a new class of accreting binaries? *Astronomy & Astrophysics*, 574:A63, February 2015. doi: 10.1051/0004-6361/201424524.
- N. Degenaar. Probing the physics of neutron stars using Terzan 5. Chandra Proposal, September 2015.
- M. C. Baglio, P. D’Avanzo, S. Campana, P. Goldoni, N. Masetti, T. Muñoz-Darias, V. Patiño-Álvarez, and V. Chavushyan. 1rxs j180408.9-342058: An ultra compact x-ray binary candidate with a transient jet. *Astronomy & Astrophysics*, 587:A102, February 2016. ISSN 1432-0746. doi: 10.1051/0004-6361/201527147. URL <http://dx.doi.org/10.1051/0004-6361/201527147>.
- A Marino, M Del Santo, M Cocchi, A D’Aì, A Segreto, C Ferrigno, T Di Salvo, J Malzac, R Iaria, and L Burderi. New insights on the puzzling LMXB 1RXS J180408.9-342058: the intermediate state, the clocked type-I X-ray bursts, and much more. *Monthly Notices of the Royal Astronomical Society*, 490(2):2300–2314, 10 2019. ISSN 0035-8711. doi: 10.1093/mnras/stz2726. URL <https://doi.org/10.1093/mnras/stz2726>.
- A. S. Parikh, R. Wijnands, N. Degenaar, L. S. Ootes, D. Page, D. Altamirano, E. M. Cackett, A. T. Deller, N. Gusinskaia, J. W. T. Hessels, J. Homan, M. Linares, J. M. Miller, and J. C. A. Miller-Jones. Potential cooling of an accretion-heated neutron star crust in the low-mass X-ray binary 1RXS J180408.9–342058. *"Monthly Notices of the Royal Astronomical Society"*, 466(4):4074–4082, 01 2017. ISSN 0035-8711. doi: 10.1093/mnras/stw3388. URL <https://doi.org/10.1093/mnras/stw3388>.
- J. L. Zdunik, M. Fortin, and P. Haensel. Neutron star properties and the equation of state for its core, 2016.

- N. Chamel, A. F. Fantina, L. Suleiman, J. L. Zdunik, and P. Haensel. Heating in Magnetar Crusts from Electron Captures. *Universe*, 7(6):193, 2021. doi: 10.3390/universe7060193. URL <https://hal.archives-ouvertes.fr/hal-03260055>.
- S. Gupta, E. F. Brown, H. Schatz, P. Möller, and K. L. Kratz. Heating in the Accreted Neutron Star Ocean: Implications for Superburst Ignition. *"Astrophysical Journal"*, 662(2):1188–1197, June 2007. doi: 10.1086/517869.
- N. Chamel, A. F. Fantina, J. L. Zdunik, and P. Haensel. Neutron drip transition in accreting and nonaccreting neutron star crusts. *Physical Review C*, 91(5):055803, May 2015. doi: 10.1103/PhysRevC.91.055803.
- S. S. Gupta, T. Kawano, and P. Möller. Neutron Reactions in Accreting Neutron Stars: A New Pathway to Efficient Crust Heating. *Physical Review Letters*, 101(23):231101, December 2008. doi: 10.1103/PhysRevLett.101.231101.
- R. Lau and et al. Nuclear Reactions in the Crusts of Accreting Neutron Stars. *"Astrophysical Journal"*, 859(1):62, May 2018. doi: 10.3847/1538-4357/aabfe0.
- O. Hamil, J. R. Stone, M. Urbanec, and G. Urbancová. Braking index of isolated pulsars. *Physical Review D*, 91(6):063007, March 2015. doi: 10.1103/PhysRevD.91.063007.
- B. Haskell and A. Patruno. Are Gravitational Waves Spinning Down PSR J 1023 +0038 ? *Physical Review Letters*, 119(16):161103, October 2017. doi: 10.1103/PhysRevLett.119.161103.
- G. Ushomirsky, C. Cutler, and L. Bildsten. Deformations of accreting neutron star crusts and gravitational wave emission. *Monthly Notices of the Royal Astronomical Society*, 319(3): 902–932, December 2000. doi: 10.1046/j.1365-8711.2000.03938.x.
- N. K. Johnson-McDaniel and B. J. Owen. Maximum elastic deformations of relativistic stars. *Physical Review D*, 88(4):044004, August 2013. doi: 10.1103/PhysRevD.88.044004.
- K. Iida and K. Sato. Spin Down of Neutron Stars and Compositional Transitions in the Cold Crustal Matter. *Astrophysical Journal*, 477(1):294–312, March 1997. doi: 10.1086/303685.
- M. E. Gusakov, E. M. Kantor, and A. Reisenegger. Rotation-induced deep crustal heating of millisecond pulsars. *"Monthly Notices of the Royal Astronomical Society"*, 453(1):L36–L40, October 2015. doi: 10.1093/mnrasl/slv095.
- J. L. Zdunik, P. Haensel, and E. Gourgoulhon. The crust of rotating strange quark stars. *Astronomy & Astrophysics*, 372:535–543, June 2001. doi: 10.1051/0004-6361:20010510.
- C. A. Faucher-Giguère and V. M. Kaspi. Birth and Evolution of Isolated Radio Pulsars. *"Astrophysical Journal"*, 643(1):332–355, May 2006. doi: 10.1086/501516.
- H.-T. Janka, A. Wongwathanarat, and M. Kramer. Supernova Fallback as Origin of Neutron Star Spins and Spin-kick Alignment. *"Astrophysical Journal"*, 926(1):9, February 2022. doi: 10.3847/1538-4357/ac403c.

- M. Fortin, F. Grill, J. Margueron, Dany Page, and N. Sandulescu. Thermalization time and specific heat of the neutron stars crust. *Phys. Rev. C*, 82:065804, Dec 2010. doi: 10.1103/PhysRevC.82.065804. URL <https://link.aps.org/doi/10.1103/PhysRevC.82.065804>.
- L.P. Pitaevskii and E.M. Lifshitz. *Physical Kinetics: Volume 10*. Elsevier Science, 2012. ISBN 9780080570495. URL <https://books.google.fr/books?id=DTHxPDfV0fQC>.
- L. D. Landau and E. M. Lifshitz. *Fluid Mechanics*, volume 6 of *Course of Theoretical Physics*. Pergamon, second edition, 1987. URL <http://www.worldcat.org/isbn/9781483161044>.
- L. D. Landau and E. M. Lifshitz. *Statistical Physics Part I*. Elsevier, Amsterdam, 3rd edition, 1980. bibtex: landa;b;sp80.
- O. Blaes, R. Blandford, P. Madau, and S. Koonin. Slowly Accreting Neutron Stars and the Origin of Gamma-Ray Bursts. *Astrophysical Journal*, 363:612, November 1990. doi: 10.1086/169371.
- J. R. Gustafson. Wolfgang pauli 1900 to 1930: His early physics in jungian perspective. 2010.
- M. Wang, W. J. Huang, F. G. Kondev, G. Audi, and S. Naimi. The AME 2020 atomic mass evaluation (II). Tables, graphs and references. *Chinese Physics C*, 45(3):030003, March 2021b. doi: 10.1088/1674-1137/abddaf.
- D. Lunney, J. M. Pearson, and C. Thibault. Recent trends in the determination of nuclear masses. *Reviews of Modern Physics*, 75(3):1021–1082, August 2003. doi: 10.1103/RevModPhys.75.1021.
- P. A. M. Dirac. The Quantum Theory of the Emission and Absorption of Radiation. *Proceedings of the Royal Society of London Series A*, 114(767):243–265, March 1927. doi: 10.1098/rspa.1927.0039.
- M. Goldhaber, L. Grodzins, and A. W. Sunyar. Helicity of Neutrinos. *Physical Review*, 109(3):1015–1017, February 1958. doi: 10.1103/PhysRev.109.1015.
- Bogdan Povh, Klaus Rith, Christoph Scholz, and Frank Zetsche. *Particles and nuclei: an introduction to the physical concepts*. Springer, 2004, 2004.
- National Nuclear Data Center. From ensdf database as of december 9, 2022., 2022. URL <https://www.nndc.bnl.gov/ensdf/>.
- H. L. Crawford, R. V. F. Janssens, P. F. Mantica, J. S. Berryman, R. Broda, M. P. Carpenter, N. Cieplicka, B. Fornal, G. F. Grinyer, N. Hoteling, B. P. Kay, T. Lauritsen, K. Minamisono, I. Stefanescu, J. B. Stoker, W. B. Walters, and S. Zhu. β decay and isomeric properties of neutron-rich ca and sc isotopes. *Phys. Rev. C*, 82:014311, Jul 2010. doi: 10.1103/PhysRevC.82.014311. URL <https://link.aps.org/doi/10.1103/PhysRevC.82.014311>.
- A. S. Parikh, R. Wijnands, J. Homan, N. Degenaar, B. Wolvers, L. S. Ootes, and D. Page. Unexpected late-time temperature increase observed in the two neutron star crust-cooling

- sources XTE J1701-462 and EXO 0748-676. *Astronomy & Astrophysics*, 638:L2, June 2020. doi: 10.1051/0004-6361/202038198.
- R. L. Merritt. Crustal Cooling in the Neutron Star Low-Mass X-Ray Binary KS 1731-260. Master's thesis, Wayne State University, Michigan, January 2017.
- J. K. Fridriksson, J. Homan, R. Wijnands, M. Méndez, D. Altamirano, E. M. Cackett, E. F. Brown, T. M. Belloni, N. Degenaar, and W. H. G. Lewin. Rapid Cooling of the Neutron Star in the Quiescent Super-Eddington Transient XTE J1701-462. *Astrophysical Journal*, 714(1):270–286, May 2010. doi: 10.1088/0004-637X/714/1/270.
- L. S. Ootes, S. Vats, D. Page, R. Wijnands, A. S. Parikh, N. Degenaar, M. J. P. Wijngaarden, D. Altamirano, A. Bahramian, E. M. Cackett, C. O. Heinke, J. Homan, and J. M. Miller. Continued cooling of the accretion-heated neutron star crust in the X-ray transient IGR J17480-2446 located in the globular cluster Terzan 5. *Monthly Notices of the Royal Astronomical Society*, 487(1):1447–1461, July 2019. doi: 10.1093/mnras/stz1406.
- A. S. Parikh, R. Wijnands, L. S. Ootes, D. Page, N. Degenaar, A. Bahramian, E. F. Brown, E. M. Cackett, A. Cumming, C. Heinke, J. Homan, A. Rouco Escorial, and M. J. P. Wijngaarden. Consistent accretion-induced heating of the neutron-star crust in MXB 1659-29 during two different outbursts. *Astronomy & Astrophysics*, 624:A84, April 2019. doi: 10.1051/0004-6361/201834412.
- N. Degenaar and R. Wijnands. The soft quiescent spectrum of the transiently accreting 11-Hz X-ray pulsar in the globular cluster Terzan 5. *Monthly Notices of the Royal Astronomical Society*, 412(1):L68–L72, March 2011. doi: 10.1111/j.1745-3933.2011.01007.x.
- Laura S. Ootes, Dany Page, Rudy Wijnands, and Nathalie Degenaar. Neutron star crust cooling in ks 1731–260: the influence of accretion outburst variability on the crustal temperature evolution. *Monthly Notices of the Royal Astronomical Society*, 461(4):4400–4405, Jul 2016. ISSN 1365-2966. doi: 10.1093/mnras/stw1799. URL <http://dx.doi.org/10.1093/mnras/stw1799>.
- N. Chamel, A. F. Fantina, J. L. Zdunik, and P. Haensel. Experimental constraints on shallow heating in accreting neutron-star crusts. *Physical Review C*, 102(1):015804, July 2020. doi: 10.1103/PhysRevC.102.015804.
- Z. Medin and A. Cumming. Time-dependent, Compositionally Driven Convection in the Oceans of Accreting Neutron Stars. *The Astrophysical Journal*, 802(1):29, March 2015. doi: 10.1088/0004-637X/802/1/29.
- D. G. Yakovlev, A. D. Kaminker, O. Y. Gnedin, and P. Haensel. Neutrino emission from neutron stars. *Physics Reports*, 354(1-2):1–155, November 2001. doi: 10.1016/S0370-1573(00)00131-9.

- M. Prakash, M. Prakash, J. M. Lattimer, and C. J. Pethick. Rapid Cooling of Neutron Stars by Hyperons and Delta Isobars. *The Astrophysical Journal, Letters*, 390:L77, May 1992. doi: 10.1086/186376.
- H. Y. Chiu and E. E. Salpeter. Surface X-Ray Emission from Neutron Stars. *Physical Review Letters*, 12(15):413–415, April 1964. doi: 10.1103/PhysRevLett.12.413.
- D. Page. Neutron Star Cooling: I. In Werner Becker, editor, *Astrophysics and Space Science Library*, volume 357 of *Astrophysics and Space Science Library*, page 247, January 2009. doi: 10.1007/978-3-540-76965-1_11.
- B. L. Friman and O. V. Maxwell. Neutrino emissivities of neutron stars. *The Astrophysical Journal*, 232:541–557, September 1979. doi: 10.1086/157313.
- D. G. Yakovlev and K. P. Levenfish. Modified URCA process in neutron star cores. *Astronomy & Astrophysics*, 297:717, May 1995.
- D. Blaschke, G. Ropke, H. Schulz, A. D. Sedrakian, and D. N. Voskresensky. Nuclear in-medium effects and neutrino emissivity of neutron stars. *Monthly Notices of the Royal Astronomical Society*, 273(3):596–602, April 1995. doi: 10.1093/mnras/273.3.596.
- A.V. Senatorov and D.N. Voskresensky. Collective excitations in nucleonic matter and the problem of cooling of neutron stars. *Physics Letters B*, 184(2):119–124, 1987. ISSN 0370-2693. doi: [https://doi.org/10.1016/0370-2693\(87\)90553-3](https://doi.org/10.1016/0370-2693(87)90553-3). URL <https://www.sciencedirect.com/science/article/pii/0370269387905533>.
- D. N. Voskresensky. Neutrino Cooling of Neutron Stars: Medium Effects. In D. Blaschke, N. K. Glendenning, and A. Sedrakian, editors, *Physics of Neutron Star Interiors*, volume 578, page 467. 2001.
- P. S. Shternin, M. Baldo, and P. Haensel. In-medium enhancement of the modified Urca neutrino reaction rates. *Physics Letters B*, 786:28–34, November 2018. doi: 10.1016/j.physletb.2018.09.035.
- M G. Alford and S. P. Harris. β equilibrium in neutron-star mergers. *Physical Review C*, 98(6):065806, December 2018. doi: 10.1103/PhysRevC.98.065806.
- L. P. Kadanoff, G. Baym, and J. D. Trimmer. Quantum Statistical Mechanics. *American Journal of Physics*, 31(4):309–309, April 1963. doi: 10.1119/1.1969482.
- T. Matsubara. A New Approach to Quantum-Statistical Mechanics. *Progress of Theoretical Physics*, 14(4):351–378, 10 1955. ISSN 0033-068X. doi: 10.1143/PTP.14.351. URL <https://doi.org/10.1143/PTP.14.351>.
- T. Lundberg and R. Pasechnik. Thermal Field Theory in real-time formalism: concepts and applications for particle decays. *European Physical Journal A*, 57(2):71, February 2021. doi: 10.1140/epja/s10050-020-00288-5.

- P.A Zyla and m. et al. Review of Particle Physics, 2020-2021. RPP. *PTEP*, 2020:083C01. 2093 p, 2020. doi: 10.1093/ptep/ptaa104. URL <https://cds.cern.ch/record/2729066>.
- R. L. Workman and et al. Review of Particle Physics. *PTEP*, 2022:083C01, 2022. doi: 10.1093/ptep/ptac097.
- N. Cabibbo. Unitary Symmetry and Leptonic Decays. *Physical Review Letters*, 10(12):531–533, June 1963. doi: 10.1103/PhysRevLett.10.531.
- M. Kobayashi and T. Maskawa. CP-Violation in the Renormalizable Theory of Weak Interaction. *Progress of Theoretical Physics*, 49(2):652–657, February 1973. doi: 10.1143/PTP.49.652.
- M. Oertel, A. Pascal, M. Mancini, and J. Novak. Improved neutrino-nucleon interactions in dense and hot matter for numerical simulations. *Physical Review C*, 102(3):035802, September 2020. doi: 10.1103/PhysRevC.102.035802.
- J. A. Pons, S. Reddy, M. Prakash, J. Lattimer, and J. A. Miralles. Evolution of Protoneutron stars. In J. Paul, T. Montmerle, and E. Aubourg, editors, *19th Texas Symposium on Relativistic Astrophysics and Cosmology*, page 252, December 1998.
- CompOSE. Rg(sly4) general purpose equation of state as of december 9, 2022., 2022. URL <https://compose.obspm.fr/eos/134>.
- C. J. Horowitz and M. A. Pérez-García. Realistic neutrino opacities for supernova simulations with correlations and weak magnetism. *Physical Review C*, 68(2):025803, August 2003. doi: 10.1103/PhysRevC.68.025803.
- S. Bacca, K. Hally, M. Liebendörfer, A. Perego, C. J. Pethick, and A. Schwenk. Neutrino Processes in Partially Degenerate Neutron Matter. *The Astrophysical Journal*, 758(1):34, October 2012. doi: 10.1088/0004-637X/758/1/34.
- N. Metropolis. Monte-Carlo: In the Beginning and Some Great Expectations. In R. Alcouffe, R. Dautray, A. Forster, G. Ledonois, and B. Mercier, editors, *Lecture Notes in Physics, Berlin Springer Verlag*, volume 240, page 62. 1985. doi: 10.1007/BFb0049035.
- S. Hannestad and G. Raffelt. Supernova Neutrino Opacity from Nucleon-Nucleon Bremsstrahlung and Related Processes. *The Astrophysical Journal*, 507(1):339–352, November 1998. doi: 10.1086/306303.
- R. G. Timmermans, A. Yu. Korchin, E. N. van Dalen, and A. E. Dieperink. Soft electroweak bremsstrahlung: Theorems and astrophysical relevance. *Physical Review C*, 65(6):064007, June 2002. doi: 10.1103/PhysRevC.65.064007.
- A. Schmitt and P. Shternin. Reaction Rates and Transport in Neutron Stars. In Luciano Rezzolla, Pierre Pizzochero, David Ian Jones, Nanda Rea, and Isaac Vidaña, editors, *Astrophysics and Space Science Library*, volume 457 of *Astrophysics and Space Science Library*, page 455, January 2018. doi: 10.1007/978-3-319-97616-7_9.

Dany Page. NSCOOL code from d. page, 2006. URL <http://www.astroscu.unam.mx/neutrones/NSCool/>.

Morgane Fortin. NSCOOL code from d. page revised by m. fortin, 2020. URL https://github.com/ganetin/Crust_cooling.